Towards Bio-inspired Photonic Vapour Sensors

Timothy Andrew Starkey

School of Physics

University of Exeter

A thesis submitted for the degree of

Doctor of Philosophy

August 2014

Towards Bio-inspired Photonic Vapour Sensors

Submitted by Timothy Andrew Starkey to the University of Exeter as a thesis for the degree of Doctor of Philosophy in Physics
August 2014

This thesis is available for Library use on the understanding that it is copyright material and that no quotation from the thesis may be published without proper acknowledgement.

I certify that all material in this thesis that is not my own work has been identified and that no material has previously been submitted and approved for the award of a degree by this or any other University.

Timothy Andrew Starkey
August 2014

This thesis is dedicated to the memory of
Valerie Hilton and Raymond Starkey,
both of whom are sorely missed.

Acknowledgements

The production of this thesis is a testament to the collective knowledge, wisdom, time, effort and support of many brilliant people, so here I would like to thank those people that have been with me for the ride...

First, I thank my supervisor Prof. Pete Vukusic for giving me this wonderful opportunity; it has been a truly formative and valuable time in my life! There have been beers, curries, travelling and badminton, all intermixed with the occasional supervisor meeting. I certainly did not expect to leave university knowing quite so much about butterflies, so thank you Pete!

Second, I extend my utmost gratitude to Dr. Radislav Potyrailo. Radislav certainly made this Ph.D an exciting three and a bit years of research, and I feel very fortunate to have worked with him. Whenever I have spent time with Radislav, I have always tried to absorb some of his energy, creativity and passion for science and sensing. I am especially thankful to Radislav and Elena for making me feel so welcome during my stay at General Electric – there was always a plentiful supply of devilled eggs and cold beer!

In the School of Physics I have been fortunate to be surrounded by people with so much enthusiasm for their subject that they have shared it around. Prof. Roy Sambles certain falls into this category. Roy first suggested I consider a Ph.D in Exeter, so I thank him for putting the idea into my head, and for the useful questions and discussions. I also thank Prof. GP Srivastava for agreeing to add me to his ever-growing list of mentees. GP is another person who is always willing to give up his time to stop and check that things are going smoothly, in and out of physics. Having both Roy and GP as personal tutors was definitely one of the few bonuses of studying combined honours!

The close family of natural photonicists deserve a special thank you; these are the people that I always sat and scratched my head with first. In Pete's absence Dr. Stephen Luke and his associate Dr. Caroline Pouya did an excellent job of filling the unofficial secondary supervisor. Steve was always on hand to provide the most unavailing comfort in times of Ph.D woes,

with the classic "*it will all be fine*" (and I guess it is). I have still yet to meet anybody with quite the same outlook on Ph.Ds, so Steve certainly added some much needed variety. Dr. Caroline Pouya has always been there for all sorts of interesting conversations and bug-related questions... I will never forget that Caz once loved a post timepiece subway, and that she always insists she will not travel as a passenger in my car, until the next time she is a passenger in my car. Dr. Matt Nixon has been there from the start, and I find it reassuring to see that we have both been affected over the course of a Ph.D, probably by physics and an absence of windows... a fact need only be evidenced by the amount of shouting and unnecessary beatings that have occurred since I moved down to the basement. This madness comes from somewhere and Dr. Alfie Lethbridge has always been around to top it up to a full measure. Alfredshift is certainly the culprit for developing my irritating habit of unnessesarily joining words together and other physics-related puns. Luke McDonald and Ali Humphrey are the other current basementeers. Rather than thank Luke, I'm going to apologise for any long-lasting psychological damage that I might have caused: "*how do you get that beetle so shiny?*". I offer Ali a big thank you for all of his varied group meeting presentations over the past three years (yeah?!).

The wider photonics group has been a great environment to work in thanks to these people: Dr. Ed Stone, Dr. Celia Butler, Dr. Melita Taylor, Dr. Lizzy Brock, Dr. Matt Biginton, Dr. Peter Hale, Dr. Sam Hornett, Prof. Al Hibbins, Dr. Al Murray, Dr. Simon Berry, Joe Dockrey, Laura Parke, Dr. Sara Núnez-Sáñchez, Dr. Nina Meinzer, Dr. Ian Hooper, Nick Cole, Ben Tremain, Gareth Ward, and Chris Forrest and the numerous others that I've forgotten (sorry). Laura deserves extra credit for her patience, and for taking me to the pub when it was sunny. Another essential group of people have been the Imperial patrons, in particular Dave Colridge, Dr. James Bell and Dr. Barbara Sarri!

Leading up to writing my own thesis I witnessed many people doing battle with theirs. Of those people Dr. Helen Rance prepared me most for what was about to happen! Helen has been a fab housemate and friend, so a great big thank you for that!

Chester Burbidge – thank you for being a great friend and housemate. I do not 'judgement' you for leaving when you did! I also thank Dr. Daniel Smith for the countless fingers of Johnnie Walker we both consumed whilst he was writing "*the novel*".

Cheers to Dr. Chris Holmes, Dr. Matt Lockyear and the RC contingent who were always around for a quick rad coffee to find out 'WosGoss?', and the occasional surf.

I also thank those Stratford friends, particularly Marc Downes and Sam Thorpe, who are always there to go out for a quick catch-up over a beer on my sporadic visits home, and who are always quite content in knowing quite simply that I do something with butterflies. Dr. Rebecca Atkinson, knowingly or not, was hugely influential in my continued study at Exeter, and I thank her for the nurture that got me to this stage. Sam Godding has been a never-ending source of obscure physics questions, curries, beer and hangovers (then bacon). Sam thank you for being there to keep my sanity, and occasionally testing it.

I extend my huge thanks to my family, Mum, Dad and Alison, for their love and support during my time in Exeter.

Abstract

Many highly-evolved bio-photonic structures, which tailor the propagation of light by coherent optical scattering, have been investigated. These natural designs, which have many diverse ecological functions, are becoming increasingly studied as sources of innovation and inspiration for a range of scientific, technological, and commercial applications. The brilliant blue colour reflected from the scales of the *Morpho* butterfly is just one example of nature's ability to manipulate light and colour strongly.

In this thesis, the photonic structure present in the scales of the *Morpho* butterfly is investigated as a source of bio-inspiration in the pursuit of high-performance photonic vapour sensors. The intention of this is to outperform classical sensor approaches which traditionally suffer from poor selectivity between chemical species. By measuring the change in reflectance from the iridescent scales of the *Morpho* butterfly, both a sensitive and, critically, a selective response to chemical vapours can be obtained. Here, the origin of this unique multivariable vapour-induced optical response is investigated, and this biological template is further explored as a source of innovation for the mature field of chemical sensing.

By using synergy between experimental and theoretical techniques, a mechanism for the sensitive and selective response of the *Morpho* butterfly's scales to different chemical vapour environments is elucidated. This mechanism arises from combined chemical and physical effects within the photonic nanostructure. Following this, demonstrations of this biological template's vapour response attributes, which have large and desirable diversity in the optical responses, are made. These response attributes are visualised in the spectral changes associated with optical excitation conditions, such as from different angles and polarisation states, and also in the temporal response profiles. Finally, theoretical sensor designs that outperform the *Morpho* scales are described. Simple principles that might improve the currently unacceptable levels of selectivity in contemporary sensor implementations are outlined and the vapour response of a *Morpho*-inspired photonic structure is presented.

Contents

Contents i

List of Figures vii

List of Tables xiii

1 Thesis Overview 1

1.1 Thesis outline . . . 2

2 Overview of Colour Production in Biological Systems 7

2.1 Introduction . . . 7

2.2 Historical perspective . . . 9

2.3 Biological photonic crystals . . . 10

2.3.1 Biological photonic crystals in 1D . . . 10

2.3.2 Biological photonic crystals in 2D . . . 12

2.3.3 Biological photonic crystals in 3D . . . 14

2.4 Colour production in biological structures through diffraction and scattering . . . 16

2.4.1 Diffraction grating structures . . . 17

2.4.2 Scattering structures . . . 17

2.5 Colour mechanisms and bio-inspired applications of *Morpho* butterflies . 18

2.5.1 Iridescent scales in butterflies . . . 18

2.5.2 Overview of colour production in *Morpho* butterflies . . . 18

2.5.3 *Morpho*-related bio-inspired applications . . . 25

2.6 Summary . . . 28

3 Photonics Theory 29

3.1 Introduction . . . 29

3.2 Maxwell's equations . . . 30

3.3 Photonic crystals . . . 30

3.4 The reflection of electromagnetic waves at a boundary . . . 34
3.4.1 Reflection from a single interface . . . 34
3.4.2 Reflection from a thin film . . . 38
3.5 Interference from a multilayer stack . . . 39
3.6 Factors affecting reflectance in 1D biological systems . . . 41
3.6.1 Effect of number of layers . . . 41
3.6.2 Angle-dependence of reflection . . . 43
3.6.3 Effect of refractive index contrast . . . 45
3.6.4 Effect of optical absorption . . . 46
3.7 Diffraction from periodic structures . . . 47
3.8 Summary . . . 48

4 Overview of Classical Chemical Sensing 49
4.1 Introduction . . . 49
4.2 Definition of a chemical sensor . . . 50
4.3 Design principles of a chemical sensor . . . 50
4.3.1 The sensor receptor . . . 51
4.3.2 The sensor transducer . . . 52
4.3.3 Signal processing . . . 53
4.4 Characteristics and attributes of an ideal sensor . . . 54
4.5 Optical sensors . . . 55
4.5.1 Waveguide sensors . . . 57
4.5.2 Interferometers . . . 58
4.5.3 Surface plasmon resonance sensors . . . 59
4.5.4 Photonic crystals . . . 61
4.5.5 Other photonic sensors . . . 64
4.6 Sensor arrays . . . 65
4.7 Summary . . . 65

5 Theoretical, Experimental and Data Analysis Techniques 67
5.1 Experimental methods . . . 68
5.1.1 Introduction . . . 68
5.1.2 Optical measurements . . . 68
5.1.3 Vapour generation . . . 69
5.1.4 Example measurement . . . 71
5.2 Photonic simulation techniques . . . 72
5.2.1 Introduction . . . 72
5.2.2 Transfer Matrix Method (TMM) . . . 72

5.2.3 Finite Element Method (FEM) . . . 74
5.2.4 Finite-Difference Time-Domain (FDTD) method . . . 79
5.3 Multivariate analysis tools . . . 80
5.3.1 Introduction . . . 80
5.3.2 Principal Components Analysis (PCA) . . . 81
5.4 Summary . . . 85

6 The Vapour Response of *Morpho* Butterflies 87
6.1 Introduction . . . 87
6.2 Background . . . 88
6.3 *Morpho sulkowskyi's* photonic structure . . . 89
6.4 Experimentally observed vapour response . . . 91
6.4.1 Wetting of a *Morpho* wing . . . 91
6.4.2 Observations of low-concentration vapour exposures . . . 92
6.4.2.1 Humidity cycles . . . 93
6.4.2.2 Vapour cycles . . . 95
6.4.2.3 Summary . . . 97
6.5 Mechanism of unique vapour response . . . 97
6.5.1 Optical modelling of *Morpho* vapour responses . . . 98
6.5.1.1 Developing a model for optical simulations . . . 98
6.5.1.2 Uniform vapour adsorption . . . 99
6.5.1.3 Another adsorption hypothesis . . . 102
6.5.1.4 Preferential vapour adsorption . . . 103
6.5.2 Experimental evidence of vapour mechanism . . . 110
6.5.3 Origin of the naturally occurring chemical gradient . . . 112
6.6 Conclusions . . . 113

7 High-Performance Sensing using *Morpho* Scales 117
7.1 Introduction . . . 117
7.2 Diversity in optical response . . . 117
7.2.1 Experimental measurements . . . 118
7.2.2 Theoretical model . . . 119
7.2.3 Spectral diversity in vapour response . . . 121
7.2.4 Temporal-dependence of vapour response . . . 122
7.2.5 Polarisation-dependence of vapour response . . . 124
7.2.6 Angle-dependence of vapour response . . . 128
7.2.7 Discussion . . . 128
7.3 Effect of measurement condition on vapour response . . . 131

7.3.1 Experimental measurement conditions . . . 131
7.3.2 Comparison of temporal measurements . . . 132
7.3.3 Comparison of spectral measurements . . . 134
7.3.4 Comparison of Principal Components Analysis . . . 134
7.3.5 Summary . . . 137
7.4 Functionalisation of natural *Morpho* scales . . . 138
7.4.1 Optical modelling of 'functionalised' photonic structure . . . 138
7.4.2 Summary . . . 143
7.5 Conclusions . . . 143

8 Bio-inspiration for Selective Sensors 145
8.1 Introduction . . . 145
8.2 Vapour selectivity of multilayered films . . . 146
8.2.1 Vapour adsorption upon multilayer lamellae . . . 147
8.2.2 Chirped multilayer designs . . . 153
8.2.3 Summary . . . 158
8.3 Exploration of bio-inspired 'tree'-like structures for vapour sensing . . . 159
8.3.1 Evolution of reflectance properties: from multilayers to ridge-lamellae structures . . . 160
8.3.1.1 Model development . . . 160
8.3.1.2 Spectral features . . . 161
8.3.1.3 Resonance and electromagnetic field enhancement . . . 163
8.3.2 Investigation of *Morpho*-like structures for sensing applications . . . 165
8.3.2.1 Refractive-index sensing with resonant modes . . . 165
8.3.2.2 Vapour selectivity of ridge-lamellae nanostructures . . . 169
8.3.3 Vapour response of nanofabricated structures . . . 173
8.4 Conclusions . . . 175

9 Conclusions and Future Work 177
9.1 Conclusions . . . 177
9.2 Future work . . . 181
9.3 Publications and presentations . . . 183
9.3.1 Refereed papers . . . 183
9.3.2 Conference proceedings . . . 184
9.3.3 Oral presentations . . . 184
9.3.4 Poster presentations . . . 184
9.3.5 Online presentations . . . 185

A Vapour Generation and Concentration 187

B Experimental Evidence for the Vapour Response Mechanism 189

C Analysis of Vapour Adsorption on Chirped Multilayers 197

D High-Q Resonances in Bio-inspired Dielectric Structures 203

References 211

Contents

List of Figures

2.1 Examples of a metallic and a non-metallic colour appearance achieved in two biological reflectors using 1D photonic crystal arrangements. . . . 11
2.2 Examples of biological 2D photonic crystal arrangements present in the peacock feather and the polychaete worm *Pherusa* sp. 13
2.3 Electron microscopy of the 3D photonic crystal arrangement within the scales of the *Parides sesostris* butterfly. 15
2.4 Diamond photonic crystal structure present in the weevil *Lamprocyphus augustus*. 15
2.5 Cross-section images of two different coloured wing-scales of the beetle *Eupholus magnificus*, revealing differences in the order, which gives rise to the different scale colour. 16
2.6 Schematic illustrations of the classifications of iridescent scales. 19
2.7 Appearance and scale structure of *Morpho rhetenor*. 22
2.8 Appearance and scale structure of *Morpho didius*. 23
2.9 Iridescent photonic *Morpho*-mimetic makeup. 26
2.10 Schematic of *Morpho* butterfly sensing principle. 27

3.1 Reduced Brillouin zone schematics comparing a homogeneous non-dispersive dielectric slab and a 1D photonic crystal. 33
3.2 Schematic illustrations for the analysis of the reflectance and transmittance of radiation at an interface. 34
3.3 Schematic diagrams for the treatment of multiple reflections within a thin film. 39
3.4 Reflectance dependance on number of layers for a typical ideal multilayer film. 42
3.5 Reflectance dependance on incident angle for an ideal multilayer film. . 44
3.6 Reflectance map showing the theoretical dependence of normal incidence reflectance on refractive index contrast for an ideal multilayer 46

3.7 The effect on reflectance at normal incidence of absorption coefficient for an ideal multilayer. 47

4.1 Schematic of basic sensor operation. 51
4.2 Sensor schematic for a sensing film coated transducer, displaying the competing requirements for a selective and reversible sensor. 52
4.3 Growth of research entries for chemical, and optical chemical sensors. . . 56
4.4 Sensor schematics for extrinsic and intrinsic type waveguide sensors that operate through amplitude and wavelength modulation. 58
4.5 A schematic representation of a Surface Plasmon Resonance sensor in the Kretschmann configuration. 60
4.6 Examples of two 3D photonic structures used for optical sensing. 62
4.7 Colorimetric array illustrating sensor array fingerprint principle 66

5.1 Schematic diagram of bifurcated probe apparatus. 69
5.2 Schematic diagram and a photograph of the bubbler vapour generator. . 71
5.3 Typical spectral reflectance data from the wings of *Morpho rhetenor* for two methanol vapour exposures. 73
5.4 Schematic representation of an example unit cell for FEM modelling. . . 76
5.5 Schematic diagram of a single mesh element in which the electric field components are interpolated from during the solution process. 77
5.6 Images displaying mesh and electric field plots upon the unit cell for FEM modelling. 78
5.7 Schematic of a single Yee cell in Cartesian coordinates. Each E-field component is positioned at the centre of the edge, and the H-field component at the centre of the face. 79
5.8 Diagram of different statistical methods used for the quantification and classification of multivariate datasets. 81
5.9 Example PCA analysis of normal distributions with different mean and standard deviation values. 83

6.1 A photograph and comparison of reflectance of a male *Morpho sulkowskyi* butterfly with the *Morpho rhetenor*. 90
6.2 Transmission electron micrographs of a cross-section though a *Morpho sulkowskyi* ground scale. 91
6.3 Photograph and theoretical spectra illustrating the effect of wetting the *Morpho* photonic structure. 92

6.4 Diagram illustrating the experimental arrangement of the illumination of the sample, and collection of scattered light, with respect to the orientation of the ridge structure within the wing scales. 93
6.5 The optical response of *Morpho rhetenor* to 10% relative humidity. . . . 94
6.6 Optical response and PCA analysis of *Morpho rhetenor* upon exposure to water, methanol and ethanol vapours at 0.18 P/P_0. 96
6.7 Images showing the development of a *Morpho*-like structure for optical simulations. 99
6.8 Reflectance spectra for uniform vapour adsorption of model vapour upon the *Morpho* nanostructure. 100
6.9 PCA scores analysis of calculated reflectance of uniformly covered *Morpho*-ridge structures, which demonstrates a non-selective vapour response. 101
6.10 PCA loadings data for uniform vapour coverage on the *Morpho* structure. 102
6.11 Visualisation of the conformal epicuticle layer covering the ridge structure. 104
6.12 Rendered images of assumed adsorbed vapour distributions, with top, middle, and bottom regions, for the 'gradient' adsorption hypothesis of vapour selectivity. 104
6.13 Reflectance spectra for different preferential adsorption of model vapours upon the *Morpho* nanostructure. 106
6.14 PCA analysis of the calculated reflectance from *Morpho* ridge structures with an assumed gradient of vapour adsorption. 107
6.15 PCA loadings data for gradient vapour coverage on the *Morpho* structure. 108
6.16 PCA scores plots for combined data analysis of uniform and gradient vapour upon the nanostructure. 109
6.17 Results of across-ridge scanning using reflected and fluorescence light for spatial chemical polarity mapping. 111
6.18 Spatial distribution of polarity of individual ridges over their heights before and after a mild treatment with oxygen plasma. 112
6.19 Schematic illustration of the mechanism of the selective response of *Morpho* butterfly scales to different vapours. 114

7.1 Diagram of experimental arrangement for the investigation of angle and polarisation diversity of *Morpho* scales. 119
7.2 Images used to develop an optical model for simulation with the FDTD technique. 120
7.3 Results of the spectral analysis of response of the *Morpho* structure to ten vapours. 122

7.4 Theoretical demonstration of spectral diversity of *Morpho* scales response to different model vapour adsorptions. 123
7.5 Temporal response of *Morpho* scales to ten model vapours at five selected wavelengths. 124
7.6 Comparison of measured and calculated reflectance from the *Morpho* scales when illuminated with two linear polarisations. 125
7.7 Experimental dynamic differential reflectance profiles for acetonitrile vapour exposures on the *Morpho* scales probed with two linear polarisations. . . 126
7.8 Intensity maps displaying the time-averaged power distributions when the *Morpho* structure is probed light of with two linear polarisations . . 129
7.9 Experimentally explored diversity of spectral response with changing angle of illumination and of detection. 130
7.10 Diagram illustrating the experimental arrangement of illumination of the sample, and collection of scattered light, with respect to the orientation of the ridges for the forward- and back- scatter measurement. 132
7.11 Demonstration of the temporal response measured for back- and forward-scattered light from the *Morpho* scales. 133
7.12 Spectral responses measured upon vapour exposures for back- and forward-scattered light from the *Morpho* scales for a range of vapour concentrations. 135
7.13 A comparison of back- and forward-scattered measured spectra for water, propanol and methanol vapours. 136
7.14 PCA scores analysis of the back- and forward- scattered light, displaying a selective response for both measurement conditions. 137
7.15 Examples of *Morpho* ridge-structures following coating depositions aimed to alter vapour selectivity. 139
7.16 Rendered images of modelled adsorbed vapour distribution for liquids condensed on vertical, and then horizontal regions, for top, middle, and bottom sections, for the investigation of a functionalised *Morpho* nanostructure. 139
7.17 Simulated reflectance spectra for a model 'functionalised' *Morpho* ridge structure. 141
7.18 PCA analysis of simulated reflectance spectra for a model 'functionalised' *Morpho* ridge structure, showing all regions are resolvable from one another in PCA space. 142

8.1 Multilayer reflector for the investigation of a simplified *Morpho* design. . 147
8.2 Analysis of the multilayer reflectance upon model vapour adsorption on the simplified ten lamellae multilayer with no extinction coefficient. . . . 149

8.3 Analysis of the multilayer reflectance upon model vapour adsorption on the simplified ten lamellae multilayer with a small extinction coefficient. 150
8.4 Analysis of the effect of optical absorption in the multilayer's reflecting lamellae on the sensitivity and selectivity of model vapour adsorption. . 151
8.5 PCA analysis of a twenty layer multilayer stack with optically-absorbing lamellae 152
8.6 Exploration of chirped-multilayer structures for vapour selectivity and sensitivity analysis. 155
8.7 Comparison of the reflectance of a multilayer with regular and chirped layer periodicities upon model vapour adsorption. 156
8.8 Analysis of model vapour adsorption on chirped multilayer designs. . . . 157
8.9 Schematic diagrams for bio-inspired model dielectric structures. 161
8.10 Reflectance maps for incidence angles from 0 to 70 degrees for dielectric structures 162
8.11 Demonstration of the high-Q resonant modes within the ridge-lamellae dielectric structures. 164
8.12 Spatial mapping of the relative electric field intensity through the region of high field enhancement of the fundamental resonance. 166
8.13 Exploration of Fano resonance effects for a sensitive vapour response . . 167
8.14 Investigation of the frequency-shift of the fundamental resonant peak when vapour is adsorbed in or out of the region of field enhancement. . 167
8.15 SEM images of the cross-section of PMMA ridge-lamellae nanostructures. 169
8.16 Optical parameters for common volatile organic compounds, and schematic diagrams for a modified model ridge-lamellae structure. 170
8.17 Reflectance and PCA analysis for model vapour adsorption upon 'modified' lamellae reflectors 172
8.18 Comparison of the ability of natural and bio-inspired nanostructures to detect individual model vapours and their mixtures in the presence of humidity background. 174

9.1 Achieving vapour-selectivity in bio-inspired nanostructures inspired by *Morpho* butterflies 179

B.1 Assessment of spectral and dynamic responses to vapours of a classic chemically uniform sensing material such as porous silicon. 190
B.2 Comparison of spectral responses of *Morpho* scales and a classic chemically uniform sensing material such as porous silicon to methanol, ethanol, propanol, butanol, and water vapours. 191

B.3 Results of imaging of intact butterfly scales using time-of-flight secondary ion mass spectrometry. . . . 192
B.4 Positive ion ToF mass spectra and total ion chromatograms of analysis of butterfly wing extracts using solvent-extraction liquid chromatography-ToF-MS. . . . 193
B.5 Validation of the origin of the vapour-response selectivity of *Morpho* scales by measurements of vapours of similar refractive indices and different polarities. . . . 194
B.6 Validation of the origin of the vapour-response selectivity of *Morpho* scales by measurements of vapours of different refractive indices and different polarities before and after a mild oxygen plasma treatment. . . . 195

C.1 Complete reflectance dataset and associated PC scores plot for multilayer structures. . . . 198
C.2 Exploration of chirped-multilayer structures for vapour selectivity and sensitivity analysis. . . . 199
C.3 Complete reflectance dataset and associated PC scores plot for chirped multilayer structures. . . . 200
C.4 Analysis of model vapour adsorption on additional chirped multilayer designs. . . . 201

D.1 Rendered schematic for dielectric structure 4 depicting the result of expanding the unit cell geometry, and the plane of incidence which is perpendicular to the ridge-structure. . . . 204
D.2 Reflectance maps for dielectric structure 3 displaying high-Q resonant features . . . 205
D.3 Example TEM images of fabricated dielectric structures and reflectance spectra displaying high-Q features . . . 206
D.4 Demonstration of the high-Q resonant modes within the ridge-lamellae dielectric structures when model vapour is sorbed in the region of high-field intensity. . . . 207
D.5 Exploration of Fano resonance effects for a sensitive vapour response . . 208
D.6 Demonstration of the high-Q resonant modes within the ridge-lamellae dielectric structures when model vapour is sorbed in the region of high-field intensity. . . . 209

List of Tables

3.1 List of published values of refractive indices of materials present in a range of animal and plant biophotonic structures. 45

4.1 Summary of the mechanism and attributes of photonic crystal sensors that utilise a colorimetric readout 63

A.1 Table of common volatile organic compounds with their respective vapour pressures, and associated parts-per-million concentration values for the partial vapour pressures generated by the bubbler system. 187

List of Tables

Chapter 1

Thesis Overview

The biological world is filled with many highly evolved structural designs by which light and colour are manipulated [1–4]. Colour appearances produced by wavelength-selective coherent scattering, through the interaction of light with micro- and nano-structures, are commonly termed structural colours. Colours produced by this process are present in many different animal [2–4] and plant [5–7] phyla.

The photonic structures present in these natural systems are becoming increasingly studied as sources of inspiration for a range of technological, commercial and industrial applications. In recent years the naturally formed photonic structures in the wing scales of tropical *Morpho* butterflies have begun to provide novel bio-inspiration within the sensing community [8, 9]. In vapour sensing experiments the scales imbricated on the *Morpho* butterflies' wings are able to transduce the presence of chemical vapours through measurement of the changes in optical signal. Analysis of reflectance demonstrates a sensitive and selective optical response to various low-weight volatile organic compounds, including alcohols and water [8].

Despite the use of chemical sensors in a vast number of applications, the ability to detect trace levels of chemical vapours in real time represents a significant challenge to the current generation of chemical sensors [10]. Understanding the mechanism of the vapour response observed in *Morpho* butterflies may help to develop new sensors, without the need for complex and cumbersome sensor arrays, that meet the current demands for these analytical devices.

In this thesis the mechanism of the unusual multivariable vapour response exhibited by the photonic structures in the wing scales of *Morpho* butterflies is investigated, and bio-inspiration is taken to stimulate fresh approaches for the development of real-time, simplified, yet selective and sensitive sensors.

1.1 Thesis outline

This thesis consists of nine chapters. Two chapters are literature reviews; one focusing on structural colour in biological systems, and the other providing an overview of electromagnetic-type sensor approaches. One chapter details the theory that describes the physical processes that occur within the photonic structures of *Morpho* butterflies to produce the coherent scattering of light. Three chapters comprise experimental and theoretical investigations into the vapour response of the scales of *Morpho* butterflies, and their synthetic bio-inspired counterpart structures. Of the remaining chapters, one provides an introduction to the thesis content, another details the methods used in the investigations, and the final chapter provides a conclusion of the results presented in this thesis, and suggests potential future avenues of work. Additionally, there are four appendices that contain supplementary data to support the discussions within the experimental chapters. A more in-depth chapter-by-chapter overview is given below.

Chapter 2

Chapter 2 reviews the field of structural colour in biological systems, with a particular emphasis on the colours of butterflies in the *Morpho* genus. It begins with a short historical perspective. Following this, biological photonic crystals with periodicities in one, two and three dimensions are discussed. To conclude, a more detailed description of the mechanisms of colour production in the scales of the *Morpho* butterfly, and examples of *Morpho*-related bio-mimicry and bio-inspired studies, are described.

The basis of this chapter is formed from the review article:

> Starkey, T. and Vukusic, P. Light manipulation principles in biological photonic systems. *Nanophotonics*, **2**, 289 (2013). Ref. [11].

Chapter 3

Chapter 3 details the physical mechanisms by which light is coherently scattered to produce the variety of optical effects observed in the biological systems reviewed in Chapter 2. To begin, Maxwell's equations are defined. Using these, a short introduction to the theory of photonic crystals is given, and then the physical consequences of light interacting with a one-dimensional photonic crystal are outlined. This leads to a discussion of the main factors that affect the optical properties of biological photonic crystals. Finally, diffraction from periodic structures is described.

Part of this chapter is based upon the content in the review article:

Starkey, T. and Vukusic, P. Light manipulation principles in biological photonic systems. *Nanophotonics*, **2**, 289 (2013). Ref. [11].

Chapter 4

Since the topic of this thesis is a marriage between biological optics and sensing, Chapter 4 contains a short review of traditional sensing approaches. To begin, the definition and basic operating principle of a sensor are described. Following this, a number of sensing approaches that transduce an analytical-chemical signal through measurement of electromagnetic radiation are outlined. To conclude, some of the challenges inherent in current sensor array implementations are presented.

Chapter 5

Chapter 5 details the experimental, theoretical and data processing tools used in the investigations in Chapters 6, 7 and 8. The experimental methods for optical measurements and vapour generation are outlined, and spectral reflectance data of a sample measurement is shown. The theoretical tools used to simulate the electromagnetic response of the *Morpho* butterfly and bio-inspired structures are then described. These approaches include the Transfer Matrix Method, the Finite Element Method and the Finite-Difference Time-Domain technique. Finally, the multivariate analysis used to process experimental and theoretical spectral data is demonstrated.

Chapter 6

Chapter 6, the first experimental chapter, investigates the origin of the unusual response of the *Morpho* butterfly scales to chemical vapours. The response obtained through the measurement of the reflectance from the scales, is both sensitive and selective between different chemical vapours. This study finds that the local chemistry of the epicuticle material within the photonic nanostructure provides a mechanism by which this response can be obtained. The chemical environment, in which a gradient of chemical polarity exists, facilitates the preferential adsorption of vapour molecules within the photonic structure. These different spatial vapour adsorptions are transduced spectrally as a selective response between different spatial vapour adsorption scenarios.

The basis of this chapter is formed from the published work:

Potyrailo,* R.A., Starkey,* T.A., Vukusic, P., Ghiradella, H., Vasudev, M., Bunning, T., Naik, R.R., Tang, Z., Larsen, M.,

> Deng, T., Zhong, S., Palacios, M., Grande, J.C., Zorn, G., Goddard, G., and Zalubovsky, S. Discovery of the surface polarity gradient on iridescent *Morpho* butterfly scales reveals a mechanism of their selective vapor response. *Proceedings of the National Academy of Sciences of the United States of America*, **110**, 15567 (2013). Ref. [12], (* denotes equal contribution),

and in part from results presented in:

> Starkey, T.A., Vukusic, P., and Potyrailo, R.A. Toward bioinspired nanostructures for selective vapor sensing: diverse vapor-induced spectral responses within iridescent scales of *Morpho* butterflies. *MRS Proceedings*, **1621**, mrsf13 (2014). Ref. [13].

Chapter 7

Chapter 7 contains further investigations of the *Morpho* scales as a source of bioinspiration in the pursuit of selective photonic vapour sensors. A number of diverse response attributes are demonstrated, the effect of measurement conditions is considered, and the *Morpho*'s photonic structure is subjected to a model 'functionalisation' investigation. Each of these investigations show the biological sensor template in the butterfly scales to have many desirable properties that might be incorporated into sensor designs of the future.

Some of the results presented in this chapter are published in:

> Starkey, T.A., Vukusic, P., and Potyrailo, R.A. Toward bioinspired nanostructures for selective vapor sensing: diverse vapor-induced spectral responses within iridescent scales of *Morpho* butterflies. *MRS Proceedings*, **1621**, mrsf13 (2014). Ref. [13].

Other results are being prepared in manuscripts provisionally titled:

> 'Multivariable signal transduction in photonic nanostructures of *Morpho* butterfly scales for high-performance vapor sensing', and 'Design and fabrication of photonic vapour sensors inspired by *Morpho* butterflies: towards outperforming conventional sensor arrays.'

Chapter 8

In Chapter 8, the focus of this thesis shifts from the photonic structure present in the scales of butterflies to bio-inspired sensor designs. To begin, simple concepts that might be incorporated into existing sensor films to enhance selectivity are shown theoretically. It is shown that through tuning optical adsorption and by changing the layer periodicities of a simple multilayer stack the vapour-response selectivity and sensitivity can be significantly altered. Following this, the vapour response of a ridge-lamellae-type structure, which more closely resembles the nanostructure in the *Morpho*, is investigated. This structure-type, which collaborators were able to fabricate, is shown both theoretically and experimentally to have excellent potential as a photonic nanostructured sensor.

Some of the results presented in this chapter form part of the submitted work in:

> 'Design and fabrication of photonic vapour sensors inspired by *Morpho* butterflies: towards outperforming conventional sensor arrays.'

Chapter 9

Chapter 9 contains the final concluding remarks of the thesis. A summary of the main conclusions from each of the experiment- and theory-based chapters is made. Some suggestions for future work, towards the creation of bio-inspired sensors, are made. Finally, a list of publications, talks and poster presentations produced during this Ph.D project are listed.

Chapter 2

Overview of Colour Production in Biological Systems

2.1 Introduction

The science of light and colour manipulation generates interest across a range of disciplines, from mainstream biology, across multiple physics-based fields, to optical engineering. Furthermore, the study of light production and manipulation is of significant value to a variety of industrial processes and commercial products. Among the several key methods by which colour is produced in the biological world, this chapter sets out to describe some of the structures present in animal and plant systems that produce colour through the mechanism of coherent optical scattering. Not only has this theme been a very rapidly growing area of physics-based interest, but also it is increasingly clear that the biological world is filled with highly evolved structural designs by which light and colour strongly influence behaviours and ecological functions.

Colour production in biological systems may be divided into two principle categories: the first is usually associated with chemical processes such as absorption and luminescence; the second relates entirely to coherent scattering processes that underpin the interaction of light with materials that have periodic variations in refractive index (RI).

Pigmentation is the most common biological means of colour production and is the consequence of the wavelength-selective absorption of light by chromophores, the name given to colour-producing molecules [1]. The molecular structure of a pigment determines the wavelength band over which it absorbs strongly. If white light is incident upon a pigment, the resulting scattered light will have some proportion of the light subtracted from the incident spectrum. Pigmentary colour in a biological species is usually synthesised by their physiological processes, although some animals obtain

these absorbing molecules through their diet [14]. Pigments that are synthesised by many insects include melanins, pterins, ommochromes, tetrapyrroles, papiliochromes and quinones, while carotenoid and flavonoid pigments are generally obtained from their diet [14]. Colours produced using pigments are often relatively broadband and cause relatively low-intensity diffuse angle-independent hues.

Modified chromophore chemistry leads to the inelastic scattering processes that give rise to fluorescent colour emission. The common fluorophore-based emissions observed in biological systems usually comprise near-UV absorption with many examples of emission in the blue and green colour wavelengths. Use of fluorescence emission for signalling has been observed in many animals including parrots, spiders and stomatopods [15–17], whilst the directional control of fluorescence emission by photonic crystals has been studied in Swallowtail butterflies [18].

Chemiluminescence is a less common process for colour production, in which light emission arises from a chemical reaction. In biological systems this process is called bioluminescence [1, 14]. A well-known example of which is the firefly, a species of the Lampyridae beetle family [19]. These light emitting chemical processes are seen in a broad range of organisms, including fungi, bacteria, fly larvae, millipedes and earthworms [20], and many deep-sea marine animals [21].

The non-pigment-based pathway to colour production is described in terms of structural colour. This phrase is used to describe the wavelength-selective scattering that arises from the interaction of light with structures that have physical dimensions on the order of the wavelength of light. Coherent scattering [22] produces the often vivid optical effects attributed to these structures. The characteristics of this in biological systems can be: intense reflected narrow-band or broad-band colour [23, 24], metallic appearances [25], angle-dependent (iridescent) appearances [26, 27], directional colour variation [28], low-reflective absorbing [29] or transparent systems [30], and strong polarisation signatures [31].

In this chapter, a range of structurally coloured systems present in different animal and plant phyla are described. First, biological systems comprising photonic crystals with 1D, 2D and 3D structural periodicities are discussed, before describing other photonic structures, such as diffraction gratings and scattering structures. The coherent optical scattering associated with the scales of the insect order of Lepidoptera are then discussed before making a summary of a range of investigations that have focused specifically on *Morpho* butterfly species. Finally a brief review is made of the growing field of bio-inspired research to which *Morpho* photonics has contributed. The review presented in this chapter has been adapted from a published review article titled 'Light manipulation principles in biological photonic systems' by T. Starkey and P. Vukusic, in Nanophotonics, Volume 2, Issue 4, Pages 289–307, Year 2013 in Ref. [11].

2.2 Historical perspective

Some of the earliest scientific investigations into the science of structural colour phenomena were made by Hooke and Newton. In his 1665 microscope study Micrographia, Hooke remarked on "*All the colours of the Rainbow*" produced by cleaving seemingly colourless muscoy glass [32]. Hooke suggested that the iridescent colour of a peacock feather might be due to an "*indefinite number of plain and smooth Plates, heaped up, or incumbent on each other*" [32]. Newton also studied the iridescence of peacock feathers and remarked that a "*great variety of colours*" are produced when blowing upon a soapy liquid [33].

The early 20th century saw more thorough investigations by Mason, Onslow, Rayleigh and others [34–40]. Their studies of the colours of bird feathers, butterfly wing-scales and beetle elytra elucidated some of the roles played in colour production by structures comprising multiple reflecting layers. The different visual appearances of many biological systems were attributed to different specific physical phenomena, namely diffraction, interference and scattering by small particles [41].

The invention, and development, of the electron microscope (EM) in the 1930s and 1940s enabled the investigation of biological and synthetic features having micro-scale dimensions. The first EM studies reported on the colour-producing structures found within bird feathers, and within the scales of butterflies and beetles [42, 43]. Although limited in the image quality and resolution they offered, elaborate multilayer structures with features smaller than the wavelength of light were identified [44].

One of the first mathematical treatments of the optical properties of thin films was undertaken by Rayleigh in 1887 [45]. Later, Abelès, in 1949, published a rigorous and useful method to obtain the reflection and transmission of thin films [46]. In 1968, intended for an audience of those interested in biological reflectors, Huxley published a recursive method for calculating the reflection and transmission of regularly spaced non-absorbing multilayer films [47]. His discussion emphasised the optical effects relating to layer thicknesses, wave phase and amplitude. In 1972, Land elucidated Huxley's results in the context of the coloured appearance of many biological systems, describing the structure, function and constituent materials of the optical systems present in a wide variety of animals [48].

Ghiradella *et al.*, in 1972, described the bright ultraviolet reflection from a male *Eurema lisa* butterfly, demonstrating that its structural (UV) colour was derived from a very unusual microstructure that appears 'tree-like' in cross-section [49]. Optical measurements combined with electron micrographs revealed the branches of these tree-like 3D ridges formed multilayer reflecting lamellae that were responsible for its UV-iridescent colour appearance [49]. This was one of the key early examples of a struc-

turally coloured insect system featuring a photonic structure that was rather distinct from the more regular 1D semi-infinite multilayered structures theoretically described by Huxley. Two later studies examining *Callophrys* butterflies in the 1970s, described the diffraction of light from 3D simple-cubic networks of ordered porous elements. These were among the earliest studies of highly ordered biological three-dimensional photonic crystals [50, 51].

Modern research into the optics of biological systems has undergone a great deal of change. Plants and animals are not only being investigated to elicit better understanding of their evolutionary, developmental and biological functions; multidisciplinary research into all aspects of such natural systems is extremely active. Greater emphasis is now placed not only on understanding how these structures manipulate light, but also how technology might learn from or incorporate such complex structures into devices or processes.

2.3 Biological photonic crystals

Photonic crystals with 1D, 2D and 3D periodicities exist across a range of animal and plant families. Many studies have shown different photonic crystal arrangements, use-strategies and optimisation protocols so that the host system can achieve a specific optical appearance. In achieving this, systems often employ more than one of these periodicities, or involve pigmentation, to contribute to the overall macroscopic colour appearance. Some of these different previously studied systems containing 1D, 2D and 3D periodicity are presented.

2.3.1 Biological photonic crystals in 1D

One dimensional photonic crystals, or multilayers, are extremely prevalent in butterflies, beetles and fish reflectors [48]. These biological systems achieve a huge number of different optical appearances through the use of simple dielectric materials. Research into multilayered systems has shown a huge variety in the optical properties and behavioural functions of these coloured systems including narrow- and broad-band colour [52], non-metallic [53–55] and metallic colour, and polarising behaviour [31, 56, 57].

An efficient route to achieve a narrowband intense colour reflection are reflectors of two or more refractive indices with uniform repeating periodicity. The beetle *Torynorrhina flammea* uses a multilayer structure comprising many chitin and melano-chitin layers with layer periodicities close to that of an ideal multilayer (discussed later in Section 3.5) to achieve highly intense colour [58], see Figures 2.1(a) and 2.1(c). These layer thicknesses show variability across this beetle species in order to alter the narrowband

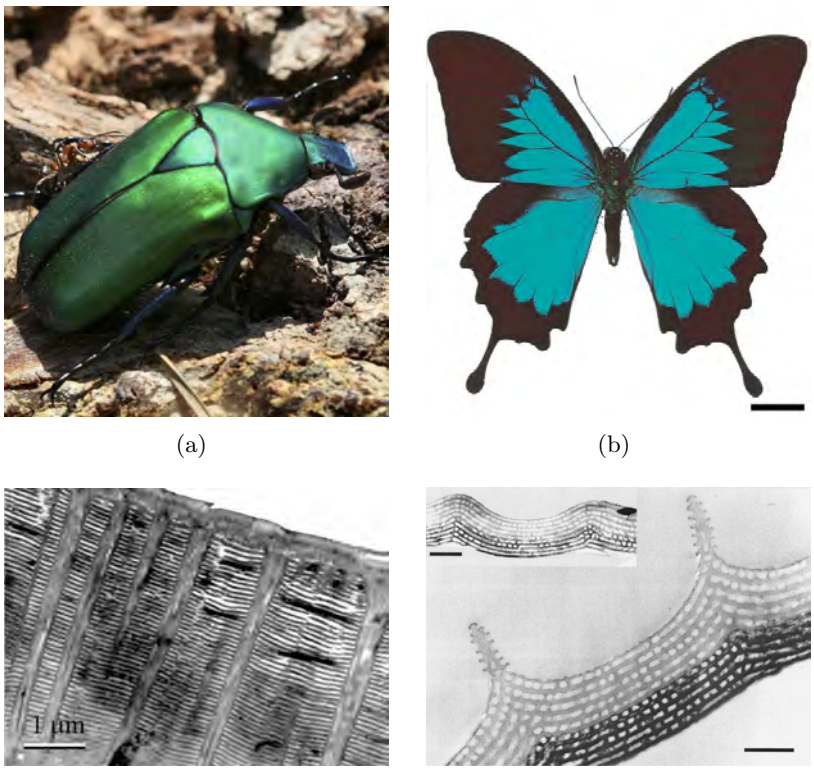

Figure 2.1: Examples of a metallic and a non-metallic colour appearance achieved in two biological reflectors using 1D photonic crystal arrangements. (a) and (b) photographs of *T. flammea* and *P. ulysses*, respectively. (c) and (d) show their associated TEM cross-sections of the 1D photonic crystals. Images reprinted from Ref. [58] and Ref. [53] with permission of P. Vukusic. [Scale bars: (b) 1.5 cm, (c) and (d) 1 µm].

colour reflected.

In contrast, a broadband reflection response can be achieved through mechanisms such as pairs of multilayer reflectors, chirped, or chaotic periodicities in the refractive index profile. The metallic silver reflections commonly observed in fish scales [59] and gold colouration commonly seen in beetle elytra [52, 60, 61] arise through refractive index profiles varying in this way. Broadband colour production is also seen through variation of perpendicular structural periodicity relative to the systems outer surfaces. The pointillistic addition of coherent scatter by this varying periodicity can result in a metallic broadband colour appearance [62].

A metallic, and iridescent, appearance is a common visual aesthetic of 1D reflectors. In biological systems, large planar areas of uniform 1D crystal commonally form this charactistic, like those structures of the silver and gold reflectors discussed previously

[52, 59–61]. The metallic aesthetic may also be achieved through small relative differences in spatial alignment of adjacent multilayered structures, like those in the scales of *Morpho rhetenor* [63].

Contrasting non-metallic and often non-iridescent colour is also widely seen in naturally formed multilayer structures. This can arise from the addition of optical contributions from juxtaposed 1D photonic crystals creating a pointillistic colour mixing effect. This has been studied in beetles [64], fish [65] and plants [7].

Another modification to the more planar geometries to yield non-metallic colours is the addition of punctae, or a modulation of the component multilayer. The bowl-like curvature of the multilayers on the wings of *Papillio ulysses* creates a non-metallic and broadly angle-independent colour [53], see Figure 2.1(b) and 2.1(d). Alternatively the wrinkling of the structure present in the damselfly *Ryothemis resplendens* produces a non-metallic colour, whilst retaining angle-dependant colour reflections [66].

Natural 1D multilayers have also been seen to exhibit different strategies to control the polarisation behaviour of reflected light. A pair of helicoidal reflectors separated by a half–wavelength cuticle layer in the exocuticle of some *Scarabaeidae* beetles allows only the reflection of right-hand circularly polarised light [23]. Other reflection behaviour with cholesteric liquid crystal analogues have been studied in beetles [31, 56] and plants [7].

2.3.2 Biological photonic crystals in 2D

2D photonic crystals in biological systems are much less prevalent than those with 1D or 3D periodicities, and are associated with some avian feathers [67], mammalian eyes [68] and marine creatures [69, 70].

The plumage of male peacocks contains many differently coloured iridescent feathers. Their colours arise from 2D photonic structures made from arrays of melanin rods connected by keratin within the feather barbules (see Figure 2.2(a) and Figure 2.2(b)) [67]. The diverse colours reflected by the different feathers are determined by the lattice constant of the structure [71]. In another example of a 2D photonic crystal in avian feathers the barbules of black-billed magpies exhibit a structure that has a lattice of holes within a chitin matrix [72].

The iridescent multi-coloured cylindrical spines of the polychaete worm, *Pherusa* sp., comprise a 2D photonic crystal that has an optimised hexagonal packing arrangement of hollow cylindrical channels in a chitin medium (see Figure 2.2(c)). The hexagonal order (see Figure 2.2(d)) is limited to mono-crystalline domains of different orientations resulting in an overall polycrystalline effect. The structure is tuned with respect to lattice constant and packing fraction so that its response is optimised [70]. The

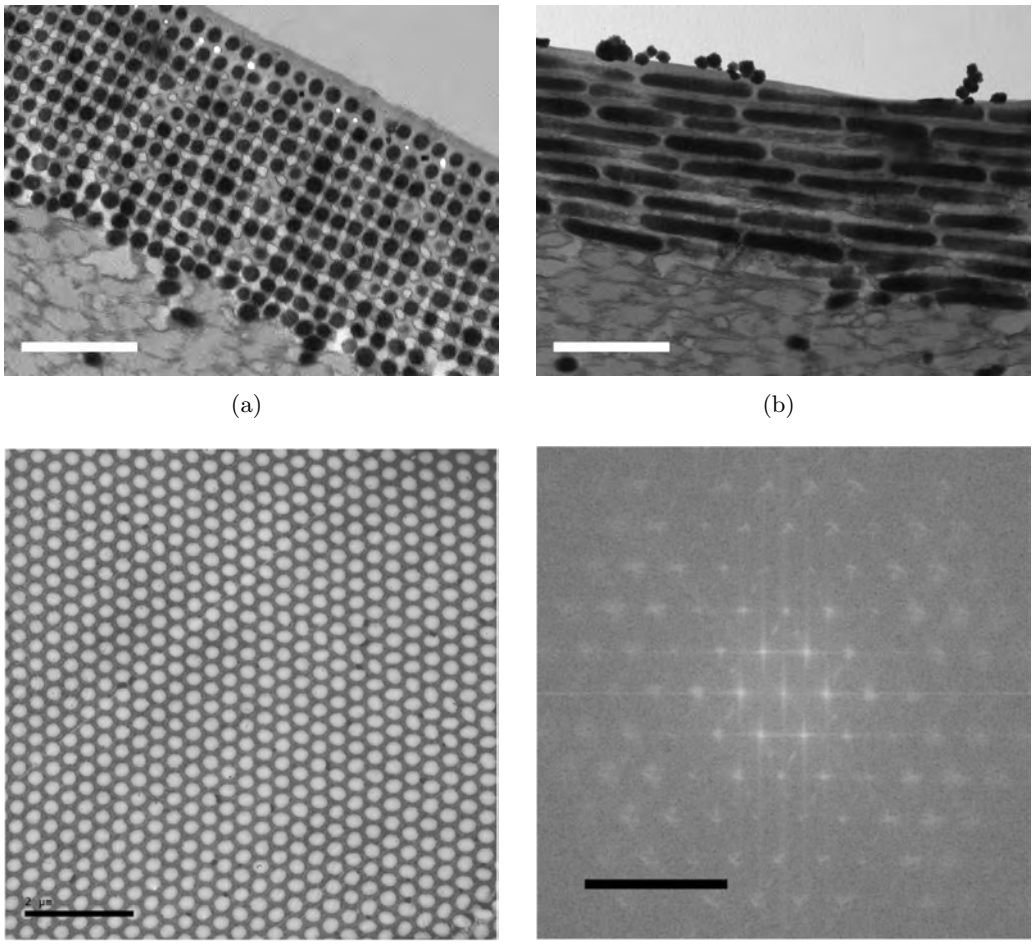

(a) (b)

(c) (d)

Figure 2.2: Images of (a) transverse and (b) longitudinal TEM cross-sections of a blue peacock feather, with respect to the barbule axis. (Images courtesy of P. Vukusic). (c) TEM image and (d) the corresponding fast fourier transform, illustrating the hexagonal order present in the cross-section through a *Pherusa* seta. (Reprinted from Ref. [70], with permission of APS). [Scale bars: (a) and (b) 500 nm, (c) 2 µm, and (d) 10 μm^{-1}].

sea mouse, *Aphrodite* sp., also a polychaete worm, contains a similar hexagonal close packed arrangement of channels [69].

2.3.3 Biological photonic crystals in 3D

3D periodic biological structures are more common than 2D examples. They are present in the scales of many butterflies and beetles and in the feathers of some birds. The way in which these structures are fabricated is not well understood in all cases, but some are believed to use the dynamic self-assembling processes associated with lipid-bilayer interactions [73, 74].

Photonic systems with gyroidal crystal structures are found in Papilionid and Lycaenide butterfly scales. The scales of the *Parides sesostris* butterfly, for instance, contain intra-scale domains of the gyroidal photonic crystal [75] with varying crystal domain orientations, as shown in Figure 2.3. The pointillistic multicolour contribution of differently oriented domains results in a colour-averaging effect that produces an angle-independent overall green colour [26, 76]. Extensive modelling of the electromagnetic responses of the *P. sesostris* gyroid structure has shown that it has a filling fraction optimised to maximise the reflected bandwidth for light incident normal to the structure [77, 78]. The photonic structures present in the scales of another butterfly, *Callophrys rubi*, also appear to have an optimised filling fraction [76].

A variety of other 3D biological photonic crystal geometries have been found. The diamond photonic structure is considered a special case due to it being the most isotropic periodic structure of the more commonly encountered crystal classes [80]. The multi-domained photonic crystal in the weevil *Lamprocyphus augustus*, was the first discovered example of this (see Figure 2.4) [79]. Despite the limited refractive index contrast between chitin and air that form its system, there is a cumulative photonic band gap (discussed in Chapter 3) at green wavelengths for different crystal planes. The diamond photonic crystal arrangement has also been discovered in the scales of other beetles [81].

Another beetle-based example of photonic crystals demonstrates the contrasting optical properties of highly ordered 3D structures versus quasi-ordered 3D structures. *Eupholus magnificus* exhibits two differently coloured bands (see Figure 2.5(a)) across its elytra, one of which is metallic in appearance due to specular reflection from a highly ordered structure. The second coloured band has a less intense reflection, which results from greater diffuse reflection from the less ordered structure. Analysis of the associated scales shows that this difference arises from the 3D arrangements of cuticle within the scales shown in Figure 2.5(b) and Figure 2.5(c) [82]. The coexistence of these two contrasting forms of 3D structural order in the same species is uncommon in

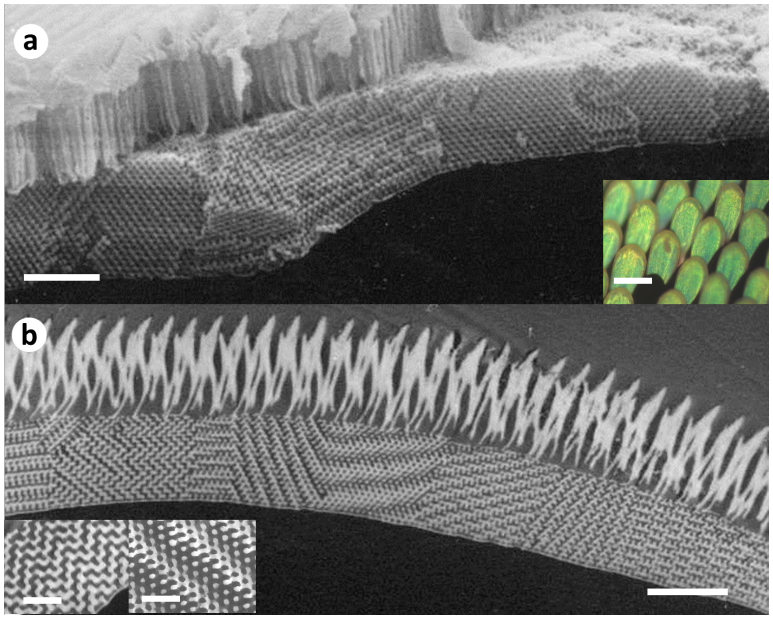

Figure 2.3: (a) SEM image of a cleaved cross-sectional face of *P. sesostris'* iridescent scale showing the lattice structure; inset optical microscope image of the green iridescent scales. (b) TEM image of a thin cross-section through the iridescent scale of (a). The range of different tessellation patterns (two of which are inset) are effected by variations in the orientation of the gyroid lattice within domains through the scale. (Images courtesy of P. Vukusic). [Scale bars: (a) 4 μm, (inset 100 μm), and (b) 4 μm (inset 1 μm)].

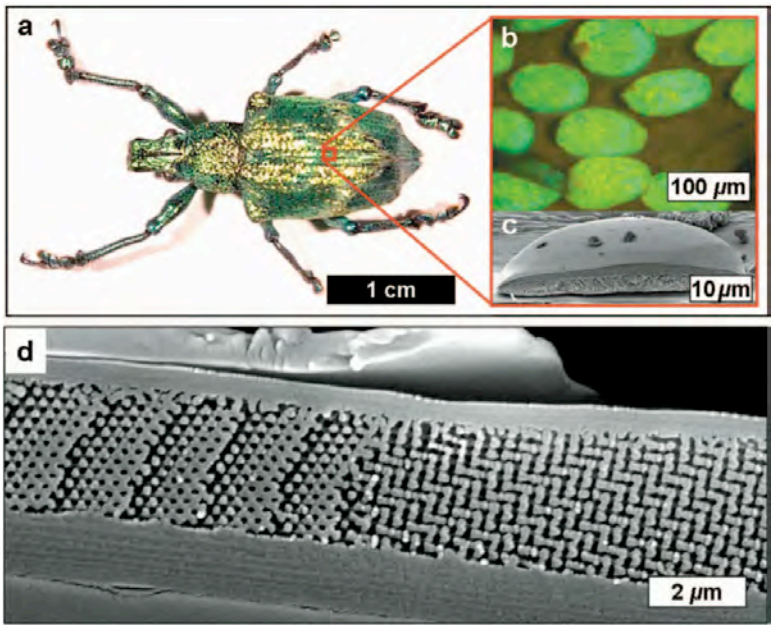

Figure 2.4: (a) Photograph of the *L. augustus* weevil. (b) Optical micrograph of the green individual scales. (c) and (d) SEM images of a single scale cross-section. (Reprinted from Ref. [79], with permission of APS, and M.H. Bartl).

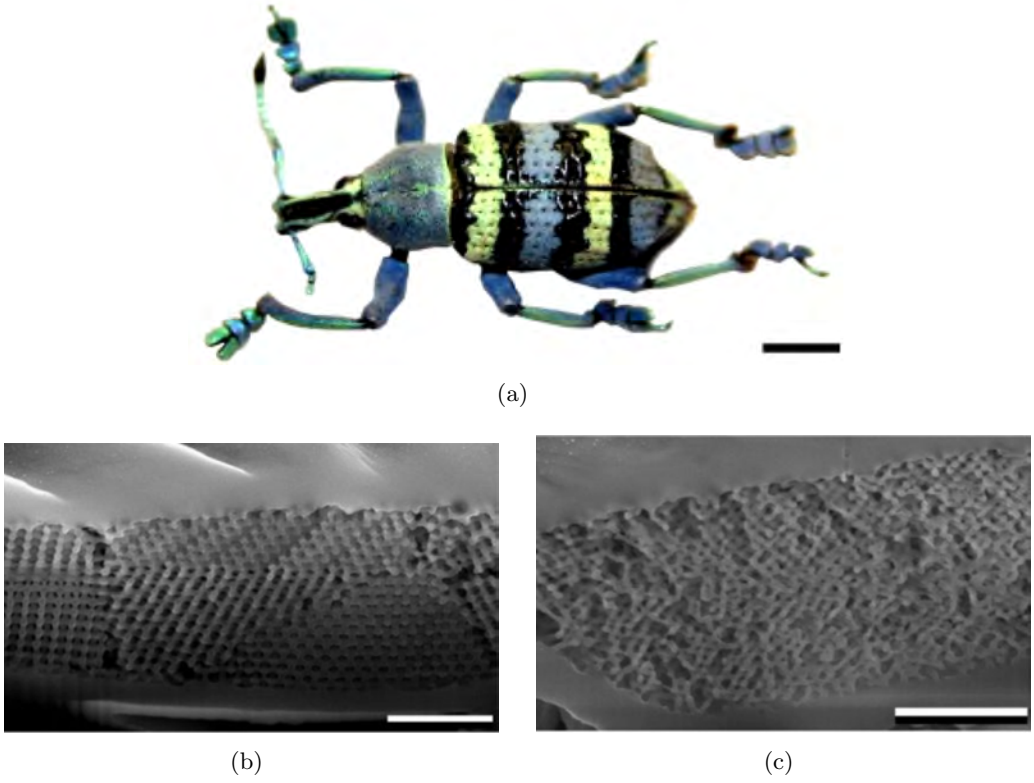

(a)

(b)

(c)

Figure 2.5: (a) Photograph of *E. magnificus*. (b) and (c): SEM images of a fractured (b) yellow scale, showing the highly periodic 3D lattice, and a fractured (c) blue scale, showing the contrasting quasi-ordered structure. (Reprinted from Ref. [82], with permission of OSA and C. Pouya). [Scale bars: (a) 4 mm, (b) and (c) 2 μm].

biological systems.

2.4 Colour production in biological structures through diffraction and scattering

Whilst the discussion of the previous section focussed on photonic crystal structures exhibiting a modulation of the refractive index in one, two or three spatial dimensions, other structural mechanisms exist in biological systems for the manipulation of light.

The structural order associated with diffraction gratings, and the disorder associated with the random scattering of light are other common physical components of structurally coloured systems. These elements can both be seen in isolation and as part of more complex hierarchical structures comprising photonic crystals.

2.4.1 Diffraction grating structures

Diffraction by regular structures, with a periodicity on the order of the wavelength of visible light, will split incident light into multiple beams called diffracted orders. Colour appearance arises through this mechanism due to the wavelength-dependant angle-dispersion of polychromatic incident light.

Diffraction grating stuctures, with 1D periodicities ranging from approximately 0.8 to 1.2 microns, are common on the surfaces of beetle elyta [61] and the petals of several species of flora [83]. The morphology of Coleoptera produces a number of different diffraction grating-like structures capable of reflecting iridescent colour. Regular gratings in 1D, and semicontinuous tubular surface structures, are seen on the eltyra of Sphaeridiinae gen. sp. and *Aglyptinus tumerus* respectively [61]. Similar striations and ridges are seen on petals [6, 83]. The hallmarks of these reflections are rainbow-like colour within distinct diffracted orders.

In contrast to these reflection gratings that produce colour solely through diffraction, the pairing of a surface diffraction grating with another structure can be exploited in biological systems for creating conspicuous appearances. For instance, the scattering of light impinging upon, or reflected from a photonic crystal, by diffraction grating elements, can enhance a broadband spectral and angle-dependant colour appearance of the photonic crystal arrangement. The effects of these idealised topologies may enhance the diffraction efficiency from such structures [84, 85]. Diffraction gratings with a mono-grating periodicity are seen above the 2D photonic crystal of *M. didius* [86] and above the 3D gyroid crystal of *P. sesostris* (P. Vukusic, unpublished), in both instances the broad-angle colour appearance is enhanced.

2.4.2 Scattering structures

Light interacting with random structures exhibiting disorder in element size on the order the wavelength of visible light produces non-preferential scattering of all wavelengths of incident light.

Nature is seen to achieve non-preferential scattering using a variety of different scattering elements to produce intense whiteness. Bead structures in the wings of the *Pieris rapae* butterflies produce a matt-white colouration for improved conspecific visual discrimination [87, 88], whilst random cuticle networks of connected filament-like structure in the scales of *Cyphochilus* beetles produce remarkable whiteness and brightness relative to white synthetic materials [24, 89]. A polarisation-dependent reflectance in biological white structures can arise through some alignment of the otherwise random fiberous strands [66].

As in the case of diffracting elements above or within a photonic crystal, random

scatterers play a role in diffusing the colour appearance when incorporated into a photonic solid.

2.5 Colour mechanisms and bio-inspired applications of *Morpho* butterflies

2.5.1 Iridescent scales in butterflies

Although *Morpho* butterfly photonics will be described in detail, it is useful first to compare their structures to the broad array of other types of photonic systems in Lepidoptera. The structural colour of lepidopteran wings is primarily due to the micro- and nano- structural elements present within their wing-scales. These scales are formed from insect cuticle, which is also used for mechanical functions such as armour and body structure [90, 91]. The morphology of scales is complex. They are formed by the secretion of cuticle from an epithelial cell on the wing substrate. For the formation of a scale, bristle or hair the cell extends a protrusion, shapes it appropriately and secretes cuticle around the entire surface [92]. Details of scale structure and formation are elucidated elsewhere [91, 93–95].

A generic lepidopteran scale has longitudinal ridges that extend down its length. These are often connected by a series of supporting arches, or crossribs. Fine structures, such as lamellae and microribs, can be located on the ridges [91]. Further structures, that are sometimes highly periodic in 2D or 3D, may also be found between the ridges and the lower lamina of the scale.

The scales that are structurally coloured can be broadly classified based on the type and location of the optically reflecting and scattering elements within them. The classification has been loosely divided into three types. Type I scales comprise multilayer structures on the scale ridging. Type II scales have multilayered, or 1D periodic, structure within the scale body. Type III scales have 3D periodic structure within them, or other and more hierarchical pairings of structural designs. Figure 2.6 schematically represents the basic scale designs and indicates the location on or within the scale of the periodic structure [96]. The scales of the *Morpho* butterfly exhibit Type I scales.

2.5.2 Overview of colour production in *Morpho* butterflies

The *Morpho* species (Lepidoptera: Nymphalidae: Morphinae) is a genus of large tropical butterflies that inhabit lowland forest and montane regions of Central and South America [97]. The genus contains many species and subspecies, with some variety in colour appearance and scale type [98]. For the purpose of discussing their visual ap-

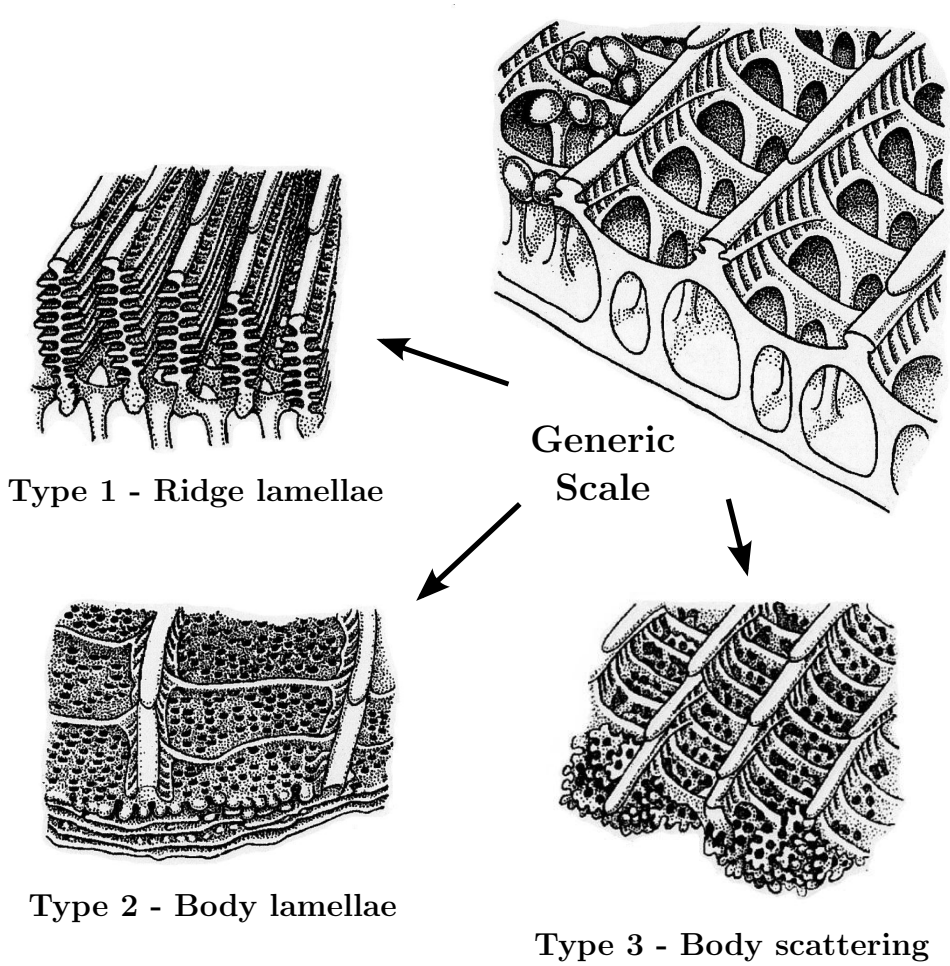

Figure 2.6: Schematic illustrations of the classifications of iridescent scales. Each scale is a variation upon the generic scale template. (Adapted from Ref. [91], with permission of H. Ghiradella).

pearance they can be divided into four groups, namely brownish *Morphos*, bright blue *Morphos*, chalk-white *Morphos*, and gloss-white *Morphos* [97].

The conspicuous appearance of bright blue *Morpho* butterflies (Figure 2.7(a) and 2.8(a)) has placed them among the most widely studied and collected butterfly species. The naturalist H.W. Bates remarked upon the dazzling lustre and blue flashes of the *Morpho rhetenor* that could been seen from "*a quarter of a mile off*" [99]. Its bright iridescent colour is believed to enable long-range conspecific communication [100].

Structural colour in bright *Morphos* has been known for over a century. Its dorsal wing surfaces are imbricated with Type I iridescent scales [63]. The ventral wing surfaces often appear dull brown with melanin pigmentation. *M. rhetenor* is a well-studied example of a bright blue *Morpho*; its appearance and wing-scale structure are shown in Figure 2.7.

Since 1999, there has been broad interest in the investigation of the structural colour of *Morpho* butterflies. Before this, most understanding came from the observations of Mason and others, on the biological materials present in the scales, and from low quality images obtained through early optical and electron microscopy. More recently, many thorough investigations have used high magnification electron micrographs and rigorous optical measurements, with parallel theoretical analyses, to explain the striking appearance of these insects.

Knowledge that butterfly wing-scales are the colour-centres from which their overall wing appearance arises was developed some time ago. However, such wings are adorned with tens of thousands of scales, many of which overlap partially, are tilted spatially with respect to each other and have inherent small structural variability (see Figure 2.7(b) and Figure 2.8(b)). These factors complicate the optical response from the wing and render it difficult to deconvolve and identify the photonic role of individual structural elements from the whole wing. Early experimental optical studies on *Morpho* and other lepidopteran wings comprised recording reflection spectra from wing samples using large diameter optical beams. More recent studies, however, have led to a significant improvement in understanding these systems by direct optical interrogation of their individual constituent photonic elements.

Single isolated butterfly scales' photonic properties were first described from experimental measurements on two species of *Morpho* butterfly [63]. These two *Morpho* species are bright blue in colour but rather different in their visual appearance: *M. rhetenor* is brilliantly intense and metallic blue in appearance (see Figure 2.7(a)), whereas *M. didius* reflects a much more diffuse blue colour (see Figure 2.8(a)). Scanning and transmission electron microscopy (SEM and TEM) reveal both *Morphos'* exhibit a layer of Type I scales next to their dorsal wing substrate, referred to as ground scales (see Figure 2.7(c) and (d), and Figure 2.8(c) and (d)). *M. didius* also exhibits a second

layer of additional near-transparent scales, referred to as cover scales, that completely overlay the ground scales (see Figure 2.8(d)).

Absolute angle- and polarisation-resolved measurements of optical reflection and transmission from single scales, detached from *Morphos*' wings, reveal striking differences in the scattering properties of each species' scales. *M. rhetenor's* brightly coloured ground scales reflect 75% of the intensity of incident blue light [63]. This is a remarkably high value considering the factors that are discussed in Section 3.6.3; namely, the relatively low refractive index contrast of the system's periodic structure, the melanin content of the scales that leads to broadband absorption, the incomplete occupancy of the lamellae and imperfections in the precise periodicity of the structure. Additionally, scattering from individual *M. rhetenor* ground scales is diffusely spread in angle into two broad lobes. *M. didius* ground scales do not show this scattering pattern.

At the whole-wing level the effects of multilayer interference are demonstrated by the reflected blue colour. The individual optical contribution of the cover scale, the ground scale and the wing substrate, however, cannot be separately discerned. An advantage of the single scale measurement approach is that specific scattering mechanisms can be attributed directly to intra-wing-scale structures. For instance, strong diffraction can be recorded in transmission through isolated cover scales of *M. didius*. This is not discernable directly from reflection data taken from *M. didius*' wings which themselves are adorned with such cover scales.

These optical observations arise due to the nature of *Morpho* wing-scale structures. Their cross-sections reveal the discretised multilayer units comprising periodic lamellae of alternating cuticle and air layers (see Figure 2.7(d)). An individual multilayer unit exhibits a characteristic tapered shape as well as an asymmetry of lamella positioning around its central stem. This not only reduces the effective multilayer occupancy, but also gives rise to its characteristic bi-lobed angle-distribution of optical scatter.

The observed differences between the absolute reflectance of blue light from the ground scales of *M. rhetenor* and *M. didius* are due to the differing number of lamellae present in each species' discretised multilayer unit; there are nine to eleven lamellae in *M. rhetenor* (see Figure 2.7(a)) and six to eight lamellae in *M. didius* (see Figure 2.8(a)) [63]. Diffraction by the cover scales of *M. didius* is the underlying reason for the key difference in visual appearance between *M. didius* and *M. rhetenor*. This creates significantly greater diffuse scattering in reflection for *M. didius*, due to the broader angle-spread associated with diffraction of both incident broadband light and the blue light reflected from the ground scales. This cover scale serves as a selective and isotropic diffuser of blue light in order to distribute reflectance over a wider range of solid angles [86]. The absence of such cover scales in *M. rhetenor* leads to a greater degree of specular reflection and the more metallic blue appearance of the species. Structural

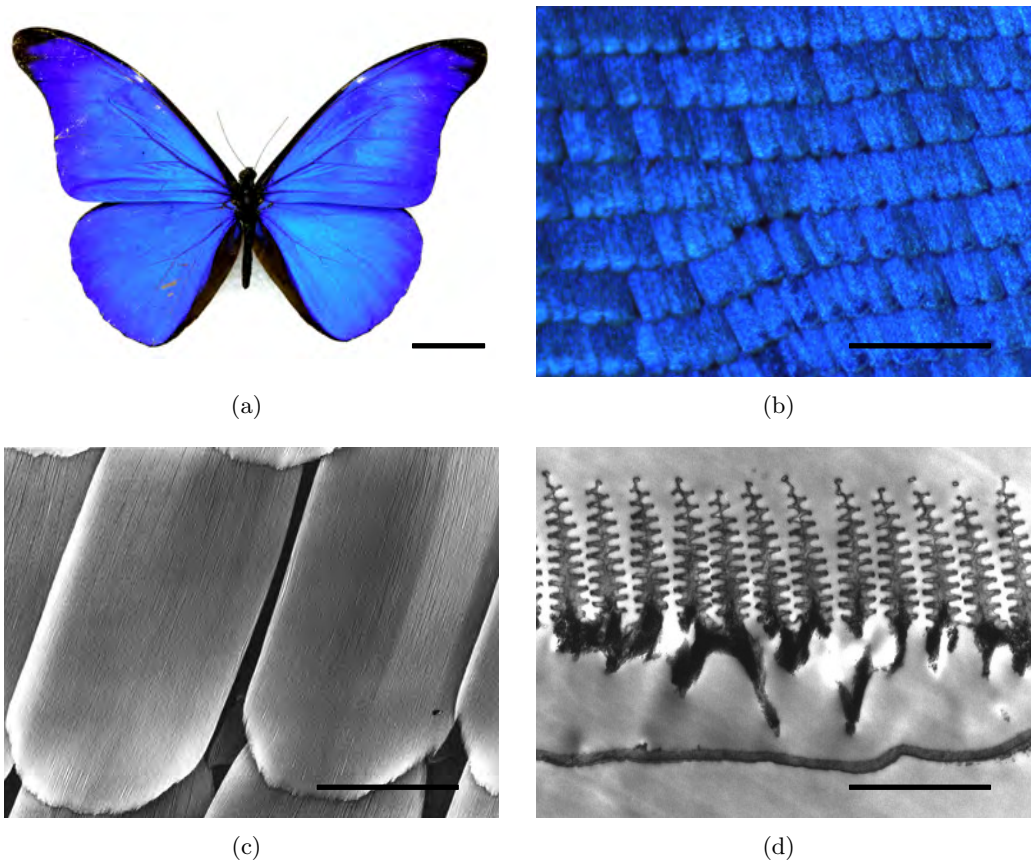

(a) (b)

(c) (d)

Figure 2.7: Appearance and scale structure of *Morpho rhetenor*: (a) Photograph of *M. rhetenor*. (b) Optical microscope image of *M. rhetenor's* imbricated blue iridescent scales. (c) SEM image of *M. rhetenor's* iridescent scale, with visible ridge patterning running down the length of the scale. (d) TEM cross-section of *M. rhetenor*. (Images courtesy of P. Vukusic). [Scale bars: (a) 2 cm, (b) 1 mm, (c) 100 µm, and (d) 2 µm].

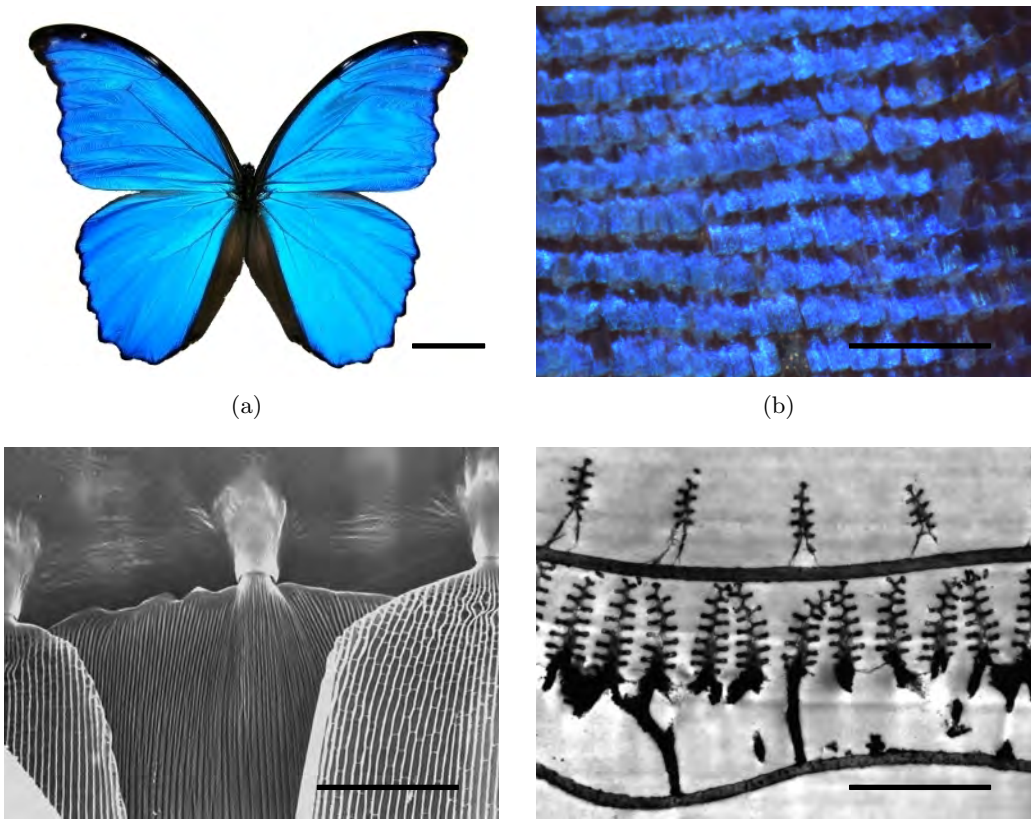

(a) (b)

(c) (d)

Figure 2.8: Appearance and scale structure of *Morpho rhetenor*: (a) Photograph of *M. didius*. (b) Optical microscope image of *M. didius'* scales with discernible over-layed cover scales. (c) SEM image of an *M. didius* ground scale, with over-laying cover scales either side. Also visible are the sockets by which the scales attach to the wing membrane. (d) TEM cross-section of *M. didius* showing a cover scale above, and a ground scale below. (Images courtesy of P. Vukusic). [Scale bars: (a) 2 cm, (b) 1 mm, (c) 40 μm, and (d) 2 μm].

irregularity is another contributing factor to the observed wide-angle distribution of light scattered from *Morpho* scales. A simple diffraction model indicates that irregularity in the heights of the ridges within the scale results in its observed wavelength and angle-dependence [101, 102]. The reflected light may be described by an incoherent sum of diffraction arising from the discrete multilayered units [101, 102].

The saturation of the colour appearance of *Morphos* is not solely attributable to structural colour. The localisation of melanin content throughout the ground scales leads to an enhancement of the saturation of blue reflection due to the absorption of complementary wavelengths. This reduces backscatter from the underside of the wing membrane and ventral wing-scales [103]. The contrast in a TEM image of a *Morpho* ground scale generally shows a heterogeneous greyscale gradient through the photonic structure [104]. This greyscale contrast strongly implies the presence and extent of melanin content in a scale due to the differential uptake of heavy-metal stains during the TEM sample preparation process [53]. Optical modelling appears to confirm the role and presence of absorbing pigment in these systems [53, 104].

The absence of melanin in what would be an otherwise highly reflective *Morpho* ground scale leads to a significant desaturation of the blue reflection [103]. The bright blue wings of *M. cypris*, for instance, exhibit small regions of wing, in patches and in stripes, which do not contain any melanin. Non-absorbed light which is then scattered between the disordered interfaces of structural components in the dorsal scales, ventral scales and wing substrate in these regions results in their bright white appearance [103]. Other biological structures achieve whiteness through the broadband scattering of light from disordered and pigment-free sub-wavelength structures, some of which are highly optimised for brightness [24, 87, 105].

Penetration of the wing, or an isolated scale, by a wetting fluid such as alcohol, leads to strong modification of the interference conditions. Use of a fluid of RI close to that of water produces a bright green reflection [63]. If the fluid's RI more closely matches that of the cuticle itself, however, then index-matching processes remove any strong scattered intensity or colour. When a system is fully index-matched by a fluid the measurements of light transmitted through it can be used to quantify the absorption arising from the melanin content within the scale [63]. Alternative theoretical approaches, such as the effective medium model, can be employed to fit simulated reflectance to measured reflectance to obtain the complex refractive index of the insect cuticle [106].

The complexity of the *Morpho* structure, comprising discrete units of multilayering and a degree of biological noise in its periodicity, renders it very challenging to model accurately. While straightforward optical multilayer theoretical approaches, described in Chapter 5, offer a basic means to quantify reflection from *Morpho* scales, they are limited. More sophisticated modelling approaches, which are able to cater for such

hierarchical periodicities and multi-dimensional structures, are required to meet the challenge of describing and understanding these systems more accurately. The more successful of these approaches include Finite Element Method (FEM) modelling [107] and Finite-Difference Time-Domain (FDTD) techniques [108]. They both involve the schematic representation, in either 2D or 3D, of the *Morpho* multilayer reflecting unit or a series of these units, simulating optical illumination at a set angle or polarisation, then solving Maxwell's equations to obtain reflectance and transmittance information.

Simple *Morpho* geometries for use with FDTD techniques usually feature the characteristic discrete tree-like units comprising rectangular dielectric blocks. These are geometrically arranged to mimic the distribution of the lamellae associated with *Morpho* scales. Numerical calculation of the hemispherical scatter from such simplified 2D geometries demonstrates the spectral dependence of the tapering and asymmetry of lamellae within the structures [109–111]. 3D FDTD models can help explore the effect of changing the alignment and offset of lamellae on the luminance and colour of scattered light [112, 113]. It also provides more scope with which to study the variation of a broader set of geometric parameters of more realistic *Morpho*-like structures. Using non-standard-FDTD, which uses higher-order FD approximations, enables some incorporation of small irregularities in the heights of the discrete multilayer structures relative to one another [114]. The discrete nature of such multilayer units, with some height variation, modifies the angular distribution of reflection and enhances the wide-angle reflection for shorter wavelengths [114]. Once this optical data is calculated, it can be used to generate the bidirectional reflectance distribution function [115], for which good experimental data exists [116]. This theory can then lead to remarkable graphical rendering of photo-realistic *Morpho* wings [117].

2.5.3 *Morpho*-related bio-inspired applications

Nature provides a suite of designs for bio-inspired applications. The plant Arctium, commonly known as burdock, inspired one of the best known and commercially realised applications. The hooked tips of the barbs on its seed burrs catch effectively on the loops provided by animal fur or human clothing, thereby acting as a good means for dispersal. The mechanism associated with this adhesiveness led to the design and manufacture of Velcro™ [118].

Structurally coloured animals and plants continue to inspire a number of technological and industrial applications. Brilliant whiteness in the thin elytral scales of *Cyphochilus* beetles, achieved at very low material cost, elicits interest in the development of optimised paper coating technology [24, 119]. Biological antireflection protocols, at work in some of the transparent wings and ommatidial eye surfaces of

Figure 2.9: Iridescent photonic *Morpho*-mimetic makeup. (Image courtesy of L'Oreal).

Lepidoptera, form potential templates for improving photovoltaic efficiencies [120, 121]. Advanced fabrication techniques have enabled the manufacture of stretchable iridescent fibres inspired by the design and colour appearance arising from multilayer structures found in certain tropical plant seeds [122].

Interdisciplinary scientific interest in the colour appearance of *Morpho* butterflies appears to have led to advances in several specific applications in areas such as textile, reflectors, cosmetics, and in sensing.

Morphotex® was the first example of a synthetic bio-inspired textile. The iridescent appearance of the cloth is produced by pigment-free fibres comprising a multilayer core structure made of alternating polyester and nylon layers [123]. Control of layer thicknesses in each fibre tunes the fabric colour appearance and the absence of dye renders it extremely colourfast.

The ability to finely control multilayer structure fabrication in more complex geometries enables technological mimicry of the desirable colour appearance exhibited by butterflies such as *Morpho*. Specially tailored layer-by-layer deposition of dielectric material can be used to produce flexible multilayer thin film dielectric reflectors that display remarkable bright and angle-independent reflection similar to that exhibited by *Morphos* [124]. Such reflectors have wide-ranging applications in reflective displays, packaging, and advertising.

Pigment-free cosmetic products rely on structural colour centres as the source of

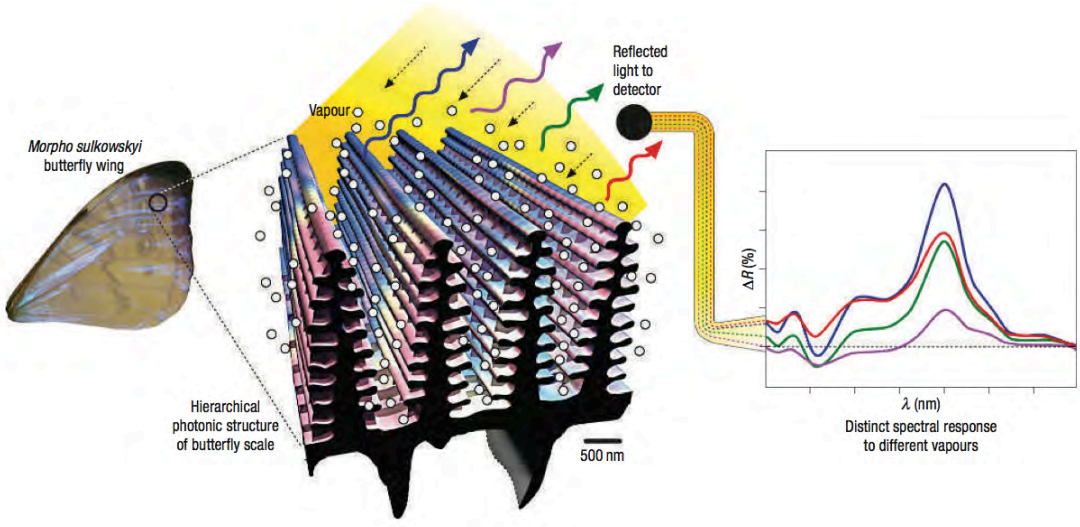

Figure 2.10: Schematic of the *Morpho*-based vapour sensing principle. Vapour present in the photonic structures of *M. sulkowskyi* iridescent scales changes the differential reflectance spectra ΔR, which provides information about the vapour environment and concentration. (Reprinted from Ref. [8], with permission of Macmillan Publishers Ltd: Nature Photonics, and R.A. Potyrailo).

the appearance they generate. Mica-based and silica-based systems incorporating periodic polymer networks are used to generate coherent scattering in photonic cosmetic applications. This basis of colour generation leads to a different appearance aesthetic compared to that associated with pigment-based cosmetics. The design of these products is closely linked to inspiration from butterflies such as *Morpho* [125], see Figure 2.9.

Colour reflections from *Morpho* wings exhibit sensitivity to the presence of chemical vapours. This arises largely because of the open access to air-spaces between the lamellae that form its reflecting elements, and the formation of thin layers of adsorbate around these lamellae. In this way, *Morpho* butterflies' photonic structures offer bio-inspired protocols for chemical vapour sensing [8]. By measuring change in reflectance upon exposure to low concentrations of different chemicals, the *Morpho* scale structure serves as a natural transducer of the chemical signal. Analysis of reflectance demonstrates sensitive and selective optical response to various low-weight organic vapours including alcohols and water. A schematic of this technique is shown in Figure 2.10. While this is an interesting avenue of bio-inspired exploitation, this effect appears to serve no discernable biological function to the animal itself unlike, for example, the humidity-induced colour change observed in *Dynastes hercules* beetles, that is providing new inspiration for humidity sensing applications [126–128].

Another area of high performance sensing to which *Morpho* butterflies have con-

tributed is the optical transduction of thermal radiation. The colour reflectance response of *Morpho* wings can offer sensitivity to mid-wavelength infrared radiation [9]. Iridescent scales doped with carbon nanotubes produce thermally-induced reflectivity changes giving rise to detectable visible-range colour shifts [9]. These colour shifts relate to the thermal expansion and refractive index changes, which are modulated by mid-infrared radiation.

2.6 Summary

In this chapter, aspects of biological photonics have been reviewed. In doing so, examples of naturally occurring 1D, 2D and 3D photonic crystals have been summarised. In addition other structures seen in natural systems have been described, particularly diffracting and scattering structures.

The main focus of this background review has been on presenting work relating to the *Morpho* butterfly. This is a well-studied species that has a striking structurally coloured bright blue appearance arising from a distinctive and somewhat hierarchical periodic structural origin. Its optical design is one of now many organisms that have inspired technological directions for use and exploitation, and some of these were discussed near the end of this review.

In biological systems, the optical cause and effect that is associated with the capability of periodic structures to manipulate light, thereby giving rise to distinct optical appearances due to tailored colour and polarised light reflection, are now the subject of genuine interdisciplinary scientific interest. Achieving precise understanding of the mechanism with which an exotic-looking animal or plant derives its intense saturated colour, its deep black or brilliant white appearance, or possibly even its dramatic linear or circular polarisation signature, can be an eminently exciting and scientifically rewarding process. From the perspectives of evolutionary diversity, behavioural biology and general zoology, materials science, mainstream optics and photonics, self-assembly chemistry and bio-inspired technology, the study of light and colour manipulation in biological systems is yielding rich reward.

Chapter 3

Photonics Theory

3.1 Introduction

Biological systems can produce a wealth of colour and exciting optical effects through the control of light by a variety of photonic structures, such as those examples discussed in Chapter 2. It is widely accepted that the coherent scattering of light, which may produce such colour effects, can arise though several fundamental structural contributions [4]. These contributions may be from thin film [46] or multilayer interference [47], diffraction or scattering [129] or photonic crystals [130, 131]. Even in the simplest natural systems, the observed structural colour effects are often due to many of these contributions simultaneously.

In this chapter, some of the physics fundamental to understanding the manipulation of light in biological reflectors is described. To begin, Maxwell's equations are presented, before a general description of photonic crystal theory is described. Following this, two aspects more specific to the colour production mechanisms of *Morpho* butterflies are discussed; namely, multilayer interference and diffraction. As a vehicle for this, a short derivation of the Fresnel coefficients of reflectance and transmittance from a single interface is made, then the reflectance of a single thin film is considered. This description is then extended to multiple reflecting layers. The optical properties of the constituent materials, the number of layers, and the angle of incidence are then elucidated for biological multilayer reflectors. Finally, the theory and use of diffraction in biological reflectors is described.

The content presented in this chapter expands on that published in the review article titled 'Light manipulation principles in biological photonic systems' by T. Starkey and P. Vukusic, in Nanophotonics, Volume 2, Issue 4, Pages 289–307, Year 2013 in Ref. [11].

3.2 Maxwell's equations

Maxwell's equations are the four fundamental relations that describe electric and magnetic phenomena in free space and in media. The equations were deduced by Maxwell in his four-part work 'On Physical Lines of Force' published between 1861 and 1862 [132]. Of the one hundred and sixty five equations listed in Maxwell's original work, it was Heaviside that later grouped the four that are known Maxwell's equations [133]. These are:

$$\nabla \cdot \mathbf{E}(\mathbf{r}, t) = \frac{\rho_{\text{free}}}{\epsilon_o}, \tag{3.1}$$

$$\nabla \cdot \mathbf{B}(\mathbf{r}, t) = 0, \tag{3.2}$$

$$\nabla \times \mathbf{E}(\mathbf{r}, t) = -\frac{\partial \mathbf{B}(\mathbf{r}, t)}{\partial t}, \tag{3.3}$$

$$\nabla \times \mathbf{H}(\mathbf{r}, t) = \mathbf{J}(\mathbf{r}, t) + \frac{\partial \mathbf{D}(\mathbf{r}, t)}{\partial t}, \tag{3.4}$$

where $\mathbf{E}$ is the electric field vector, ρ_{free} is the free charge density, ϵ_o is the permittivity of free space, $\mathbf{B}$ is the magnetic induction, $\mathbf{H}$ is the magnetic field, $\mathbf{J}$ is the electric current vector, $\mathbf{D}$ is the electric field displacement vector, $\frac{\partial}{\partial t}$ is the partial derivative with respect to time, and $(\mathbf{r}, t)$ denotes the variables for position and time.

Each equation was deduced by Maxwell to describe his own experimental observations. Equation 3.1 is commonly called Gauss's law, and relates the divergence of an electric field to the charge creating it. Equation 3.2 is more often unnamed, and states that magnetic monopoles cannot exist. Equations 3.3 and 3.4 relate the electric and magnetic components, and are know as Faraday's Law and Ampère's law (with Maxwell's correction), respectively. It is generally accepted that Maxwell's equations are true for all macroscopic situations that can be observed.

3.3 Photonic crystals

A photonic crystal (PhC) is a structure with a periodically changing dielectric constant that influences the propagation of electromagnetic radiation. By arranging periodically varying refractive indices (RIs) in one, two or in all three spatial directions, opportunities arise to bend, slow and tailor the propagation of light [134]. In the late 1980s the modern field of photonic crystals was born, principally following the works of John and of Yablonovitch [130, 131]. These works developed the analogy between electrons

propagating through solid matter, with a periodic potential, and photons propagating through a periodic dielectric structure. Biological systems contain many different examples of PhCs with regular RI periodicities [3, 4, 48], some of which were presented in Chapter 2. They not only exist in plain 1D geometries, such as with more simple multilayer systems, but are also found in 2D and 3D arrangements. Such structural designs, and the light and colour to which they give rise, often confer specific visual appearances that underpin particular biological functions.

Photonic crystals exhibit many analogous properties to those of the well understood crystal lattice. Concepts such as reciprocal space, Brillouin zones and dispersion relations exist for PhCs. In a crystal lattice, an electron propagates through a potential arising from the surrounding atoms [135]. In a PhC, photons travel though macroscopic dielectric media in much the same way; consequently many of the same properties can be seen. PhCs can exhibit desirable and tunable properties such as the photonic band gap (PBG). PBGs forbid the propagation of certain frequencies/energies of electromagnetic radiation though the dielectric crystal [136].

Another property of PhCs is their scale invariance [134]. In atomic physics the fundamental length scale is set by the spatial scale of lattice potential (usually on the order of the Bohr radius) [134]. In PhCs this is not the case: PhCs scale with incident radiation. This property is a convenient tool when characterising the response of PhC structures on the nanoscale, as they can be scaled up to structures to the order of centimetres, then interrogated by microwave radiation [115].

In PhC theory, the frequencies of photons that are allowed to propagate in a dielectric crystal can be solved as eigenvalue problems [134]. In order to study the propagation of electromagnetic (EM) radiation through a PhC, a 'master equation' that describes the fields is obtained. Using the master equation, together with Maxwell's divergence equations, all of the electromagnetic properties of a PhC can be described. The treatment of this problem is now described following the approach made in Ref. [134]. The formulation of this equation is considered here for lossless dielectric materials with linear dependence to the EM fields. By making these material assumptions for a permittivity profile $\epsilon(\mathbf{r})$, Maxwell's equations, Equations 3.1-3.4, can be expressed as:

$$\nabla \cdot [\epsilon(\mathbf{r})\mathbf{E}(\mathbf{r},t)] = 0, \tag{3.5}$$

$$\nabla \cdot \mathbf{H}(\mathbf{r},t) = 0, \tag{3.6}$$

$$\nabla \times \mathbf{E}(\mathbf{r},t) + \mu_0 \frac{\partial \mathbf{H}(\mathbf{r},t)}{\partial t} = 0, \tag{3.7}$$

$$\nabla \times \mathbf{H}(\mathbf{r},t) - \epsilon(\mathbf{r})\epsilon_0 \frac{\partial \mathbf{E}(\mathbf{r},t)}{\partial t} = 0, \tag{3.8}$$

where ϵ_0 and μ_0 is the permittivity and permeability of free space, respectively. As a mathematical convenience, a harmonic expansion is used to express the $\mathbf{E}$ and $\mathbf{H}$ fields as a product of the spatial and time dependent components, yielding:

$$\mathbf{E}(\mathbf{r},t) = \mathbf{E}(\mathbf{r})e^{-i\omega t}, \tag{3.9}$$

$$\mathbf{H}(\mathbf{r},t) = \mathbf{H}(\mathbf{r})e^{-i\omega t}, \tag{3.10}$$

where ω is the angular frequency.

By substituting these fields into Maxwell's curl equations, Equations 3.7 and 3.8, the relation between $\mathbf{E}$ and $\mathbf{H}$ is then given by:

$$\nabla \times \mathbf{E}(\mathbf{r}) - i\omega\mu_0\mathbf{H}(\mathbf{r}) = 0, \tag{3.11}$$

$$\nabla \times \mathbf{H}(\mathbf{r}) + i\omega\epsilon_0\epsilon(\mathbf{r})\mathbf{E}(\mathbf{r}) = 0. \tag{3.12}$$

Expressing these equations solely in terms of $\mathbf{E}$ and $\mathbf{H}$ yields equations that give a full EM description of the fields propagating through a crystal with spatial dielectric profile $\epsilon(\mathbf{r})$. Either of the two equivalent expressions define the properties of the PhC:

$$\nabla \times (\nabla \times \mathbf{E}(\mathbf{r})) = \left(\frac{\omega}{c}\right)^2 \epsilon(\mathbf{r})\mathbf{E}(\mathbf{r}), \tag{3.13}$$

$$\nabla \times \left(\frac{1}{\epsilon(\mathbf{r})}\nabla \times \mathbf{H}(\mathbf{r})\right) = \left(\frac{\omega}{c}\right)^2 \mathbf{H}(\mathbf{r}). \tag{3.14}$$

where c is the velocity of light in a vacuum.

Since Equation 3.14 is always Hermitian, and hence can be treated as an eigenvalue problem, it is usually referred to as the master equation. The modes of the field, and their frequencies, are given by the solution of this eigenvalue problem, that depends solely on properties of the dielectric constant. In a PhC with symmetric translational periodic variations of the dielectric constant in one, two or three dimensions, $\epsilon(\mathbf{r})$ is a symmetric translation of the dielectric constant, whose reciprocal can be expanded as:

$$\frac{1}{\epsilon(\mathbf{r})} = \sum_{\mathbf{G}} b_{\mathbf{G}} e^{i\mathbf{G}\cdot\mathbf{r}}, \tag{3.15}$$

where $\mathbf{G}$ the reciprocal lattice vector [135].

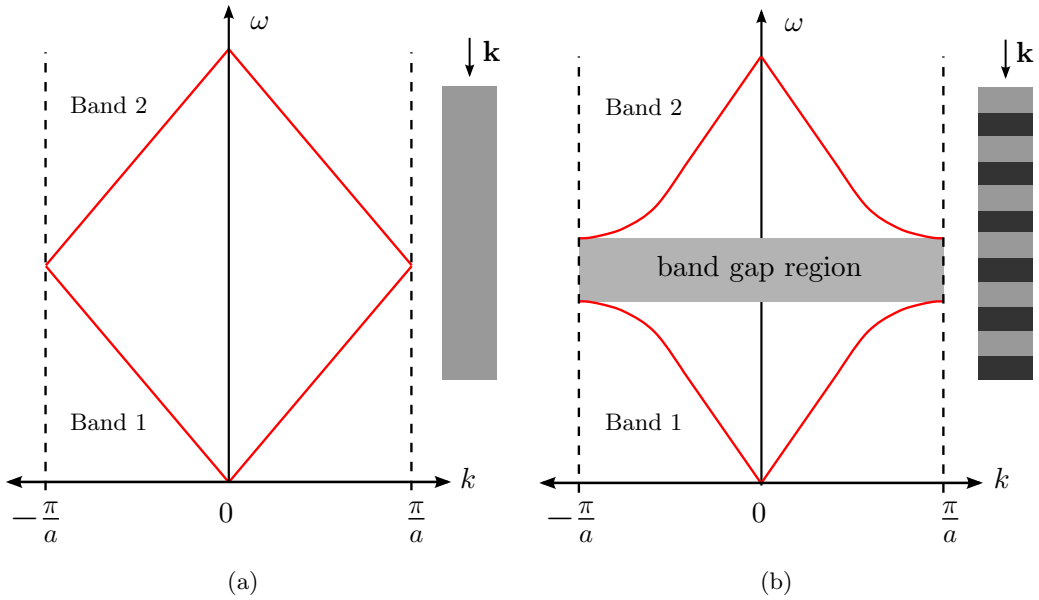

Figure 3.1: Reduced Brillouin zone schematic for: (a) a homogeneous non-dispersive dielectric slab, and (b) dispersion diagram for 1D photonic crystal. The inset images indicate the RI variation considered in each case, with radiation incident with wavevector **k**. The introduction of the regular periodicity (a) in 1D creates the PBG, where impinging radiation with a frequency within this region is unable to propagate.

It is now useful to outline the physical consequences of light incident on a 1D PhC, especially in relation to the more traditional treatment of multilayer reflection. To this end, consider the propagation of light in a homogeneous non-periodic medium. By using the reduced Brillouin zone (BZ) representation for this system [135] its dispersion diagram can be simplified to a series of photonic bands, with one band originating from each BZ, as shown in Figure 3.1(a).

If this medium is replaced with one that has periodically changing RIs, for instance, a 1D system comprising high and low RI layers, the original reduced BZ band diagram is distinctly modified. Light incident with a wavelength satisfying the resonant conditions of the system, as dictated by the periodicity and RIs of the layers, creates standing waves at two different energies. Their presence results in a frequency range in which electromagnetic radiation incident on the 1D PhC is forbidden from propagating, since the group velocity at the band edge is zero. This region, shown in Figure 3.1(b), is the PGB, the size of which is strongly influenced by the constituent RIs of the PhC.

Having shown the dispersion properties of a PhC with a periodic variation in RI profile in 1D, the reflectance of a finite number of reflecting layers in 1D can now be considered. In order to do this, a discussion of the reflectance from an interface is used

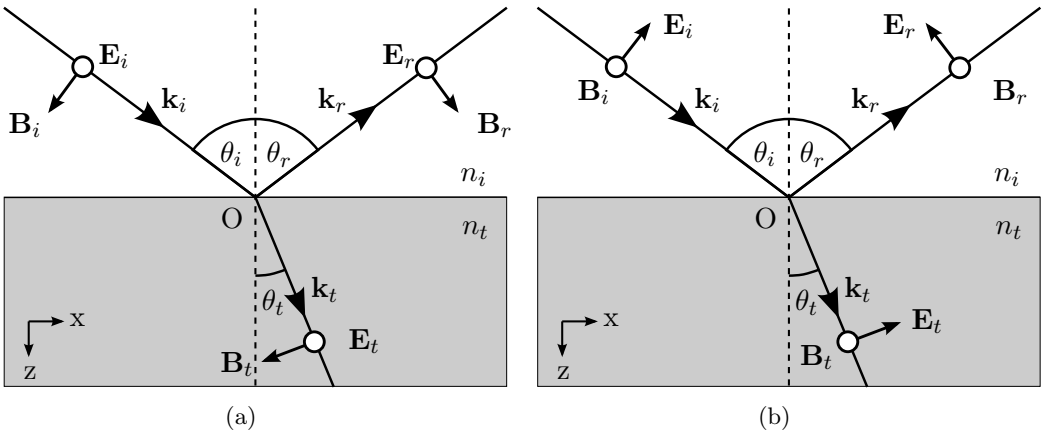

Figure 3.2: Schematic illustrations for the analysis of the reflectance and transmittance of radiation at an interface. (a) Case 1: where the incident E-field is perpendicular to the plane of incidence, and (b) Case 2: where the incident E-field is parallel to the plane of incidence.

to derive the Fresnel equations, after which the reflectance of a thin film and multilayer film can be considered.

3.4 The reflection of electromagnetic waves at a boundary

3.4.1 Reflection from a single interface

The fundamental physical mechanism of structural colour generation arises through the interaction of electromagnetic (EM) waves incident upon a series of interfaces that bound dissimilar media. An EM wave incident upon the interface between two media of different RI may either be reflected, transmitted, guided, or a combination of these. The extent to which these optical properties occur is determined by the material properties of both media, the polarisation state of the EM wave, and the angle at which the EM wave is incident upon the interface.

The reflectance and transmittance properties of an EM wave incident upon an interface can be calculated from the Fresnel equations. These expressions, that were first deduced by Fresnel, quantify the wave amplitudes of the reflected and transmitted beams in terms of the optical properties of the media and the direction of propagation of the beam with respect to the interface. The derivation of the reflected and transmitted wave amplitudes for linear polarisations is now shown using momentum considerations for non-magnetic, isotropic, inhomogeneous media. This derivation follows the approach of many standard texts [137–139].

First, from Maxwell's equations it can be shown that an EM wave exists if the electric field **E** is orthogonal to the magnetic induction **B** and also orthogonal to the direction of travel, such that:

$$\mathbf{B} = \frac{\mathbf{k} \times \mathbf{E}}{\omega}, \tag{3.16}$$

where **k** is the wave vector in the direction of propagation and ω is the angular frequency.

Where a wave is incident at an angle θ_i from the normal of an interface two cases may be considered: Case 1, where the incident E-field is perpendicular to the plane of incidence, termed transverse electric (TE) or s-polarised, or Case 2 where the wave has incident E-field parallel to the plane of incidence, called transverse magnetic (TM) or p-polarised (here the plane of incidence takes its usual meaning). Both cases are shown in Figure 3.2. The subscripts i, r and t used in Figure 3.2, and in the description herein, denote the incident, reflected and transmitted components, respectively, for the fields, angles, and wave vectors.

For a monochromatic plane wave incident from a material of RI n_i, to a material of RI n_t, as shown in Figure 3.2, the incident fields, $\mathbf{E}_i$ and $\mathbf{B}_i$, are given by:

$$\mathbf{E}_i(\mathbf{r}, t) = \mathbf{E}_{0_i} e^{i(\mathbf{k}_i \cdot \mathbf{r} - \omega t)}, \tag{3.17}$$

$$\mathbf{B}_i(\mathbf{r}, t) = \frac{1}{v_i}(\mathbf{k}_i \times \mathbf{E}_i), \tag{3.18}$$

The field components for both the reflected and transmitted wave components have fields of equivalent form, given by:

$$\mathbf{E}_r(\mathbf{r}, t) = \mathbf{E}_{0r} e^{i(\mathbf{k}_r \cdot \mathbf{r} - \omega t)}, \tag{3.19}$$

$$\mathbf{B}_r(\mathbf{r}, t) = \frac{1}{v_r}(\mathbf{k}_r \times \mathbf{E}_r), \tag{3.20}$$

$$\mathbf{E}_t(\mathbf{r}, t) = \mathbf{E}_{0t} e^{i(\mathbf{k}_t \cdot \mathbf{r} - \omega t)}, \tag{3.21}$$

$$\mathbf{B}_t(\mathbf{r}, t) = \frac{1}{v_t}(\mathbf{k}_t \times \mathbf{E}_t). \tag{3.22}$$

At a point on the interface, for instance point O in Figures 3.2(a) and 3.2(b), appropriate boundary conditions (BCs) can be imposed to obtain the reflection and transmission coefficients. In both of the cases stated, the tangential **E** and **H** ($= {}^{\mathbf{B}}/_{\mu}$) field components must be continuous across the boundary.

Case 1: s-polarisation (transverse electric)

For Case 1, where the incident E-field is perpendicular to the plane of incidence (see Figure 3.2(a)), the continuity across the boundary requires:

$$\mathbf{E}_{0i} + \mathbf{E}_{0r} = \mathbf{E}_{0t}, \tag{3.23}$$

$$-\frac{|\mathbf{B}_{0i}|}{\mu_i}\cos\theta_i + \frac{|\mathbf{B}_{0r}|}{\mu_i}\cos\theta_r = -\frac{|\mathbf{B}_{0t}|}{\mu_t}\cos\theta_t. \tag{3.24}$$

Since the magnitude of the **B** component is the scaled magnitude of the **E** component, given by $|\mathbf{B}| = {}^{|\mathbf{E}|}/_{v}$, where v is the phase velocity of the wave, Equation 3.24 may be expressed in terms of the **E** components:

$$-\frac{|\mathbf{E}_{0i}|}{v_i\mu_i}\cos\theta_i + \frac{|\mathbf{E}_{0r}|}{v_i\mu_i}\cos\theta_r = -\frac{|\mathbf{E}_{0t}|}{v_t\mu_t}\cos\theta_t. \tag{3.25}$$

The angular frequency is common between incident, reflected and transmitted waves, so that any position $\mathbf{r}$ on the interface the wave vectors must satisfy:

$$\mathbf{k}_i\cdot\mathbf{r} = \mathbf{k}_r\cdot\mathbf{r} = \mathbf{k}_t\cdot\mathbf{r}. \tag{3.26}$$

As a consequence of this condition, Snell's Law of Refraction, $n_i\sin\theta_i = n_t\sin\theta_t$, and the Law of Reflection, $\theta_i = \theta_r$, can be shown. Using these results, and assuming non-magnetic media ($\mu_i = \mu_r = \mu_t = \mu_0$), the E-components can be eliminated to produce two expressions, one with E_r and E_i terms, and the other with E_t and E_i:

$$\frac{\mathrm{E}_r}{\mathrm{E}_i} = \frac{v_i\cos\theta_i - v_t\cos\theta_t}{v_i\cos\theta_i + v_t\cos\theta_t}, \tag{3.27}$$

$$\frac{\mathrm{E}_t}{\mathrm{E}_i} = \frac{2v_i\cos\theta_i}{v_i\cos\theta_i + v_t\cos\theta_t}. \tag{3.28}$$

(Note: the notation has been simplied so that $\mathrm{E}_i \equiv |\mathbf{E}_{0i}|$, and so on).

Case 2: p-polarisation (transverse magnetic)

For Case 2, where the incident E-field is parallel to the plane of incidence (see Figure 3.2(b)), the continuity across the boundary requires:

$$|\mathbf{E_{0i}}|\cos\theta_i - |\mathbf{E_{0r}}|\cos\theta_r = |\mathbf{E_{0t}}|\cos\theta_t, \tag{3.29}$$

$$\frac{|\mathbf{B}_{0i}|}{\mu_i} + \frac{|\mathbf{B}_{0r}|}{\mu_r} = \frac{|\mathbf{B}_{0t}|}{\mu_t}. \tag{3.30}$$

Using the standard relations and assumptions used for the consideration of s-polarised waves, Equation 3.30 can be expressed as

$$n_i|\mathbf{E}_{0i}| + n_r|\mathbf{E}_{0r}| = n_t|\mathbf{E_{0t}}|. \tag{3.31}$$

Fresnel's equations

By re-expressing Equations 3.27 and 3.28, and combining Equations 3.29 and 3.31 with the standard relations previously used (and the simplification of notation), these equations can be expressed in a more familiar formulation as Fresnel's equations:

$$r_s = \left(\frac{\mathrm{E}_{0r}}{\mathrm{E}_{0i}}\right)_s = \frac{n_i\cos\theta_i - n_t\cos\theta_t}{n_i\cos\theta_i + n_t\cos\theta_t}, \tag{3.32}$$

$$t_s = \left(\frac{\mathrm{E}_{0t}}{\mathrm{E}_{0i}}\right)_s = \frac{2n_i\cos\theta_i}{n_i\cos\theta_i + n_t\cos\theta_t}, \tag{3.33}$$

$$r_p = \left(\frac{\mathrm{E}_{0r}}{\mathrm{E}_{0i}}\right)_p = \frac{n_t\cos\theta_i - n_i\cos\theta_t}{n_t\cos\theta_i + n_i\cos\theta_t}, \tag{3.34}$$

$$t_p = \left(\frac{\mathrm{E}_{0t}}{\mathrm{E}_{0i}}\right)_p = \frac{2n_i\cos\theta_i}{n_t\cos\theta_i + n_i\cos\theta_t}, \tag{3.35}$$

where s and p denote the polarisation of radiation, and r and t denote the reflected or transmitted amplitude coefficient.

From Fresnel's equation it can be seen that the RI, or more importantly the contrast of RI, strongly affects the magnitude of the Fresnel coefficients. This consequently affects the reflectance and transmittance intensities, which are found by squaring the associated coefficients:

$$R = rr^*, \tag{3.36}$$

$$T = \frac{n_t\cos\theta_t}{n_i\cos\theta_i}tt^*, \tag{3.37}$$

where R and T denotes the reflection and transmission intensities, respectively.

It is not possible to examine the optical properties of a thin film, or multiple thin films, using solely the Fresnel coefficients for each layer in these 1D optical structures; the optical path difference must be considered.

3.4.2 Reflection from a thin film

The most common form of PBG structure in biological systems is the 1D periodicity associated with multilayers. It is found widely in the integument and scales of many insects [3, 4, 48] and fish [57, 59, 140]. The photonic band structure relating to simple 1D multilayers can be considered using basic ideas of interference. To illustrate this consider the thin film, shown in Figure 3.3(a), that has thickness d and RI n_2. The incident and exit media RIs are n_1, and n_3, respectively. Light that enters the film at an angle of θ undergoes a reflection from the top and bottom interface. The optical path difference (OPD) between these two reflections is $2dn_2\cos\theta$. For constructive interference to occur these reflections should be in phase. The conditions for this, for wavelength λ, are given by:

$$\left(m+\frac{1}{2}\right)\lambda = 2n_2 d\cos\theta \qquad \text{for } n_1 < n_2 < n_3, \tag{3.38}$$

and

$$m\lambda = 2n_2 d\cos\theta \qquad \text{for } n_1 < n_2 > n_3, \tag{3.39}$$

where m is an integer [138]. To describe wavelength-dependent reflection more accurately, however, the multiple reflections that occur within the film must be considered [129]. Figure 3.3(b) displays the amplitudes of waves undergoing multiple reflections in a thin film as a product of Fresnel coefficients. The sum of all reflected ray amplitudes is:

$$r = r_{12} + t_{21}r_{23}t_{21}e^{-i2\delta} + t_{21}r_{23}^2 t_{21}t_{21}e^{-i4\delta} + t_{21}r_{23}^3 t_{21}^2 t_{21}e^{-i6\delta} + ..., \tag{3.40}$$

where r_{12} and t_{12} are the Fresnel reflection coefficients at the interface between medium 1 and 2, and the phase difference arising from the film thickness is:

$$\delta = \frac{2\pi n_2 d\cos\theta}{\lambda}. \tag{3.41}$$

By summing appropriate amplitudes, the overall reflection coefficient associated with the films two interfaces is [129]:

$$r = \frac{r_{12} + r_{23}e^{-i2\delta}}{1 + r_{23}r_{12}e^{-i2\delta}}. \tag{3.42}$$

The total reflectance can be calculated using $R = |r|^2$. This can be used to predict the colour reflection of simple structurally coloured systems.

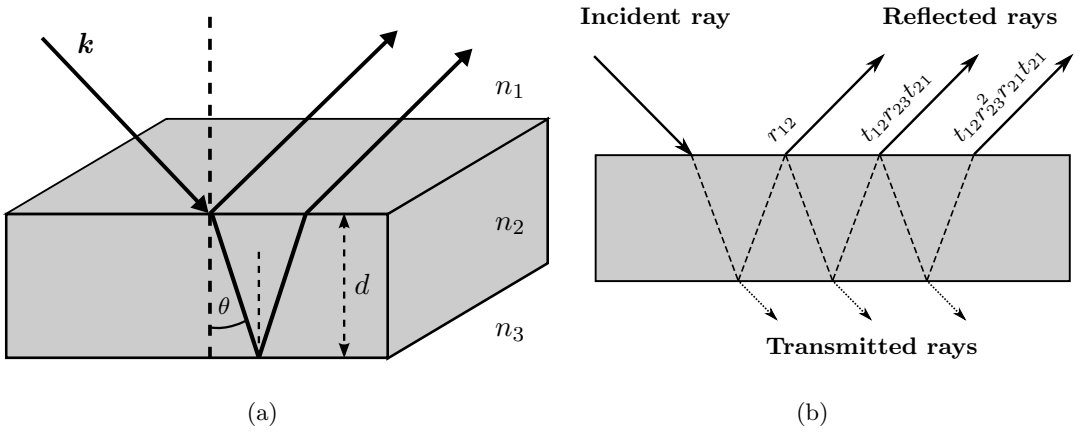

(a) (b)

Figure 3.3: (a) A schematic of thin film interference, and (b) a schematic illustrating the number of reflections that are considered for a full treatment of thin film reflection or transmission.

3.5 Interference from a multilayer stack

The most common method for the production of vivid, metallic colours in biological systems is achieved with multiple thin films, or multilayer systems. Here, peak reflectance can be determined using the same geometric considerations as were made for single thin films.

Consider multilayers comprising pairs of thin films; layer 1 has RI equal to n_1 and thickness d_1; layer 2 has RI n_2, and thickness d_2. Light is incident at an angle θ_0 from a medium with RI n_0. The condition for constructive interference is now

$$m\lambda = 2\left(d_1\sqrt{n_1^2 - n_0^2\sin^2\theta_0} + d_2\sqrt{n_2^2 - n_0^2\sin^2\theta_0}\right), \tag{3.43}$$

where m is an integer. A multilayer where the condition for constructive interference occurs in the two layer film and both layers simultaneously is known as an ideal multilayer [48]. For layer 1 this occurs when:

$$\left(m'\lambda + \frac{1}{2}\right) = 2d_1\sqrt{n_1^2 - n_0^2\sin^2\theta_0}, \tag{3.44}$$

where m' is a positive integer, and the $\frac{1}{2}$ takes account of the π phase shift. For normal incidence this reduces to the quarter wavelength condition, given by:

$$\frac{\lambda}{4} = n_1d_1 = n_2d_2. \tag{3.45}$$

Ideal multilayers are a special case, however. Although they are found in some

biological examples, such as some fish species' scales [59], the majority of biological multilayers are non-ideal. In these systems the optical thicknesses of layers in each medium can be subject to considerable variability from the ideal multilayer condition, while still exhibiting iridescent colour appearances [55].

A full consideration of wavelength-dependent, polarisation-dependent and angle-dependent reflectance from multilayer systems is commonly performed using transfer matrix methods [129, 141], recursion techniques [58] or iterative approaches [47, 142]. Here Rouard's approach is discussed as set out in [142], as a means to demonstrate these behaviours. In the following derivation simple loss-less dielectric materials are considered, however, the same considerations can be made to derive the optical properties of structures comprising materials with complex optical constants ($n^* = n + ik$) [142].

In the same way in which an expression for the reflectance of a thin film may be obtained, Rouard's technique can be used to calculate the reflectance from an ensemble of thin films. The approach works by calculating the reflectance of the multilayer stack in terms of an effective reflection coefficient and phase factor.

Consider a multilayer stack with n layers, where the $(n+1)^{\text{th}}$ layer is the incident medium, the n^{th} layer is the top layer, and the 1^{st} layer denotes the bottom layer, and 0^{th} layer is the exit medium.

Rouard's technique begins from the bottom of the multilayer stack. The reflection coefficient, r_{10}, arises from the interface of the last layer and the exit medium. By using the expression arrived at for a single thin film (Equation 3.42) the reflection coefficient at the interface between layer 2 and layer 1 may be expressed as:

$$\rho_{21}e^{i\Delta_{21}} = \frac{r_{21} + r_{10}e^{-i2\delta_1}}{1 + r_{10}r_{21}e^{-i2\delta_1}}, \tag{3.46}$$

where $\rho_{21}e^{i\delta_{21}}$ is our effective reflection coefficient. The next step is then to express the effective reflection coefficient for the interface above in terms of the effective reflection coefficient of the interface below. By doing so the effective reflection coefficient for the interface between layer 3 and layer 2 is given by:

$$\rho_{32}e^{i\Delta_{32}} = \frac{r_{32} + \rho_{21}e^{i\Delta_{21}}e^{-i2\delta_2}}{1 + \rho_{21}e^{i\Delta_{21}}r_{32}e^{-i2\delta_2}}, \tag{3.47}$$

and so on. The reflectance of the stack of m layers is simply given by the square of the complex reflectance amplitude, $\rho_{m+1,m}$:

$$R_m = |\rho_{m+1,m}|^2. \tag{3.48}$$

By generating reflectance spectra using this technique, the dependence of multilayer

reflectance on; 1) the number of layers, 2) the RI contrast of layers, 3) the angle of incidence, and 4) the effect of material absorption, is discussed.

3.6 Factors affecting reflectance in 1D biological systems

Several important variables contribute to the reflection from 1D photonic crystals, or multilayers. In biological systems, these variables can be set or controlled by the animal's or plant's morphology, behaviour or local ecology. The optical effect of, for instance, the number of layers or extent of optical absorption in a system can be very dramatic, making the difference between a highly reflective and conspicuous insect, and one that is dull and inconspicuous. The important factors affecting the reflectance of biological reflectors are outlined below.

3.6.1 Effect of number of layers

The reflectance from a theoretical ideal multilayer, modelled with peak reflectance at 500 nm, is shown in Figure 3.4(a) for 3, 9 and 27 layers, and in Figure 3.4(b) for much higher layer numbers. The reflectance shows characteristic multilayer spectral features, with a maximum in reflectance at the peak wavelength and a series of side band minima and maxima.

Using iterative methods, the peak reflectance for an ideal multilayer at normal incidence comprising alternating high RI (n_{high}) and low RI (n_{low}) layers, becomes [142]:

$$R = \frac{\left(\frac{n_{\text{high}}}{n_{\text{low}}}\right)^{2s} n_{\text{high}}^2 - n_{\text{inc}} n_{\text{out}}}{\left(\frac{n_{high}}{n_{\text{low}}}\right)^{2s} n_{\text{high}}^2 + n_{\text{inc}} n_{\text{out}}}, \tag{3.49}$$

where s denotes the number of high and low RI layer pairs in the system of $(2s+1)$ layers, and the RI of the incident and exit media are denoted by n_{inc} and n_{out}, respectively. As layer number increases, this reduces to:

$$R \simeq 1 - \left(\frac{4 n_{\text{inc}} n_{\text{out}}}{n_{\text{high}}^2}\right)\left(\frac{n_{\text{high}}}{n_{\text{low}}}\right)^{2s} \tag{3.50}$$

and the peak reflectance rapidly approaches unity. The region of 100% reflectance is the photonic band gap described earlier. Figure 3.4(b) shows that with increasing layer number, the peak reflectance increases to the point where the condition for this PBG is met. The spectral width of a 1D multilayer's PGB is governed by the constituent RIs of the layers [134].

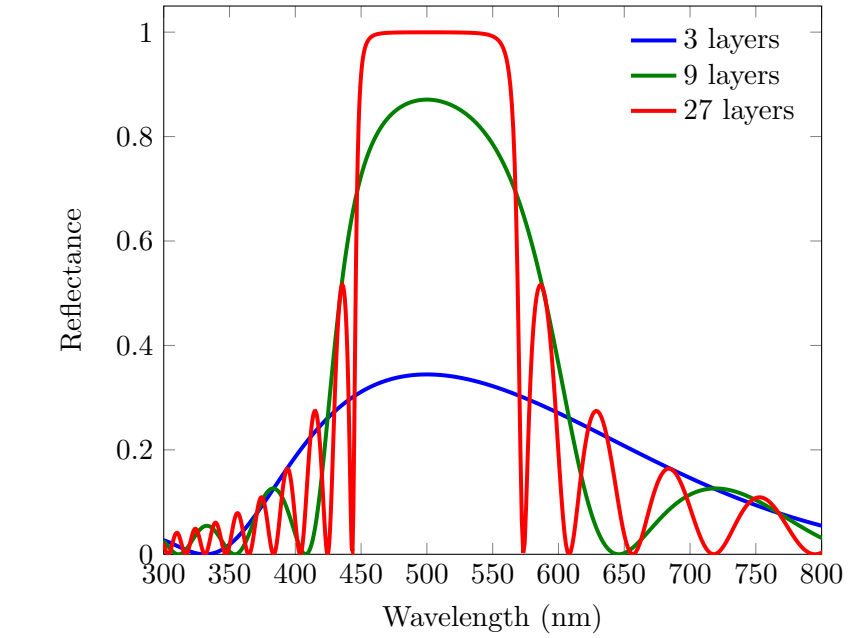

(a)

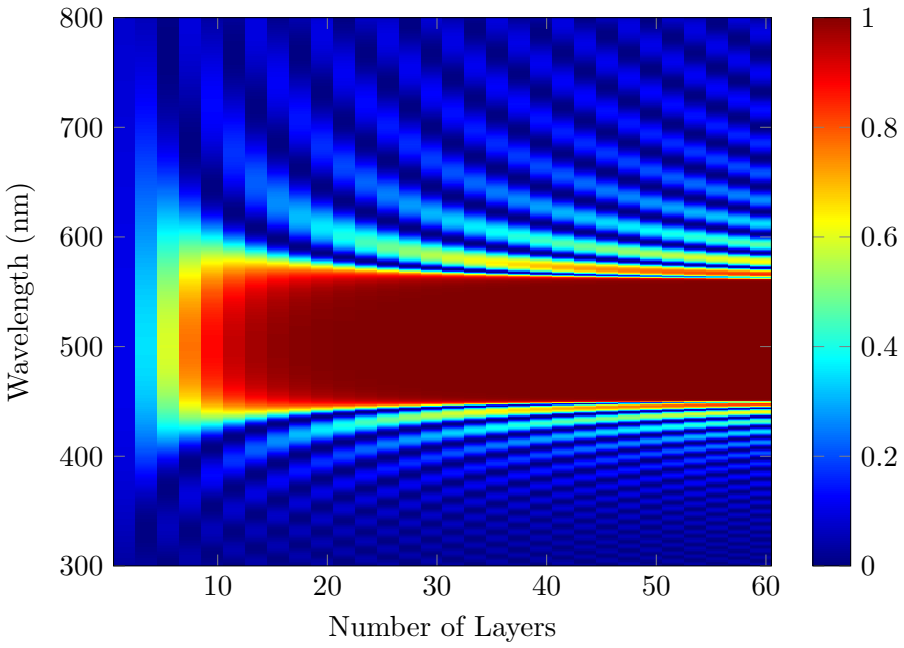

(b)

Figure 3.4: (a) Normal incidence reflectance of an ideal multilayer for 3, 9 and 27 layers, and (b) a reflectance map showing the theoretical variation of normal incidence reflectance with increasing layer number, the colour-scale axis represents reflected intensity (indicated in the labelled colour scale bar). Reflectance was calculated for a multilayer with $\lambda_{\text{peak}} = 500$ nm, $n_1 = 1.40$ and $n_2 = 1.00$.

Most structurally coloured biological species have evolved a relatively limited number of layers in their reflecting systems. This is the result of a balance between the relative cost and benefit of layer number with respect to the functions for which each system has evolved. Examples in which biological multilayering comprises 20 layers or more do exist but are rather uncommon [23]. Many examples exist in which fewer than 20 layers are found [54, 55, 143–145]. Species with high layer number tend to display much more intense colour reflections, and if the layers are relatively well aligned, this appears as a metallic-looking reflection due to the specular nature of the bright reflection [60, 63].

3.6.2 Angle-dependence of reflection

The phenomenon of iridescence, namely the change of hue with viewing angle, is a common hallmark of colour produced by periodic structure. Generally, a reflectance maximum will shift to shorter wavelength at larger angles, a property that can be understood using momentum considerations. Light incident normally, that satisfies the resonance condition, has wavevector $k_0 = k_z$. Light incident at some angle, θ, (shown in Figure 3.5(a)) will have wavevector $k_0 = k_x + k_z$. To retain the resonant condition, k_z must remain constant, leading to a required increase in k_0. Figure 3.5(b) shows the characteristic iridescent reflectance of unpolarised light for a typical ideal multilayer.

In addition to spectral position, the intensity of the peak reflectance band changes with incident angle. For unpolarised light, with increasing incident angle, the reflected intensity decreases to a minimum at the Brewster angle [146]. Beyond this, reflectance increases rapidly. The hierarchical and multi-component nature of biological reflectors often prevents clear discrimination of Brewster reflection features. Some biological examples of Brewster reflection, where multilayer structures are relatively flat and uniform across an area larger than the incident beam spot size, have been described [60, 144]. Certain fish species employ the natural birefringence of their constituent guanine material to inhibit the Brewster effect, and neutralise the associated polarised reflection feature [57].

The iridescent, or angle-dependent colour reflection property ascribed to multilayers is inhibited in some animal species; for instance, insects with multilayer structures often display bright structural colour that does not change hue with angle. To achieve this they exploit the addition of reflected colour from spatially juxtaposed pointillistic colour-centres to achieve angle independent reflection [26, 64].

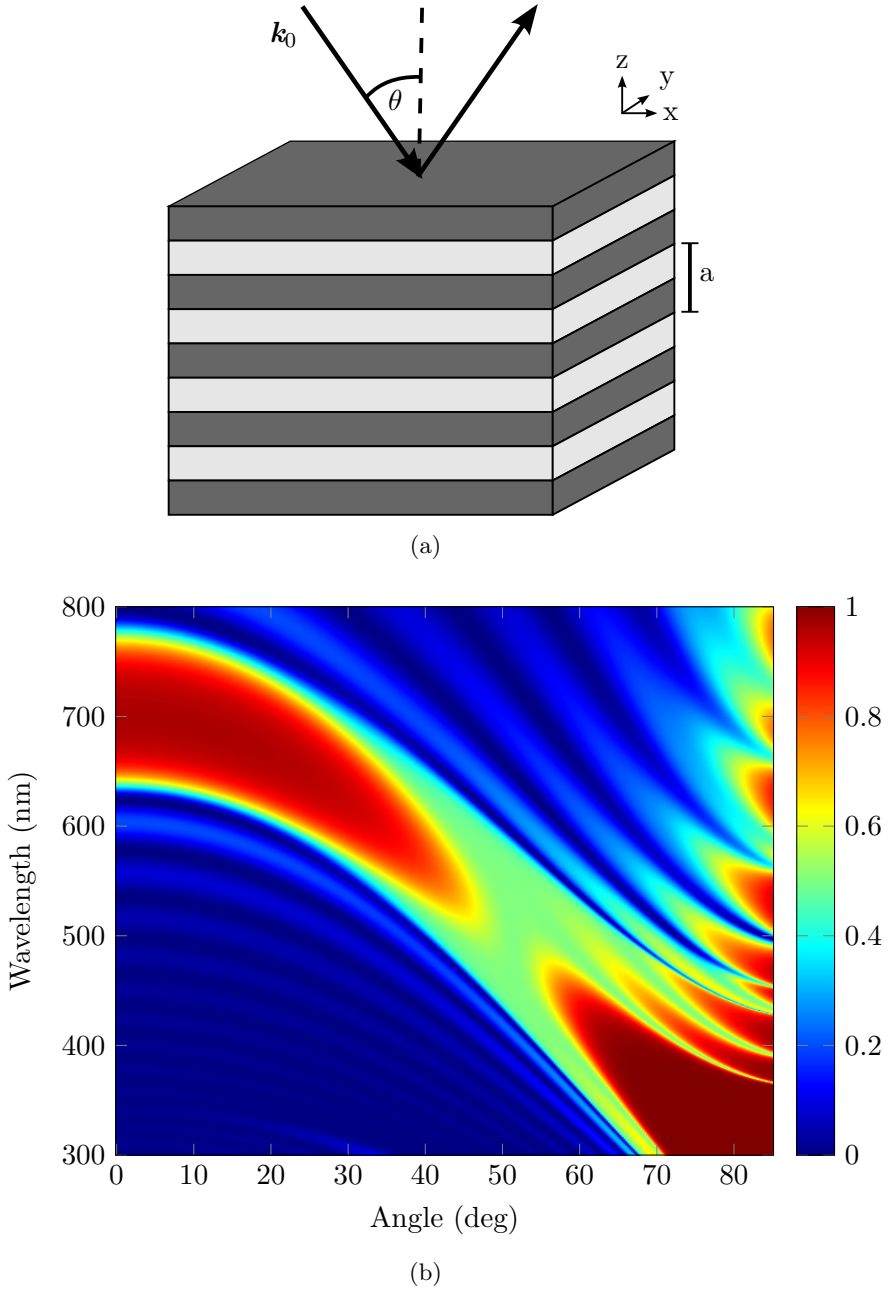

Figure 3.5: (a) A schematic diagram showing a generic multilayer having light incident with momentum components in the xz-plane, and (b) reflectance map showing the angle-dependence of unpolarised theoretical reflectance from an ideal multilayer with $\lambda_{\text{peak}} = 700$ nm at normal incidence, the colour-scale axis represents reflected intensity (indicated in the labelled colour scale bar).

3.6.3 Effect of refractive index contrast

The contrast between the high RI, n_{high}, and low RI, n_{low}, causes a pronounced effect on the reflectance. Figure 3.6 shows the dependence of normal incidence unpolarised reflection on increasing RI contrast, ($n' = n_{\text{high}}/n_{\text{low}}$) for an ideal 1D 20-layered system using a fixed $n_{\text{low}} = 1$. In the absence of absorption as the index contrast increases, both intensity and width of the reflected band increase. For this arrangement, 100% reflectance is achieved when n'= 1.54.

The dependence of reflected intensity on n' is a constraining factor for biological systems due to the limited range of materials that are naturally available to animals and plants. While, in technology, photonic systems may be designed and fabricated using a range of high-index materials, including metals and semiconductors, biological processes are limited largely to the use of simple dielectric materials. These rarely have RI values in excess of approximately 1.8, and the systems rarely have RI contrasts in excess of approximately 1.56. The RIs of some common materials found in previously studied bio-optical systems are shown in Table 3.1. RI dispersion in several bio-optical materials has also been measured experimentally [145, 147, 148].

The materials from which structurally coloured biological systems are fabricated clearly do not prevent the manipulation of light, for instance in the creation of bright coloured reflections. They do, however, limit the extent to which a complete PBG can be established by the structures they form [134].

Table 3.1: List of published values of refractive indices of materials present in a range of animal and plant biophotonic structures. High and low RI values are denoted by n_{h} and n_{l} respectively. In systems exhibiting birefringence, the ordinary and extraordinary RIs are denoted as n_{o} and n_{e}, respectively.

System	Material	Refractive Index
Insecta	Cuticle (Lepidoptera)	$n_{\text{h}} = 1.56$ [36, 63], $n_{\text{l}} = 1.00$ (air)
	Cuticle (Coleoptera)	$n_{\text{h}} = 1.68$ (melanin rich), $n_{\text{l}} = 1.56$ [145]
Aves	Keratin & Melanin	$n_{\text{h}} = 1.69$ (melanin) [144], $n_{\text{l}} = 1.54$ (keratin) [149], $n_{\text{l}} = 1.55$ to 1.57 (keratin) [147]
Fish	Guanine	$n_{\text{o}} = 1.80$ [59], $n_{\text{o}} = 1.83$ & $n_{\text{e}} = 1.46$ [57], $n_{\text{l}} = 1.33$ (water)
Flora	Cellulose	$n_{\text{h}} = 1.53$ (dried) & $n_{\text{h}} = 1.42$ (hydrated) [7, 150], n_{l} =1.33 (water)
Phytoplankta	Amorphous silica	$n_{\text{h}} = 1.46$ [151], n_{l} =1.33 (water)
Crustacea	Carbonates	$n_{\text{o}} = 1.50$ & $n_{\text{e}} = 1.70$ [152], n_{l} =1.33 (water)
Bacteria	Peptidoglycan	$n_{\text{h}} = 1.40$ [153], $n_{\text{l}} = 1.33$ (water)

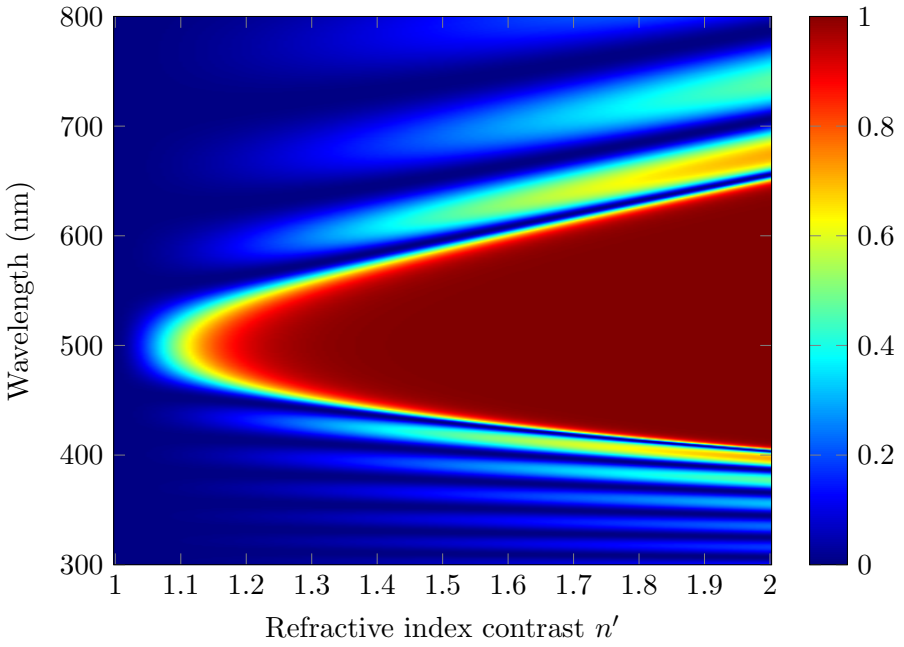

Figure 3.6: Reflectance map showing the theoretical dependence of normal incidence reflectance on RI contrast for a system comprising a 20-layer ideal multilayer, using fixed values $\lambda_{\text{peak}} = 500$ nm and $n_{\text{low}} = 1.00$. The colour-scale axis represents reflected intensity (indicated in the labelled colour scale bar).

3.6.4 Effect of optical absorption

Optical absorption in a dielectric medium attenuates light propagating through it according to the Beer-Lambert Law [138]. The absorption-related changes observed in the spectral response of a multilayer depend on whether the absorption is present in the high or low RI layers. When absorption is present in the high RI layers there is a large attenuation of the high-wavelength band-edge, as shown in Figure 3.7. The opposite is true when absorption is present in the low RI layers. The location-dependent presence of optical absorption therefore, not only can reduce overall reflected intensity, but it also can shape the spectral response.

The high RI layers in biological systems usually contain light-absorbing pigments. Whilst the real component of RI of many bio-optical tissues have been well characterised, the imaginary component quantifying the absorption is less well known. Melanin is a common absorbing pigment present in insect cuticle, and has very wide spectral absorbance due to its molecular conjugation [154].

A broadband absorbing pigment, such as melanin, has biological application in photoreceptor shielding, thermoregulation, photoprotection, camouflage and mechanical strength [154]. It can also be exploited to enhance aspects of colour reflection, for instance in the damselfly *Neurobasis chinensis chinensis*, which employs an absorbing

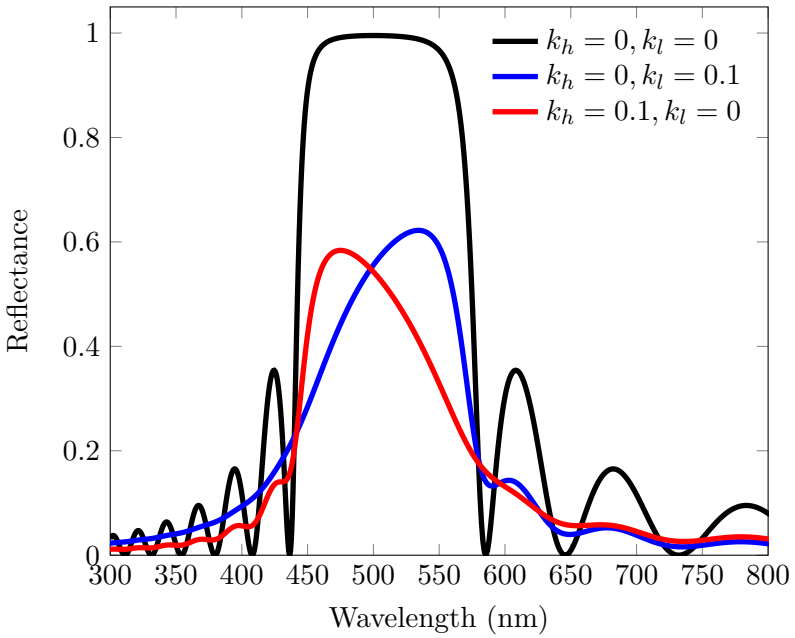

Figure 3.7: The effect on reflectance at normal incidence of absorption coefficient (k) for an ideal multilayer with $\lambda_{\text{peak}} = 500$nm. (The imaginary component of the RI in the high and low layers is denoted by k_{h} and k_{l}, respectively).

layer of melanin below the multilayer reflector as a mechanism to enhance reflected colour saturation [29]. This approach is adopted to varying degrees by a great many animal species [4]. In some species, the absence of melanin in or under a reflecting system desaturates the reflected colour so much that the surface region appears white [103].

One of the first measurements of the complex refractive index of insect cuticle in *Morpho* butterflies found $n^* = (1.56 \pm 0.01) + i(0.06 \pm 0.01)$ using a fluid immersion technique [63]. Further studies have characterised the wavelength dependence, and concentration-related effects of melanin in biological materials [145, 147].

3.7 Diffraction from periodic structures

The diffraction of light from regularly spaced structures is another mechanism by which light is manipulated to form colour appearances. A structure that exhibits regular 1D or 2D periodicity in one plane is called a diffraction grating [155]. When light is reflected from or transmitted through a diffraction grating light is diffracted, and consequently dispersed, providing the grating periodicities are on the order of the wavelength of light.

For light diffracted by a 1D grating structure that is illuminated normal to the surface discrete diffracted orders are formed. The number of orders, n, and the angle,

θ_n, to which incident light, of wavelength λ, is scattered is given by:

$$n\lambda = d \sin \theta_n, \tag{3.51}$$

where d is the pitch of regularly spaced diffracting elements. This equation demonstrates that the interaction of incident white light with a grating periodicity on the order of the wavelength, scatters higher wavelengths to larger angles. This dispersion of light creates rainbow-like colour appearance. When light is incident at an angle θ_i from the normal, the full grating equation can be used to determine the direction in which light is scattered:

$$n\lambda = d(\sin \theta_n + \sin \theta_i). \tag{3.52}$$

The diffracting structures studied in a number of species, including Lepidoptera [51, 62], Coleoptera [156] and Flora [6], produce colour-appearance or enhance the pigmentary- or structural-colour present. These structures often enhance the visibility of the specimens for specific ecological functions. For instance, some *Morpho* butterflies likely use diffraction gratings to enhance their appearance for signalling to other *Morphos* [63]. On the other hand, these structures may also be used to signal between species. For example, the diffractive effects observed in some flowers are used to solicit pollinators for seed dispersal [6].

3.8 Summary

In this chapter, the theory that underpins some of the fundamental mechanisms by which colour is produced using structure in biological systems has been discussed. These are namely by photonic crystals, by thin and multilayer interference, and through diffraction.

The propagation of light through a 1D photonic crystal was discussed, before elucidating the reflectance behaviour for common 1D biological reflectors. The key aspects that govern the optical properties of multilayer reflectors were discussed in a biological context. It was seen that the number of layers, and the RI contrast between layers, strongly influences the intensity of light reflected.

Chapter 4

Overview of Classical Chemical Sensing

4.1 Introduction

The practical uses of chemical sensors are realised in a vast number of applications, such as in industrial processes, environmental studies, agriculture, clinical settings, and military technologies [157]. These applications stimulate growth in research into all aspects of high performance sensing, due to the nature of specific sensor requirements. Consequently there is a raft of different sensing approaches. Despite this, sensor devices often share many common desirable properties. A few examples (chosen from many) include, a large dynamic range, ergonomic design, long-term stability, multicomponent detection, fast response speed, and a reversibility of response [158].

Sensor science is an extremely active and broad multi-disciplinary field, requiring the attention of chemists, biologists, mathematicians, physicists and engineers. The biology and chemistry required to attract a specific molecule to a receptor can be extremely complex. Once bound, measuring a physical property of the sample in order to generate a useful analytic signal can be challenging. Beyond this, the data recorded by a sensor needs to be interpreted to provide some useful information about the composition or sample components measured. The creation of ambitious sensors requires all steps in this process to function together. Since the 1950s the pursuit of creating sensors for the detection of volatile vapours and trace-level molecules has produced huge advances in receptor and transducer engineering, and the necessary associated data processing techniques [159, 160].

In this chapter a brief background to the field of sensing is presented as an aid for later discussions, and to add context to the research presented in this thesis. To begin, the basic definition of a sensor is presented, before outlining basic sensor operation.

The attributes and characteristics of an ideal sensor are then described. Following this, a review of different optical- and electromagnetic- type sensors is presented, with discussion of the different optical phenomena used to obtain analytic information from a chemical sample. Sensor arrays are then discussed, before moving on to some current challenges that exist in the detection of volatile organic compounds. These challenges offer the motivation for the exploration of new designs with fast, selective, and sensitive responses to their surrounding chemical environment.

4.2 Definition of a chemical sensor

The field of sensing contains a vast range of sensing approaches, operational requirements and parameters to measure sensor performance. Consequently it is possible to dream up a new sensing requirement, and therefore a new sensor, for every desired scenario. Such a scenario may be for a sensor to be functional across a range of temperatures or pressures. For this reason the notion of a 'perfect' sensor is flawed and instead this idea is replaced with that of an 'ideal' sensor, that will behave with characteristics and attributes that are required for its effective operation.

Despite the impossibility of a 'perfect' chemical sensor, and the many applications for which a sensor might be used, an all-encompassing definition given by International Union of Pure and Applied Chemistry (IUPAC) for a chemical sensor simply states: *"A chemical sensor is a device that transforms chemical information, ranging from the concentration of a specific sample component to total composition analysis, into an analytically useful signal"* [161]. The more modern 'Cambridge definition' reflects the growing requirements, such as physical size, signal process time, environmental conditions and response reversibility, that these new devices are designed for: *"Chemical sensors are miniaturised devices that can deliver real-time and on-line information on the presence of specific compounds or ions in even complex samples"* [162]. A recent review of chemical-transduction through optical interactions states that optical chemical sensors *"employ optical transduction techniques and are based on reagents that change their optical properties on interaction with the analyte of interest"* [163].

Whilst other definitions of what a chemical sensor is, how it should operate and how it should perform exist [160], these definitions presented give a clear statement as to the function of such a device.

4.3 Design principles of a chemical sensor

The principle of a chemical sensor operation is to provide an analytic signal, through two components, namely a receptor and a transducer [164]. The receptor transforms

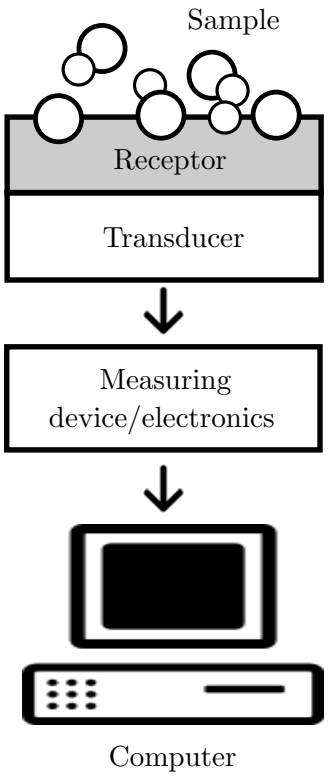

Figure 4.1: Schematic of basic sensor operation: molecules of the sample interact with the receptor film, which is in turn transduced. This signal is often transmitted or amplified by electronic devices before reaching a computer where the signal is processed to display the results. This figure is adapted from a schematic in Ref. [165].

the chemical information into a form of energy which is then measured by the transducer. The transducer then transforms this energy into an analytic signal that contains information about the sample. The operating principle of the transducer determines the classification to which the sensor belongs [161]. Modern chemical sensors often require additional computational processes to extract the analytical information from the transducer signal. This fundamental sensing model is depicted in Figure 4.1.

4.3.1 The sensor receptor

The receptor's function is to interact with, usually selectively, the molecules of the analyte being measured. This interaction can be through the means of physical absorption, ion exchange and liquid-liquid interactions [165], which occur at the interface between the receptor and the sample.

The most common receptors are made from material films, which are then coated on the physical transducer, or an array of transducers. Figure 4.2 shows a schematic

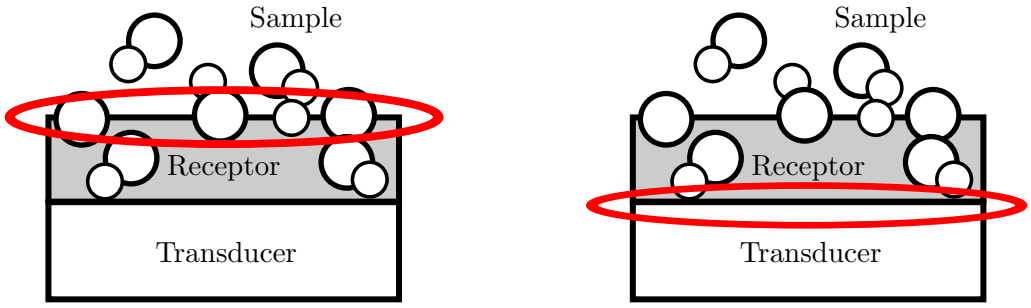

Sensor receptor selection
for chemical recognition

Transduction mechanism
for signal generation

Figure 4.2: Sensor schematic for a sensing film coated transducer, the two requirements for a selective sensor with acceptable sensitivity. The high-energy interaction between sample and receptor is required for binding of an analyte to the receptor film to provide acceptable selectivity, which then has to be transduced by appropriate means to obtain an analytic signal. This figure is adapted from images by R. A. Potyrailo.

of this process.

The development of receptor films is made challenging by a huge number of requirements. An example of two very important, but conflicting requirements, for a sensing film is for it to be selective to an analyte gas and also reversible. For a highly selective response the sensing film requires a high-energy (usually electrostatic) interaction with the analyte gas, however, to be reversible the interaction between analyte and film should be low-energy [166]. For these reasons, the surface chemistry, biology (in the case of biochemical sensors) and physical properties of receptor films can often be a limiting factor in the realisation of ambitious sensor designs.

Modern development of sensing materials relies upon combinatorial and high throughput screening to find suitable candidates for sensing materials [158]. Such screening has lead to the development of a number of inorganic and organic sensing materials. Metal oxides and polymer materials are common receptor films. Other materials are developed through a number of different approaches [157].

4.3.2 The sensor transducer

The transducer's function is to convert the chemical information, usually concentration, into some measurable form of energy, which is often an electrical signal. Many methods exist to produce a changing electrical signal, i.e. voltage, current or resistance, from the non-electrical quantity.

Common measurands are acoustic, biological, chemical, electrical, magnetic, optical and thermal, with each presenting a huge array of different measurable properties [167]. The most common transduction methods for microsensors, of these measurands, are piezoresistance, piezoelectric, capacitive, thermoelectric, optical and radiation-based techniques [168].

Piezoresistive transducers exploit the piezoresistive effect, demonstrated in many materials where the application of pressure or changes to material composition alter the electrical resistance producing an electric signal. Piezoelectric transducers operate in much the same way as piezoresistive ones, but in this case a change in electrical charge is generated upon a change in pressure across a material's surface [168].

A number of methods work with changes in electrical signals generated by the interaction of a measurand with thin or bulk film materials [168]. An example of a resistive technique different to that of piezoelectric transducers is a capacitive sensor, where the interaction with the dielectric film between two metal plates alters the capacitance. This interaction may be due to some external pressure between the two plates, or equally it could be the absorption of a vapour into the dielectric film, as used in some moisture sensors. More recently, the impedance of sensing films, altered by the adsorption of vapours, has been measured with radio frequency identification (RFID) sensors to yield a selective signal to parts-per-billion concentrations of volatile vapours [169]. Such wireless implementations have wide application in creating wireless sensor networks and where invasive sensors are not suitable [170–173].

Optical sensors usually measure wave phase, amplitude, polarisation, velocity or spectral features with photosensitive instruments. The interaction of specific chemicals with sensing films that are either in contact with light through evanescent fields, or in the path of optical wave propagation creates these differences in optical response [159]. These different transduction types are discussed in greater detail in Section 4.5.

4.3.3 Signal processing

Modern chemical sensors often require additional signal processing in order to extract analytical information. This arises from the increasingly complex designs that are used in the pursuit of selective and sensitive responses to target analytes. The designs used to achieve this often consist of arrays of sensors elements with different target specific receptor films. These are commonly called sensor arrays and are discussed in more detail in Section 4.6. The data these devices generate often have broad overlapping sensitivity profiles, resulting in the need for considerable analysis of multi-dimensional data.

To overcome these challenges, many well-established techniques have been devel-

oped. These computation methods often involve data reduction and pattern recognition techniques. A comprehensive review of analysis methods for chemical sensor arrays can be found in Ref. [174].

The analysis of optical data, in this thesis, obtained both through theoretical calculations and experimental measurements, has almost exclusively been analysed using Principal Components Analysis (PCA). A discussion of this method is made in Chapter 5.

4.4 Characteristics and attributes of an ideal sensor

Sensor performance can be described by many attributes, both static and dynamic. Of these the dynamic range, detection limit, sensitivity, response time, resolution, accuracy, precision, hysteresis and drift, and selectivity are commonly used [165, 175]. Some of these terms become useful in discussions later in this thesis, and so are briefly described here:

Dynamic range

The dynamic range defines the range of analyte concentrations for which the sensor will provide an accurate signal.

Limit of detection

The limit of detection is the smallest concentration that is detected by a sensor at a signal-to-noise ratio of three [165].

Resolution

The resolution defines the smallest measurable change in analyte concentration [165].

Response time

The response time is the time taken to detect a measurable change in concentration [165].

Selectivity

The term selectivity describes a sensor's ability to respond either selectivity to a group of analytes or to a specific analyte [165].

Sensitivity

In general the sensitivity is used to describe the signal change per unit concentration of analyte. In practice the sensor's sensitivity is dependant on sensitivity of the individual components [175]. For instance, the sensitivity maybe the convolution of the transducer, signal processor and supporting electronics.

4.5 Optical sensors

Optical sensors are a class of electromagnetic sensors operating over the optical frequencies from ultraviolet to infrared. Optical sensors transduce signal by measuring changes in the amplitude, phase, polarisation, and in spectral features, when the analyte is present. Temporal measurements, such as differences in time-of-flight or in lifetimes of the fluorescent or luminescent decay of chemical species, may also be used.

In some schemes wavelength-dependant signals are recorded from the reflection, transmission or absorption of electromagnetic radiation, and measure some physical property of the measured analyte. Certain chemical species also exhibit chemiluminescence or fluorescence, which can also be measured.

Perhaps the earliest reported instance of a chemical test using a change in optical appearance is reported in Roman times. Pliny the Elder (23-79 AD), the author and natural philosopher who had an interest in metallurgy, developed a papyrus test to detect counterfeit Greek coins [176]. To test for ferric ions present in potentially forged copper coins, a papyrus soaked in fruit extracts was used as a test strip after the coins had been dissolved in acid [177]. Information about chemical compounds, chemical properties or physical characteristics transduced through some change of colour in this way is indicative of an indicator or label method. Applications of such methods continued in the 17th century to detect the concentrations of ferric ions [177]. Development and understanding of materials undergoing chemical responses continued in the 19th century [178]. Detection of uric acid and pH-concentration with test strips became more widely used, whilst systematic research into these detection observations were made later in the century by Goppelsroeder, an early contributor to the field of paper chromatography [178]. Numerous tests for the identification of gases and organic compounds [179] ensued, although it was much later that the term 'optical' became associated with these methods [177]. Of the tests using this method the most known and commercially successful is the pregnancy test [180].

The field of optical sensing is now far more than just the detection through indicators. Since the late 1980s the research and development into optical sensors has undergone considerable expansion. Figure 4.3 shows the growth of optical sensors in

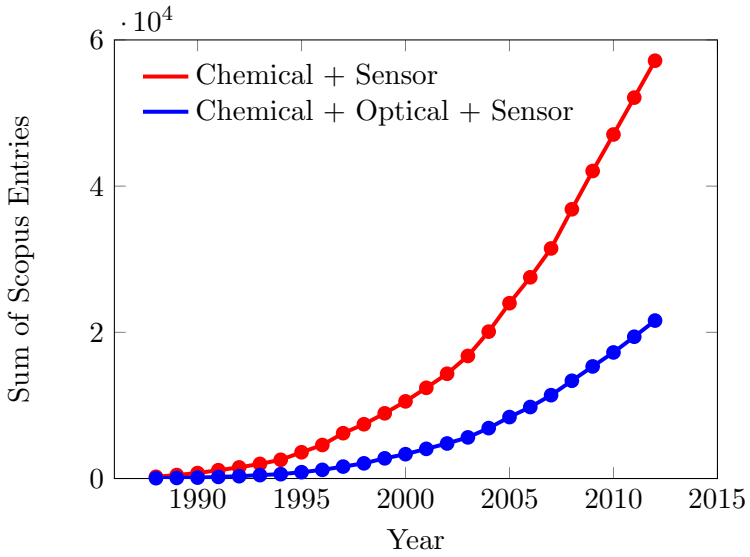

Figure 4.3: Cumulative sum of entries for the search terms 'Chemical + Sensor' and 'Optical + Chemical + Sensor' in the Scopus library since 1988.

the literature from 1988 to 2012. In 2012, the term *Optical Chemical Sensor* accounted for $\sim 44\%$ of Scopus [181] entries within the search term *Chemical Sensor*. There are many reasons for such active growth in this area of optical sensing. Ref. [177] offers several factors for this growth, summarised as follows: Recent improvements have been made to the quality of light sources, such as LEDs and diode lasers; sources have been developed at increasingly lower cost, greater stability, smaller size and lower energy consumption. Technological advances in the sensitivity and quality of measurement devices, such as photodiodes and charge-coupled devices, have also undergone enhancements for detection of visible and near-IR wavelengths. Waveguide optics, fibres and components to integrate into other devices, are now available for infrared wavelengths. Great advances in the development of sensing films, which are commonly used as the receptor layers in optical sensors, have rapidly improved. Polymer chemists have developed more biocompatible materials and organic polymers, as discussed in Section 4.3.1. Interdisciplinary research has shown a steady increase facilitated by teaching and conferences for all aspects of optical sensor technology. Finally, many new methodologies have been developed.

Optical sensors may be further classified by the physical phenomena they employ (and also the application for which they were designed) to transduce a signal. Some of the most common examples are described in the following sections.

4.5.1 Waveguide sensors

Waveguide sensors are a class of optical sensors that not only have diverse applications, but are also diverse in the use of analytical chemistry, waveguide optics and the parameters of light measured.

Optical sensors, such as waveguide sensors, are able to perform 'direct' analyte recognition, where inherent optical features of an analyte are detected, but also 'indirect' analyte recognition, where additional reagents or receptor films coupled to the optode (the optical transduction element) allow the light to interact with the analyte. The physical measurands in direct recognition are fluorescence-based, absorption-based, or refractive index-based [182]. Indirect interactions often cause the reagent/receptor film to undergo some change of optical property, like those mentioned previously, for measurable changes in optical signal [183].

A further way to classify these devices may be by the role of the sensor in the transduction of a chemical signal, resulting in two broad categories, namely whether a sensor is 'extrinsic' or 'intrinsic'. These names are related to the configuration of the sensing optics. Figure 4.4 displays a selection of different schematics for extrinsic and intrinsic type waveguide sensors that operate through amplitude and wavelength modulation.

The waveguide component's main function in an extrinsic sensor is to connect the sensor instrument to the sample area, or sensing device [183]. The advantage of such a design is the versatility in practical use. For example, the flexibility, size and miniaturisation, chemical stability and the limited electromagnetic interaction with external fields has made the fibre optic waveguides widely used in health care applications [183, 184]. In contrast to the extrinsic waveguide sensor, an intrinsic waveguide sensor plays a role in the detection of the analyte by some transduction of the signal [183].

The physical phenomenon underpinning the detection of analyte molecules is their interaction with the probing electromagnetic field. In waveguide optics, the propagation of light, and its allowed electromagnetic field distributions, have been widely studied. It is known that light confined within a waveguide core has electric field present in the core, but also an exponentially decaying tail to the electromagnetic field that extends beyond the bounding interfaces of the waveguide. The presence of a 'sensing' field in these regions allows for the detection of analyte molecules both in the waveguide core region and the waveguide cladding. The intensity of the electromagnetic field inside the core is far greater than that outside the core.

Detection of vapours using the electromagnetic field within the core requires a mechanism for vapour diffusion into the core material. This can be achieved using a porous matrix as the guiding material; however, this approach can be unfavourable due to large

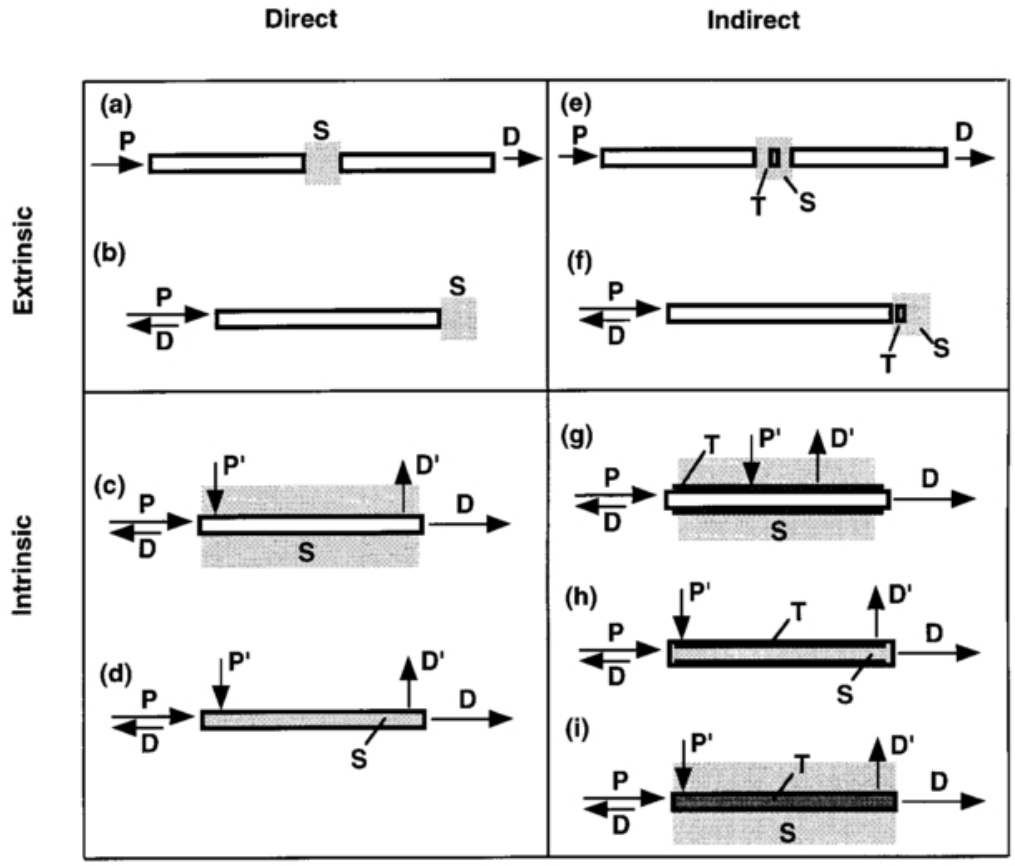

Figure 4.4: Sensor schematics for extrinsic and intrinsic type waveguide sensors, that operate through amplitude- and wavelength-modulation. Configurations: (a), (e) transmission; (b), (f) single-ended; (c), (g) evanescent-wave; (d), (h) hollow waveguide; (i) sensing waveguide. S = sample (shaded area), T = transducer, P = probe radiation, D = detected radiation, P and D correspond to side-excited and side-detected radiation, respectively. This figure is reprinted with permission of R. A. Potyrailo from Ref. [183].

absorption/deabsorption times and reversibility requirements. Therefore, sensing with the evanescent field is more common despite the relative difference in electromagnetic field intensity. This is usually performed through the interaction between the analyte material absorbed to receptor material on the waveguide cladding and the evanescent fields extending beyond the boundary of the waveguide core.

4.5.2 Interferometers

Sensing using interferometry techniques, incorporating waveguide optics, is common for refractive index based sensing of a chemical species, and is conducted with the same principles as waveguide sensors [182].

An interferometer with a configuration such as the Mach-Zehnder structure splits an incident beam of electromagnetic radiation into two beams of equal intensity [185]. Each beam travels through individual waveguide branches. A chemo-optical signal can then be obtained by measuring the phase difference that occurs between the two interfering beams that arises due to a change in dielectric constant of the sensing branch's waveguide [185].

This is just one example of many interferometer configurations that exists for the detection of chemical species [186]. Chemical signals can not only be obtained through measurements of the phase difference, but can be derived through changes in wave amplitude, or measureable changes in different linear polarisations, just as in the case of waveguide sensors.

4.5.3 Surface plasmon resonance sensors

Biological and chemical sensing through the phenomenon of surface plasmon resonance (SPR) is extremely common, and began in the early 1980s [187, 188]. The physics of surface plasmon resonance has been extensively studied across different wavelength regimes at the Thin Film Photonics group at Exeter, and other groups worldwide [189, 190]. The resonance phenomenon in sensing applications is usually utilised at optical frequencies and occurs between a dielectric/metal boundary.

In a typical SPR sensor, see Figure 4.5, the flat surface of a half circular prism is coated with a thin metal film functionalised with a receptor molecule, also known as the ligand. Light incident through the prism undergoes total internal reflection (TIR) at the flat boundary for incident angles equal to, or greater than, the critical angle as dictated by the permittivity of the bounding media. Upon TIR at the interface an evanescently decaying electric field is present in the metal film. This can cause the oscillation of free electrons at the metal's surface, creating surface plasmon resonance [189].

The absorption of incident light, and the angle at which SPR in the metallic film occurs, is strongly influenced by the change of refractive index of the thin metallic layer. Therefore SPR techniques are extremely sensitive to changing concentration and refractive index of absorbed molecules. Analytic signals maybe obtained through measurements of intensity, angle, wavelength or phase [191].

As a field, SPR sensing has undergone huge growth in techniques to measure properties of biological and chemical analytes in gases and liquids. Commercially, SPR sensors represent the most invested-in optical sensor technologies, yielding numerous different methods to obtain direct real-time analyte information at high throughput [192].

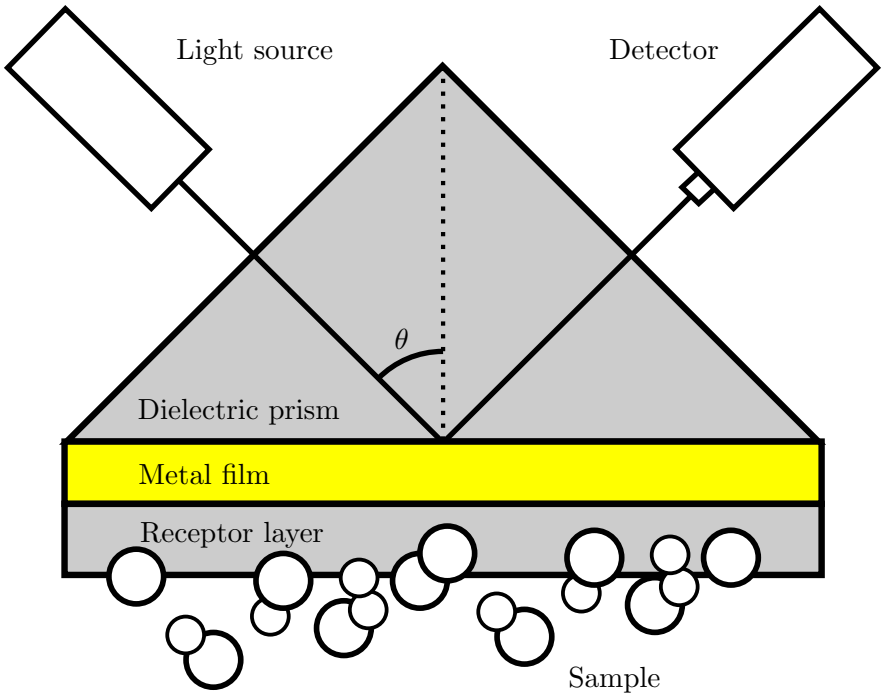

Figure 4.5: A schematic representation of a Surface Plasmon Resonance sensor in the Kretschmann configuration. In this configuration a metal film, that has been functionalised to act as a receptor, is in contact with the dielectric prism. Incident radiation evanescently decays through the metal layer and surface plasmons are excited on the metal/receptor boundary.

More recently there has been an emergence in sensing methodologies using localised SPR (LSPR) [193]. LSPR is a plasmon resonance that is excited on metallic structures such as nanoparticles, nanoholes, or nanowells [193]. The spectral features associated with the local electric field enhancement of these metallic geometries are strongly influenced by the local dielectric environment, as well as their size, shape and composition [194]. LSPR, like traditional prism- or grating-coupled SPR sensing, is highly sensitive to changes in the refractive index, or dielectric constant, of an adsorbed analyte. LSP resonances can be tuned to occur near molecular electronic resonances to yield dramatically different wavelength shifts compared to those that would be obtained solely by a refractive index induced shift [195].

Fine control of such plasmonic resonances promises an exciting future for this type of sensing approach. Furthermore, the progress in optical metamaterials and nanocrystal structures may add further capabilities for high performance multianalyte sensing with LSPR resonances [196].

4.5.4 Photonic crystals

Sensing biological and chemical molecules absorbed in photonic structures is becoming an increasingly active area of research driven by the new capabilities in the controlled fabrication, and understanding, of the self assembly of complex dielectric architectures. As previously described, the interaction of the analyte's intrinsic dielectric properties with the probing radiation is required to provide sensitivity to absorbed molecules. Studies into the properties of photonic crystals have revealed opportunities within dielectric structures to tailor the propagation of light in order to enhance the electric field in particular spatial regions, and to slow or prevent the transmission of light [134].

To date, the investigation into sensing with photonic structures at the optical regime has been largely focussed to the investigations involving colloidal crystals [197, 198], dielectric nanoparticles [199], inverse opals [128, 200], porous silicon films [201–203] or other photonic crystal topologies [204]. Analytical signals from the reflection or transmission of light from these structures is obtained either through multivariate analysis or through the assumption that the refractive index of the analyte is proportional to the shift of a particular wavelength, often the wavelength of peak reflectance.

The vapour response of structurally coloured colloidal structures (see Figure 4.6) have been investigated at low [197] and high [198, 205] vapour concentrations. At high concentrations the absorption of vapour produces larger spectral shifts in the optical response than that of low concentration interactions. These shifts at high-concentration show a linear relationship with vapour partial pressure, and when combined with the change in reflectance amplitude, provide a sensitive response to different refractive

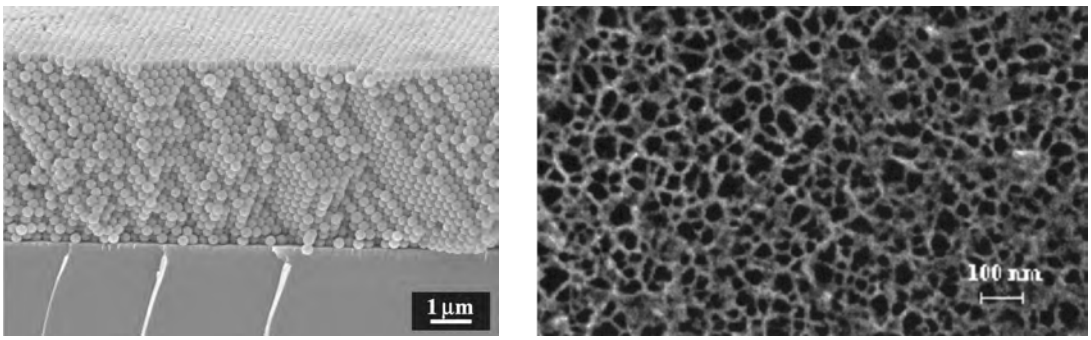

(a) (b)

Figure 4.6: Examples of two 3D photonic structures used for optical sensing: (a) displays a typical SEM image of a cross-section of an inverse opal structure (Image reprinted with permission of author, from Ref. [205]), and (b) shows an SEM image of a porous silicon matrix (Image reprinted with permission of author, from Ref. [206]).

indices [205]. Similar optical responses are observed due to the swelling of colloidal elements in the presence of water and ethanol vapour [198]. At low-concentrations these films have been shown selectively to sense multiple low-concentration analytes [197]. Unlike at high-concentration the colour-shift approach does not reveal information about the chemical species; instead measurement of the differential reflectance is combined with multivariate analysis to give good vapour discrimination in a single sensing film [197].

The inverse opal is the inverse structure to that of close packed colloid spheres. Just as in the case of colloid films, infiltration of the structure by organic liquids can cause drastic changes in the perceived colour appearance due to the changes in coherent scattering conditions [200, 207]. Recent engineering of the structural and chemical tunability of the wettability of inverse opal structures to a number of alcohols, and alkanes, has shown such films to be an attractive method of creating a simple and inexpensive way to create colorimetric indicator films [200, 208]. Such films also have potential uses in colorimetric humidity indication [209].

Photonic crystals with 1D periodicity, namely thin films [214, 226] and multilayer stacks [201], have been studied as structures for the sensing of volatile organic compounds in their vapour phase. 1D multilayer reflectors comprising porous layers have been common choices for such studies. Using a porous matrix (see Figure 4.6), such as porous silicon, vapour is able to absorb into the bulk of the matrix, which influences the effective refractive index of the film as described by the Bruggeman effective medium approximation [201]. The refractive index change upon the introduction of vapour to the porous layers influences the position of the peak reflected wavelength [201]. Time-

Table 4.1: Summary of the mechanism and attributes of photonic crystal sensors that utilise a colorimetric readout.

Sensing approach	Species detected	Mechanism	Sensitivity	Selective	References
LSPR in metallic nanoparticles	Organic vapours	SPR enhanced electric fields used to sense changes in local permittivity, measured by a change in resonant peak position	1-20 ppb	No	[193, 195, 210–212]
Colloidal crystal films	Organic vapours	Infiltration of vapours into the crystal film causes a wavelength shift in the Bragg reflected wavelength peak	$\sim 10^{-3}$ nm/ppm	Limited	[197, 198, 205, 213]
Porous silicon films	Organic vapours	Absorption of vapours into the porous matrix causes changes to the effective permittivity of the film, transduced by interferometry	500 ppb	No	[201, 203, 214]
Bragg reflector gratings	Organic vapours	Vapour adsorption and absorption within the photonic crystal modify the coherent scattering conditions, which cause changes in reflectance	$\sim$ 450 nm/RIU	No	[215–219]
Hierarchical biological photonic structures	Organic vapours (RI)	- Modification of coherent scattering conditions by vapour adsorptions, which are measured through spectral changes in reflectance	1 - 2 ppm	Yes	[8, 13, 220–223]
	(pH)	- Addition of responsive pH sensitive polymer network into the photonic structure alters scattering conditions by swelling	pH 7.95 - 9.99	N/A	[223, 224]
	(Humidity)	- Absorption of water vapour causing geometry modification by swelling causes a modification to the scattering conditions	High conc.	N/A	[128, 209, 225]

resolved reflectance measurements of vapour diffusion can provide information about the distribution of spatial concentration through the capillary dynamics of absorbed vapours within the porous matrix [202]. The degree of control in the synthesis (e.g. layer thickness, material composition and porosity) of structures, such as Bragg reflectors, makes the tunability of the sensing response possible [227]. Bragg reflectors comprising layers of porous silicon with alternating porosity have been used to identify organic vapours through measurements of diffusion within the crystal [228].

A summary of the mechanisms and attributes of photonic crystal sensors that utilise a colorimetric readout is presented in Table 4.1. Photonic crystals have also been studied as a basis for sensing a number of other measurands, including temperature, pressure, humidity and ionic species. A comprehensive overview of these fields can be found in Ref. [229] and Ref. [223].

At present the real applicability of these sensor designs and their scalability for practical applications is an important subject. For real-life sensor applications the ability to produce (and reproduce) large-scale nanostructured materials or optical cavities under the constraints of reasonable cost, fabrication quality, size and speed is essential. The progress in fabrication processes, driven by a range of multidisciplinary applications, has resulted in improvements to the all aspects of production [230–233]. This means that scalability of nanofabrication materials and structures at large scale is becoming less of an obstacle in realising photonic sensing devices, and this will continue to improve.

4.5.5 Other photonic sensors

Modern development in photonic sensors, for both the chemical and biological domain, has seen huge diversification of sensor designs, with the incorporation of sensing films into photonic structures for optical or electromagnetic transduction [234].

Resonant sensors, such as microcavities, ring resonators or microresonators, attract attention due to their sensitivity to refractive index, related to the resonant quality factors [235]. Numerical investigations into ring resonators show that interactions of model vapour analytes with the sensor geometry create spectral shifts of resonant modes related to thicknesses of polymer sensor films and refractive index [236]. The incorporation of chromophore-doped polymer films into ring resonators, and Bragg grating structures has been shown to enhance detector sensitivity of such sensors [237]. Resonant detection principles have also been demonstrated with whispering gallery modes for liquids [238] and vapours [239, 240].

A large number of practical situations have been identified where sensing without wires is advantageous [172]. Electromagnetic radiation is apposite for such situations

where sensor components sit independently of each other. In the chemical domain conventional radio frequency identification (RFID) tags, coated with a polymer sensor film, have been used for wireless detection of specific target vapour analytes at low concentration [169]. Multianalyte information is detected by measurement of the RFID's complex impedance coupled with multivariate statistical analysis upon vapour exposures [169]. The transmitted signal containing complex impedance, and the identification of the tag, can be detected wirelessly [169].

4.6 Sensor arrays

As described in Section 4.4, there are a large number of requirements and performance criteria by which a modern chemical sensor may be judged. For this reason it is often the case that a 'single' sensor is insufficient for practical use, for instance, it may not have a large enough dynamic range. In the early 1980s it became accepted practice to combine sensors into arrays to overcome the conflicting requirements of fast response time and high selectivity [241].

Combining sensors into arrays to allow the measurement of many sensor elements allows for 'fingerprint'-type recognition of chemical species [242]. There are advantages associated with the array approach: first, the parallel operation of several sensors increase the reliability of measurements, for instance if an element fails [165]. Secondly, arrays allow for the measurement, and data processing of additional variables simultaneously [165], the effect of which can enhance the quantification and identification of measurands. Figure 4.7 illustrates the vapour 'fingerprint' through the visualisation of colour changes upon the vapour exposure of colour-sensitive films [243].

In the pursuit of highly sensitive and selective sensors arrays, sometimes termed electronic noses or tongues, arrays have evolved to complex larger platforms, with arrays being reported with up to 2^{16} individual elements [244]. With such arrays, factors such as size, power consumption, electronics and data analysis become inhibitive for certain applications. Despite these developments, a number of key challenges are still present, namely the identification and quantification of target analytes in complex mixtures, high and closely related interferences [166].

4.7 Summary

In this chapter, a brief overview of sensor concepts and approaches for chemical vapour detection has been described as a foundation for later discussions made in this thesis. Chemical sensors, often miniaturised devices, determine information about the components or composition of a chemical environment. This is achieved with a receptor and

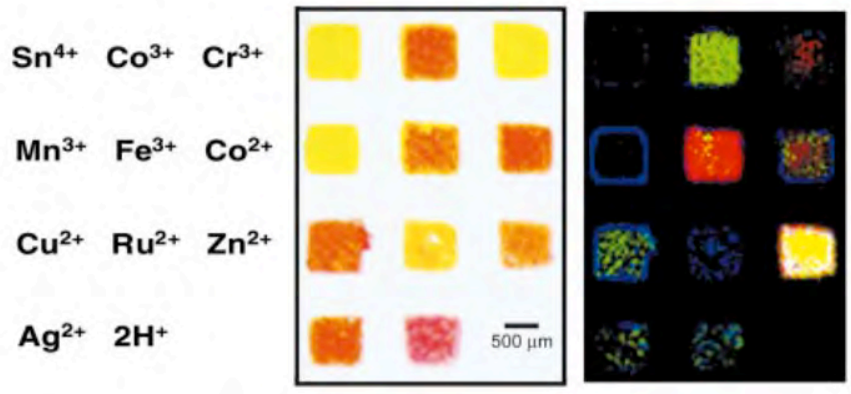

Figure 4.7: A colorimetric array illustrating the fingerprint principle for a sensor array. (Left) illustrates the location of metalloporphyrin materials. (Right) displays the colour change profile after exposure to *n*-butylamine vapour. This figure is reprinted from Ref. [243].

a transducer element, and often involves data processing.

A number of different transduction approaches have been highlighted, with dicussion focused on optical and other electromagnetic techniques. These involve the measurement of wavelength, intensity, polarisation or phase, which is modulated by an intrinsic property of the analyte. Refractive index is the intrinsic property measured by many optical sensors. Individual sensors are often implemented into sensor arrays as a method to enhance sensor performance. The benefits and limitations of this approach were discussed.

Research into sensor technology is a rapidly expanding interdisciplinary field. Despite the huge advances in sensor technology, a number of key challenges still exist for biological and chemical detection [10]. At present the selective, sensitive, and fast detection of analytes at ultra-low concentration (ppb - ppt) levels presents a significant challenge for existing sensors and sensor arrays, and fail to reach the demands required by current defence and military applications [10, 245]. For these reasons, new sensing approaches, where real-time, selective and sensitive vapour responses are obtained without cumbersome electronics and large sensor array platforms, are highly sought after.

Chapter 5

Theoretical, Experimental and Data Analysis Techniques

There are many different approaches routinely used to measure and calculate the optical properties of naturally occurring photonic structures [115], such as those present in the scales of *Morpho* butterflies. Often experimental quantification of the optical properties is made using spectrometry, before the structures responsible are investigated using microscopy techniques. Furthermore, theoretical approaches can be used to provide deeper insight into the physical mechanisms that create the visual appearances.

The optical properties, and associated structure, of *Morpho* butterflies are well documented, with many studies reporting on the subtle differences between *Morphos'* in the same genus [98, 101] (as discussed in Chapter 2). In this thesis investigations comprise both the use of experimental measurements and theoretical calculations to explore related synthetic vapour adsorption effects upon the structures present in *Morpho* butterflies, and their bio-inspired structures. In the course of these studies, measured and calculated results have often been analysed with multivariate data analysis to reveal any complex trends with the data.

In this chapter, the experimental techniques and theoretical tools used in this work are described. First, the experimental methods used to perform vapour measurements are discussed; namely, these are the methods of vapour generation and the optical equipment used to measure the resulting spectral changes. Following this, the theoretical electromagnetic simulation tools, both the Finite Element Method (FEM) and the Finite-Difference Time-Domain method (FDTD), employed to explain these observations, are detailed. Finally, an explanation of the data analysis technique, Principal Components Analysis (PCA), used to extract information from the measured and calculated spectral data, is presented.

5.1 Experimental methods

5.1.1 Introduction

To perform the vapour exposure measurements, and subsequent multivariate analysis, present in this thesis, the change in reflectance is measured upon the exposure of *Morpho* scales or other artificial structures, to chemical vapours.

The experimental data presented was measured at General Electric Global Research Center (Niskayuna, NY, USA) during research visits in the course of this Ph.D project. The optical measurement technique and vapour generation method are now described in Section 5.1.2 and 5.1.3 before illustrating this measurement type with an example vapour exposure upon the scales of *M. rhetenor* in Section 5.1.4.

5.1.2 Optical measurements

In the vapour exposure measurements presented in this thesis, a number of different experimental measurement conditions are used to illuminate a sample, and then measure the reflected light. Whilst the specific measurement conditions are described in the relevant sections, here, the general measurement process is outlined.

To illuminate the sample, a bifurcated probe, also called a fibre bundle, is used. The bifurcated probe allows the illumination of a sample through a core fibre, and has surrounding fibres to collect the light scattered back to a small solid angle around this illumination fibre. Figure 5.1 displays a schematic of a bifurcated probe that can be used for illumination and detection. In general, this probe-based approach is not widely implemented in optical measurements because it makes quantitative comparison to physical models more challenging. However, here it is chosen in some scenarios because both the illumination and detection can be achieved with a single fibre bundle, which has obvious advantages in sensor implementations.

The probe bundle was mounted in an adjustable clamp to provide the adjustment of the illumination angle and relative distance to the sample. Samples were illuminated with light from a stabilised Ocean Optics HL-2000-FHSA halogen light source, and scattered light was measured with an Ocean Optics QE65000 spectrometer.

As discussed in Section 4.5.4, existing photonic nanostructured sensors exhibit a significant colour change only at relatively high concentrations of detected vapours. For these low-concentration vapour exposures, where the spectral shifts are relatively small, the differential reflectance spectral response, $\Delta R(\lambda)$, of the sample is measured. Here the differential reflectance is defined as

$$\Delta R(\lambda) = 100\% \times \frac{R(\lambda)}{R_0(\lambda)}, \tag{5.1}$$

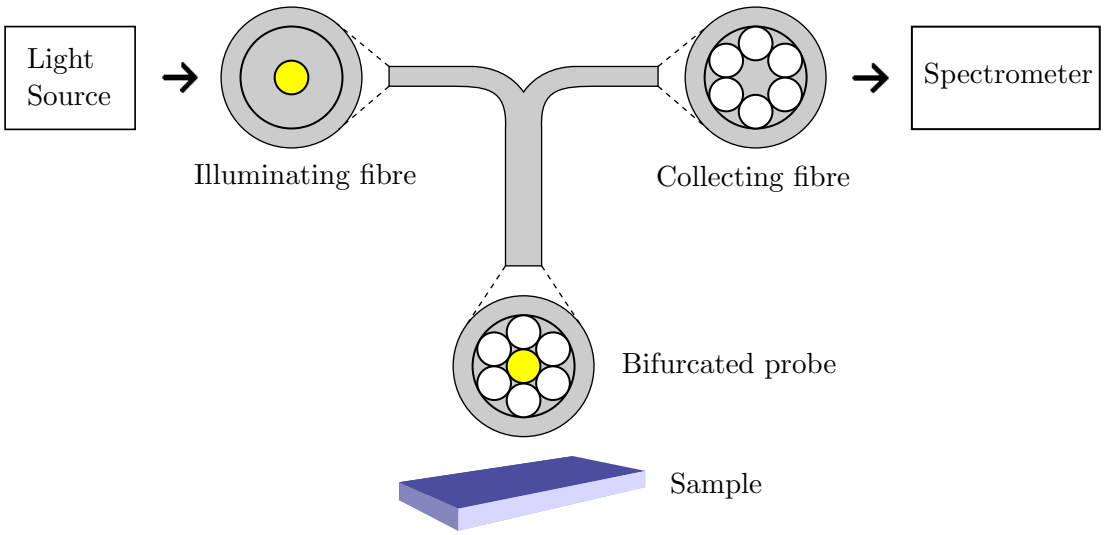

Figure 5.1: Schematic diagram of bifurcated probe apparatus. The central fibre illuminates the sample. The surrounding fibres collect light scattered over a small solid angle back towards the illuminating fibre. This solid angle is defined by the distance of the fibres from the sample.

where $R(\lambda)$ and $R_0(\lambda)$ are the spectra measured from the sample upon exposure to an analyte and a carrier gas, respectively. Thus, the common features in the two spectra before and during vapour exposure cancel, and the $\Delta R(\lambda)$ spectrum accentuates the subtle differences due to presence of vapour. Following the normalisation to the differential reflectance measurement, the value of differential reflectance is 100% at all wavelengths before vapour exposure. Measurements are then recorded over a user defined time period, using a LabVIEW-driven user interface.

5.1.3 Vapour generation

To perform low-concentration vapour exposure experiments, a reliable vapour generation technique is required in order to provide a continuous flow of a known constant vapour concentration. A number of techniques exist for the delivery of vapours; these are often used in chemical vapour deposition processes, where vapour is generated from solid, liquid, or gaseous samples [246]. For vapour delivery in the experiments presented in this thesis, the vapour is generated from the liquid-phase using a bubbler system built in-house by R. A. Potyrailo at General Electric Global Research Center (Niskayuna, NY, USA).

The bubbler works by flowing a carrier gas through a vessel containing the analyte liquid. A simple schematic of a bubbler is shown in Figure 5.2(a). An inert carrier gas, in this case nitrogen (N_2), is flowed into the vessel and is bubbled through the volatile

liquid. The gas flow that leaves the headspace of the container is a mixture of the carrier gas and analyte vapour. If the flow gas is delivered at a constant flow, and the temperature of the system is known and assumed to be constant, the concentration of the vapour generated can be calculated through consideration of the partial pressures of carrier gas and vapour in the headspace.

First consider a closed container of liquid. In equilibrium the number of molecules evaporating from the liquid is equal to the number condensing back to the liquid, this occurs at the saturated vapour pressure P_0. When a flow of carrier gas is introduced through the bubbler, the headspace in the container is a mixture of vapour and carrier gas. The mole fraction of vapour molecules in the headspace, x_{vapour}, is given by the ratio of vapour pressure P_0 to the total pressure in the headspace, P_{total}, simply stated as:

$$x_{\text{vapour}} = \frac{P_0}{P_{\text{total}}}. \tag{5.2}$$

By assuming the composition of the vapour flow from the headspace is the same as the vapour/gas mixture in the headspace, the flow of vapour out of the headspace, f_{vapour}, can be expressed in terms of the carrier flow into the bubbler unit, f_{carrier}, as [247]:

$$f_{\text{vapour}} = f_{\text{carrier}} \frac{P_0}{P_{\text{total}}}. \tag{5.3}$$

In practice this flow rate needs to be modified by an efficiency factor, ϵ, to account for the bubbler's efficiency in converting liquid to the vapour phase.

In this apparatus the total flow of carrier gas, F_{carrier}, is kept constant. To control the quantity of vapour in the output flow, the flow of carrier gas to the bubbler, f_{carrier}, is varied. Therefore, the concentration (conc.) of vapour in the output gas/vapour flow can be expressed in terms of the total vapour flow, F_{vapour}, and the carrier gas flow to the bubbler, f_{carrier}:

$$\text{conc.} = \frac{f_{\text{vapour}}}{F_{\text{carrier}}} = \epsilon \left(\frac{P_0}{P_{\text{total}}} \right) \frac{f_{\text{carrier}}}{F_{\text{carrier}}}. \tag{5.4}$$

This description provides a simple explanation of the process involved for vapour generation. Calibration of the experimental apparatus takes further account of the assumptions made. Table A.1 in Appendix A contains examples of the vapour concentrations generated for different flow rates of common volatile organic compounds presented in this thesis.

The bubbler system is controlled by a LabVIEW interface and allows for the control of flow concentrations, and generation of primary, binary and higher order vapour

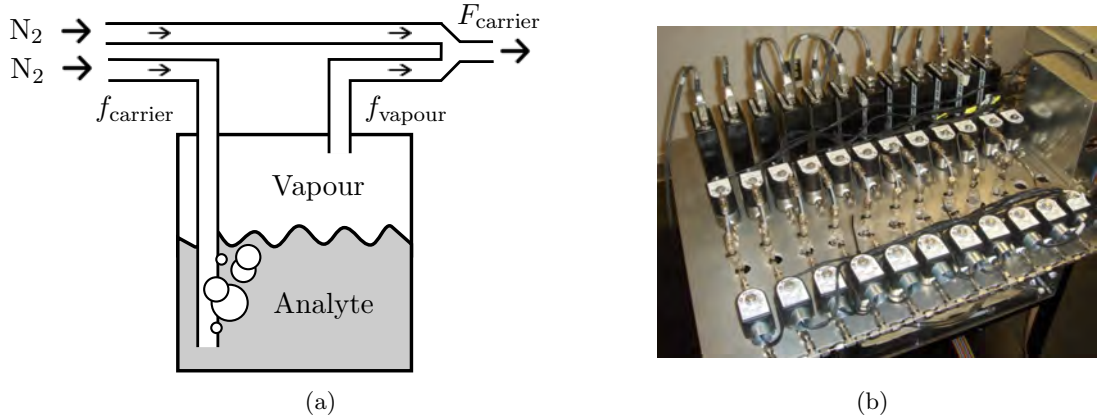

Figure 5.2: (a) A schematic diagram of the bubbler vapour generator: N_2 is flowed into the vessel containing the analyte sample, the flow leaving the headspace of the vessel is then a carrier gas/vapour mixture which is then delivered by flexible tubing to the sample, and (b) photograph of the 10 channel vapour generator at General Electric Global Research Center (Niskayuna, NY, USA). (Photograph courtesy of R. A. Potyrailo).

mixtures. The flow is delivered through flexible tubing mounted in an adjustable clamp to allow positioning of vapour flow with respect to the sample. A photograph of this bubbler system is shown in Figure 5.2(b).

5.1.4 Example measurement

To illustrate this differential reflectance measurement process, a methanol-exposure experiment performed on the scales of *M. rhetenor* is shown in Figure 5.3. Two different concentrations of methanol are generated and flowed onto the iridescent scales with a rest period of pure carrier gas to observe the recovery of the scales after each exposure.

To begin, normalisation of the measurement is performed. Figure 5.3(a) displays the raw reflectance measured before normalisation to the differential reflectance measurement. Visualisation of the raw spectra is important to ensure that any adjustments to the integration time can be made to prevent spectral changes during the vapour exposure saturating the spectrometer. Once the normalisation to record the differential reflectance has been performed, the value of differential reflectance at all wavelengths is 100%.

Figure 5.3(b) displays the temporal changes of differential reflectance across visible wavelengths. Upon vapour exposure, an abrupt change in reflectance occurs indicating a rapid change in reflectance, as visualised by the change of colour in the differential reflectance map.

Whilst the presentation in Figure 5.3(b) has utility for visualising such a large

quantity of data, it becomes useful to look at the temporal profile for fixed wavelengths, or the differential reflectance at fixed times; examples of these are shown in Figure 5.3(c) and 5.3(d), respectively.

In this thesis, analysis of the differential reflectance during the vapour exposure is commonly performed to make observations about the diversity of spectral response. Any diversity in response may result in a selectivity between the spectral measurements. In addition, specific wavelengths are chosen to illustrate interesting features in the temporal response.

5.2 Photonic simulation techniques

5.2.1 Introduction

Photonic simulation tools allow for the quantification of the electromagnetic response arising from the interaction of incident probing radiation with material and structure. The most commonly calculated properties are the reflectance and transmittance of a sample, but the versatility of many approaches allows further information to be obtained, such as the electric field distribution when these interactions occur. To calculate a given sample's optical response, information about the structural dimensions and material properties are input, and then the problem can be solved with an appropriate analytical or numerical modelling technique. Whilst many different approaches exist, in this thesis discussion is limited to the Transfer Matrix Method (TMM), the FEM and FDTD techniques. The suitability of a method is often determined by the complexity of structure and the output parameters required. Each of these techniques is described in the following sections.

5.2.2 Transfer Matrix Method (TMM)

To compute the reflectance and transmittance properties of one-dimensional reflectors, analytic techniques, such as the transfer matrix method, are suitable. The TMM is one of a number of well-established methods for the analysis of wave propagation through stratified media [248]. Since this technique is extensively documented elsewhere [129, 141, 248], the method is only briefly outlined here.

For the analysis of reflectance and transmittance from multiple one-dimensional dielectric reflecting layers, the thickness and refractive index (or permittivity) of each layer is required. These parameters are used to form a matrix that describes the optical properties of each layer. As Maxwell's equations require the conservation of the electric displacement vector across each layer boundary, a treatment of the amplitudes of forward and backward propagating waves within the structure can be made. By taking

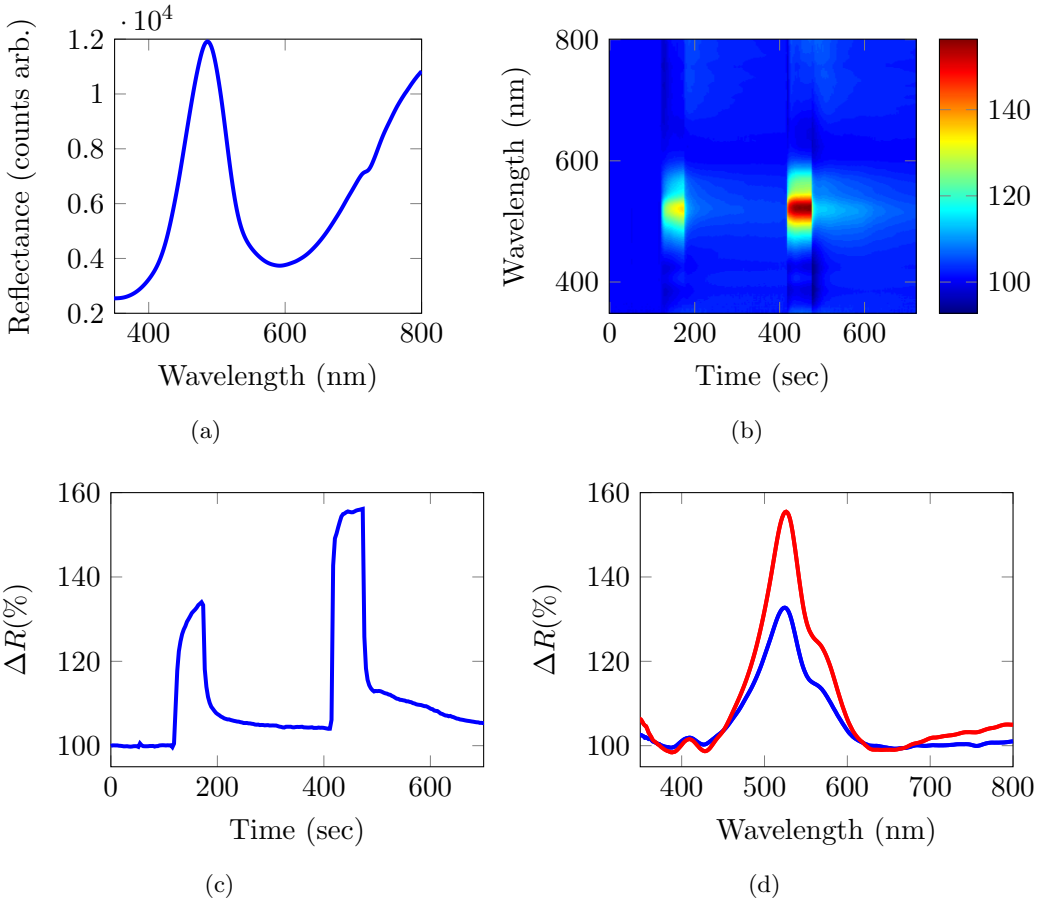

Figure 5.3: Typical spectral reflectance data from the wings of *M. rhetenor* for two methanol vapour exposures: (a) Displays the raw reflectance spectrum, (b) shows the ΔR reflectance map during vapour cycles, (c) displays the temporal profile for a fixed wavelength of 525 nm, and (d) the ΔR spectrum at the peak reflectance, for the first and then second exposure, respectively. This measurement was performed with the bifurcated probe arranged at 30 degrees from normal, out of the nanostructure ridge-plane.

the product of all layer matrices, the Fresnel reflection and transmission amplitudes are found, which are then used to calculate the reflectance and transmittance [248]. This method can be utilised for a range of incident angles, for different linear polarisations, and for absorbing media.

The main advantage of this approach, over the Finite Element and Finite-Difference Time-Domain methods discussed next, is the rapid calculation speed. It is useful for providing relatively quick qualitative reflectance and transmission spectra of more complex structures exhibiting colouration through multilayer interference, and may also be used to verify the results of more complex modelling techniques. The greatest disadvantage of this approach is the limited applicability to complex structures; the TMM can only be used for one-dimensional structures without more complex processing methods, such at the Chandezon method [249].

In this thesis, calculations utilising this method were performed using the commercial package, TFCalc [250], and an in-house code compiled in MATLAB.

5.2.3 Finite Element Method (FEM)

To simulate the electromagnetic (EM) response of geometries of greater complexity than those of one-dimensional multilayer reflectors, numerical or analytic techniques must be used.

The inherent random and elaborate structures in many biological reflectors mean that analytical approaches, such as modal-matching, are not appropriate for the investigations in this thesis. Instead numerical techniques are used.

FEM is a widely used technique for calculating the electromagnetic properties of wide range of structures [107]. Since its inception, FEM has been used to simulate the EM responses of electronic and antenna components [251]. More recently, FEM has been used by researchers to investigate a number of different EM effects, for example in the fields of plasmonics [252, 253] and metamaterials [254, 255]. The FEM technique has also been implemented by several research groups to investigate the EM properties of biological samples [78, 104, 256, 257].

In this thesis, Ansoft's High Frequency Structure Simulator (HFSS) [258] FEM software is used. HFSS is a three-dimensional full wave EM field simulation package that solves electric field components. Building and solving a model takes several steps; first, a unit cell that represents the structure is created and assigned material properties. Second, boundary conditions and excitation conditions are applied to the unit cell. Following this, a mesh of small elements to represent the structures in the unit cell is generated. Finally, the electric field components associated with each mesh element are calculated in order to obtain reflectance, transmittance and other field information.

Each of these steps are now outlined in further detail.

Building a model

To construct a model, designs and geometries can be drawn using the built-in CAD interface or imported from other software. For designs with regular shapes the three-dimensional CAD tool is ideal. Where geometries are more complex, these can be rendered in purpose-built software, such as SolidWorks [259], and imported into HFSS.

For structures with regular periodicities, or structures that can be assumed to have periodic features for modelling purposes, an appropriate unit cell may be created. Figure 5.4(a) shows a unit cell for a one-dimensional multilayer reflector, consisting of eleven thin dielectric layers separated by air. Once a unit cell containing the geometry is rendered, each volume in the cell is then assigned a material. In this thesis, the materials are limited to dielectrics. In the example structure, shown in Figure 5.4(a), the reflecting layers would be assigned a refractive index n_{layer}, and the remaining material n_{air}.

Assigning boundaries and excitations

For the structures modelled with the FEM considered in this thesis, periodic boundary conditions (BCs) are used. Periodic BCs enable a unit cell to be repeated throughout space to allow the EM modelling of periodic planes, using Bloch-Floquet expansion theory [135].

In HFSS, the periodic BCs are defined using a master boundary and a slave boundary pair. Both boundaries are required to have consistent mesh and electric fields. Figures 5.4(b) and 5.4(c) each show a master-slave boundary pair (denoted by blue lines) for the example multilayer unit cell.

In addition to these periodic BCs, further BCs need to be imposed on the top and bottom of the unit cell in order to terminate the electric fields in the model. To achieve this termination, the models in this thesis use fictitious materials, called perfectly-matched layers (PMLs), that absorb all EM radiation impinging on them. Finally, an excitation source is needed to illuminate the structure. For the investigations here, a plane wave illumination was used with different polarisation, incident angle and frequency parameters.

Meshing and solving

To simulate the response of a structure, the model is first 'meshed'. The meshing process involves subdividing the model unit cell into smaller spatial volumes in which the electric fields are later solved. This is done by adding mesh elements, also called

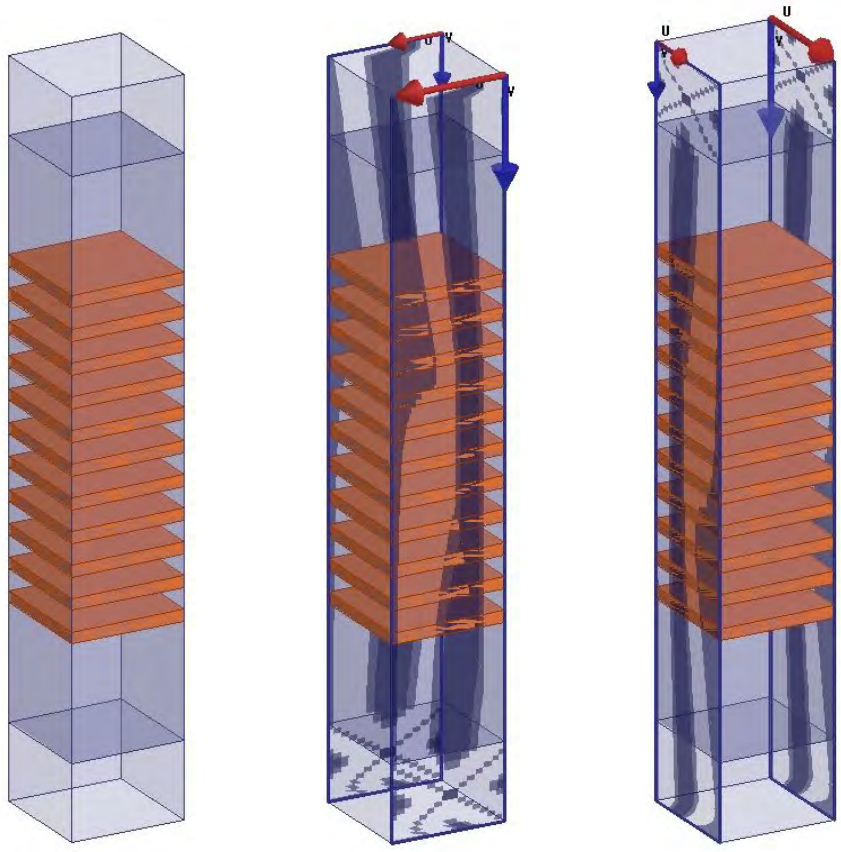

(a) (b) (c)

Figure 5.4: (a) Displays the schematic of a unit cell for a multilayer reflector with eleven dielectric layers separated by air, and with air above and below the structure (representing the incident and exit media, respectively). (b) and (c) show master-slave boundary pairs that repeat the unit cell periodically in two different orthogonal planes. In this example, the repetition of the unit cell would create a structure with a large multilayer area and the same fixed multilayer periodicity of alternating air-dielectric layers.

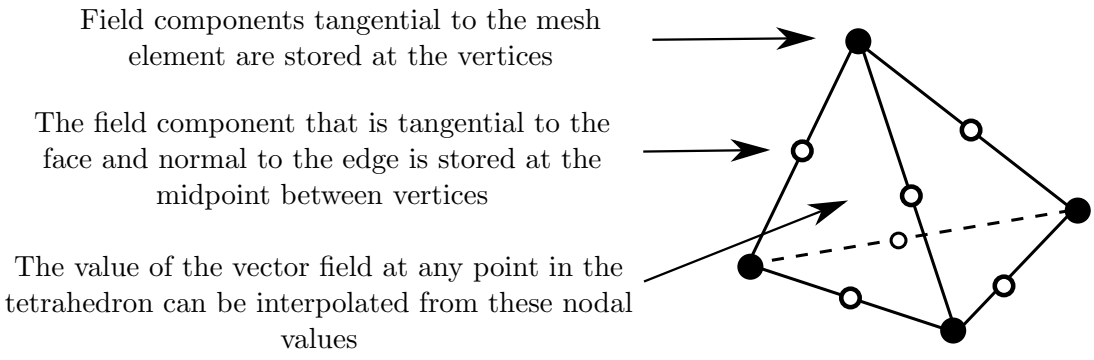

Figure 5.5: Schematic diagram of single mesh element, displaying the vertices and midpoints, in which the electric field components are interpolated during the solution process. (Image adapted from HFSS software documentation).

tetrahedra, to approximate the rendered structure and surrounding space. Figure 5.5 displays a rectilinear mesh element, in which the electric field is later interpolated. Curvilinear mesh elements, that have curved sides connecting the vertices, can also be added to curved sections to provide a better approximation to two and three dimensional surfaces. The automatic mesh settings in HFSS add mesh using algorithms that factor in the geometry, material properties and the excitation wavelength of the simulation [260]. During the solution process, further adaptive meshing occurs. This adds additional mesh to spatial regions where the electromagnetic-fields are rapidly changing. In general, the automated mesh functions produce a good approximation of the rendered geometries. If the mesh is insufficient, for instance in areas of fine structure, mesh can be manually seeded in those areas. Figure 5.6(a) displays a diagram of the mesh plotted on the surface of the unit cell previously described.

HFSS's solution is calculated by numerically solving using Maxwell's equations in vector potential form [260]. The electric fields can be interpolated at any point in each mesh element using the field components at the vertices and midpoints of the connecting lines (see Figure 5.6(a)). At the start of the solution process, an initial guess is made for the matrix of unknowns that describes Maxwell's equations [260]. This matrix is recursively updated, during which the adaptive mesh process takes place, until an error tolerance has been reached.

A convergence process decides when an acceptable tolerance, defined by the user, has been achieved. This is determined by using the percentage change in the local energy of each tetrahedron between each solution iteration. As this relative change decreases between solutions, the model is assumed to have converged. Once converged, the electric fields are then solved for the frequency range defined.

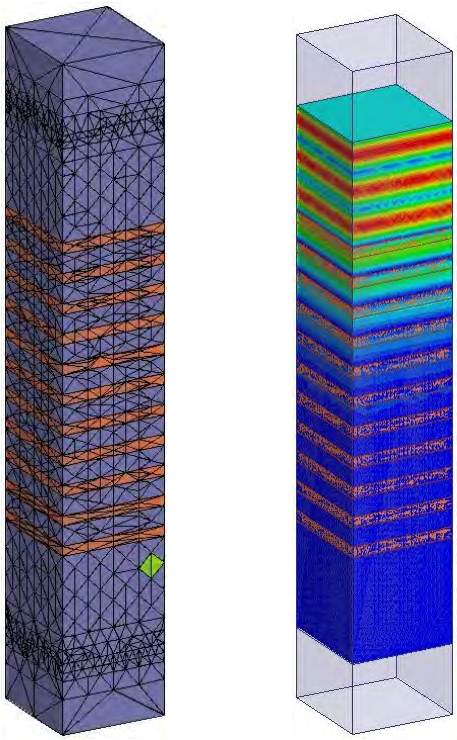

(a) (b)

Figure 5.6: (a) Displays the example multilayer unit cell with the initial mesh plot overlayed. Regions of higher mesh density can be seen around the reflecting layers, and the interface between the air and PMLs. (b) shows a typical plot of the time-averaged electric field overlayer on the multilayer unit cell (Red regions correspond to high E-field intensity).

Data extraction

A range of quantities can be obtained from the solved FEM model. Reflectance and transmittance are obtained from the scattering matrix, and are frequently used in later investigations. In addition, the electric fields can be used to calculate the spatial distribution of many quantities, such as the Poynting vector, or magnetic field. Figure 5.6(b) displays a typical time-averaged electric field distribution for the multilayer example previously described, where red regions correspond to high electric field intensity.

Advantages and limitations

The FEM technique has a number of advantages and limitations. The main advantage over analytical methods is its ability to model complex structures. The in-built CAD tools and facility to import rendered three-dimensional objects in HFSS makes creating

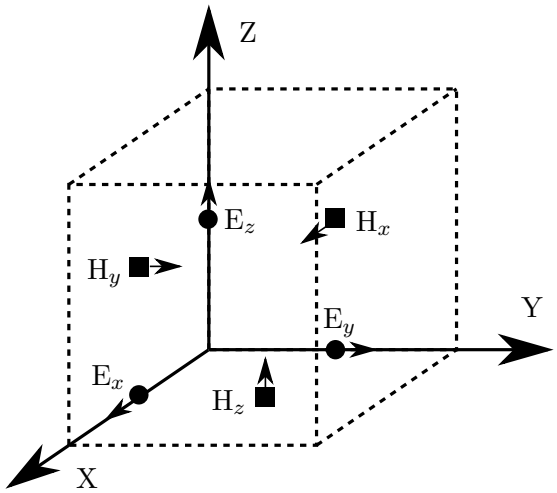

Figure 5.7: Schematic of a single Yee cell in Cartesian coordinates. Each E-field component is positioned at the centre of the edge, and the H-field component at the centre of the face.

models relatively straightforward.

With the ability to model such complex structures comes a cost; solving the electric fields is computationally demanding. Increasing model size and complexity requires a large number of mesh elements to produce an accurate solution. Another limitation specific to this software is the inability to calculate the reflectance and transmittance properties of a finite sample. To overcome this limitation a FDTD package is used.

5.2.4 Finite-Difference Time-Domain (FDTD) method

Where the FEM technique is not appropriate or is unable to simulate the EM response for specific modelling demands or illumination conditions, the FDTD method has been used.

The FDTD method has many similarities to the FEM technique; the FDTD technique also solves Maxwell's equations for complex geometries in two and three dimensions. Like FEM models, FDTD models are sub-divided into smaller mesh elements in which the EM fields are solved. These mesh elements are named Yee cells, after Yee, who first proposed this solution methodology for electromagnetics [108]. Figure 5.7 displays a single Yee cell. Unlike the FEM, which produces a frequency domain solution, the FDTD technique is a time domain solution [261]. The solution is generated by solving Maxwell's curl equations in space as a function of time [261]. To obtain a frequency domain solution, fourier transforms are performed during the solution process [262].

The FDTD spectral data presented in this thesis was calculated using a commeri-

cal package called 'FDTD Solutions' by Lumerical [263]. Like HFSS, described in the previous section, similar boundary conditions and excitation conditions can be defined in FDTD Solutions, and therefore are omitted from discussion here. Instead, the additional functionality is outlined. First, an FDTD solution allows large finite models (large relative to those possible with the FEM) to be simulated on a desktop PC. In addition to the reflectance and transmission properties, greater functionality can be incorporated into a solution by using EM-field calculations. For instance, in this thesis, these functions have been used to calculate the angle-resolved scatter from finite models. This allows flexibility in tailoring the simulated 'illumination' and 'measurement' conditions, to approach that of more realistic experimental measurements.

Advantages and limitations

Advantages of the FDTD technique are its fast solution time, ability to model finite samples, and the ability to do further field calculations. As with the FEM models, FDTD models are often limited in size and spatial resolution by the mesh. To provide accurate solutions high mesh is required which comes at the cost of time and processing power. The relative mesh technology in these numerical solutions is better for the FEM method, which means the FDTD requires more mesh to create finer resolution of fine structure for the models simulated.

5.3 Multivariate analysis tools

5.3.1 Introduction

As discussed in Section 4.3.3, modern chemical sensors often require additional signal processing in order to extract chemical information. Similarly, in this thesis, the chemical vapour signal contained in the measured or calculated reflectance, upon vapour exposure or model vapour adsorption, requires additional signal processing to obtain information.

In the measurements described, large multivariate datasets are recorded upon low-concentration vapour exposure, where 'multi' corresponds to the large number of wavelengths over which a spectrum is sampled. In the low-concentration regime, changes in the chemical environment do not produce a noticeable change in the reflected colour, or show any obvious linear trends such as a linear shift in peak reflected wavelength with vapour concentration or refractive index. Instead, subtle changes occur across the visible wavelengths.

To investigate potential trends in such datasets, a challenge arises where the quantity of data is large, and where data has high-dimensions. A number of statistical

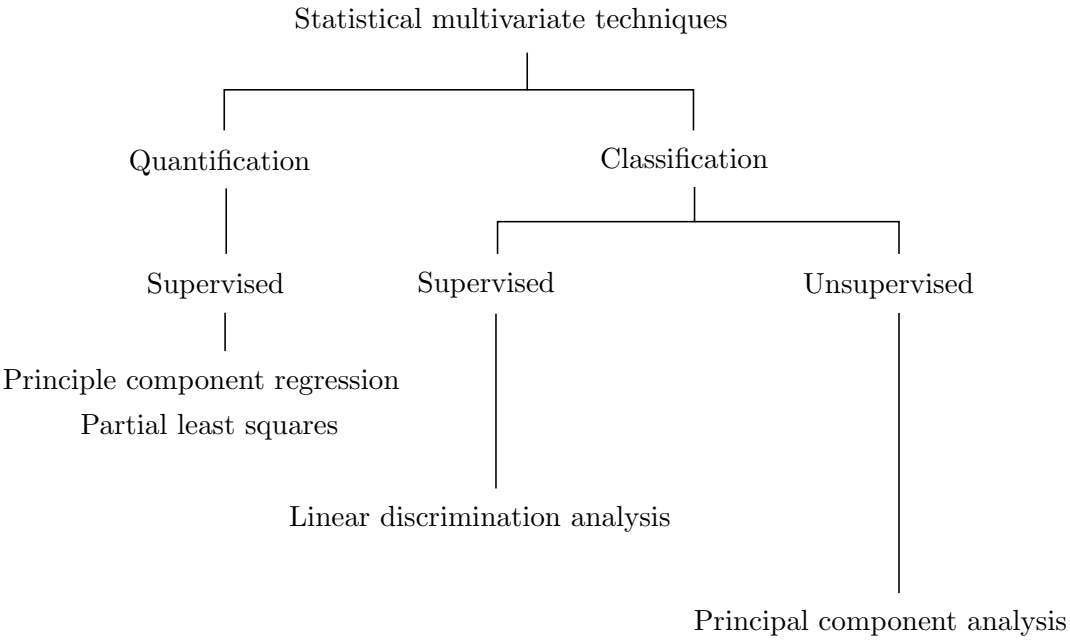

Figure 5.8: Diagram of different statistical methods used for the quantification and classification of multivariate datasets. (This diagram is adapted from Ref. [174]).

methods exist to reveal trends in complex data [174, 264]; multivariate statistics is one such approach. These methods often work by data reduction in order to visualise trends and clustering. Figure 5.8 displays a diagram of different multivariate techniques for the quantification and classification of high-dimensional data.

For analysis of data presented in this thesis, classification of the trends observed upon vapour exposure is a primary interest, therefore, Principal Components Analysis (PCA) is used. PCA is widely used by analytic chemists for data mining and compression [265]. In the next section, the basic processes of this analysis are described, before illustration of the power of this analysis using an example dataset.

5.3.2 Principal Components Analysis (PCA)

PCA is a robust and widely used unsupervised statistical analysis that reduces the dimensionality of a dataset containing a large number of interrelated variables. This process is achieved by transforming the original variables to a new set of variables, that are called Principal Components (PCs), which are uncorrelated and contain the most variation of the original dataset [266]. This is done by reducing data dimensionality by projecting the original variables onto a lower dimensional subspace. This process removes data corresponding to the smallest variation in the dataset to reduce data redundancy in the new dataset [266].

The following description, set out in Ref. [267], briefly outlines the outputs following the PCA analysis. Consider the data matrix $\mathbf{X}$ with m rows $\times$ n columns, where a column represents a variable, and a row represents a sample. PCA decomposes $\mathbf{X}$ into a sum of r $\mathbf{t_i}$ and $\mathbf{p_i}$ vectors, where r less than or equal to the smaller dimension of $\mathbf{X}$ [267]:

$$\mathbf{X} = \mathbf{t_1 p_1^T} + \mathbf{t_2 p_2^T} + ... + \mathbf{t_k p_k^T} + ... + \mathbf{t_r p_r^T}. \tag{5.5}$$

The $\mathbf{t_i}/\mathbf{p_i}$ pairs are arranged in descending order of variance captured, and after k components, where the variance is small, often truncated. The $\mathbf{t}$ vector contains the 'scores' values, which describe how each sample relates to one another. The $\mathbf{p}$ vector contains the 'loadings' values, which describe how each variable relates to one another.

The mathematics of this procedure relies upon linear algebra to find an eigenvector decomposition of the original data matrix. This is usually done with a singular value decomposition, although other methods exist [266]. The PCA process is described in many publications [174, 265, 266], and in several good tutorials [268, 269]. It is difficult to provide an intuitive description of these processes, so a more in-depth description is left to the sources above. Instead, results of a sample analysis are presented to illustrate the PCA outputs.

To demonstrate the analysis a dataset of normal distributions of the form

$$f(x, \mu, \sigma) = \frac{1}{\sigma\sqrt{2\pi}} \exp\left(-\frac{(x-\mu)^2}{2\sigma^2}\right) \tag{5.6}$$

was calculated, where μ and σ are the mean and standard deviation, respectively. The distributions also have a 10% noise (with normal distribution) added; four of these example distributions are shown in Figure 5.9(a). Figure 5.9(b) displays the combinations of the mean and standard deviations used to generate the distributions for the sample dataset.

Data preprocessing is performed before the analysis. Preprocessing of the data can be done by commonly employed mean-centering and autoscaling methods. The mean-centering method calculates the mean of each distribution and subtracts this from the distribution. Autoscaling method uses mean-centering followed by dividing each variable by the standard deviation of the spectrum [267]. Mean-centering is used here, as autoscaling is more appropriate when analysing datasets where the variables have different units or where one sample's variables have significantly different values, both of which would weight an analysis.

The data analysis presented in this thesis has been analysed using the PLS toolbox (Eigenvector Research, Inc.) operated with MATLAB. Figure 5.9(c) and 5.9(d) display

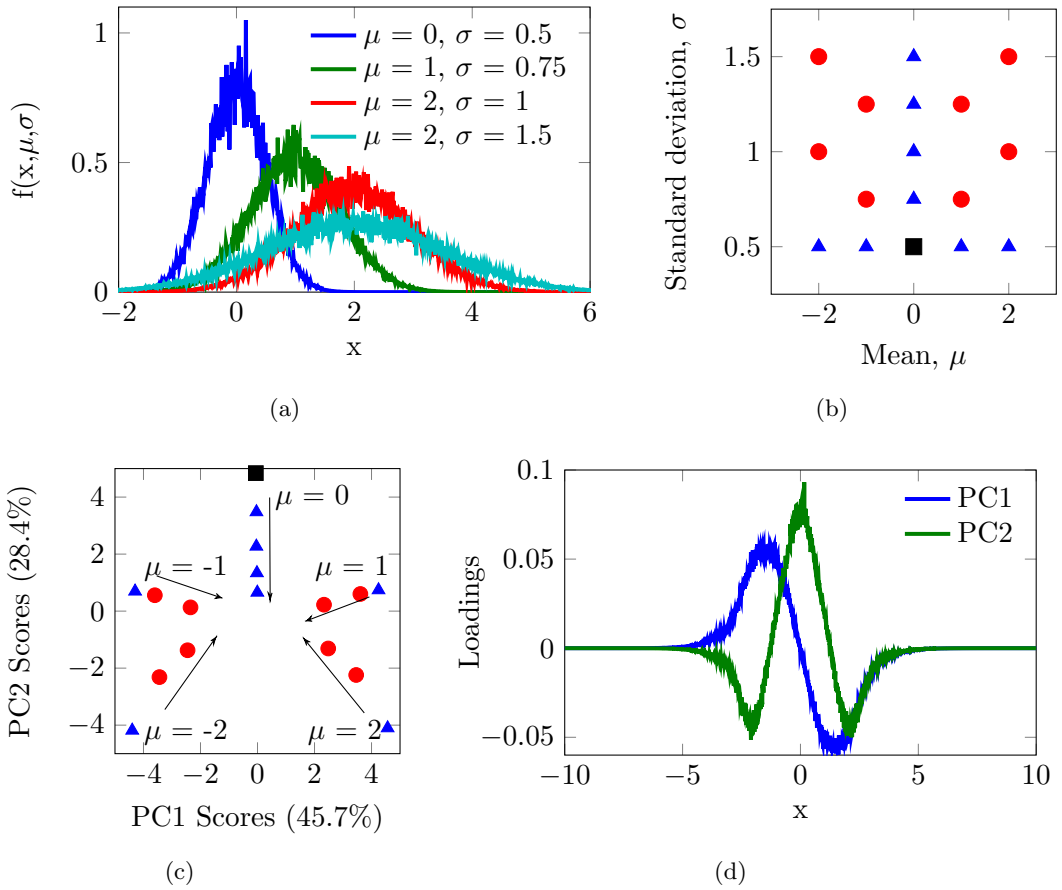

Figure 5.9: Example PCA analysis of normal distributions with different mean and standard deviation values. (a) Displays four distributions with different means and standard deviations, with a simulated 10% noise with normal distribution. (b) Profile of the seventeen normal distributions generated for analysis. (c) and (d) display a scores plot and loadings plots for the first two PCs, respectively. (c) Shows that the different mean values of these distributions cause the greatest spread in the first PC, indicating the mean accounts for the greatest difference between distributions of different distributions. The marker symbols in (b) and (c) are consistent between plots. The arrows represent increasing standard deviation values, indicating that the distribution curves become less distinct from one another as the standard deviation increases. (d) The loadings indicate which x-variables contribute most to the variation in each PC.

a scores plot and loadings plots for the first two PCs, respectively.

A number of observations can be made using the scores plot in Figure 5.9(c): First, the percentage of variance captured in each PC provides the first indication of how different each sample might be with respect to the others. These values indicate how the points in this space can be differentiated; if nearly all variance of the dataset is captured in the first PC then points are less differentiated in the two dimensional PC1-PC2 plane, however, if the variance is captured with a large number of PCs, good differentiation of points may be possible in two or more dimensions. The percentage of total variance captured in each PC is 45.7% and 28.4%, respectively, indicating the possibility for good differentiation between these normal distributions. Second, the distribution of data points, which each represent a calculated distribution, show how correlated each normal distribution is with respect to one another. The points representing distributions with $\sigma = 0.5$ and $\mu = \pm 2$ are spread furthest in space from the point representing the distribution with $\sigma = 0.5$ and $\mu = 0$, indicating that their variables are the least correlated; as such they are the 'most different'. The closer the data points, the more correlated their variables are. The arrows on Figure 5.9(c) point in the direction of increasing standard deviation; they are seen to point to the centre of the PCA space. This is expected; visually, distributions with large standard deviations become increasingly less discernable from each other, indicating increasingly correlated variables. Finally, PCA analysis shows a trend which is a track formed of points with varying standard deviation for fixed means, as indicated by the arrow lines. The loadings, shown in Figure 5.9(d), show how each variable contributes to the variance captured in each PC.

Whilst for this example trends and information about the distributions may be obvious, and could be quantified using other techniques, PCA becomes an invaluable tool where the data to be analysed contain complex trends. The scores and loadings information are used in the understanding of trends in measured and calculated optical data throughout this thesis.

In the spectral data analysed throughout this thesis, the small changes in the optical signals, associated with chemical adsorptions to the photonic structure, display complex trends. The spectral features do not display linear shifts, for example, a shift of the peak reflected wavelength upon vapour adsorptions of increasing optical thickness, instead the wavelength variables change intensity in a convoluted way. Using the interpretations the of PCA analysis described above, some general comments can be made about the desirable outputs required for optical sensing using butterflies and their bio-inspired counterparts. First, since a large spread in the PC scores space indicates the greatest difference of the wavelength variables, a sensor that maximises the spatial distribution of these points, which each correspond to a single measurement, is highly desirable.

Second, since a PC captures an amount of the total percentage variance of the dataset, a processed dataset where the variance of the data is distributed evenly among PCs has great utility. This is because it allows trends in the data to be visualised in a higher dimensional space - and potentially gives further access to data structures that may exist within the spectral data. Finally, the loadings information, which quantifies the contribution of a single wavelength to the total variance of each PC, is useful when deciding which variables are actually important in transducing the chemical information from the optical signal.

5.4 Summary

In this chapter, the experimental measurements and theoretical techniques used in the investigations in this thesis have been considered. First, the optical measurement and vapour generation processes were described, and then illustrated with a sample methanol vapour measurement on the scales of *M. rhetenor*. Following this, three different techniques for the computation of optical effects in biological reflectors were discussed. Finally, the multivariate statistical method PCA was described and then demonstrated with a sample dataset.

Chapter 6

The Vapour Response of *Morpho* Butterflies

6.1 Introduction

In this chapter, the mechanism for the unusual multivariable vapour response of the photonic structures in the wing scales of *Morpho* butterflies is investigated. To begin, the initial discovery of this response is presented, before discussion of other examples in the literature that have examined similar vapour responses in naturally occurring photonic structures. The photonic structure of *Morpho sulkowskyi* is then discussed, before experimentally and theoretically demonstrating the change in optical reflectance that arises when a volatile liquid or vapour is present within these iridescent scales, and the scales of *Morpho rhetenor*. Possible mechanisms for this unusual response are then hypothesised before demonstrating, through electromagnetic simulations, vapour-exposure measurements and characterisation experiments, that the general mechanism of selective vapour response is achieved by preferential spatial adsorption of analyte molecules upon the photonic structure. The origin of the chemical gradient pattern of polarity responsible for these interactions within the butterfly scales is then discussed. To conclude, these results are summarised and their importance in optical sensor development is presented before suggesting some further applications in other fields.

The work presented in this chapter was undertaken in collaboration with researchers at General Electric Global Research Center (Niskayuna, NY, USA), the Air Force Research Laboratory (Wright-Patterson Air Force Base, OH, USA), the State University of New York (Albany, NY, USA), and has been published in the work titled 'Discovery of the surface polarity gradient on iridescent *Morpho* butterfly scales reveals a mechanism of their selective vapor response' in Proceedings of the National Academy of Sciences of the United States of America, Volume 110, Issue 39, Pages 15567-15572,

Year 2013 in Ref. [12], and in work titled *'Toward bioinspired nanostructures for selective vapor sensing: diverse vapor-induced spectral responses within iridescent scales of Morpho butterflies'* in MRS Online Proceedings, Volume 1621, Year 2014 in Ref. [13].

6.2 Background

The ability of sensors to exhibit a sensitive *and* selective response to different volatile vapours is poor. At present, modern analytical instruments designed or implemented in practical scenarios, such as micro-gas analysers [270], ion-mobility spectrometers [271] and mass-spectrometers [272, 273] struggle to perform this task under the requirements that exist for such devices. In order to achieve a desirable level of selectivity, sensors with increasingly large sensor arrays have been developed [244]. For the reasons set out in Chapter 4, this approach is not an elegant solution to the problem and more recently has begun to stimulate alternative simple, but selective, sensor approaches to address this requirement [264, 274].

Inspired by the review article Ref. [3], by Vukusic and Sambles, General Electric researchers speculated that the iridescent colour of the nanostructures described in the review would be strongly influenced by their ambient chemical surroundings [275]. Their highly cited work [8] into the vapour response of *Morpho* butterflies, in 2007, reported several interesting and unexpected results. They reported that, by coupling optical reflectance measurements with multivariate analysis, an analytic signal that discriminated closely related vapours (water, methanol, ethanol and isomers of dichloroethylene) could be transduced by the iridescent scales in low-concentration vapour atmospheres. This analytic signal distinguished each vapour from one another when measurements of individual vapours were performed separately, and provided information about the vapour concentration. Concentration information was obtained by the magnitude of the change in reflectance, ΔR, and vapour identity was related to the information inherent in the spectral features of the datasets.

The work suggested physical adsorption and capillary condensation into the 'pores' created between the lamellae as mechanisms to explain the observed temporal and steady-state responses due to the different interactions of a vapour's surface tension, molar volume, molecular shape and molecular size [8]. Hence, it was proposed that the unusual selective response was solely due to the nanostructured scale of *M. sulkowskyi*.

Following this initial study, a number of other works were published by other research groups in similar themed areas of research. Similar experimental measurements were reported on a number of other structurally coloured butterflies from the *Morpho*, *Chrysiridia*, *Pseudolycena* and *Cyanophrys* species [220]. A larger range of volatile organic compounds (VOCs) demonstrated the same fast, reproducible and concentration-

dependent responses previously reported [220]. Differences in the change in reflectance signal were pronounced between the wing samples of different insects, and the features in the reflectance spectra for each VOC were different with respect to one another [220]. Ammonia vapour was shown to have the most pronounced effect upon reflection [220]. Temporal measurements performed for a series of on/off vapour exposures show that the ammonia exposure did not return to the baseline signal before the exposures began, which suggests irreversible interactions with the structure's material [220].

Other studies have experimentally and theoretically explored the change in colour that occurs when *Morpho* scales are immersed in light molecular-weight alcohols [221, 276–278].

This bio-inspired vapour sensing idea has inspired similar research into pH sensitive photonic structures. One study has incorporated a pH-sensitive polymer network into the scales of *Chrysiridia rhipheus* (Sunset Moth) [224]. To induce a colour change, small variations in the photonic crystal periodicities arise due to the swelling/deswelling processes of the pH sensitive synthetic polymer coating. Synthetic pH sensors that use structural colour mechanisms have also been explored [200].

In summary, since the initial work on the vapour selectivity in *Morpho* scales, several studies have performed similar investigations on both the VOCs and pH-sensitive structures. These studies have shown simliar findings as the initial work, but with analysis often at much higher vapour concentrations. Despite this interest, there has been no validation of the suggested mechanism responsible for these unusual vapour responses. In this chapter, a rationale for this selective and sensitive vapour response is explored. This investigation forms a primary objective of this Ph.D project.

6.3 *Morpho sulkowskyi's* photonic structure

The *Morpho sulkowskyi*, also called the 'Pearl *Morpho*', is a small neotropical butterfly exhibiting an iridescent appearance derived from structural colour mechanisms. *M. sulkowskyi* does not exhibit a metallic blue colour appearance like that of *M. rhetenor*, instead it has a white iridescent colour appearance. Its iridescent holographic-like appearance is shown in Figure 6.1(a).

The reflectance of *M. sulkowskyi* and *M. rhetenor*, illuminated and measured using an integrating sphere, is shown in Figure 6.1(b). The reflectance spectrum of *M. sulkowskyi* has a broad reflectance peak from UV to cyan/green wavelengths, with a lower intensity reflectance region beyond these wavelengths toward the IR. This spectral profile, with broad reflectance above $\sim 30\%$ for all wavelengths, produces its silvery appearance. In contrast, *M. rhetenor*'s reflectance exhibits a narrower more intense reflectance peak in the spectral region corresponding to blue wavelengths, and much lower

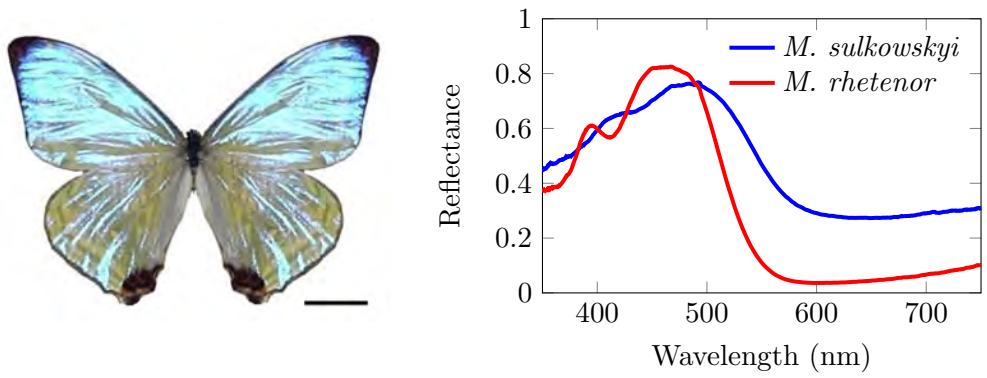

(a) (b)

Figure 6.1: (a) A photograph of a male *M. sulkowskyi* butterfly, and (b) reflectance of *M. sulkowskyi* and *M. rhetenor* measured with an integrating sphere. [Scale bar: (a) 15 mm].

intensity reflection for wavelengths beyond 550 nm. This low intensity region explains the more vivid blue colour-appearance as there is an absence of reflected complementary colour. To elicit better understanding of these visual differences, the photonic structures can be examined.

The colour-producing structures in the wing are very similar within their species group. Type I iridescent scales, as described in Chapter 2, adorn the wings of the male *M. sulkowskyi* butterflies. A typical cross-section, imaged by transmission electron microscopy (TEM), through a *M. sulkowskyi* ground scale, and a higher resolution image of a single ridge-lamellae structure, is shown in Figures 6.2(a) and 6.2(b), respectively. The lamellae in the ridge structures of *M. sulkowskyi* have relatively regular spacing in comparison to *M. rhetenor* and other *Morphos* such as *M. didius* [101]. Previous studies have shown that the reflectivity of both *Morphos*, due to their lamellae contribution, are essentially the same and the difference in colour-appearance arises due to the absorption/transmission properties of the scales [101]. Thus the contrast in colour may be attributed to the presence of optical absorption, by melanin pigmentation, within the insect cuticle. As discussed in Section 2.5, the presence of melanin in *M. rhetenor* absorbs complimentary colours. In contrast, *M. sulkowskyi* has relatively little pigment absorbing green/red wavelengths as evidenced by observations of transmission through its wing [101].

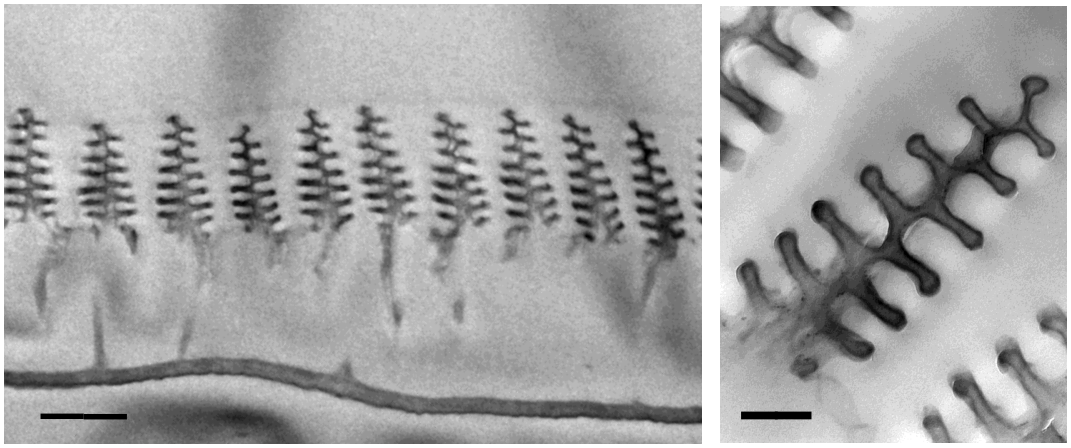

(a) (b)

Figure 6.2: Transmission electron micrographs of a cross-section though a *M. sulkowskyi* ground scale: (a) image displaying multiple ridge-lamellae structures, and (b) a higher resolution image of a single ridge-lamellae structure. [Scale bars: (a) 1 µm, and (b) 200 nm].

6.4 Experimentally observed vapour response

6.4.1 Wetting of a *Morpho* wing

As an introduction, before discussing low-concentration vapour exposures to butterfly scales, in this section the effect of wetting the iridescent scales is described. Many previous studies examining the optical properties of structurally coloured insect exoskeleton materials have used wetting and immersion techniques [36, 37, 41, 63]. These involve matching the refractive index of the constituent material with the refractive index of the wetting fluid by displacing the air within the structure. When this condition is met, the *Morpho* scales with wetting fluid effectively become a homogenous medium, which removes the iridescent colour-appearance. The colour-appearance changes from blue toward red wavelengths, which is termed a 'red-shift' of the reflected peak wavelength. Figure 6.3(a) displays the colour change from blue to green when prop-1-ol (IPA), which has refractive index $n = 1.38$, is dropped onto the wing of *M. rhetenor*. This colour change, which arises from the increase of optical path length in the low refractive index layer, occurs extremely rapidly (<1 sec) before slowly reversing to the original colour-appearance.

This modification to the interference condition in the *Morpho* wing can be illustrated simply by considering the reflectance of a quarter-wavelength stack comprising six high RI layers, with $n_{\text{high}} = 1.56$, separated by low RI index layers, of $n_{\text{low}} = 1$,

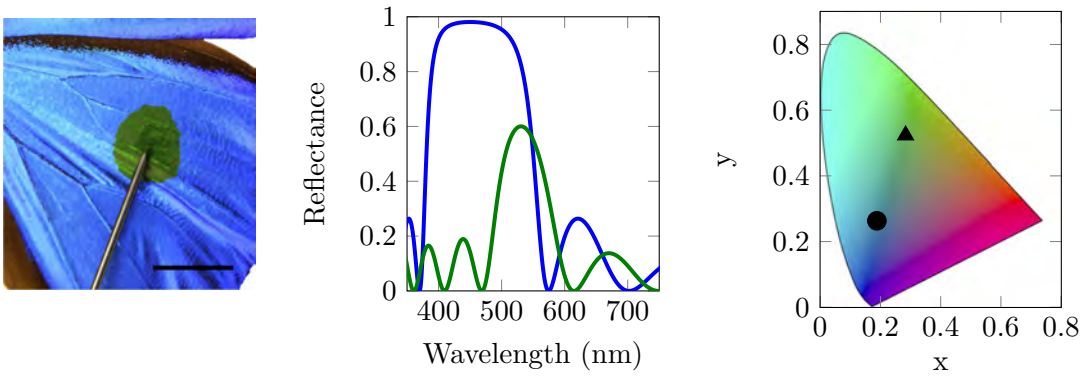

(a) (b) (c)

Figure 6.3: (a) A photograph of a wing-section of *M. rhetenor* with a drop of prop-1-ol which changes the colour-appearance from blue to green. (b) Reflectance calculated for a quarter-wavelength stack with low-RI 'air' layers of $n = 1$ (blue line) and then with 'air' layers replaced with a RI of $n = 1.38$ (green line) to simulate that of a model 'solvent'. (c) Visualisation of the perceived change of colour-appearance using the CIE colour space for calculated reflectance for 'air' (circle marker) and 'solvent' (triangle marker) low-RI layers for the multilayer described in (b). There is a colour-shift from blue to green in the CIE space. [Scale bar: (a) 50 mm].

with a peak wavelength of $\lambda_{\text{peak}} = 450$ nm. The reflectance of this system is computed for $n_{\text{low}} = 1$ and then $n_{\text{low}} = 1.38$ to represent the presence of air and then a solvent. These computed reflectance spectra are shown in Figure 6.3. As observed in the photograph (Figure 6.3(a)), the spectra of the modelled solvent-filled multilayer stack (Figure 6.3(b)) red-shifts the peak reflectance from 450 nm to $\sim$ 530 nm. In addition the intensity of reflection changes as the quarter-wavelength (ideal multilayer) interference condition is no longer satisfied. Using the CIE colour-space [279] the colour change as perceived by human vision, associated with this spectral shift, can be displayed, see Figure 6.3(c). This wetting experiment illustrates an exaggerated effect of the low-concentration vapour effects that are described herein.

6.4.2 Observations of low-concentration vapour exposures

Having discussed the optical effects arising upon wetting of *Morpho* scales in the previous section, it is useful to present experimental measurements of low-concentration vapour effects within these scales before discussing the origin of their unusual vapour selectivity. It is also useful to observe whether this selective response is unique to *M. sulkowskyi*, or whether this can be seen in another similar structure. To answer this question low-concentration vapour exposure measurements were performed upon the wing-scales of *M. rhetenor*; first humidity cycles are presented, before other volatile

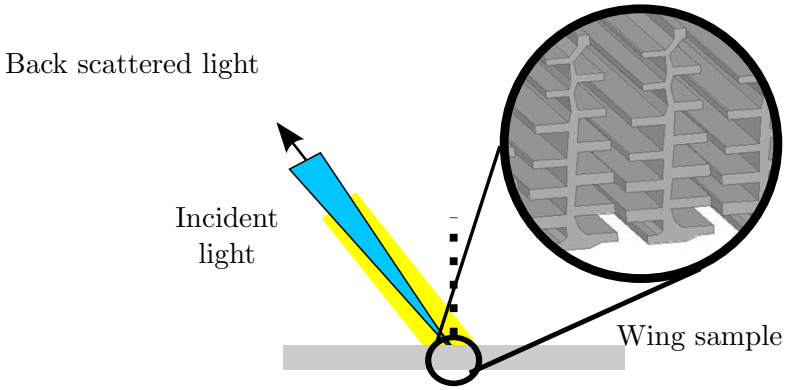

Figure 6.4: Diagram illustrating the experimental arrangement of the illumination of the sample, and collection of scattered light, with respect to the orientation of the ridge structure within the wing scales.

organic compounds (VOCs) are used.

6.4.2.1 Humidity cycles

To examine the response of *M. rhetenor* scales to ambient humidity, a bifurcated probe was positioned at $\sim$ 30 degrees from the normal to illuminate and measure the reflectance from a $\sim$ 2 mm beam spot on a section of wing. Figure 7.1 shows the probe illumination relative to the ridge orientation within the scales. An inert carrier gas (N_2), delivered with a 450-mL/min total flow rate from a 1/8-inch-diameter tube, is then flowed onto the butterfly wing at an angle of approximately 45 degrees to the surface, with vapour flow orientated to flow along the ridges of the photonic structure. Before the exposure measurement, the raw reflectance is viewed to ensure that any change in reflectance will not saturate the spectrophotometer. The raw spectrum measured before these humidity cycles is shown in Figure 6.5(a). It should be highlighted that this spectrum is un-normalised. Before the exposures begin, this raw spectrum is normalised with respect to itself to provide a measurement of the change in reflectance (also referred to as the differential reflectance). Here the change in reflectance, ΔR, was measured as $\Delta R(\%) = (R/R_0 - 1) \times 100\%$, where R_0 is the raw spectrum, and R is the measured spectrum. Following normalisation, exposures to the 10% ambient humidity of the laboratory were performed by turning the carrier gas flow off and then on in 50 second intervals.

The temporal profile for a fixed wavelength of 525 nm is shown in Figure 6.5(b). When the carrier flow is turned off, a rapid change in reflectance occurs until this change begins to plateau. Upon the reintroduction of carrier gas, a rapid return towards the

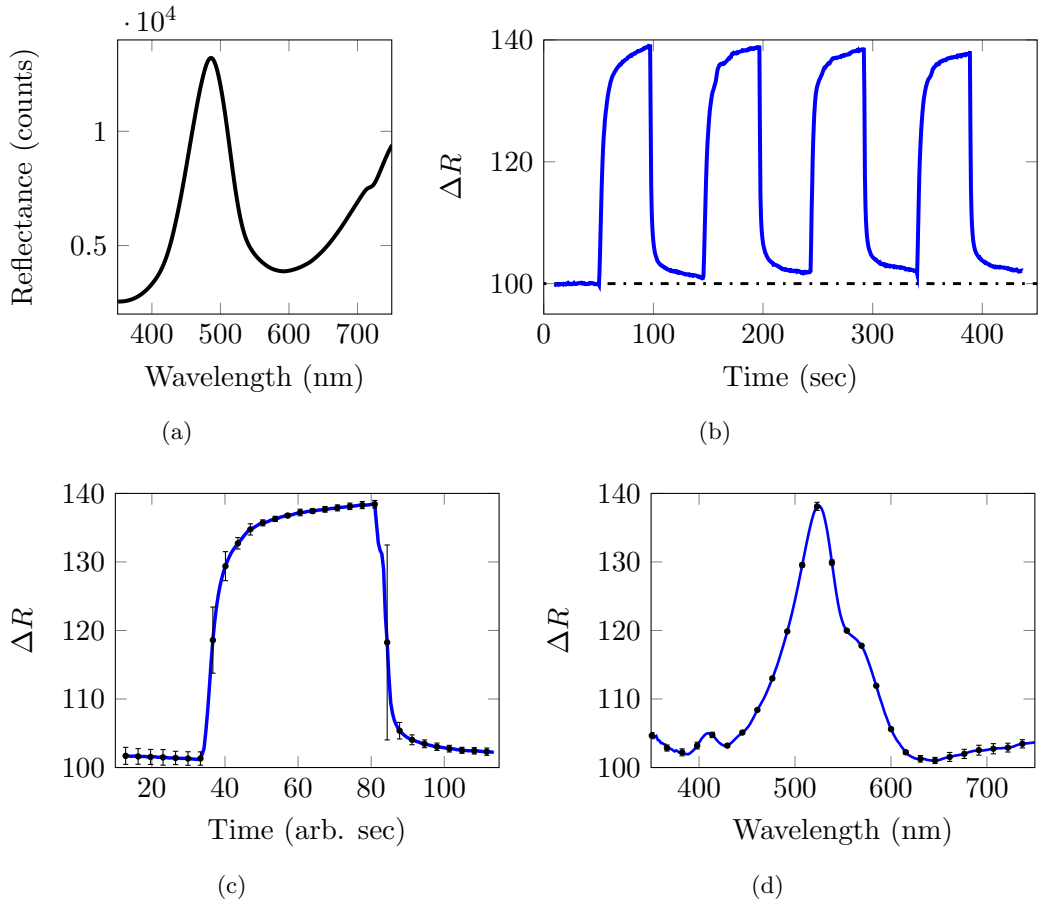

Figure 6.5: The optical response of *M. rhetenor* to 10% relative humidity. (a) Raw reflectance spectrum before normalisation to the baseline of N_2 carrier for measurement of the change in reflectance. (b) Temporal profile for the change in reflectance for four vapour exposures to the ambient humidity at wavelength of 525 nm. (c) and (d) mean temporal and spectral profiles, respectively, for these four humidity exposures indicating good reproducibility of measurements. Error bars: $\pm$ 1 σ.

baseline reflectance is observed. Figure 6.5(c) displays the mean change in reflectance for these humidity cycles, and Figure 6.5(d) displays the mean spectra for each humidity cycle at 5 seconds before the carrier flow is resumed. Both graphs display error bars of $\pm$ 1 σ.

These results indicate good reproducibility, fast dynamic responses and reversibility when the *Morpho* scales interact with an environment of 10% ambient humidity. This humidity expressed in terms of the vapour pressure, which is more commonly used to quantify the vapour concentrations in the literature, is equal to $0.1P/P_0$ (or $\sim$ 3100 ppm).

6.4.2.2 Vapour cycles

Having observed the optical response arising from humidity exposures, the response to three different chemical species is considered next. The experimental arrangement remains as described for the humidity cycle experiment; however, the vapour delivery is altered. Instead of using an on/off style delivery, the flow rate of gas to the scales remains constant, to create a vapour exposure the vapour is mixed with the carrier gas, as described in the discussion of vapour generation in Section 5.1.3. For these measurements, water, methanol, and ethanol vapours are generated at a concentration of 0.18 P/P_0, where P is the partial vapour pressure, and P_0 is the saturated vapour pressure.

The temporal profile for these vapour exposures is displayed in Figure 6.6(a) for fixed wavelengths 440 nm, 540 nm and 640 nm. As observed for the humidity cycles, the initial response upon the introduction of vapour produces a rapid change in the reflectance until a time where the changes begin to plateau. Differences can be observed in the reversibility of the change in reflectance upon the return to a pure carrier gas flow; the water and methanol exposures quickly return to the baseline reflectance, whereas the ethanol exposure displays a slower return when comparing changes at 540 nm. Such observations of the dynamic response can indicate how the vapour molecules interact with the nanostructure; these effects are discussed in more detail in Chapter 7. Other observations of the dynamic response reveal different relative changes in reflectance at different wavelengths for the same vapour, and between vapours. For instance, large changes in magnitude are observed between vapours at 540 nm, little change is observed at 640 nm throughout the exposures and methanol vapour is the only chemical to produce a noticeable change at 440 nm. To visualise these changes at different wavelengths it is useful to look at the delta reflectance spectra.

The spectrum corresponding to 5 seconds before each vapour flow returns back to the pure carrier gas flow is shown in Figure 6.6(b). The blank spectrum is the baseline reading before the first vapour exposure. Across these measured wavelengths there are regions where little discernible difference in reflection is observed, for instance at wavelengths above 650 nm. The regions where a change in reflectance is observed correspond to red-shifts in reflection associated with the adsorption of vapour upon the scale's ridge-lamellae structure.

In order to compare this data to the earlier results [8], reporting a selective response in the scales of *M. sulkowskyi*, the spectra in Figure 6.6(b) are analysed with Principal Components Analysis. The results of this analysis are displayed as a PC scores plot in Figure 6.6(c). Each vapour condition is resolved from one another in the PC space, which indicates a selective response between these vapours.

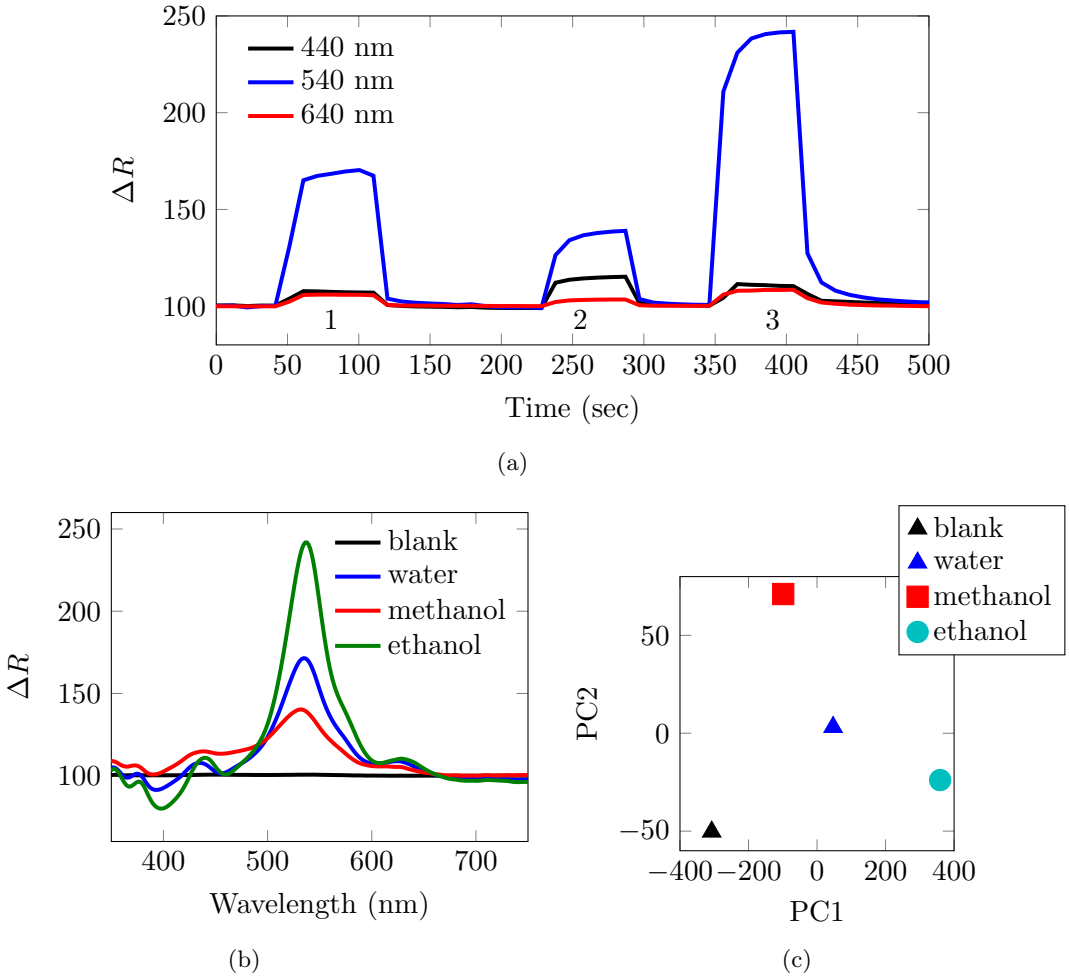

Figure 6.6: Optical response and PCA analysis of *M. rhetenor* upon exposure to water, methanol and ethanol vapours at 0.18 P/P_0. (a) Temporal profile for (1) water, (2) methanol and (3) ethanol at three fixed wavelengths for exposure measurements. (b) Differential reflectance, ΔR, at 5 seconds before the end of each vapour cycle in (a). (c) PCA scores plot of the spectra in (b), which indicates a selective response between the spectra for each vapour exposure. In (b) and (c) 'blank' denotes the spectrum of the N_2 carrier, to which this measurement is normalised.

6.4.2.3 Summary

The results shown for humidity and vapour cycles have demonstrated several things: First, the scales of *M. rhetenor* have the same fast dynamic responses of those previously reported [8]. Second, the scales can provide reproducible and reversible optical responses to different chemical species. Finally, the same selective-type vapour response is observed in the scales of *M. rhetenor* as was first observed in the scales of *M. sulkowskyi*. That is to say, each chemical can be differentiated from each other through analysis of the reflectance from the iridescent scales. This comparison suggests the mechanism that allows the differentiation of chemical vapours may be common to this ridge-lamellae structure.

6.5 Mechanism of unique vapour response

To investigate how the sensitive *and* selective vapour response shown through experimental results in Section 6.4.2 and other studies is achieved, the hypothesis set out in Potyrailo *et al.* 2007 is first considered; that is, these vapour responses arise through the combined action of physical adsorption and capillary condensation within the photonic structure [8].

These actions are suggested because similar vapour effects in porous silicon sensing films have been reported with sensitive, but not selective, responses to condensed vapours [201, 202]. This leads to the rationale that the inter-lamellae space may be considered as pores in which vapours can adsorb, and then in greater concentrations eventually cover the surface area of the ridge-lamellae structure uniformly, with the selectivity component of response being a feature achieved by the interaction of light with vapour and the photonic structure.

To study this effect theoretically, an optical model of a *Morpho*-like ridge-lamellae structure is first developed, and then the optical response of this structure upon a uniform layer of vapour adsorption is considered. During this theoretical study, a number of experimental investigations by collaborators into the selectivity mechanism were being performed simultaneously. Some of their results will be discussed in this chapter to put these theoretical results into the broader context of this collaborative research project.

6.5.1 Optical modelling of *Morpho* vapour responses

6.5.1.1 Developing a model for optical simulations

An optical model was developed to theoretically study the optical effects that arise due to vapour adsorption onto the *Morpho's* iridescent scales. First, a rendered image of a single *Morpho* scale was created from high-resolution TEM images of cross-sections through a *M. sulkowskyi* scale. The ridge in Figure 6.7(a) was chosen because the image has good contrast between the air and cuticle regions. In addition, the ultra-microtoming process used to obtain the cross-section does not appear to cause too much alteration or damage to the lamellae positions or angles. Previous studies have used both optical and electron-microscopy to image *Morpho* structures before and after ultra-microtoming, to ensure the process has not caused significant alteration to the original structure [63]. The image was then traced to create a 2-dimensional representation of the structure. Final steps were taken to smooth small features of the structure in order to reduce the structure complexity, which in turn reduces the computational demands of simulating the structure's electromagnetic response using the Finite Element Method (FEM). These steps in model development are shown in Figure 6.7(b)–(d). The final image, shown in Figure 6.7(d), was then input into commercially available FEM software (Ansys HFSS) to numerically model the reflectance of the ridge-lamellae structure across visible wavelengths.

The ridge-lamellae structure was assigned a complex refractive index of $n^* = 1.56 + 0.06i$, as previously reported in the literature [63]. Vapour adsorption was simulated as monolayer adsorption upon the structure, and assumed not to affect the material properties or optical properties of the cuticle structure. Vapour thicknesses of $t = 5$, 10 and 15 nm were selected based upon literature values [205], and refractive index values of $n = 1.3$, 1.4 and 1.5 were selected for these thin adsorped liquid layers. These values were chosen to approximate the upper and lower values of some common organic and inorganic condensable vapours [280].

Total light reflectance of bare and vapour coated ridge structures was calculated for an infinite array of ridge structures with 700 nm pitch for a planar illumination at normal incidence with the electric field oscillating parallel to the ridges. A single ridge structure without and with uniform vapour coverage is shown in Figure 6.7 (d) and (e), respectively. The reflectance of a bare ridge is shown in Figure 6.8, and has qualitatively the same broad spectral characteristics as the reflectance of the two *Morpho* butterflies shown in Figure 6.1(b). A feature of using this FEM modelling approach, where a unit cell is created and then repeated infinitely using Bloch-expansion methods, are diffractive effects related to the pitch, d, of the unit cell. In this model diffraction effects are observed for diffracted orders $m = 1$ and $m = 2$, as defined by the equation

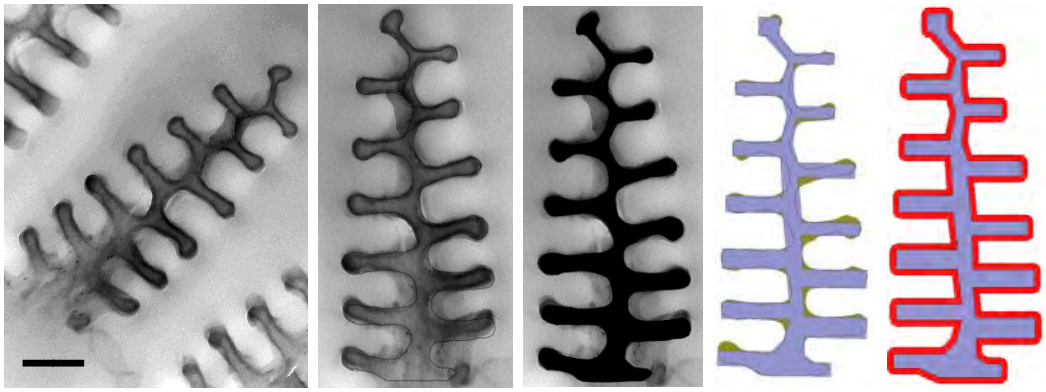

(a) (b) (c) (d) (e)

Figure 6.7: Images showing the development of a model for optical simulations of vapour adsorption: (a) TEM image of a cross-section through a *M. sulkowskyi* ground scale displaying a typical ridge-lamellae structure. (b) The ridge from (a) rotated with a traced outline. (c) Ridge outline with black fill in preparation for import into a binary model. (d) The traced ridge with the rendered image of the structure (blue structure) for input into FEM modelling software. (e) the model ridge structure with a model conformal vapour coating of uniform thickness. [Scale bar: (a) 200 nm].

$m\lambda = d \sin\theta_{\text{inc}}$ (θ_{inc} denotes the angle of incidence), and appear at 350 nm and 700 nm as expected.

6.5.1.2 Uniform vapour adsorption

In order to explain the origin of the reported selective and sensitive vapour response [8] in *Morpho* scales, first the reflectance from the *Morpho* structure upon uniform vapour adsorption upon the whole ridge was investigated.

The calculated reflectance for an uncoated structure and a coated structure with the three thicknesses and three refractive indices, as described in the previous section, is shown in Figure 6.8. Upon vapour adsorption, the reflectance red-shifts in wavelength as observed in the case of wetting. Figure 6.8 demonstrates that this red-shift is dependent on the optical thickness ($n \times t$) of the adsorbed vapour layer; the layer with $t = 5$ nm of $n = 1.3$ shifts far less than the vapour layer with $t = 15$ nm of $n = 1.5$. There is little discernible difference between the spectra of different vapour layers; the general shape is maintained for the optical thicknesses considered.

To compare these simulations to earlier experimental results [8], these spectra are analysed with Principal Components Analysis (PCA). The results of PCA for the uniformly covered *Morpho* nanostructure are presented in Figure 6.9 and Figure 6.10. Figure 6.9(a) shows a PC scores plot for the reference spectra and each vapour condi-

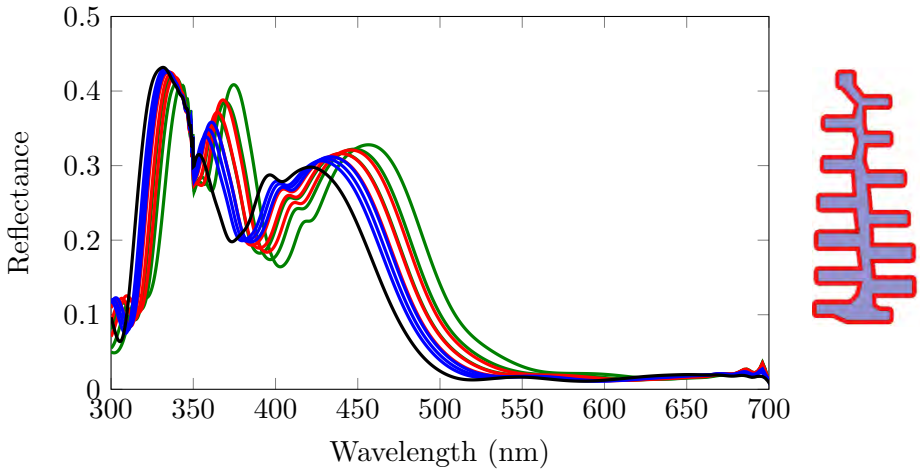

Figure 6.8: Reflectance spectra for uniform adsorption of model vapour upon the *Morpho* nanostructure. The model vapour adsorptions are calculated for refractive index $n = 1.3/1.4/1.5$ and $t = 5$ nm/10 nm/15 nm. The spectral lines are colour coded: reference spectra - black line, 5 nm, 10 nm and 15 nm vapour layers are the blue, red and green lines, respectively.

tion for the first three PCs. These simulated spectra form a track in the PCA space indicating that these vapour conditions do not produce the selective response reported previously in experiments [8]. Although Figure 6.9 shows a PC scores plot of autoscaled spectra, the PC scores plot of mean-centered spectra looked similar. The trajectories for both data preprocessing methods follow the path of increasing optical thickness of adsorbed layer ($n \times t$).

The loadings for PC1 and PC2 are shown in Figures 6.10(a) and 6.10(b) for both preprocessing methods. The percentage of variance captured in the first, second and third Principal Components for mean centered spectra was 84.3%, 13.6% and 1.73%, respectively, and for autoscaled spectra was 69.3%, 25.2% and 4.7%, respectively. The loadings for the mean centered preprocessed model, shown in Figure 6.10(a), indicate that the wavelengths between $\sim$ 325 nm and $\sim$ 500 nm contribute most to the variance in the mean-centered data set. The loadings for the autoscaled preprocessed model, shown in Figure 6.10(b) indicate that the wavelengths between $\sim$ 325 nm and $\sim$ 650 nm contribute to the variance in the autoscaled data set. As expected [281], the loadings from the autoscaled and mean-centered data sets are different.

The single trajectory in PCA space shows the same non-selective response that is observed in porous silicon sensing films, where the optical thickness of the adsorbed layer is responsible for wavelength shifts of the Bragg-wavelength [201]. As part of this collaborative research project, porous silicon samples were fabricated to provide a

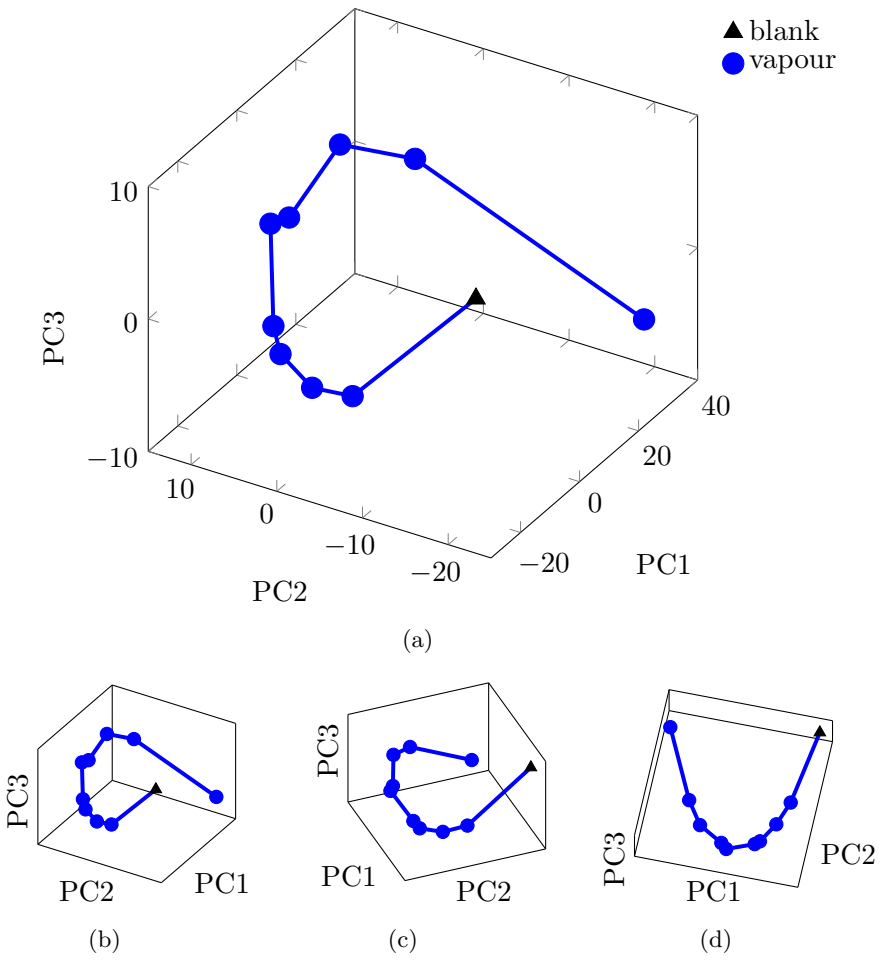

Figure 6.9: PCA scores analysis of calculated reflectance of uniformly covered *Morpho*-ridge structures: (a) PCA scores plot (autoscaled) displaying a single track of points corresponding to simulated reflectance for different model vapour conditions. This track follows increasing values of the adsorbed layer's optical thickness ($n \times t$) indicating a non-selective response between model vapours. Scores plots in (b), (c) and (d) are provided to show different perspectives of this track (shown in (a)) in the 3-dimensional PCA space.

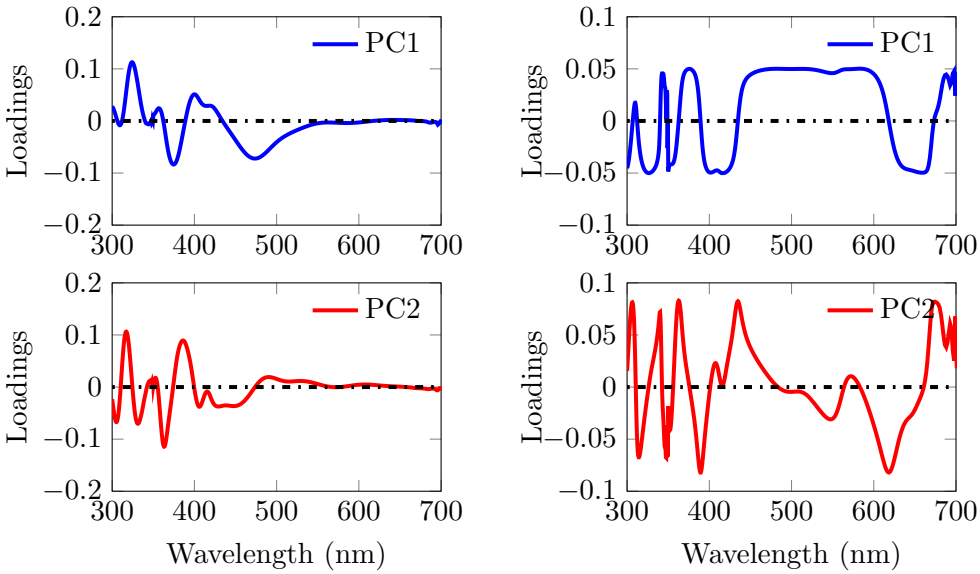

Figure 6.10: PCA loadings data for uniform vapour coverage on the *Morpho* structure: (a) and (b) display of the loadings of PC1 and PC2 for mean-centered and autoscaled processed data, respectively.

benchmark for the vapour responses observed in the *Morpho* scales. Figures B.1(A) and B.1(B) in Appendix B, display the reflectance, and change in reflectance, respectively, upon the exposure of porous silicon to a range of VOCs. PCA analysis of these spectra produce the same $(n \times t)$ track indicating a non-selective response, see Figure B.2 in Appendix B.

In summary, analysis of these simulation results show that the experimentally observed selective-response does not arise solely from the coherent scattering associated with vapour uniformly coated upon the ridge structure.

6.5.1.3 Another adsorption hypothesis

In the pursuit of understanding how selectivity is achieved within a single nanostructure, partners in this project were employing a suite of experimental techniques capable of studying the chemical properties of the iridescent scales [12]. These techniques included TEM characterisation, optical microscopy characterisation and chemical composition analysis. Upon realising that physical adsorption alone was not responsible for the vapour response, these techniques were used to explore the local chemistry within the *Morpho* scales.

First, high-resolution TEM imaging of ridge cross-sections revealed the existence

of an epicuticle surface layer [49, 282] that conformally covers the ridge structure, including lamellae, microribs, and other components, as shown in Figure 6.11(a). Image analysis of this layer found it to be 7 nm ± 2 nm thick (mean ± 1 σ). Earlier studies into the formation of arthropod epicuticle reported the composition of epicuticle to contain a complex mixture of lipid, protein, and polyphenol molecules [282–284], which form during butterfly wing development [285]. Second, the epicuticle chemistry was examined using time-of-flight secondary ion mass spectrometry (ToF-SIMS) and solvent-extraction high-performance liquid chromatography (HPLC) ToF-MS. These techniques found that the epicuticle layer comprises a variety of N-, CH-, O-, and $C_xH_yO_z$- organic fragments that originate from polar and nonpolar compounds. Results of these composition analysis techniques are shown in Figures B.3 and B.4 in Appendix B.

Based on the presence and composition of this conformal epicuticle layer, further experiments were performed to investigate the spatial distribution of the epicuticle chemistry, with particular attention to the distribution of surface polarity, and the scales' responses to vapours of different polarity. Vapour exposure measurements designed to test the scales' optical response to vapours of similar refractive index but different polarity, demonstrated a polarity-dependent response, see Figure B.5 in Appendix B.

Results from these methods provided a new hypothesis for the mechanism of selective vapour response: a vapour may be preferentially adsorbed to different regions of the *Morpho* nanostructure due to the interaction of the chemical environment with vapour polarity.

6.5.1.4 Preferential vapour adsorption

To explore this preferential adsorption hypothesis theoretically, models with three spatial regions of vapour adsorption were considered. A gradient distribution of vapour adsorption was approximated as three regions covering only the top, middle, and bottom portions of the ridge structure (see Figure 6.12). Although simulations were only for three vapours and three spatial regions on the nanostructure, this relative simplicity was sufficient to explore the premise that the vapour selectivity originates from a gradient effect.

The reflectance spectra simulated for these model vapour adsorptions are shown in Figure 6.13. Visually these spectra display a great deal more diversity than those of uniform vapour adsorption. As noted previously, the vapour layers cause the spectra to red-shift, as expected from standard multilayer interference [48]. In addition to a wavelength red-shift, different vapour locations result in discernable alterations in reflectance: first, the vapour on the bottom of the ridge results in smaller spectral

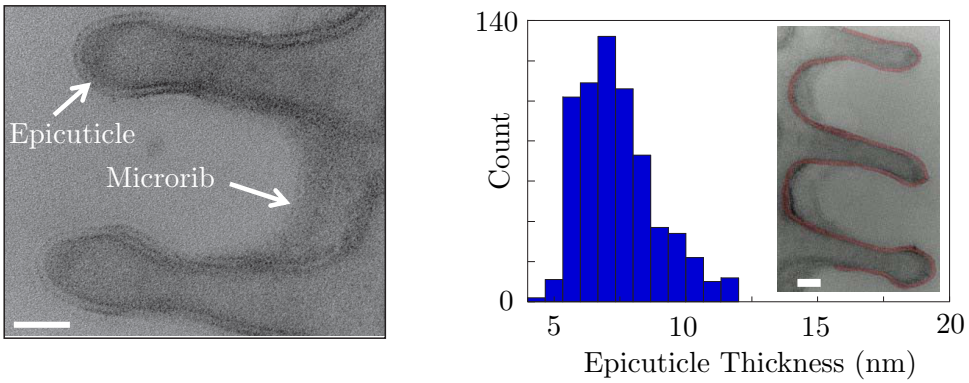

(a) (b)

Figure 6.11: (a) TEM image visualising the conformal epicuticle layer covering the ridge structure, and (b) image analysis of the conformal layer thickness, displaying a 7 nm ± 2 nm layer. This figure is reproduced from Ref. [12] with permission of the Proceedings of the National Academy of Sciences of the USA. [Scale bars: (a) and (b) inset 40 nm].

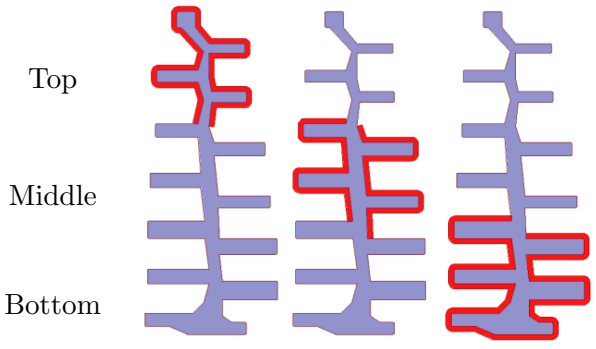

Figure 6.12: Rendered images of modelled adsorbed vapour distribution, with top, middle, and bottom regions, for the 'gradient' adsorption hypothesis of the selectivity mechanism.

shifts than vapour adsorbed on the top. Second, the spectral reflectance profiles are noticeably different for vapour adsorbed onto different spatial regions. Both of these observations arise due to the changes in coherent scattering conditions associated with the spatial position of preferential vapour adsorption: the larger relative change in lamellae layer thickness by the addition of vapour to the top of the ridge structure explains its relative larger visual spectral diversity. The average thickness of the top and bottom vapour covered horizontal lamellae is 40 nm ± 4 nm (mean ± 1 σ) and 60 nm ± 7 nm (mean ± 1 σ), respectively. Thus, a change in the optical thickness of the top layers can be considered to be a larger perturbation to the structure than vapour adsorbed to the bottom layers of the structure. Also, the attenuation of the light through the structure will also reduce the magnitude of the red-shift as observed in the reflectance spectra in Figure 6.13(c).

The results of PCA for the gradient-type vapour covered *Morpho* nanostructure simulations are presented in Figures 6.14 and 6.15. Figure 6.14 shows a PC scores plot for the reference spectrum and each vapour condition for the first three PCs. In contrast to the PCA scores plot for uniform vapour adsorption (Figure 6.9), the projection of points for each spatial location and vapour condition forms three tracks, or arms. Both preprocessing methods reveal three arms in PCA space. Each arm originates from the reference point and extends, as before, to points of increasing adsorbed optical thickness ($n \times t$). Each track arises from each spatial region within the ridge. That is to say, PCA analysis has differentiated the different spatial regions associated with the differences observed in the spectral domain. Therefore, by using this simplistic consideration of preferential vapour adsorption the experimentally observed selective-type vapour response can be reproduced through optical simulations. This provides evidence that preferential vapour adsorption to different spatial regions coupled within the interaction of light with these hierarchical ridge structures allows for the selective transduction of a chemical signal through reflectance measurements.

The loadings for PC1, PC2 and PC3 are shown in Figures 6.15(a) and 6.15(b) for both preprocessing methods. The percentage of variance captured in PC1, PC2 and PC3 for mean centered spectra this was 62.8%, 30.3% and 3.7%, respectively, and for autoscaled spectra was 49.0%, 35.6% and 10.0%, respectively. Comparison of these figures to those of the PCA analysis for the uniformly coated structure shows that the more variance is captured with higher PCs. This greater spread in our PCA space indicates that the gradient-type adsorption has larger spectral diversity than uniform adsorption.

To further compare the modelled optical response of the *Morpho*-like structure to both uniform and gradient type vapour adsorption scenarios, the reflectance datasets may be combined and analysed together. The results of this combined PCA analysis are

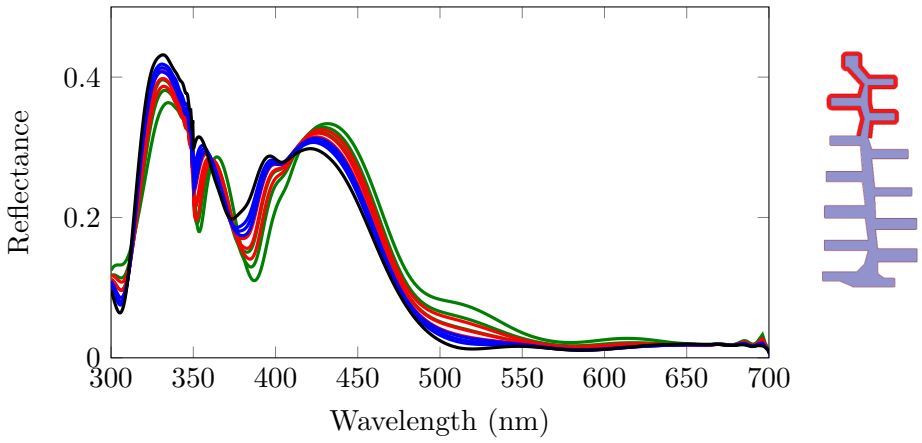

(a)

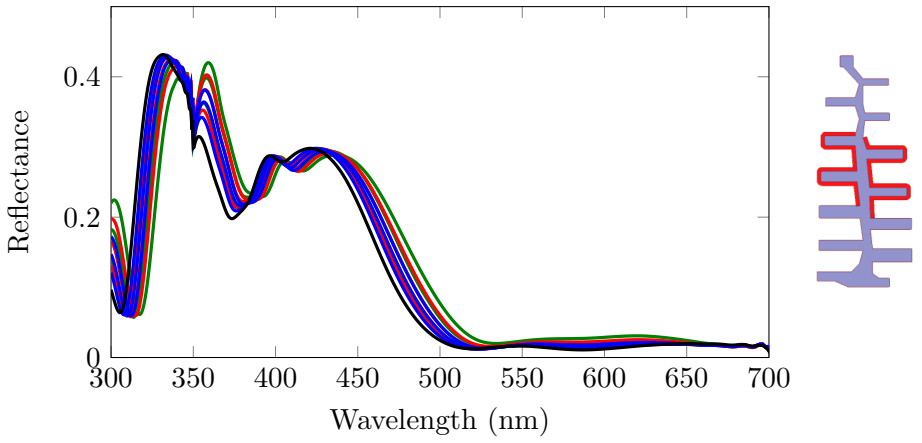

(b)

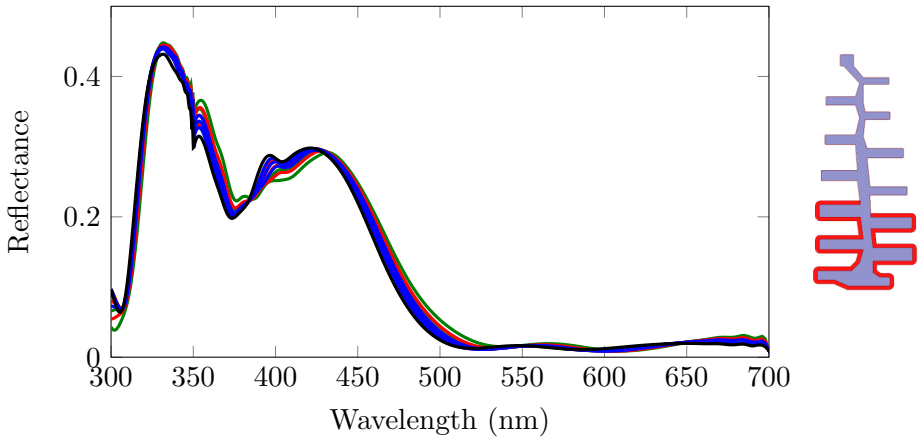

(c)

Figure 6.13: Reflectance spectra arising from different preferential adsorption of model vapour to the *Morpho* nanostructure, for vapour positions located on: (a) top, (b) middle and (c) bottom spatial regions of the ridge, as shown in Figure 6.12. Each set of spectra contains model vapour adsorptions for refractive index $n = 1.3/1.4/1.5$ and $t = 5$ nm/10 nm/15 nm. The spectral lines are colour coded: reference spectrum - black line, 5 nm, 10 nm and 15 nm vapour layers are the blue, red and green lines respectively.

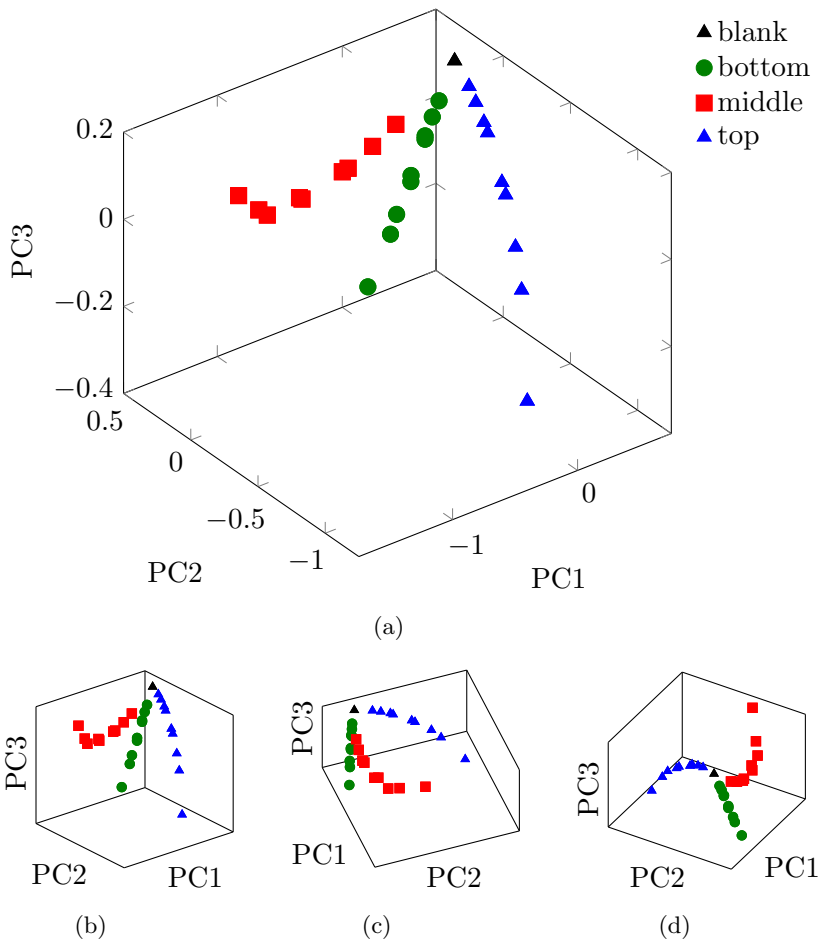

Figure 6.14: PCA analysis of the calculated reflectance from *Morpho* ridge structures with an assumed gradient of vapour adsorption: (a) PCA scores plot (mean-centered) showing a selective response that arises between model vapours coated to the top, middle and bottom spatial regions, as shown in Figure 6.12. Each arm follows the product of optical thickness ($n \times t$) of adsorbed vapour layers. Scores plots in (b), (c) and (d) are provided to show different perspectives of this track in the 3-dimensional PCA space.

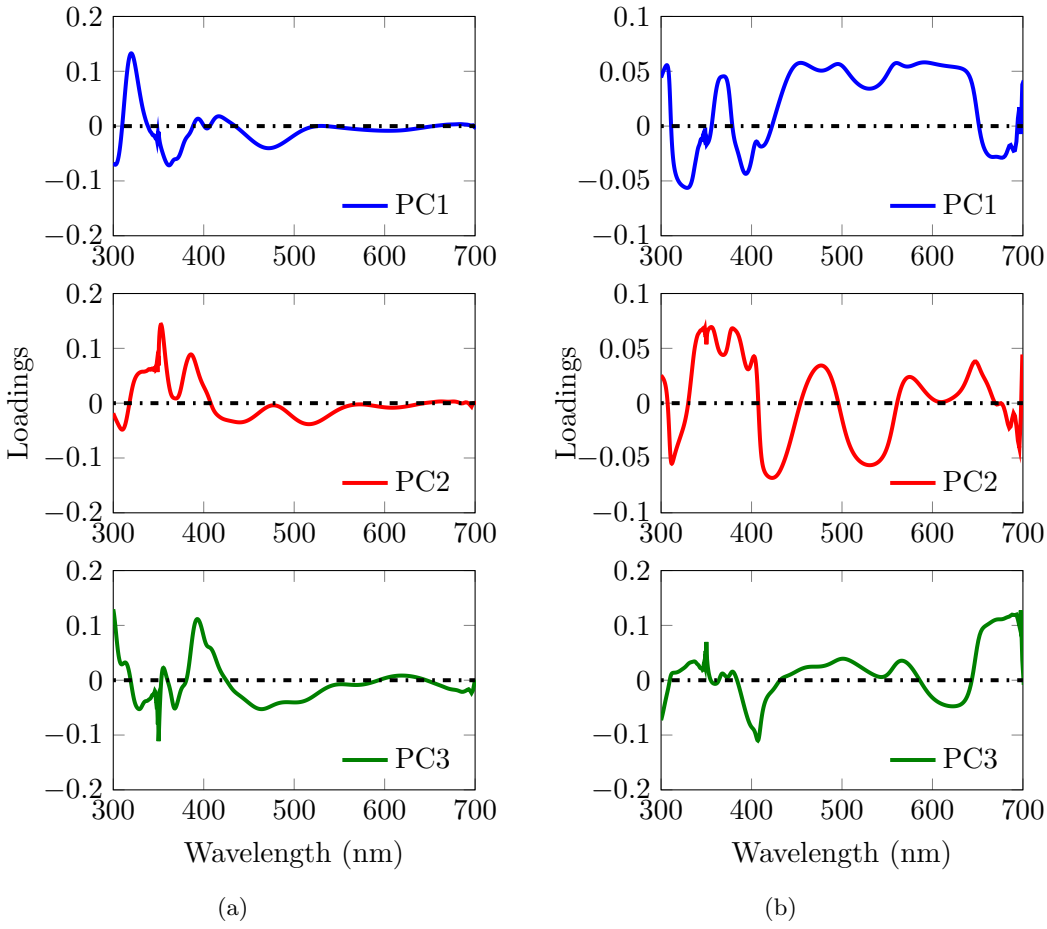

Figure 6.15: PCA loadings data for uniform vapour coverage on the *Morpho* structure: (a) and (b) display of the loadings of PC1, PC2 and PC3 for mean-centered and autoscaled processed data, respectively.

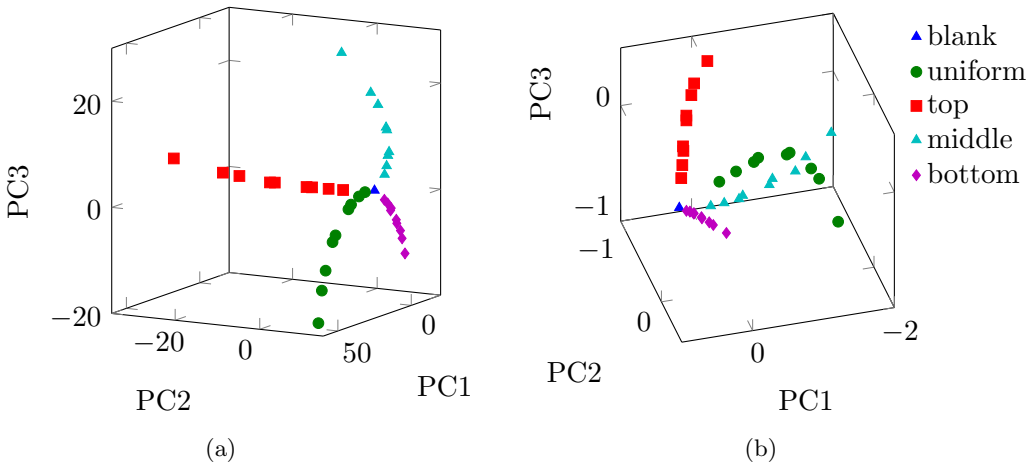

Figure 6.16: PCA scores plots for combined data analysis of uniform and gradient vapour upon the nanostructure: (a) and (b) display autoscaled and mean-centred processed data, respectively. Both preprocessing methods differentiate each different vapour adsorption scenario. The legend represents the different spatial adsorption scenarios shown in Figure 6.7(e) and Figure 6.12.

displayed in Figure 6.16. Both analysis results indicate that each modelled distribution can be differentiated from each other. The relative magnitude of each arm, corresponding to each vapour adsorption condition, is comparable to one another but is not the sum of individual responses. This demonstrates that the uniform vapour adsorption is not a simple convolution of the reflectance from the vapour-covered top, middle and bottom spatial regions of the nanostructure. Instead, the reflectance from each vapour adsorption scenario has sufficiently different specific coherent scattering conditions therefore exhibiting noticeably different spectral responses. These responses' differences are visualised through PCA analysis. In addition, the relative magnitudes of each vapour condition from the blank reference point in PCA space correspond to the relative magnitudes of wavelength red-shifts observed in the reflectance spectra. For the reasons discussed earlier in this section, such as optical absorption and relative lamellae thicknesses, the relative magnitude of the arm corresponding to vapour adsorbed on the bottom regions of the nanostructure is smaller than for vapour adsorbed to the top regions.

This analysis of computed reflectance for uniform vapour adsorption, giving a non-selective vapour response and gradient vapour adsorption which yields a selective vapour response, has similar characteristics to an experimental comparison of a selective and non-selective vapour measurement. In order to benchmark the performance of *Morpho* scales to a known non-selective sensing film, US-based collaborators

on this project performed the same vapour exposure measurements on porous silicon and scales of *M. sulkowskyi*. The PCA analysis of these measurements is displayed in Figure B.2(B), in Appendix B. Experimentally, analysis of the reflectance differentiates different vapours in the PCA space, visualised by different arms with points of increasing vapour concentration. In contrast, the PCA-analysed reflectance from porous silicon, did not differentiate different vapours, which was visualised by data points, representing different vapours and concentrations, forming a single arm.

6.5.2 Experimental evidence of vapour mechanism

By calculating the reflectance of *Morpho*-like nanostructures with assumed preferential adsorption of vapours to three spatial regions, a selective vapour response has been shown. In order to fully understand the mechanism present in the butterfly scales, this theoretical result needs to be considered in the context of further experimental data. In addition to the characterisation of the epicuticle thickness and composition, mapping the spatial distribution of its polarity was identified as a key experiment in order to understand the vapour interaction within the scales. The spatial polarity distribution was first mapped across the tops of the *Morpho* ridges and then mapped down the heights of the ridges, from top to bottom of the ridge.

These experiments were performed by collaborators using fluorescence microscopy to map the spatial polarity distribution of the ridge chemistry using standard fluorescent solvatochromic dyes such as nile red and dicyanomethylene [286]. These dyes' fluorescence emission intensity and peak position are sensitive to solvent polarity. In the fluorescence microscopy experiments the excitation conditions were kept constant whilst the fluorescence peak shifts, that red- or blue- shift in polar or nonpolar environments, respectively, are monitored. This methodology was chosen over measurement of fluorescence intensity because intensity and direction of fluorophore emission can be affected by photonic crystal topography and structure [18, 287]. Fluorescence and reflected light images were collected on an Olympus BX61 microscope using a 100× chromatic aberration-corrected, air-operated, long-focal-length objective with the spatial resolution of 350 nm. Spectra were collected with an attached spectrograph (QE65000; Ocean Optics). The *Morpho* wings were scanned with a 40 nm step size at a 100 nm s^{-1} stage scan rate.

To map the polarity distribution from above the ridge structures, multiple ($n = 4$) $\sim$ 1.7 µm-tall ridges spaced <1 µm apart were scanned using reflected light and fluorescence detection. Reflected light was used to locate the ridge tops based on maximum intensities then fluorescence was used to map the variation in fluorescence peak position from the ridge tops to the areas between the ridges. Figure 6.17 shows

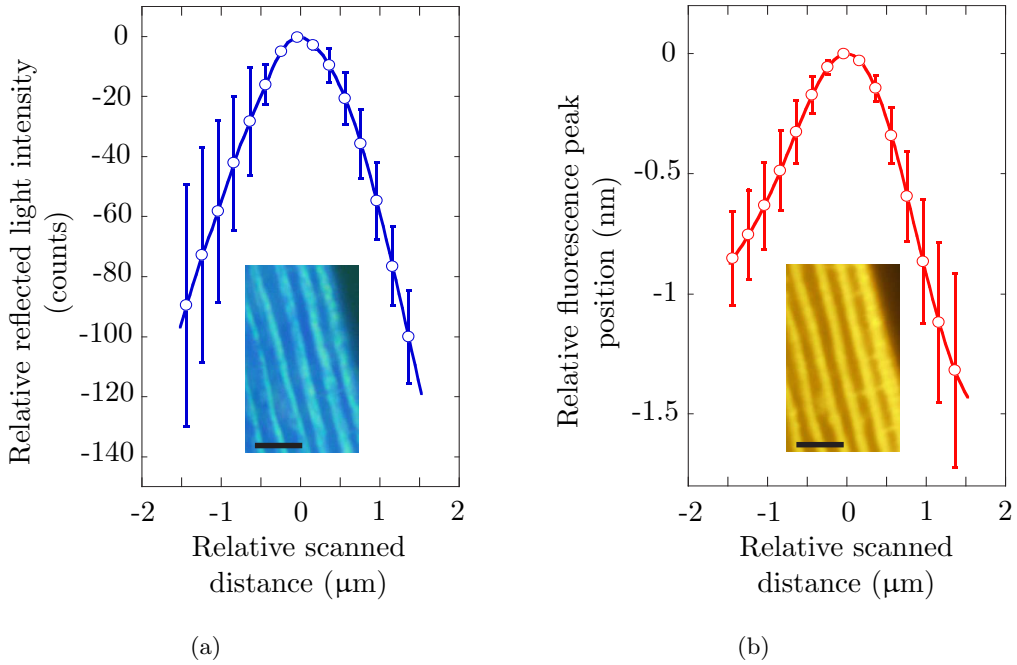

Figure 6.17: Results of across-ridge scanning ($n = 4$) using (a) reflected and (b) fluorescence light, respectively. The ridge top positions were determined based on the maximum intensities of reflected light. The relative polarity of the tops and bottoms of the ridges and of the areas between the ridges was determined based on their fluorescence peak wavelength. Data points in (a) and (b) are the mean values and error bars are 1 σ from measurements across four ridges. Inset images are high-magnification top views of the ridge structure. This figure is reproduced from Ref. [12] with permission of the Proceedings of the National Academy of Sciences of the USA. [Scale bars: (a) and (b) 10 μm].

that the ridge bottoms (inter-ridge spacing) were found to have $\sim$ 1.5 nm blue-shifted fluorescence peak compared with the ridge tops. This indicates that ridge bottoms have a more nonpolar environment compared with the ridge tops.

In addition to mapping the scale ridges from above, the spatial polarity distribution was also mapped down the height of individual ridges. Measurements of the fluorescence peak shift were made before and after a control experiment of oxygen plasma treatment, which can react with various surface groups to reduce the initial surface chemistry [288].

Figure 6.18(a) shows a high-resolution fluorescence optical microscope image of a fluorphore-stained scale cross-section. Figure 6.18(b) demonstrates that the difference in fluorescence peak wavelength between the tops and bottoms of the ridges was significantly removed after the plasma treatment. This indicates significant loss of the initial polarity gradient. Further vapour exposure measurements demonstrate that a mild oxygen plasma treatment changes vapour response selectivity from a response related

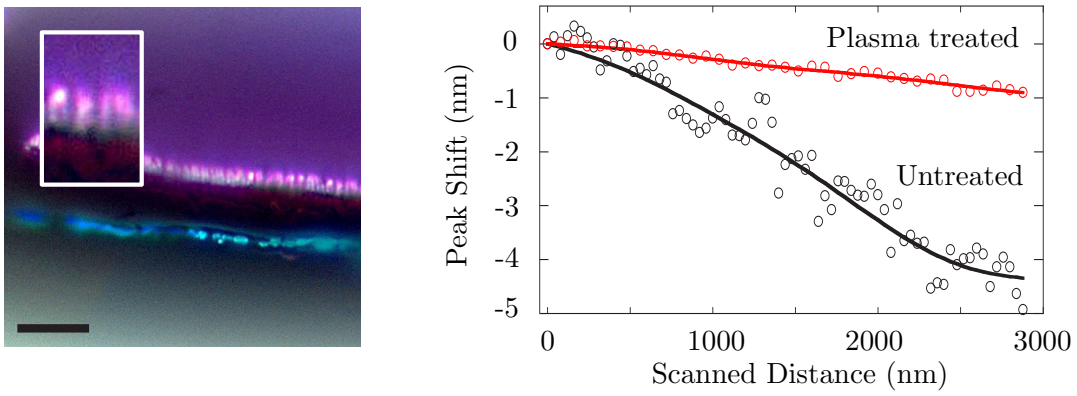

(a) (b)

Figure 6.18: Spatial distribution of polarity of the individual ridges over their heights before and after a mild treatment with oxygen plasma. (a) High magnification fluorescence optical microscopy (cross-section view) of the fluorophore-stained ridge structure on a single butterfly scale. (Inset) Higher resolution image of four individual ridges. (b) Determination of the fluorescence peak shift upon scanning vertically along an individual ridge from the top to the bottom of the ridge before and after 30 sec plasma treatment of the scales. Scan step size = 40 nm. Oxygen plasma was a control experiment to reduce the initial polarity gradient. This figure is reproduced from Ref. [12] with permission of the Proceedings of the National Academy of Sciences of the USA. [Scale bar: (a) 10 µm].

to vapour polarity to a response related to vapour refractive index (see Figure B.6, in Appendix B).

These results provide further evidence to support the hypothesis that vapours can adsorb preferentially to different regions of the *Morpho's* nanostructure, which in turn allows for the transduction of the selective vapour response through changes in reflectance. Further details about the methods and reproducibility of these experiments described in this section are published in Ref. [12].

6.5.3 Origin of the naturally occurring chemical gradient

Having elucidated the mechanism of the vapour response of the *Morpho* wing-scales it remains to discuss the origin of this biologically-formed gradient of surface polarity that runs from the polar ridge tops to the less-polar bottoms. Gradients of different origin in biological materials are known, but rarely with nanopattern features [289–291]. For the observed gradient in the *Morpho* scales, there are several potential origins: (i) variations in spatial patterning in the scale epicuticle during scale formation; such patterning may arise from stresses from elastic buckling of the outer epicuticle to produce the

ridge-lamellae [92], or may arise from propagating molecular signalling to provide local orientation and polarity [292]; (ii) variable subsurface contributions to van der Waals and other surface interactions of the same surface molecules [285, 293]; (iii) active deposition of various molecules by the epidermal cell [291]; and (iv) preferential covering of the cuticle with mobile lipid layers [294] that could accumulate in the narrow spaces on the ridge.

6.6 Conclusions

In this chapter, an investigation into the unusual vapour response of *Morpho* butterflies has been presented. To begin, it was shown that a selective vapour response can be obtained from the scales of *M. rhetenor* in low-concentration vapour exposures. The reproducibility and reversibility of the iridescent scales to ambient humidity was also demonstrated. To investigate the mechanism that causes these observations, two hypotheses of vapour adsorption were explored; the first considered a uniform vapour adsorption to the butterfly's photonic structure, whilst the second assumed the preferential adsorption of vapours adsorbed onto different spatial regions as dictated by the local chemical environment.

Optical models were developed to study the resulting optical response from these different vapour adsorptions. Vapour layers of different thicknesses and refractive indices were chosen to simulate the effects of different concentrations and vapour species. These results were then coupled with a variety of experimental techniques, performed by collaborators, to study this mechanism using a number of approaches. Finally, by using this arsenal of techniques to test, challenge and validate the existence of the localised adsorption of vapours onto the chemically-graded surface of the *Morpho* nanostructures, a likely mechanism for the selective vapour response has been identified. That is, a gradient of surface polarity, from the more-polar ridge tops down to their less-polar bottoms, that causes the preferential adsorption of individual vapours with different polarity onto the different spatial regions of the nanostructured ridge. To conclude, a number of suggestions were made as to how such a chemical gradient may form. Figure 6.19 displays a schematic of this proposed mechanism that arises through the combined physical and chemical properties of the *Morpho* scales.

The appreciation of the role of chemical gradients in photonic nanostructures opens opportunities for new design principles of gas and liquid sensors with tailored selectivity in a single sensing unit, rather than with individually fabricated and multiplexed sensors, as discussed in Chapter 4. The ability to transduce multiple vapours by using a single measurement of a nanostructured array offers a number of potential advantages over sensor arrays, such as a reduced number of noise sources, more predictable sensor

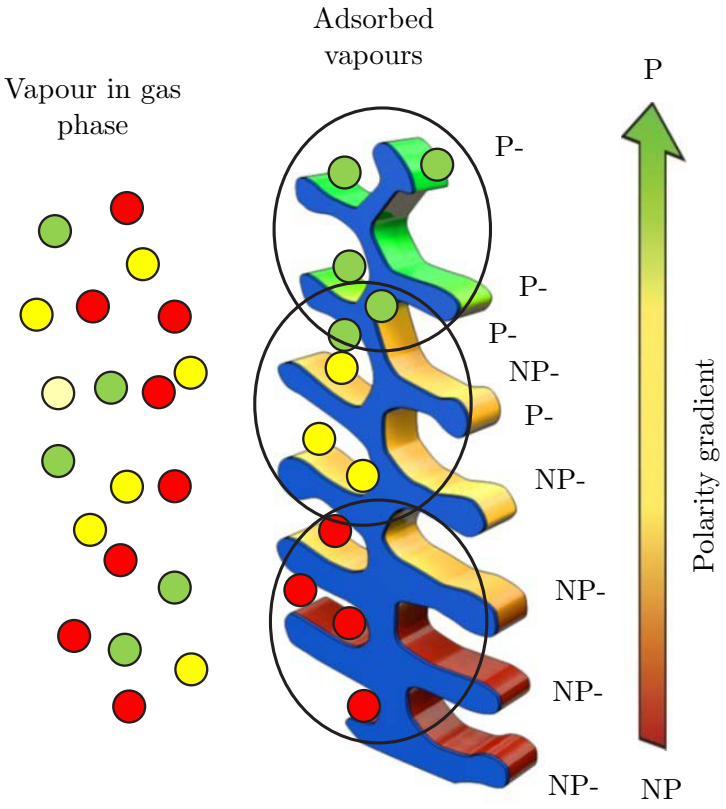

Figure 6.19: The mechanism of the selective response of *Morpho* butterfly scales to different vapours. The gradient of the surface polarity of the ridges runs from the most-polar ridge tops down to the less-polar ridge bottoms, which facilitates the preferential adsorption of vapour molecules of different polarity onto the respective regions of the photonic ridge structure. 'P' denotes chemically polar regions, and 'NP' denotes nonpolar regions. This figure is reproduced from Ref. [12] with permission of the Proceedings of the National Academy of Sciences of the USA.

ageing, and simplified packaging. These design principles present a major departure from existing approaches to sensing [295] and are related to multivariable sensors, where an individual sensor has several partially or fully independent responses [8, 274].

Results of this study could also promote significant selectivity advancements in photonic sensors based on traditional sensing materials that were discussed in Chapter 4 through the functionalisation of surface chemistry. Examples of these materials include porous silicon [201], opal structures [205], inverse opal structures [200], and others based on nanotemplated [296–298] and nanofabricated [299, 300] structures that mimic butterfly scales. Photonic sensors based on these traditional sensing materials can be upgraded with designs that promote their multivariable response.

This study can be viewed as a step in moving from the first report of the unusual vapour selectivity of *Morpho* butterflies, towards new methodologies for selective vapour sensing using chemically graded photonic nanostructures. This multivariable sensor concept should be useful for detection of multiple anticipated targeted vapours in the presence of complex backgrounds, including unknown interferences using nanofabricated bio-inspired structures. In Chapter 7, other features of this vapour response in *Morpho* butterflies are theoretically and experimentally explored, before later moving these results towards ideas for synthetic sensors in Chapter 8.

Chapter 7

High-Performance Sensing using *Morpho* Scales

7.1 Introduction

In this chapter, further aspects of the optical responses that arise upon the exposure of *Morpho* butterfly scales to low concentrations of chemical vapours are discussed. The results build on the work presented in Potyrailo *et al.* 2007 [8] and in Chapter 6.

To begin, three different aspects of the vapour response of the *Morpho* scales, which demonstrate why this biological photonic structure is interesting from a high-performance sensing perspective, are described. These response attributes are the diversity in temporal, angle and polarisation dependence of scattered light to changes of the wing-scale's chemical environment. Following this, the vapour response for two different measurement conditions are presented and compared. Finally, the *Morpho* scales are subjected to investigations designed to assess whether they could be modified chemically or functionalised to enhance their vapour response.

The work presented in this chapter was undertaken in collaboration with researchers at General Electric Global Research Center (Niskayuna, NY, USA) and the Air Force Research Laboratory (Wright-Patterson Air Force Base, OH, USA). These results have either been published or are being prepared for publication; this has been indicated at the start of the relevant sections.

7.2 Diversity in optical response

The results on the fundamentals of the interactions of vapours with biological photonic nanostructures described by Potyrailo *et al.* 2007 [8] and in Chapter 6 have critical importance due to the possibility with which they may enhance vapour selectivity

of existing sensors. Further lessons can be learnt from those interactions of vapours with the *Morpho* scales, and also from the spectral features that arise upon vapour adsorption, and the diversity associated with the resulting spectral responses.

In this section, the diverse features of the optical response from the scales of *Morpho* are discussed. Namely, these are the spectral and temporal profiles, and the angular- and polarisation-dependence of vapour-induced optical features. To begin, the experimental methods and the theoretical model used to study the responses are outlined. Following this, the diverse series of reflectance signatures are presented. Finally, the significance of these results are summarised.

The biological template in the *Morpho* scales, used here as bio-inspiration, is formed through physical and chemical processes. Each scale is formed by a single epithelial cell that secretes the outer epicuticle and the inner layers of cuticle to form lattices, pillars, and other internal scale structures. Mechanisms to shape these fine features may include surface tension and elastic buckling [91]. As discussed in Chapter 6, coherent scattering of light from *Morpho* scales [63] arises from the cooperation of regularity and irregularity of the photonic structure within a scale [301]. Imaging of the *Morpho* scales, using scanning electron microscopy, visualises an anisotropic structure of parallel ridges with their slanting lamellae, as well as microribs normal to the lamellae, and cross-ribs visible between the ridges, as described in Section 2.5 (see Figure 6.2). The reflectance for different polarisations and at different angular excitations is strongly affected by the geometric anisotropy of the structure in the wing scales. Therefore, it follows that these geometric properties, with the chemical properties previously described (in Chapter 6), might also strongly influence the diversity of optical response when comparing polarisations or different illumination angles. To study these effects in the *Morpho* scales vapour exposures and FDTD simulations are used.

The work presented in this section was undertaken in collaboration with researchers at General Electric Global Research Center (Niskayuna, NY, USA), and is being prepared for publication in a manuscript titled 'Multivariable signal transduction in photonic nanostructures of *Morpho* butterfly scales for high-performance vapor sensing'.

7.2.1 Experimental measurements

To perform vapour exposures, the bubbler system, described in Section 5.1.3, was used. Generated vapours were flowed with a 450-mL/min total flow rate from a 1/8-inch-diameter tube onto the butterfly wing at an angle of approximately 45 degrees to the surface. The vapour flow was orientated to flow along the ridges of the photonic structure. The change in reflectance, ΔR, upon vapour exposure was measured as $\Delta R(\%) = ((R/R_0) - 1) \times 100\%$, as described in Section 5.1. Ten vapours were gen-

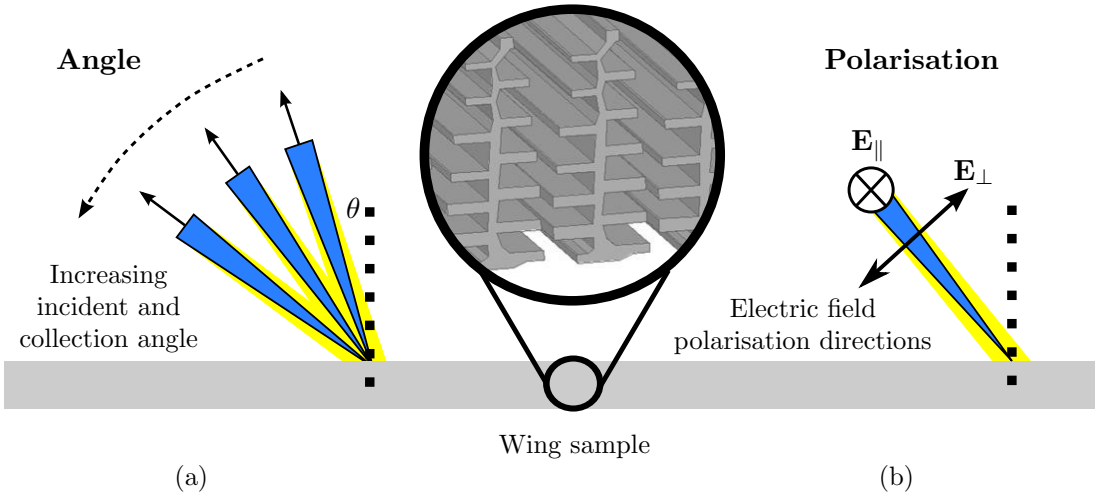

Figure 7.1: Diagram of experimental arrangement for the illumination and the measurement of scattered light, using a bifurcated probe, for; (a) different angles of incidence, and (b) two linear polarisations of scattered light, from *Morpho* scales. The *Morpho* ridge-lamellae schematic illustrates the orientation of the scale w.r.t. the changes of angle and polarisation.

erated to explore the effects from a range of volatile molecules. These vapours were: (1) water, (2) ethanol, (3) 1-methoxy-2-propanol, (4) methyl ethyl ketone, (5) acetonitrile, (6) toluene, (7) chloroform, (8) tetrahydrofuran, (9) dimethylformamide, and (10) acetone.

To perform the optical measurements, one bifurcated probe was used to illuminate (using a halogen light source), and to record (using a fibre-optic spectrograph) the reflectance from the scales of *M. sulkowskyi*. The angle, θ, of the illumination/backscatter-reflectance probe was varied from the normal to investigate different illumination/collection angles. A $\sim$ 2 mm diameter beam spot illuminated the scale. The schematic in Figure 7.1(a) depicts the orientation of the probe with respect to the ridges that run the length of the butterfly's scales. To measure two different linear polarisations, the probes were modified to incorporate Glan-Thompson calcite polarising filters. Figure 7.1(b) displays the directions in which the electric field was polarised; these were $\mathrm{E}_{\parallel}$, where the electric field is polarised to oscillate along the structure's ridge, and $\mathrm{E}_{\perp}$, where the electric field is polarised perpendicular to the ridge (defined at normal incidence).

7.2.2 Theoretical model

FDTD simulations were performed to theoretically explore the responses observed experimentally. This methodology was chosen for flexibility in modelling the specific

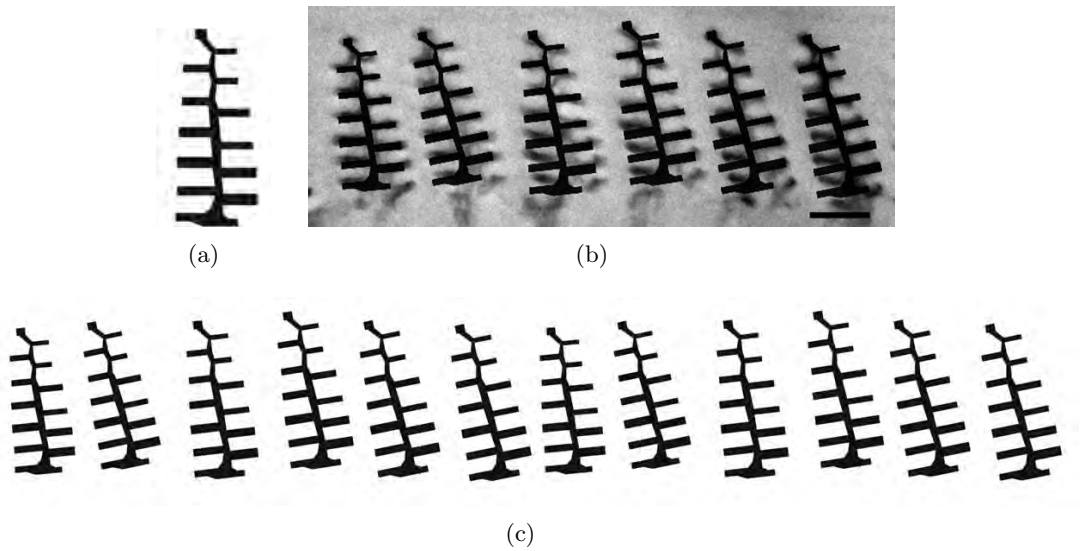

Figure 7.2: Images used to develop an optical model for simulation with the FDTD technique: (a) A single *Morpho*-like tree structure, (b) TEM image (courtesy of R. A. Potyrailo) of a cross-section through a *M. sulkowskyi* scale with the tree from (a) overlayed, and (c) the final rendered twelve-tree structure for FDTD simulations. [Scale bar: (b) 500 nm].

angular and polarisation illumination and detection conditions of the experimental set-up. A model was developed to approximate that of the *Morpho* structure. By using the model tree structure previously considered (in Section 6.5.1.1), shown in Figure 7.2(a), a rendered binary image was generated, consisting of twelve 'tree'-like structures, that could be imported into FDTD software. This was done by overlaying the model *Morpho* tree-like structure upon the TEM in Figure 7.2, which displays a cross-section through a scale from *M. sulkowskyi* showing six 'tree'-like units. The orientation angles of each overlayed tree, and its relative size and aspect ratio were adjusted to match those trees in the TEM image more closely. Once this was rendered, it was repeated to form a model comprising twelve tree units, as shown in Figure 7.2(c). This method was chosen to incorporate some of the inherent randomness and 'biological noise' [55] associated with the scale structure into the optical model.

The optical response was calculated using Lumerical's 'FDTD Solutions' package. The binary image of the *Morpho*-like structure was imported as a 2D object and assigned the optical constants reported previously in the literature [63]. The structure was enclosed by a Total-Field Scattered-Field (TFSF) boundary, and a plane wave excitation was used to illuminate the structure with a wavepacket containing visible wavelengths. The TFSF boundary treats the rendered *Morpho* structure as a non-periodic

(finite) sample, from which the light scattered from the object can be computed. To calculate the angle-resolved scatter from the structure, near- to far-field projections were calculated to produce wavelength and angle-resolved electric field information. This was used to compute the components of light back-scattered over a solid angle toward the illumination direction, to mimic the physical measurement conditions.

7.2.3 Spectral diversity in vapour response

To evaluate the *Morpho* scale's response to vapours further, beyond the responses already presented, the scales of *M. sulkowskyi* were exposed to ten model vapours. These vapours were: (1) water, (2) ethanol, (3) 1-methoxy-2-propanol, (4) methyl ethyl ketone, (5) acetonitrile, (6) toluene, (7) chloroform, (8) tetrahydrofuran, (9) dimethylformamide, and (10) acetone. The differential reflectance and the PCA analysis of the *Morpho* scales' response to ten vapours is shown in Figures 7.3(a) and 7.3(b), respectively. These measurements (each performed at a single concentration for each vapour) show very encouraging results in discriminating five out of ten vapours without any modification to the scales. In Figure 7.3(b) the most distinct points in the PCA scores space correspond to vapours; (1) water, (2) ethanol, (4) methyl ethyl ketone, (5) acetonitrile and (10) acetone. Interestingly, these vapours do not all have the largest values of refractive index, indicating that other factors affect the resulting optical response.

Using the knowledge that local chemical effects provide a mechanism for the selective responses of these scales, simulations were used to investigate this diversity of spectral response. FDTD simulations of different spatial vapour adsorptions, for vapour of a single refractive index ($n = 1.4$), were performed to confirm theoretically whether or not a diverse spectral response is observed. For these simulations six vapour adsorptions were simulated on the outer surface of the rendered *Morpho*-like structure in Figure 7.2(c). These model adsorptions are shown in Figure 7.4(a). The first three are localised adsorption upon the top, the middle and then the bottom of the tree-like structure. The last three adsorptions are over the whole structure; one has a uniform thickness, the other two are different gradient vapour adsorptions - one thick at the top (TT), the other thick at the bottom (BT) of the nanostructure.

The computed differential reflectance of these structures, with vapour overlayers is shown in Figure 7.4(b). These model vapour adsorptions produce visually diverse spectra and have different relative magnitudes. The vapour adsorptions that coat the whole of the ridge structure produce the largest changes in magnitude. When comparing the modelled differential spectra (Figure 7.4(b)) to the measured spectra (Figure 7.3(a)), there is a general agreement with the spectral positions of the positive changes in the spectrum, but the agreement is poor at lower wavelengths, where there

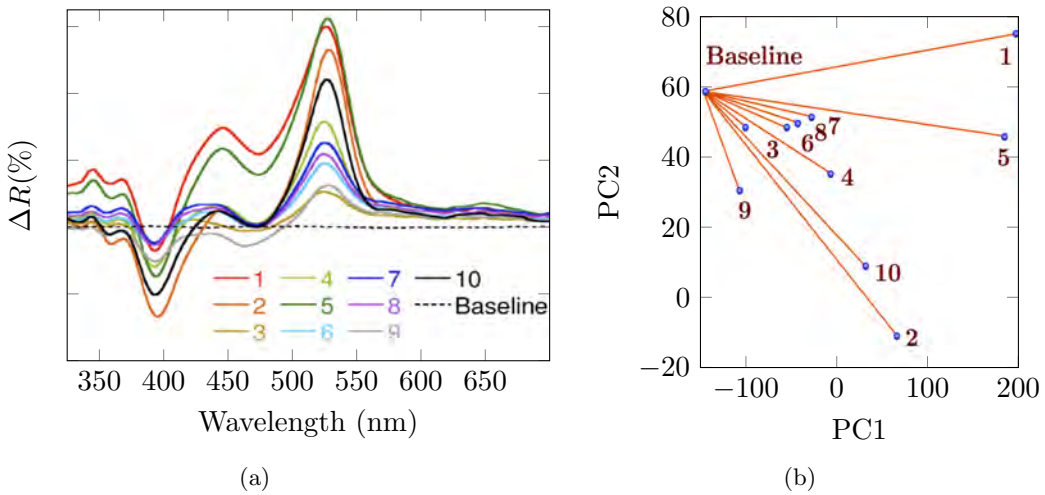

Figure 7.3: Results of the spectral analysis of response of the *Morpho* structure to ten vapours, when measured with a bifurcated probe angled at 45 degrees from the normal: (a) Differential reflectance spectra for ten vapours and baseline. (b) Scores plot of PCA model. Vapours: (1) water, (2) ethanol, (3) 1-methoxy-2-propanol, (4) methyl ethyl ketone, (5) acetonitrile, (6) toluene, (7) chloroform, (8) tetrahydrofuran, (9) dimethylformamide, and (10) acetone.

is no strong negative feature, as visualised in the experimental data. This discrepancy between datasets is attributed to differences in the approximation to the structure measured and simulated – there is often some small variation within species related to the maturity of the samples. For instance, the FDTD simulation displays a very close likeness, particularly the three vapour adsorptions with full coverage, to the differential reflectance spectra displayed in measurements on the scales of *M. rhetenor*, shown in Figure 7.12.

7.2.4 Temporal-dependence of vapour response

To understand the *Morpho* scale-vapour interactions further, the dynamic responses to ten vapours, at the same concentration, was examined. Figure 7.5 displays the temporal responses of the differential reflectance, at five fixed wavelengths, when vapour is flowed for a short 9 second cycle. To begin, the scales are subject to a dry carrier gas. As the vapour is then flowed there is an immediate response in the optical signal, followed by recovery, which begins when the vapour flow is stopped.

From the temporal responses in Figure 7.5 a number of observations in the diversity of response can be made. For instance, consider the pronounced differences in dynamic responses between vapours of water (vapour 1), ethanol (vapour 2), and acetone (vapour

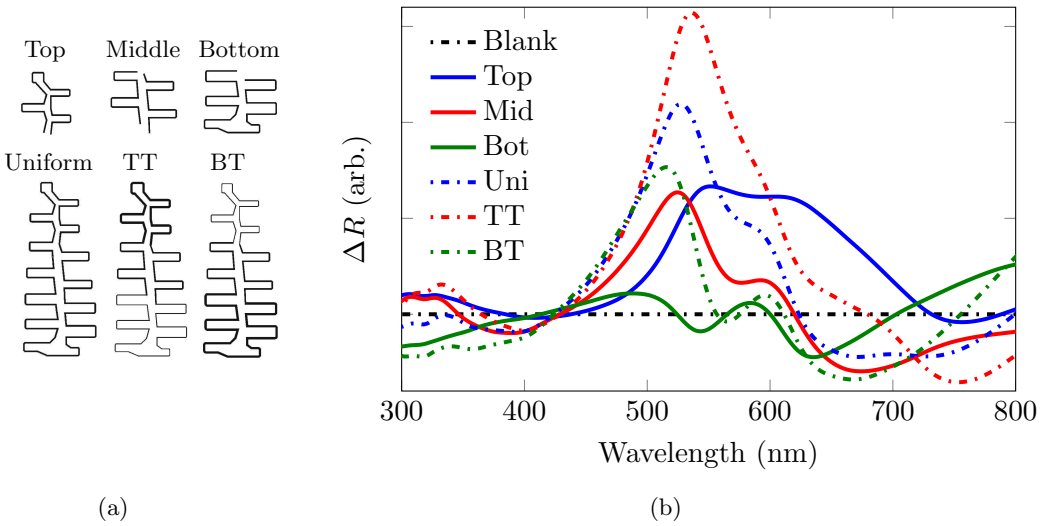

(a) (b)

Figure 7.4: Theoretical demonstration of spectral diversity of *Morpho* scales response to different model vapour adsorptions: (a) Schematic of six vapour adsorptions for FDTD simulations. Model adsorption is an approximately 10 nm uniform coverage for top, middle, bottom and uniform vapour scenarios; the gradient adsorptions have thicknesses from 5 nm to 15 nm along the height of the ridge. (b) Differential reflectance computed for the vapour conditions in (a).

5). The response to water vapour has approximately similar profiles at different wavelengths; this is something not seen for the other vapours, where quite diverse changes in the ΔR signal are observed. At the largest wavelength, 520 nm, the optical response, associated with the adsorption process, for three vapours has a step-like appearance, whilst the other vapours display a more gradual increase in the differential reflectance. At shorter wavelengths the dissimilarities in both the dynamic response and recovery profiles for different wavelengths are pronounced. Some vapours, for instance water (vapour 1) and methyl ethyl ketone (vapour 4), have wavelengths that either have positive and negative changes (i.e. rise above or fall below $\Delta R = 100\%$) in the ΔR signal for the duration of the exposure. However, the shorter wavelengths during ethanol (vapour 2) and acetone (vapour 5) exposures change ΔR response direction during the exposure.

The temporal changes observed imply dynamic changes in the distribution of vapour on the photonic structure with an increasing uptake of vapour molecules. These spectral and dynamic differences also lead to a hypothesis that scale regions of different spatial periodicity (ridges, lamellae, ribs, microribs, etc.) may individually contribute to the total spectral response at different wavelengths. As in previously studied artificial photonic structures [302], the smaller the spatial periodicity or size of the photonic

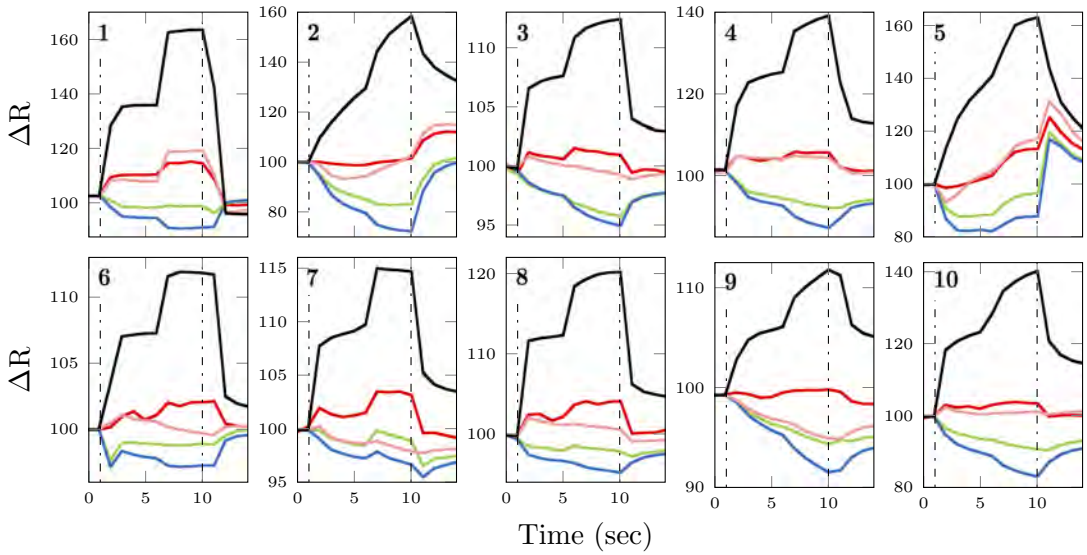

Figure 7.5: Temporal response of *Morpho* scales to ten model vapours at five selected wavelengths. The inset numbers correspond to vapours: (1) water, (2) ethanol, (3) 1-methoxy-2-propanol, (4) methyl ethyl ketone, (5) acetonitrile, (6) toluene, (7) chloroform, (8) tetrahydrofuran, (9) dimethylformamide, and (10) acetone. Wavelengths plotted: 344 nm – red, 380 nm – green, 390 nm – blue, 470 nm – pink, and 520 nm – black. The dashed lines indicate the beginning and then the end of a single vapour exposure cycle.

substructure, the shorter the response wavelengths. This diverse spectral response was due to combined action of two mechanisms, physisorption and capillary condensation of condensable vapours in the nanosize domains of the *Morpho* scales. Similar vapour adsorption mechanisms were observed in porous silicon [302–304] but the vapour measurements revealed a lack of selectivity in response.

7.2.5 Polarisation-dependence of vapour response

Encouraged by the results on spectral and temporal diversity, the polarisation-dependent changes in reflectance of the *Morpho* structure upon exposure to different vapours were explored further. As stated in the introduction to this section, the *Morpho* scales have an anisotropy in their geometry. A feature that is commonly used to define the orientation of the scale is the ridge, which runs from the socket to the distal end of the scale. This structural anisotropy causes a significant difference in the reflectance for different linear polarisations of incident light, and has been reported in a number of both experimental and theoretical *Morpho*-specific studies [104, 106, 114]. In this section, the polarisation states are defined with respect to the ridging, as shown in Figure 7.1(b).

The measured and calculated reflectance spectra for parallel ($E_{\parallel}$) and perpendicular

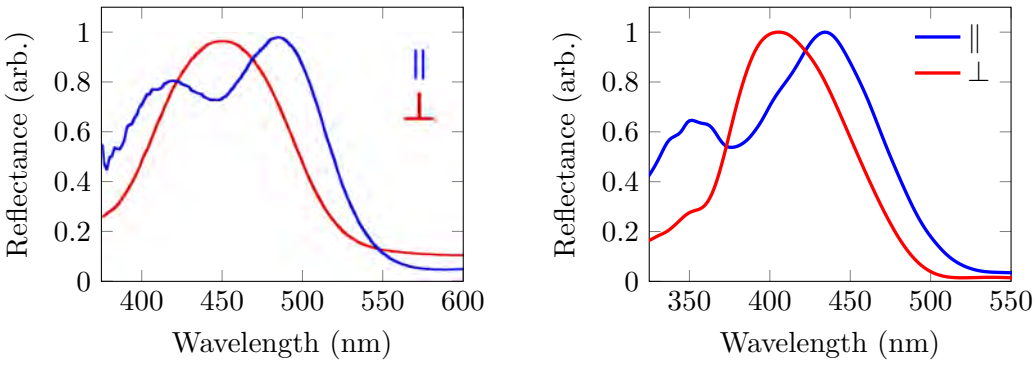

Figure 7.6: Comparison of: (a) measured, and (b) calculated reflectance from the *Morpho* scales when illuminated with two linear polarisations. The spectral shapes of the reflectance display the characteristic single and double peaks associated with the electric field polarised perpendicular ($\perp$) and parallel ($\parallel$) to the ridge direction, respectively.

($E_\perp$) polarisations, from the *M. sulkowskyi* scales and FDTD simulations are shown in Figure 7.6. The experimental and simulated results have several closely related spectral features. These are the single and double peaks observed for perpendicular and parallel polarisations, respectively. These spectral shapes are a characteristic of the reflectance from the ridge structure in *Morpho*, and have been presented in several experimental and theoretical polarisation-resolved spectra in many *Morphos* [63, 98, 104, 106]. These spectral features between polarisation occur approximately at the same relative wavelengths apart, although the simulation results are all approximately shifted by approximately −50 nm. Despite this spectral shift, which may arise from the reasons described earlier, namely differences within species and in the same butterfly, the model can be used to explore the polarisation effects in the scales.

The polarisation response of the *Morpho* structures to different vapours displays further diversity in the dynamic responses. An example of the response to increasing concentrations of one of the model vapours, acetonitrile, is presented as the differential reflectance at several wavelengths in Figure 7.7. The responses in this dataset display several interesting dynamic features: first, with the increase of the concentrations of the vapour, the complexity of the dynamic response signature increases. For example, at wavelengths of 410, 440, and 480 nm, an 'overshoot' of the response past the baseline signal (of carrier gas) occurs following the acetonitrile vapour exposure. This overshoot has a relatively long response time constant, and is observed at both polarisations at the three largest vapour concentrations. At 520 nm, this overshoot-type response was not

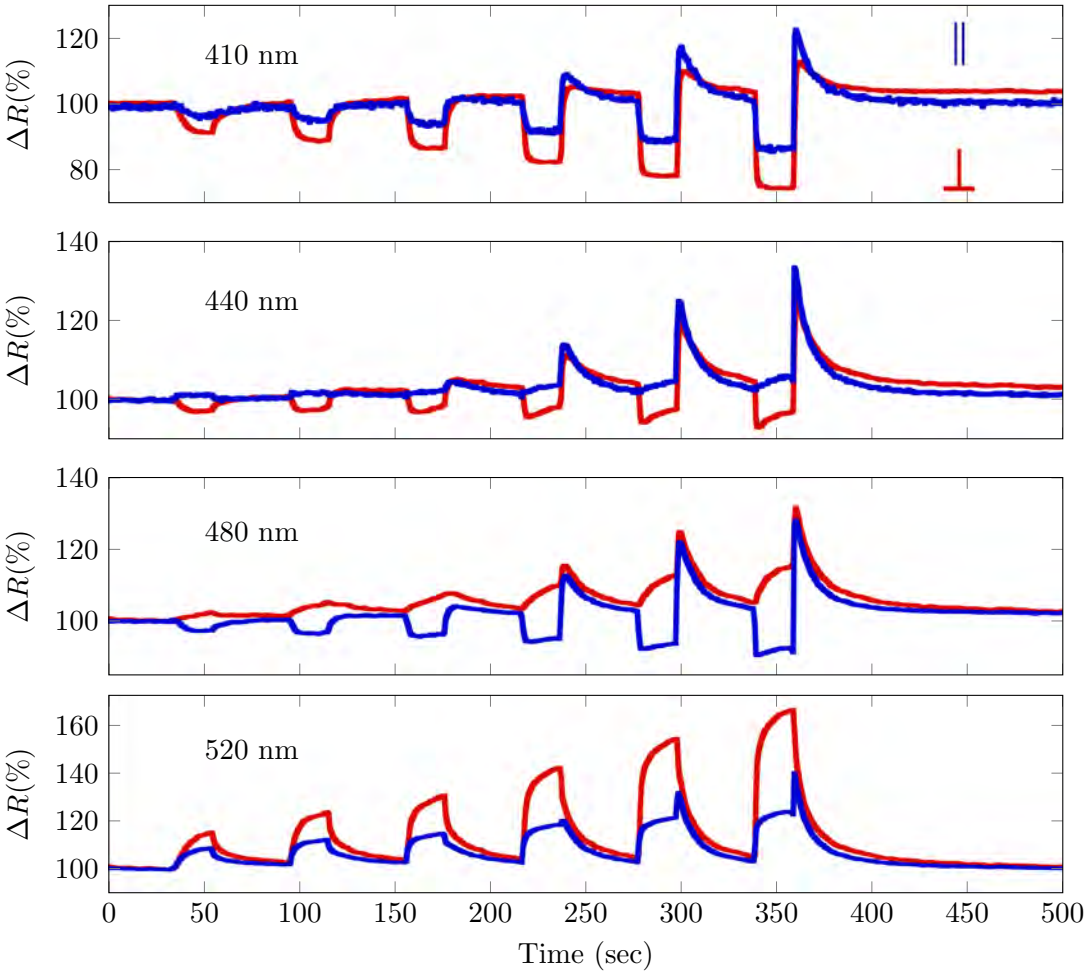

Figure 7.7: Experimental dynamic differential reflectance profiles, at wavelengths 410 nm, 440 nm, 480 nm and 520 nm, for acetonitrile vapour exposures on the *Morpho* scales probed with two linear polarisations. Acetonitrile concentrations increases between each exposure. Red lines indicate incident light with electric field polarised perpendicular ($\perp$) to the ridge. Blue lines indicate incident light with electric field polarised parallel ($\parallel$) to the ridge.

observed, instead a rapid increase of the ΔR signal for parallel polarisation is observed with a very short time constant. Second, response times for the two polarisations were in general, quite different with an exception of the depicted response at 410 nm. For example, responses at 480 and 520 nm under illumination of perpendicular polarised light were much slower when compared to the responses under the parallel polarised excitation. Third, the relative response direction under the parallel and perpendicular excitation conditions was opposite at certain wavelengths, for example at 480 nm, while it was the same at other wavelengths. These experimental results demonstrate the significant diversity of the probed regions of the *Morpho* nanostructure with polarised light. Such diversity is the key for the construction of the next generation vapour sensors with enhanced selectivity of their vapour response.

To explore the fundamental mechanism of some of these experimental observations, the vapour responses of the *Morpho*-like structure were further computed using the FDTD methodology. The dynamic differences, observed between polarisation states, strongly suggest that the electromagnetic field of the probing radiation interacts with the vapour adsorbed within the photonic nanostructure differently. To examine this, the electromagnetic field distributions that arise upon excitation of the *Morpho* structure for the parallel and perpendicular polarisations were calculated for wavelengths of 360, 400 and 440 nm. These wavelengths were chosen as they correspond to the same wavelength range displayed in Figure 7.7, when the spectral shift between the main features in the measured and the modelled spectra are accounted for. By using the electromagnetic fields, the time-averaged power distributions were calculated. Figure 7.8 displays these power intensity distributions at three wavelengths for both polarisations.

These intensity maps demonstrate two key aspects relating to the diversity of polarisation responses: first, at some wavelengths the interaction of the probe radiation (of different polarisations) had high power density in different portions of the nanostructure. In Figure 7.8, the power distribution calculated for 360 nm shows little power in the photonic structure for parallel polarised light, but for perpendicular polarised light the power density in the inter-lamella areas is much greater down the length of the ridge structure. Second, at other wavelengths the power densities have essentially the same distributions; this is seen in the intensity maps for 440 nm, where the regions of high energy occur in approximately the same spatial locations.

The different power distributions clearly show that parallel and perpendicular polarisations interact with the structure differently. This provides an explanation as to why different polarisations show different temporal behaviours in experimental measurements. For instance, if one polarisation responds more rapidly to a vapour cycle (relative to the other orthogonal polarisation) this implies that it is not sensitive to

the region in which the vapour is adsorbed. Very importantly, these results also illustrate that particular polarisations maybe more sensitive to particular spatial vapour adsorptions.

7.2.6 Angle-dependence of vapour response

The angle-dependence of the vapour responses presents interesting spectral reflectance responses. To examine the dependence the angle of the illumination and detection (shown in Figure 7.1(b)), was varied, and vapour exposures performed. By varying the angular measurement conditions, the spectral-selectivity pattern measured for different vapours, was seen to be enhanced when viewing the differential reflectance spectral profile at larger angles. Figure 7.9 illustrates that upon a small angle illumination and detection, ($\sim 20^{o}$), the diversity of spectral response to water, chloroform, and dimethylformamide is minimal: all spectral responses have a distinct negative and a distinct positive peak in ΔR at wavelengths 400 nm and 525 nm, respectively, and also share other smaller spectral features.

At larger incident angles diversity between vapours becomes more pronounced, with spectral diversity increasing upon an increase of the illumination angle to 40^{o} and 60^{o}. At the largest angle of incidence, 60^{o}, in Figure 7.9, there is a much more pronounced selectivity between the spectral profiles, especially between the water vapour and the other two chemicals.

7.2.7 Discussion

The ability of a sensor to fingerprint a vapour based upon a few straightforward measurements is highly sought after. In this section, several key measurements were shown. The vapour-induced optical response of the *Morpho* scales was seen to show significant diversity in both spectral and temporal responses simultaneously.

Experiments that probed the structure with polarised light reveal that the response-directions and response-dynamics were different between polarisations and at different wavelengths. Simulations of the electromagnetic field that arises under these illumination conditions also revealed that the interaction of light was diverse in a similar way. Different response directions, in the differential reflectance measurements, are attributed to the electromagnetic field distributions within the structure.

Further to these demonstrations, the comparison of angular excitation conditions reveals that for some analytes the diversity in reflectance can be enhanced by increasing the angle of incidence and detection of probing radiation. Again, this experimental observation is likely to be caused by the distribution of the electromagnetic field within the structure, but has yet to be explored theoretically.

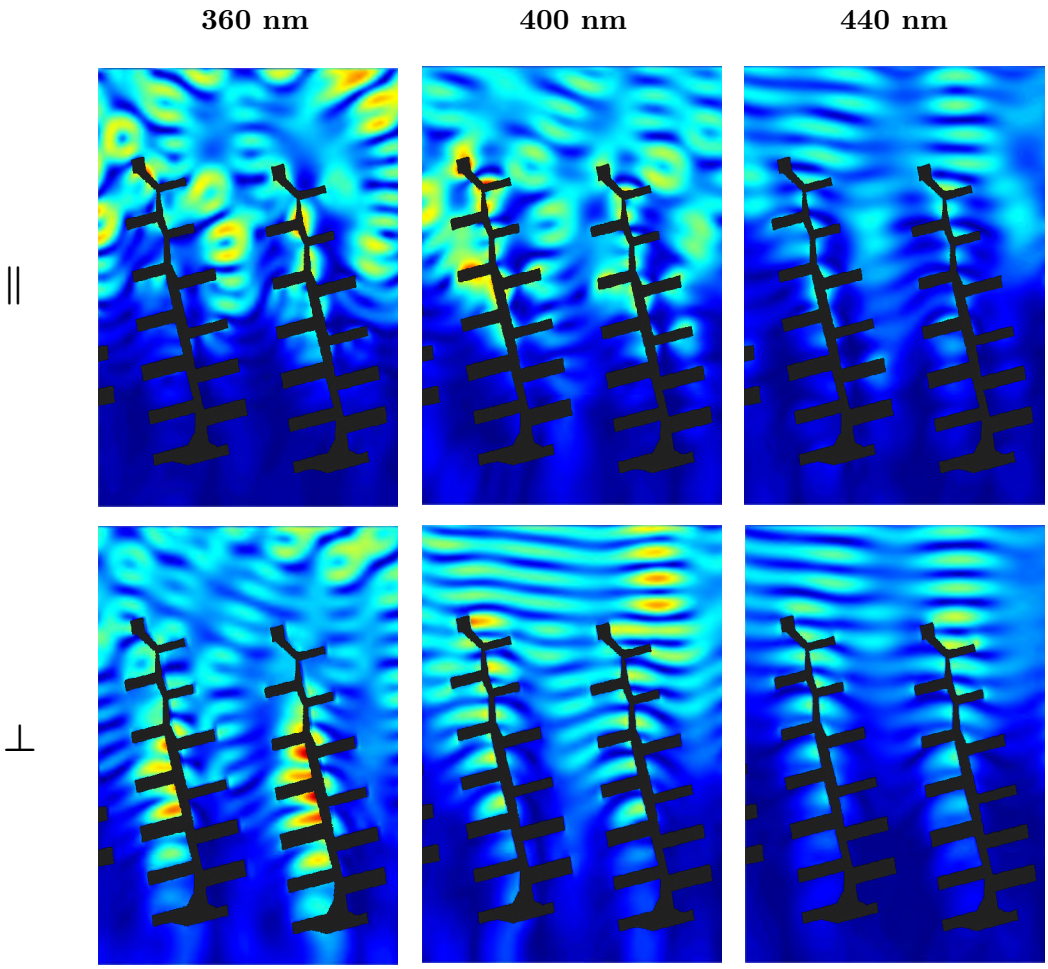

Figure 7.8: Intensity maps displaying the time-averaged power distributions when the *Morpho* structure is probed by light of two linear polarisations (as defined in Figure 7.1(b)) for wavelengths 360, 400 and 440 nm. Regions of high power intensity are shown in red, low power intensity is denoted by blue. All panels are plotted on the same intensity scale.

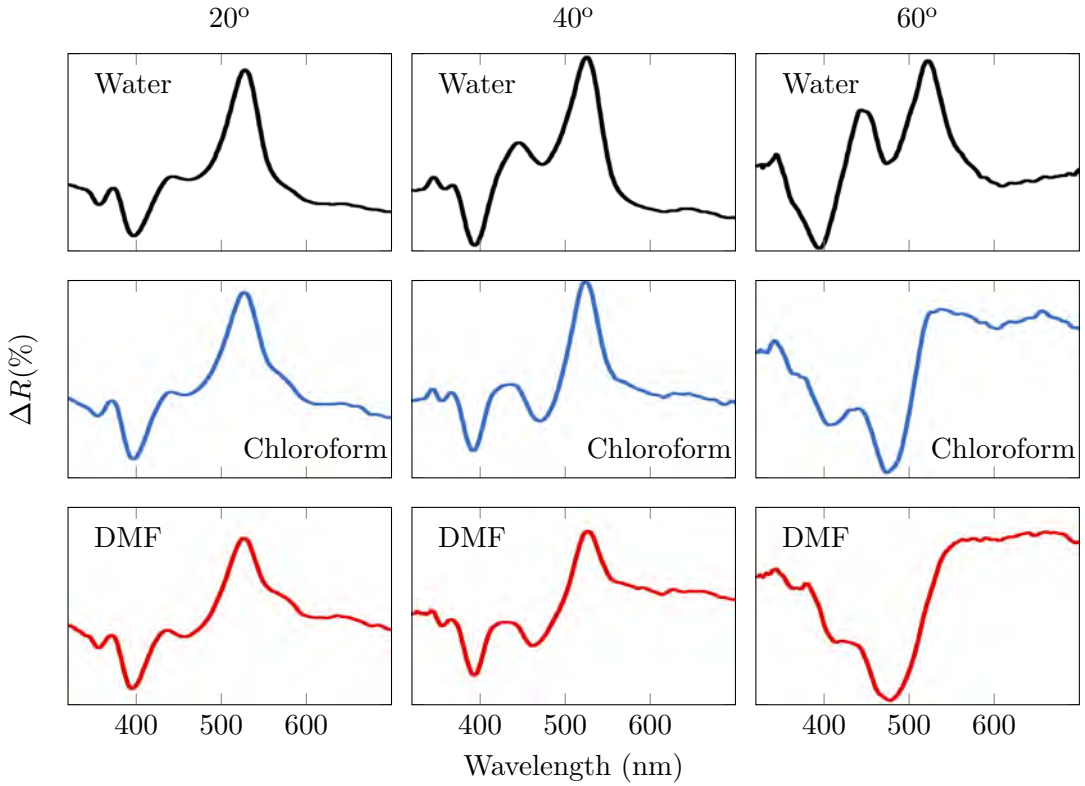

Figure 7.9: Experimentally explored diversity of spectral response with changing angle of illumination and of detection (relative to the normal to the surface). At a small angle of 20°, the ΔR spectra for water, chloroform, and dimethylformamide are almost identical. The spectral differences enhance upon an increase of the illumination angle to 40° and 60°.

The selectivity of vapour response demonstrated by the scales of the *M. sulkowskyi* is achieved by their hierarchical and anisotropic photonic structure. This knowledge should aid in designing and producing artificial nanostructures with similar functionality, where additional information about the chemical species is obtained by simultaneous measurement of two or more of the response attributes discussed.

7.3 Effect of measurement condition on vapour response

In previous studies of vapour-induced changes in reflectance from the iridescent scales of the *Morpho* butterfly, a bifurcated probe arrangement was used to illuminate and then measure reflectance at the same angle of incidence [8, 12], which henceforth shall be called a 'back-scatter' measurement. To date, this approach has allowed the measurement of selective and sensitive responses. To explore a different measurement of reflectance further, and the resulting vapour responses, a comparison between 'back-scatter' measurements, and a measurement of the specular reflection, which shall be termed the 'forward-scatter', is presented.

The work presented in this section was undertaken in collaboration with R. A. Potyrailo at General Electric Global Research Center (Niskayuna, NY, USA), and forms part of published work titled *'Toward bioinspired nanostructures for selective vapor sensing: diverse vapor-induced spectral responses within iridescent scales of Morpho butterflies'* in MRS Online Proceedings, Volume 1621, 2014 in Ref. [13].

7.3.1 Experimental measurement conditions

To measure the back- and forward- scatter, two bifurcated probes were used. One bifurcated probe was used to illuminate (using a halogen light source), and to record (using a fibre-optic spectrograph) the reflectance from the blue iridescent scales of *M. rhetenor*. This illumination/back-scatter-reflectance probe was positioned at ~ 30 degrees from the normal to the sample surface. A ~ 2 mm diameter beam spot illuminated the scale. For the measurement of forward-scattered light, another bifurcated probe was positioned at ~ -30 degrees from the normal. The schematic in Figure 7.10 depicts the orientation of both measurement probes with respect to the orientation of the ridges in the butterfly's scale.

To perform vapour exposures, the bubbler system, described in Section 5.1.3, was used. Generated vapours were flowed with a 450-mL/min total flow rate from a 1/8-inch-diameter tube onto the butterfly wing at an angle of approximately 45 degrees to the surface. The vapour flow was orientated to flow along the ridges of the photonic structure. Vapours were flowed with 0.04, 0.07 and 0.10 P/P_0 concentrations, where P

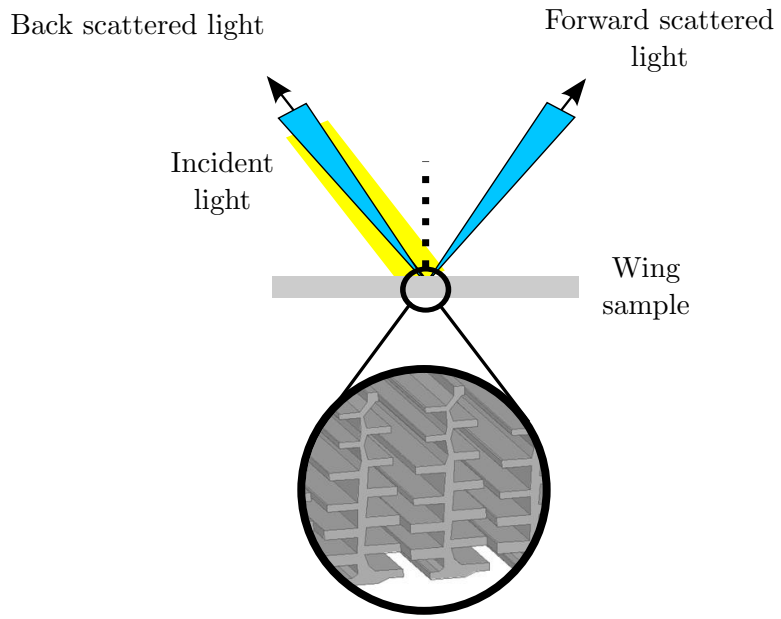

Figure 7.10: Diagram illustrating the experimental arrangement of illumination of the sample, and collection of scattered light, with respect to the orientation of the ridge structure within the wing scales.

is the partial vapour pressure, and P_0 is the saturated vapour pressure. The change in reflectance, ΔR, upon vapour exposure was measured as $\Delta R(\%) = ((R/R_0)-1)\times 100\%$, as described in Section 5.1. For these exposures, pure water, propanol and methanol vapours were generated and flowed individually, with the carrier gas (N_2), onto the scales with a 60 second 'on' cycle, followed by 360 second 'off' cycle. This on/off cycle allows the measurement of the reflectance as a result of the adsorption and desorption of vapours.

7.3.2 Comparison of temporal measurements

The temporal profiles for vapour exposures for the back- and forward- scatter measurements are shown in Figures 7.11(a) and 7.11(b), respectively. The general trends remain the same, however, differences in the dynamic evaporation for methanol vapour cycles are observed. In the back-scatter measurement (Figure 7.11(b)), the 525 nm trace begins to return smoothly to the baseline reflectance at the end of the vapour cycle, whilst the forward-scatter measurement displays a rapid return to the baseline before the ΔR signal increases again. Figure 7.11(c) shows one fixed wavelength for both measurements for this methanol cycle. Such observations can reveal information about the interactions of vapours within the structure; the temporal diversity is discussed further in Section 7.2.4.

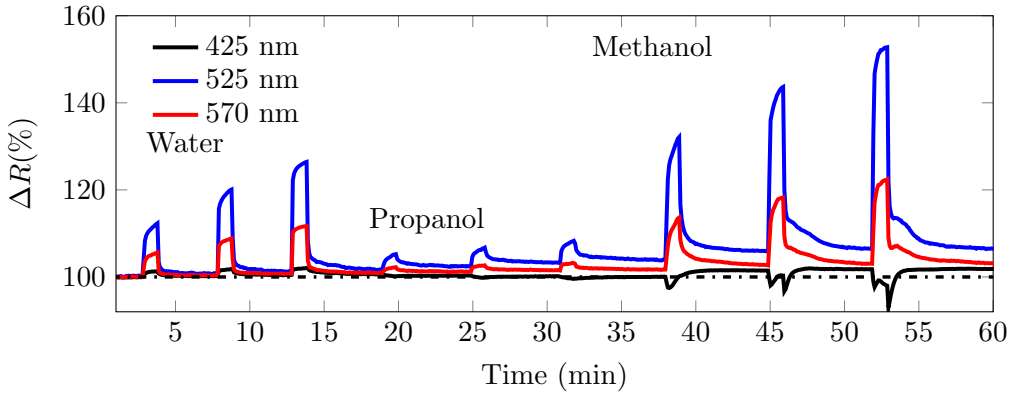

(a)

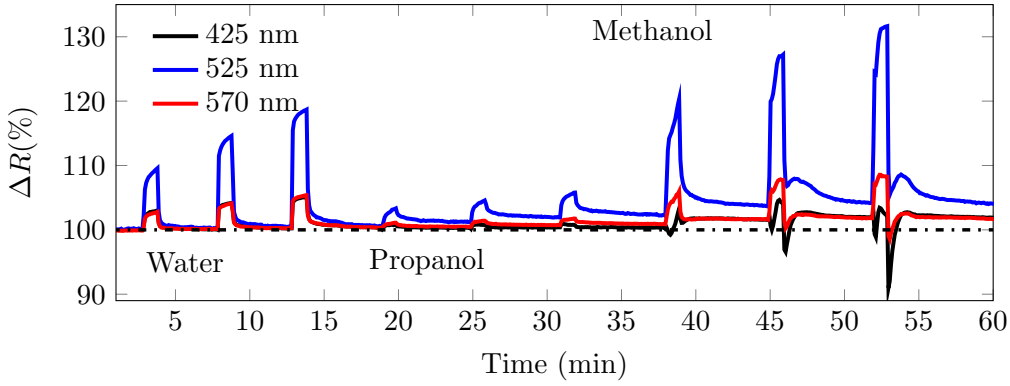

(b)

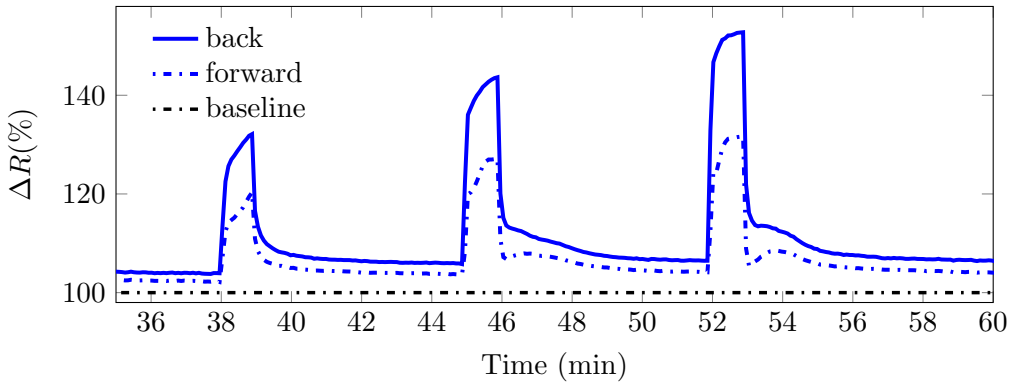

(c)

Figure 7.11: (a) and (b) show the temporal response of back- and forward-scattered light, respectively for 1 min vapour exposures of 0.04, 0.07 and 0.10 P/P_0 concentrations at three wavelengths. (c) Provides a comparison of back- (solid lines) and forward- (dotted line) scatter reflection at a single wavelength (525 nm) during the methanol exposures in the other two plots.

7.3.3 Comparison of spectral measurements

The spectra recorded by both collecting probes at the time immediately before the vapour flow is turned off for each vapour and each concentration generated are shown in Figure 7.12. In general, three observations can be made about the spectra arising from water, propanol and methanol vapour exposures. First, the change in reflectance, ΔR, at all wavelengths increases in magnitude upon increasing vapour concentration, from 0.04 to 0.10 P/P_0. Second, qualitatively the spectral shape associated with each vapour remains similar over these concentrations. Finally, these observations are true for both back- and forward- scatter measurements. An exception to these observations can be seen in the methanol vapour cycles; the lowest concentration methanol exposure does not have the same spectral profile exhibited by both higher concentration measurements. This difference is more obvious at lower wavelengths, and in the forward-scatter measurement, shown in Figure 7.12(b). In the following discussion, in Section 7.3.4, this difference is shown to arise from the presence of propanol and methanol upon the scales due to the incomplete desorption of propanol from the scale before the first methanol exposure.

The comparison of back- and forward- scatter measurements is shown in Figure 7.13, for water, propanol and methanol at a concentration of 0.07 P/P_0. In both measurements the differential reflectance has very similar magnitudes and spectral shapes. The coherent scatter of light from the hierarchical *Morpho* structures are known to produce broad blue hemispherical scattering to create a conspicuous appearance [63, 86], so this is perhaps not surprising.

7.3.4 Comparison of Principal Components Analysis

For data presented in this section, multivariate spectral analysis of the vapour response of *Morpho* scales was performed upon autoscaling [305, 306] of the measured differential reflectance spectra. Preprocessing of the data was done by the commonly employed autoscaling method, which uses mean-centering followed by dividing each variable (wavelength) by the standard deviation of the spectrum [281].

PCA scores plots of the back- and forward- scatter measurements are shown in Figures 7.14(a) and 7.14(b), respectively. In both figures, water and propanol vapour results have two tracks from the reference point; the methanol exposures do not display this behaviour. The water and propanol results display the previously described selective and sensitive response in PCA space. The methanol response differs because there was insufficient time to allow the signal to return to the baseline reading before the first methanol exposure was performed, as seen in Figure 7.11. Thus, a binary mixture of propanol and methanol is present on the ridge structure, this point is circled

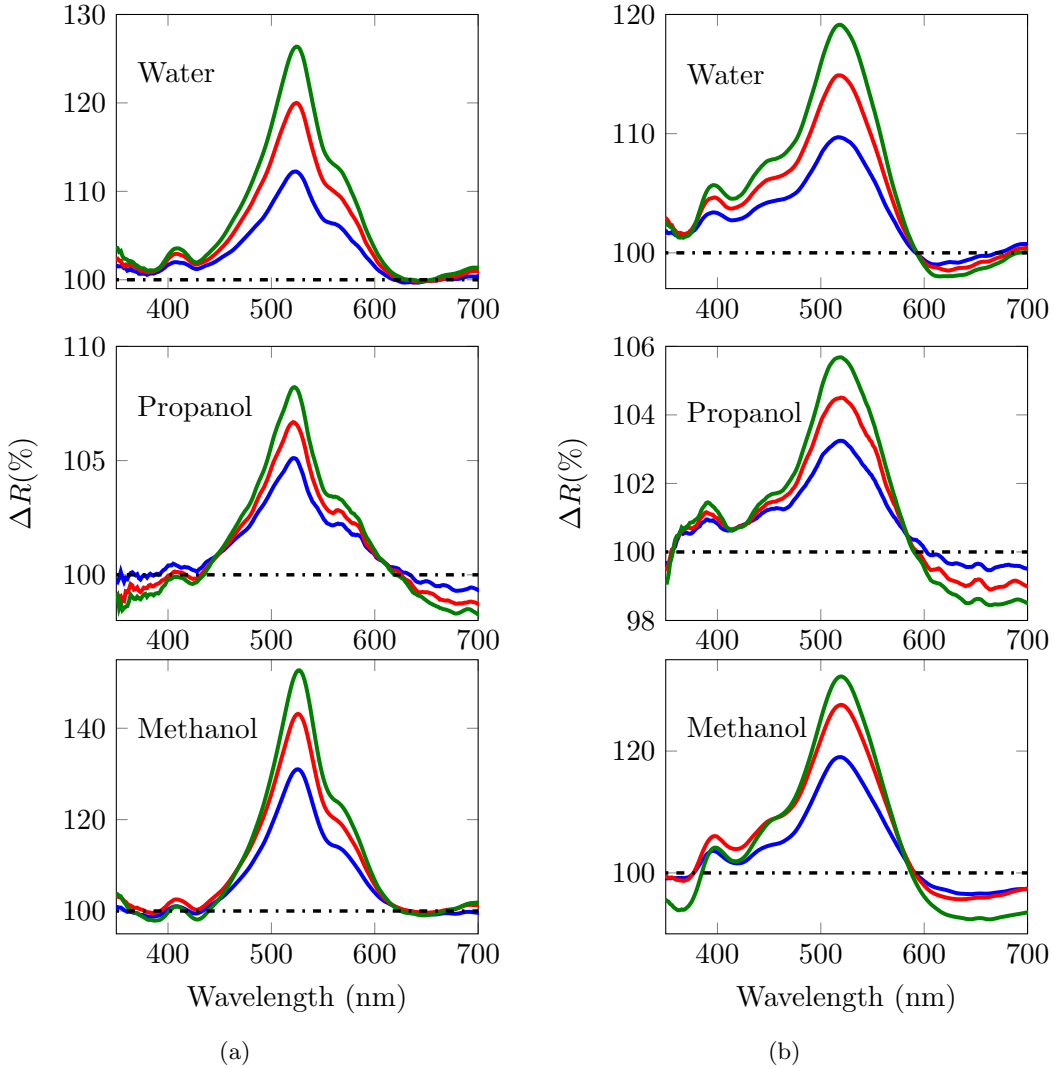

Figure 7.12: Spectral responses measured upon vapour exposures for (a) back- and (b) forward- scattered light for concentrations of 0.04 (blue lines), 0.07 (red lines) and 0.10 (green lines) P/P_0.

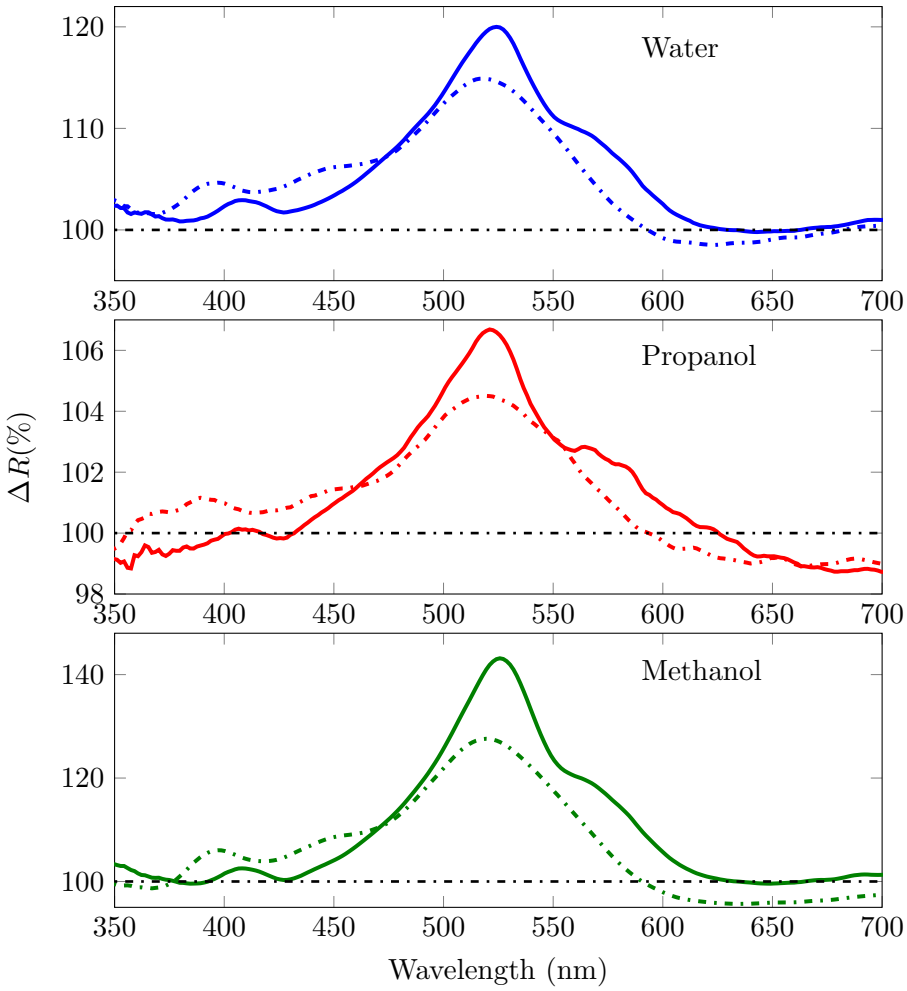

Figure 7.13: A comparison of back-scattered (solid lines) and forward-scattered (dotted lines) measured spectra for water, propanol and methanol vapours at 0.07 P/P_0 concentration.

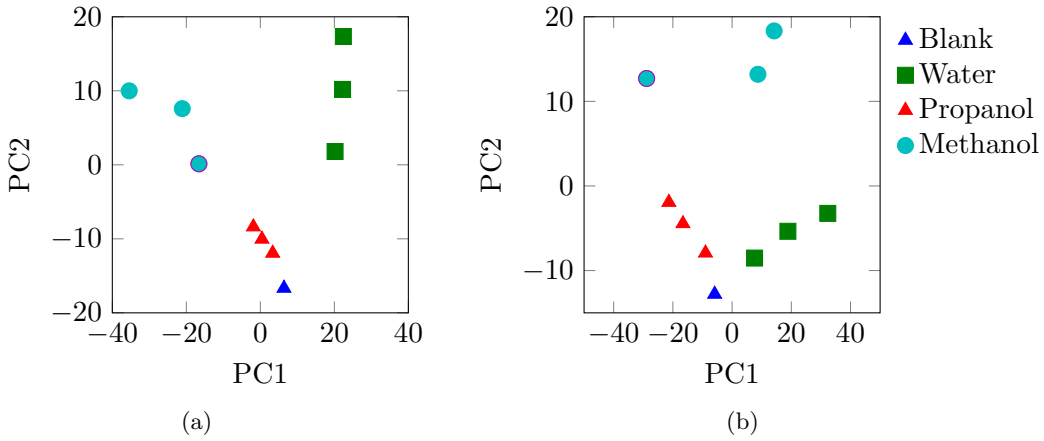

Figure 7.14: (a) and (b) PCA scores plots (autoscaled) for back- and forward-scattered reflectance respectively, for water, propanol and methanol at 0.04, 0.07 and 0.10 P/P_0. The circled point represents the 0.04 P/P_0 methanol vapour exposure.

in Figure 7.14. In both measurement positions, the PCA analysis shows a point which lies towards the track formed by the propanol exposures, this is expected as the ΔR spectrum associated with this point represents the convolution of the optical response of propanol and methanol, as discussed in Section 7.3.3 and shown in Figure 7.12.

The captured variance (autoscaled) of PC1 and PC2 for the back-scatter measurement are 72.7% and 22.0% respectively, and 76.2% and 24.2% for the forward-scatter measurement. The interesting result here is that the scores plots give similar qualitative results, with comparable variance captured on each PC, for both measurements. Such apparent insensitivity in measurement conditions may have some practical application in remote sensing situations where the fine control of the optical measurement position is not possible.

7.3.5 Summary

Here, the vapour-induced spectral responses within the scales of *Morpho* butterflies to two different measurement conditions have been discussed. The wing scales of *M. rhetenor* were exposed to water, propanol and methanol vapours and the change in reflectance for back- and forward- scattered reflected light was studied in detail. Temporal profiles show slightly different dynamics between measurements, whilst PCA analysis of both back-scatter and forward-scatter measurements provides similar response selectivity.

7.4 Functionalisation of natural *Morpho* scales

Using the knowledge obtained in Chapter 6, about the combined physical and chemical mechanism that produces the unusual selective response of the *Morpho* scales to chemical vapours, it is of interest to explore whether this effect may be enhanced to offer further inspiration for sensing.

In order to influence the vapour response of the iridescent scales, a number of techniques can be used to alter the existing materials or add to the original *Morpho* nanostructure template. Plasma treating has already been demonstrated, in Section 6.5.2, as one approach to alter the existing vapour response of the structure. Deposition is one process by which functionalisation can be added to the structure. Figure 7.15 displays images of *Morpho* ridge-structures following deposition of terthiophene and of Zinc tetraphenylporphyrin (ZnTPP) coating materials by collaborators at General Electric Global Research and the Air Force Research Laboratory.

Whilst diverse functionalisations were being assessed by experimental means, it was also of interest to investigate, through optical simulations, model 'functionalisation' scenarios. In this section, smaller 'functionalised' regions within the *Morpho* structure, are simulated to determine whether vapour adsorption in different regions can be resolved, and whether selectivity or sensitivity is enhanced.

The work presented in this section was undertaken in collaboration with researchers at General Electric Global Research Center (Niskayuna, NY, USA), the Air Force Research Laboratory (Wright-Patterson Air Force Base, OH, USA), the State University of New York (Albany, NY, USA), and is being prepared for publication in a manuscript titled 'Boosting vapor-response selectivity using nanofabricated multivariable bio-inspired photonic sensors'.

7.4.1 Optical modelling of 'functionalised' photonic structure

To consider the theoretical response of vapour adsorption to 'functionalised' regions upon the *Morpho* nanostructure, models were developed using the same technique described in Chapter 6. However, instead of three assumed vapour regions, horizontal and vertical portions of the ridge-structures were each assumed to have thin layers of condensed liquid, for top, middle and bottom sections. Figure 7.16 shows these different model vapour distributions.

The rational for simulating these distributions was that the ability to resolve these vapour distributions optically would be of critical importance for building not only highly selective sensors for certain small number of compounds, but also would open possibilities for developing individual sensors for selective detection of a broader range of compounds. To explore this, optical simulations were performed using the same

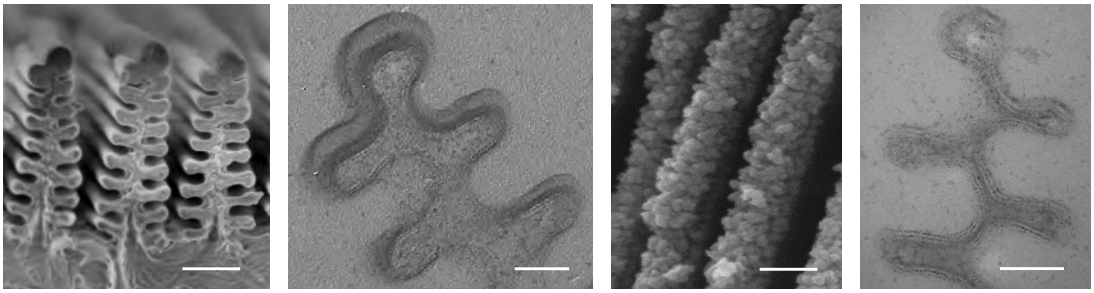

(a) (b) (c) (d)

Figure 7.15: Examples of *Morpho* ridge-structures following coating depositions aimed to alter vapour selectivity. (a) SEM image, and (b) TEM image, of a *M. sulkowskyi* scale cross-section after terthiophene deposition. (c) SEM image view of ridge tops, and (d) a TEM image of a scale cross-section of *M. sulkowskyi* after ZnTPP deposition. Images courtesy of R. A. Potyrailo and R. Naik. [Scale bars: (a) and (c) 500 nm, (b) and (d) 100 nm].

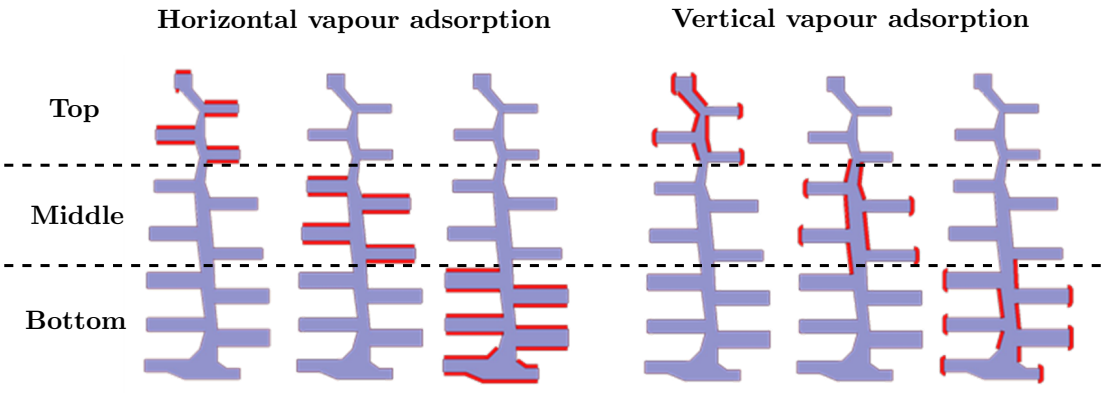

Figure 7.16: Rendered images of modelled adsorbed vapour distribution for liquids condensed on vertical, and then horizontal regions, for top, middle, and bottom sections, for the investigation of a functionalised *Morpho* nanostructure.

approach as in Section 6.5.1.1. The ridge-structure was assumed to have a complex RI of $n^* = 1.56 + i0.06$, which is assumed unaffected by vapour adsorption. The thin layers of condensed liquid were modelled with RI values of $n = 1.3, 1.4$ and 1.5, and thickness values of $t = 5, 10$ and 15 nm.

The total reflectance for each simulated vapour condition is presented in Figure 7.17. Figure 7.17(a) displays all 56 calculated reflectance spectra, and shows that they all have broad reflectance over blue wavelengths and also into the ultraviolet. To observe the differences between the reflectance spectra upon vapour adsorption, the extremes of the optical thickness ($n \times t$) are considered. Figures 7.17 (b) and (c) display the reflectance for nanostructures with horizontal vapour layers on each spatial region individually, for $n = 1.3$ and $t = 5$ nm (smallest vapour optical thickness), and for $n = 1.5$ and $t = 15$ nm (largest optical thickness), respectively. Figures 7.17 (d) and (e) show equivalent plots for vapour adsorbed onto vertical sections. The spectra for horizontal vapour coverage produces characteristic red-shifts of the peak reflected wavelengths. This red-shift is consistent with an increase of the optical thickness of the high RI layers [48]. The addition of vapour on the vertical sides of the nanostructure changes the shape of the main reflectance peak, and the peak wavelength red-shift is less prominent than for horizontal vapour coverage. This is due to the small volumes of new RI material in the inter-lamellae spaces. For both horizontal and vertical vapour adsorption scenarios, the spatial region in which the vapour is adsorbed has a large impact on the magnitude of these changes in the coherent scattering conditions, relative to the blank nanostructure. This is likely due to the larger relative change in lamellae layer thickness by the addition of vapour to the top of the ridge structure and the attenuation of the light through the structure, as previously described in Section 6.5.1.4.

PCA analysis was performed upon mean-centered datasets to assess the selectivity or sensitivity of these computed spectra. The PCA results for horizontal and vertical vapour adsorptions are displayed as PCA scores plots in Figure 7.18(a) and in Figure 7.18(b), respectively. Both scores plots show a 'three-arm' trajectory, with an arm associated with each spatial position on the nanostructure. Each point represents a vapour condition; the arm is formed from the blank spectra with points forming a line of increasing optical thickness of the vapour layers. This three-arm response in PCA space, due the spatial adsorption, for both 'functionalised' adsorption scenarios indicates that the vapour conditions can be resolved, and hence are selective, between one another.

Whilst these results show that one horizontal vapour distribution can be resolved from another horizontal distribution in a different spatial position, and the same for the vertical vapour adsorption, it does not indicate if there is selectivity between them. To assess whether such functionalisation may boost selectivity, all spectra need to be

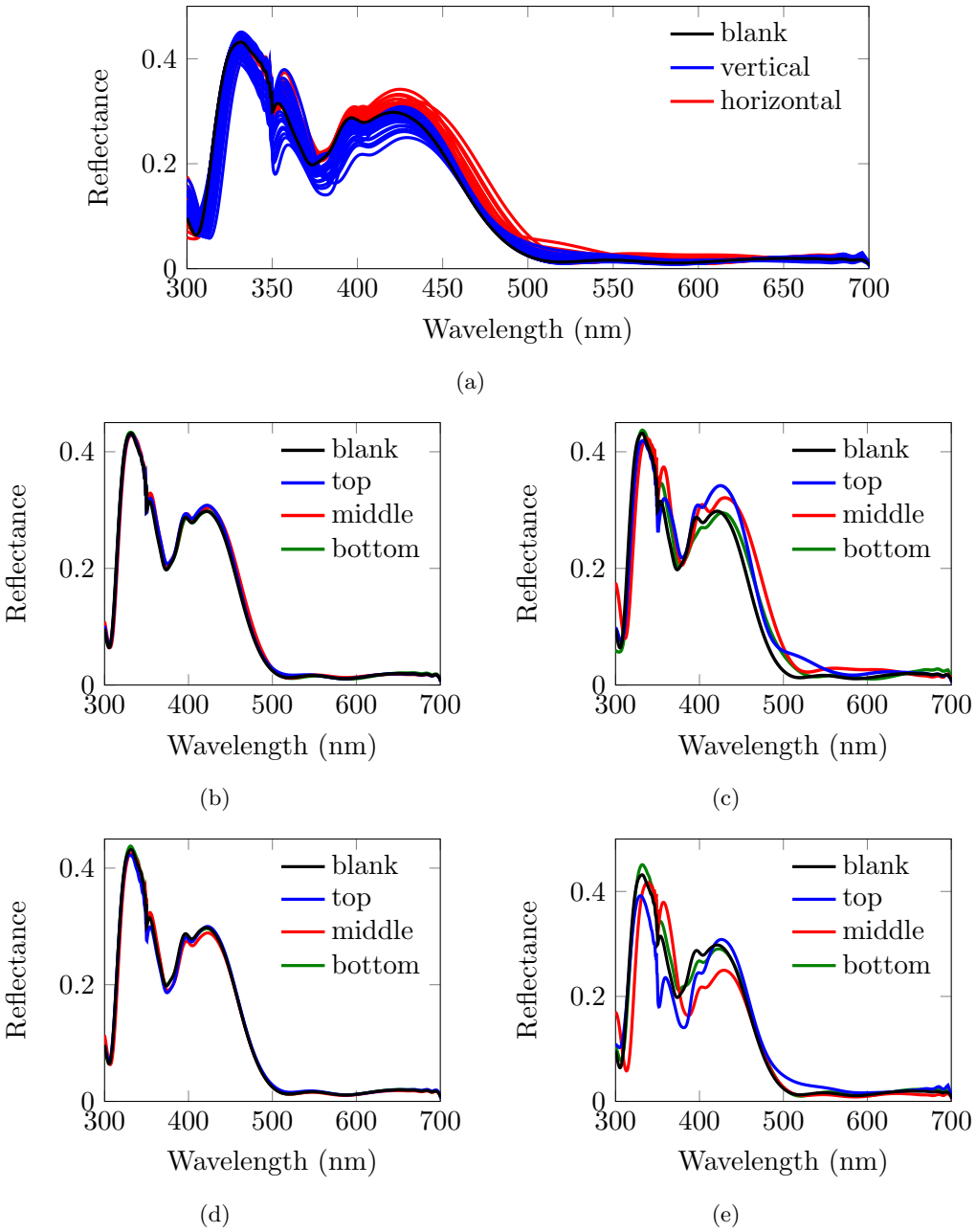

Figure 7.17: Simulated reflectance spectra for a model 'functionalised' *Morpho* ridge structure. (a) Reflectance for vapour conditions for model adsorption on horizontal and vertical regions for top, middle and bottom sections (55 spectra - 1 blank, 54 horizontal and 54 vertical). (b) and (c) display the reflectance spectra for vapour adsorbed on the horizontal surfaces of the nanostructure, for the condensed layers of $n = 1.3$ and $t = 5$ nm, and $n = 1.5$ and $t = 15$ nm, respectively. (d) and (e) display the reflectance spectra for vapour adsorbed on the vertical surfaces of the nanostructure, for the condensed layers of $n = 1.3$ and $t = 5$ nm, and $n = 1.5$ and $t = 15$ nm, respectively.

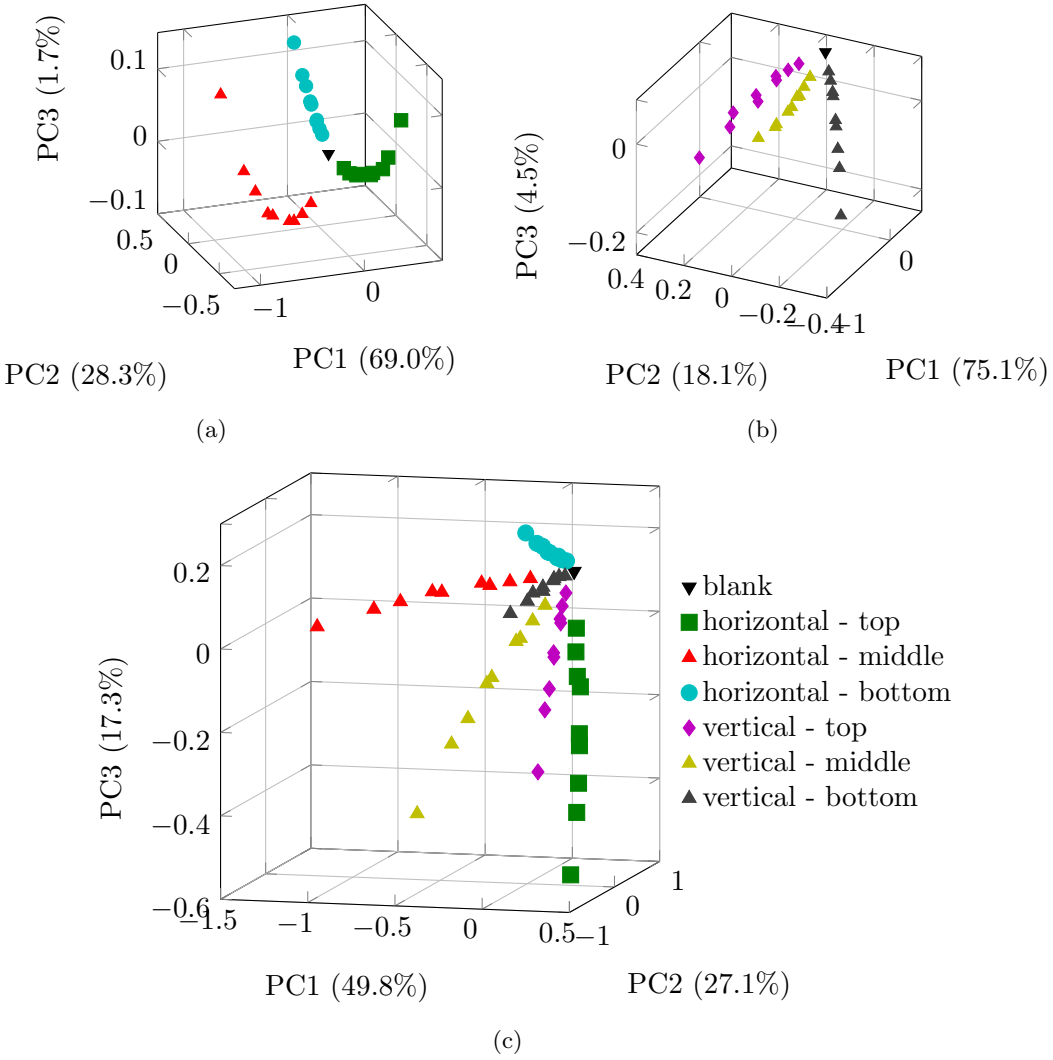

Figure 7.18: PCA analysis of simulated reflectance spectra (Figure 7.17) for a model 'functionalised' *Morpho* ridge structure: (a) and (b) display scores plots for model vapour adsorption on horizontal regions and vertical regions, respectively. In both plots, spectra corresponding to vapour adsorbed on the top, middle and bottom regions are distinguished from each other. (c) A scores plot for the combined PCA analysis of all simulated vapour conditions; results show that vapour adsorbed in each spatial distribution produces a selective response. The legend in (c) provides a key to the vapour adsorption scenarios for all plots. All datasets were processed by mean centering before analysis by PCA.

combined and analysed together. The PCA scores plot for the combined analysis of horizontal and vertical regions on the ridge structure are presented in Figure 7.18. The scores plot displays six distinct arms representing vapour adsorbed to either horizontal or vertical sections in the three spatial regions considered. Comparing the magnitudes (lengths) of these arms demonstrates that horizontal vapour adsorptions produce a greater change in the magnitude or diversity of the reflectance spectra. The percentage of variance captured by the first three PCs is 54.2% indicating higher PCs may also be used to differentiate each spectra from another. The magnitude, and the distinct arm pattern formed, show this to be a selective and sensitive response. This demonstrates that by using this nanostructure geometry with a simulated surface functionality, distinct spectral features related to the different horizontal and vertical regions of the ridges, are clearly produced for vapour adsorptions that are assumed to condense one at a time.

7.4.2 Summary

Using theoretical tools, this natural nanostructure geometry, with simulated surface functionality, was shown to be able to produce clearly distinct spectral features related to the different horizontal and vertical regions of the ridges. The vapour addition onto the horizontal lamellar surfaces modified the multilayer reflectance, red-shifting the reflectance spectra in the usual way. Vapour adsorption to the vertical sides of the ridge-type multilayer structures changed the reflectance due to their presence as small volumes of new refractive index material in the inter-lamellar spaces.

These results not only demonstrate that the spectral responses are selective between all six vapour conditions but, more critically, showed that this unoptimised dielectric structure could offer enhanced vapour selectivity with the right surface functionalisation.

7.5 Conclusions

In this chapter, the scales of the *Morpho* butterfly have been studied as a source of bio-inspiration for the chemical sensing community. It was shown that nature provides an elegant design for highly multivariable sensing, which is possible due to the hierarchical and anisotropic nanostructure of iridescent *Morpho* butterfly scales.

To begin, experimental demonstrations, using numerous volatile organic compounds, showed that the *Morpho* scales display many response attributes that are desirable for optical chemical sensing. These attributes were the diverse reflectance-response observed in spectral and temporal measurements, and also for different linear polarisations

and angular excitations. The interaction of light with vapour within the anisotropic geometry of the photonic structure in the *Morpho* wing-scales produces these diverse, and desirable features. Next, the measurement of forward- and back- scattered light was shown to provide very similar distinction between vapours and different concentrations through the analysis of the steady-state optical response, and the application to remote sensing was described. Finally, a simulation experiment on a 'functionalised' *Morpho* photonic structure was described. The functionalised adsorptions were performed on three spatial regions along the height of the tree, and also on the vertical and horizontal sections of the nanostructure. Results not only demonstrated that the spectral responses were selective between all six vapour conditions but, more critically, showed that this unoptimised dielectric structure could offer enhanced vapour selectivity with the right surface functionalisation.

To conclude, through the combination of detailed experimental and numerical studies, we have advanced the understanding of the optical effects of *Morpho* biological structures with the future goal of incorporating these lessons into vapour-sensor devices. Future bio-inspired sensor units could include anisotropic micro- and nano-structures to enhance the diversity of response, as a route to providing additional information for the fingerprinting of chemical species.

Chapter 8

Bio-inspiration for Selective Sensors

8.1 Introduction

The studies in the previous two chapters have focused on the mechanism (Chapter 6), and other aspects (Chapter 7) of the unusual vapour response observed in the scales of *Morpho* butterflies. Whilst these iridescent scales offer an attractive template for producing a selective vapour sensor, farming butterflies to make optical devices is a barbaric proposal in the 21st century (note – this was a serious suggestion made by others!). Instead, this new knowledge about the combined physical and chemical effects within these naturally evolved photonic structures can be used as inspiration in the pursuit of new bio-inspired unitary selective chemical vapour sensors.

In this chapter, some simple concepts for sensor design, that may be used in the pursuit of sensitive and selective unitary sensor devices, are discussed. First, the calculated optical response of a simple multilayer reflector is presented for model vapour adsorption, and the effects on the vapour response selectivity are described when the optical extinction of the reflecting layers is modulated. Second, the vapour response selectivity and sensitivity are shown for different 'chirped' multilayer periodicities. Next, the reflectance of five different model nanostructures are considered; these models increase in complexity from the simple multilayer to ridge-lamellae structures. The optical response and resonant features that arise in these structures are investigated before subjecting them to vapour adsorptions for the analysis of their sensing properties.

The work presented in this chapter was undertaken in collaboration with researchers at General Electric Global Research Center (Niskayuna, NY, USA), the Air Force Research Laboratory (Wright-Patterson Air Force Base, OH, USA), the State University of New York (Albany, NY, USA), and is being prepared for publication in a

manuscript titled 'Boosting vapor-response selectivity using nanofabricated multivariable bio-inspired photonic sensors'.

8.2 Vapour selectivity of multilayered films

A number of simple 1D sensor designs, that transduce an analytical signal through the change in measureable properties of light, have been investigated for vapour sensing applications [307]. These, often comprising thin or multilayered films, have been reported to produce a sensitive response to adsorbed vapours, but usually little or no selectivity is observed between the different vapours sorbed to the same structure or material [203, 214, 308]. The sensitivity of these thin films arises due to their physical construction. These films often consist of porous matrices or high surface-area topologies to which vapour can adsorb, such as in porous silicon, opal structures or nanostructured materials. Enhancing the selectivity of such films, whilst maintaining sensitivity, is an attractive prospect.

In Chapter 7, it was shown that spatial adsorption of vapour analyte can result in a selective vapour response. The development of polymeric films and increasing studies into material chemical gradients, will see a growth in the enhanced ability to achieve a high degree of control in the deposition and growth of smart materials. By assuming surface functionalisation or surface chemistry can be achieved, it is of interest to see if these simple 1D reflectors may be enhanced to generate a selective response to a range of sorbed vapours.

In this section, simple multilayer calculations are used to model vapour adsorption on a 1D reflector to determine whether the reflectance can be used to image a selective and sensitive vapour response, rather than just a sensitive response like previous published studies. To this end, the *Morpho* structure is simplified to a 1D reflector; this assumption has been made in a number of previous studies of *Morphos* in order to provide simple examination of its optical properties [63, 98, 106]. Here, the multilayer considered comprises ten lamellae, of thickness $t = 55$ nm separated by 'air' of thickness $t = 100$ nm. Figure 8.1(a) shows a simple schematic of this system, and the locations of model vapour adsorption that will be described in Section 8.2.1. The characteristic multilayer reflectance of this reflector is displayed in Figure 8.1(b) for lamellae with RI $n^* = 1.56 + i0$, separated by air layers of RI $n = 1$. This spectrum is the specular reflectance, since these reflectors are planar, and is calculated for illumination at normal incidence. For this spectrum, light is incident normally and the reflected light, which is the specular reflectance for these planar systems, is presented.

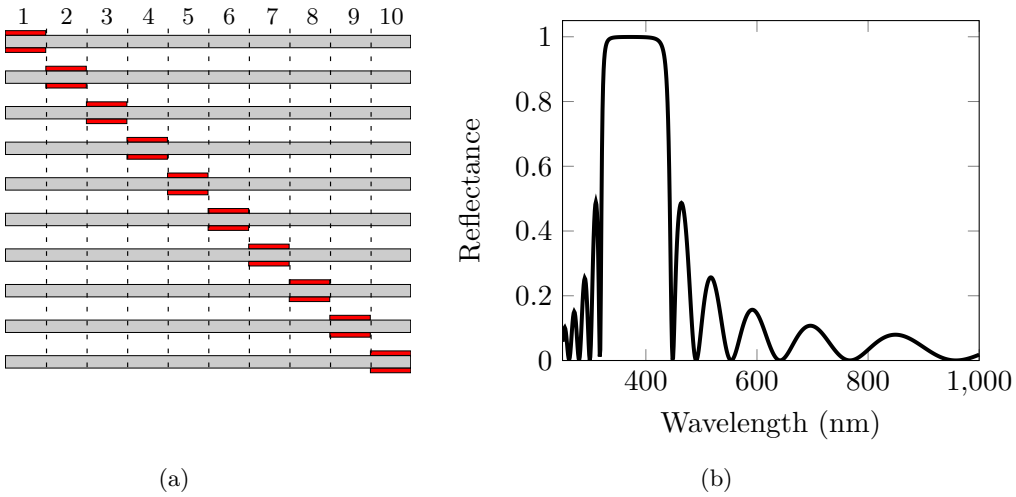

(a) (b)

Figure 8.1: Multilayer reflector for the investigation of a simplified *Morpho* design: (a) schematic of a multilayer comprising ten reflecting lamellae, with the ten model vapour adsorption scenarios considered (labelled 1-10 and represented by the small red areas). (b) Reflectance spectrum for this multilayer design, which comprises 55 nm thick lamellae layers of RI $n^* = 1.56 + i0$ separated by 100 nm layers of RI $n^* = 1.56 + i0$.

8.2.1 Vapour adsorption upon multilayer lamellae

To explore the vapour effects upon these reflecting lamellae the same model vapour conditions of uniformly adsorbed thin liquid layers are considered, as previously used in Section 6.5.1.2. These are thin layers of RI $n = 1.3$, 1.4 and 1.5 of thicknesses $t = 5$, 10 and 15 nm (these thicknesses were chosen based upon literature values of condensed vapours on porous films [205]) adsorped to each layer in turn, as displayed in the schematic in Figure 8.1(a). The first case considered is that of lamellae layers with RI $n = 1.56$ without optical absorption ($k = 0$). The rationale for this choice was that a non-optically-absorbing stack consists of material with the simplest optical properties, and also would be highly reflecting, due to the absence of optical absorption (i.e. larger reflectance than the *Morpho* scales, which comprise absorbing melanin pigment [63]). It is also hypothesised this would present the largest changes in reflectance, and hence high sensitivity, upon model vapour adsorption.

The reflectance from this non-optically-absorbing multilayer is shown in Figure 8.2(a), without and with a model vapour adsorption (vapour condition: n =1.4 and $t = 10$ nm) on lamellae numbers 1, 3 and then 5. The greatest changes in reflected intensities, relative to the blank multilayer, occur at wavelengths either side of the photonic band gap (PBG), and at the subsidiary reflectance peak maxima. PCA analysis of all vapour scenarios considered ($n = 1.3$ - 1.5; $t = 5$ - 15 nm) on each of the lamellae is

presented in Figure 8.2(b) and 8.2(c). The loadings plot, in Figure 8.2(b), confirms that the wavelength variables that contribute most variance to the analysis occur in those spectral regions indicated (namely those wavelengths either side of the PBG). The PC scores plot, for the first two PCs, in Figure 8.2(c), indicates selectivity between some layers but not others. Despite ten spatial regions of model vapour adsorption, only five 'arms', which are formed from points of increasing optical thickness of sorbed vapour at each spatial location, are visualised in the PCA space. At first glance this seems a surprising result; a degenerate vapour response between five layer-pairs (layers 1 and 10, layers 2 and 9, layers 3 and 8... etc) is observed. This means that the computed optical response (reflectance and transmittance) of each of the layers that comprise a layer-pair is identical.

This degenerate behaviour is a consequence of electromagnetic reciprocity [309]. More specifically, in the situation here, de Hoop reciprocity is observed in the absence of optical absorption. This is a consequence of the time-reversal symmetry in the multilayer system [309]. It is evident that the transmittance of light through a thin film is independent of the direction that light propagates through it, and in the absence of absorption the reflectance is independent of the propagation direction ($R+T = 1$). This is analogous to the situation with this non-optically absorbing stack. By considering the Jones matrix [129] for this system, the transmission through the stack in the reverse direction is the transpose of the matrix for forward transmission when the two directions of propagation are reciprocal to one another [309]. This is the case for the model vapour conditions on the layer-pairs described. Upon the introduction of optical absorption this reciprocal behaviour is maintained for transmitted light, but reciprocity fails for light reflected [309].

To demonstrate that the de Hoop reciprocity of the reflected component can be removed, the same calculations are performed on a system identical to that used above except for the inclusion of material optical absorption in the lamellae. Here, the lamellae are assigned an extinction coefficient $k = 0.05$. Figure 8.3(a) displays the reflectance of the multilayer without and then with vapour adsorbed to lamellae layer number 1, 3 and then 5. As in the reflectance spectra where optical adsorption was not present (see Figure 8.2(a)), the vapour adsorption results in similar changes from the reflector without vapour, namely, changes to the reflected intensities at wavelengths either side of the PBG. However, when the reflectance of the all vapour conditions is processed with PCA, there is a pronounced difference in the observed vapour response. Figure 8.3(b) shows a scores plot for the first three PCs, displaying data points corresponding to each model vapour condition in the absorbing multilayer stack. Here, a ten-'arm' response is now visualised, where each arm corresponds to a spatial vapour location as shown in Figure 8.1(a), and where data points in the arm align with increasing optical

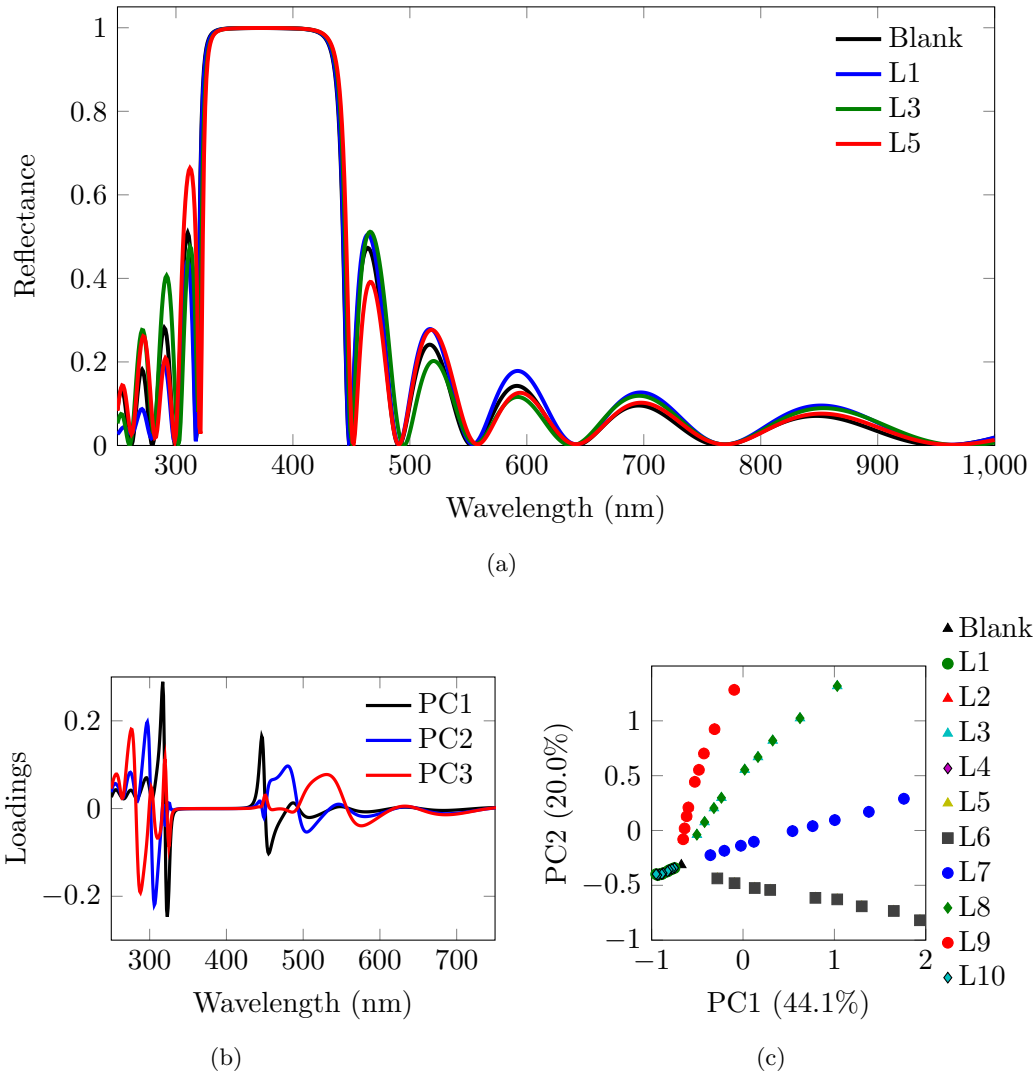

Figure 8.2: Analysis of the multilayer reflectance upon model vapour adsorption on the simplified ten lamellae multilayer with extinction coefficient $k = 0$; (a) reflectance for the blank multilayer and for vapour layers, of RI $n = 1.4$ and thickness $t = 10$ nm, on lamellae number 1, 3 and 5. PCA analysis for the mean-centered dataset containing calculated reflectance spectra (blank spectrum plus 90 simulated vapour conditions ($n = 1.3$ - 1.5; $t = 5$ - 15 nm)); (b) displays the loadings for the first three PCs, and (c) a scores plot where each marker denotes vapour adsorbed to a specific lamella layer.

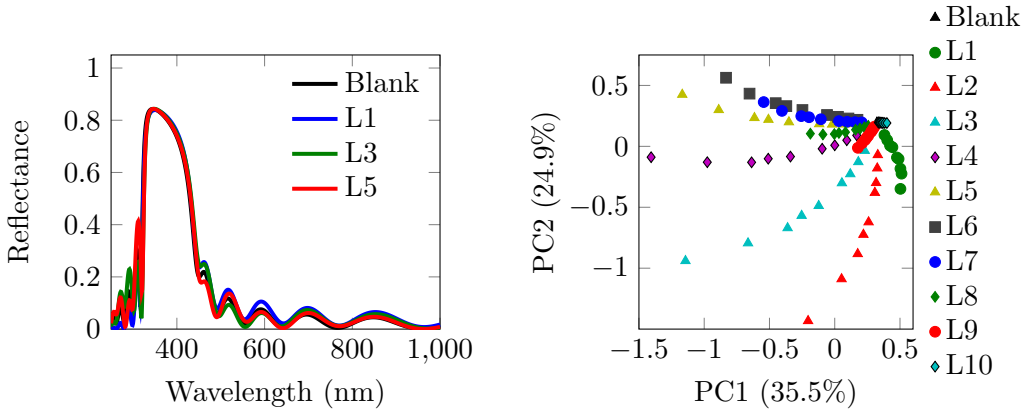

(a) (b)

Figure 8.3: Analysis of the multilayer reflectance upon model vapour adsorption on the simplified ten lamellae multilayer with extinction coefficient $k = 0.05$; (a) reflectance for the blank multilayer and for vapour layers, of RI $n = 1.4$ and thickness $t = 10$ nm, on lamellae number 1, 3 and 5. PCA analysis for the mean-centered dataset containing calculated reflectance spectra (blank spectrum plus ninety simulated vapour conditions ($n = 1.3$ - 1.5; $t = 5$ - 15 nm)); (b) a scores plot where each marker denotes vapour adsorbed to a specific lamella layer.

thickness of the sorbed model vapour. This result indicates that these spatial locations produce ten sets of unique reflectance spectra that are transduced by the multivariate analysis.

A question that naturally arises is: 'how does the sensitivity and selectivity of a multilayer's vapour response change with increasing optical absorption?'. To answer this question, the same calculations are performed for a larger extinction coefficient of $k = 0.20$, and then compared to the multilayers comprising lamellae with extinction coefficients of $k = 0$ and 0.05. The blank-reference reflectance spectra for these multilayers of different extinction coefficient are shown in Figure 8.4(a). At the largest value of material optical absorption ($k = 0.20$), the reflectance spectrum has no visible sideband minima and maxima, instead only the main reflectance peak is seen. To compare model vapour adsorptions on these multilayer systems with different material optical absorption a combined PCA model of all spectra is computed. The PCA scores plot in Figure 8.4(b) displays the combined analysis. In this 3D representation three data 'structures' are visible, associated with each extinction coefficient. The data 'structure' with the largest span in PCA space corresponds to the extinction coefficient $k = 0$, the next smallest span corresponds to $k = 0.05$, and the smallest to $k = 0.20$. The decreasing size of the data 'structure' shows that the presence of material optical absorption diminishes the sensor sensitivity, as the calculated spectra have smaller spectral differ-

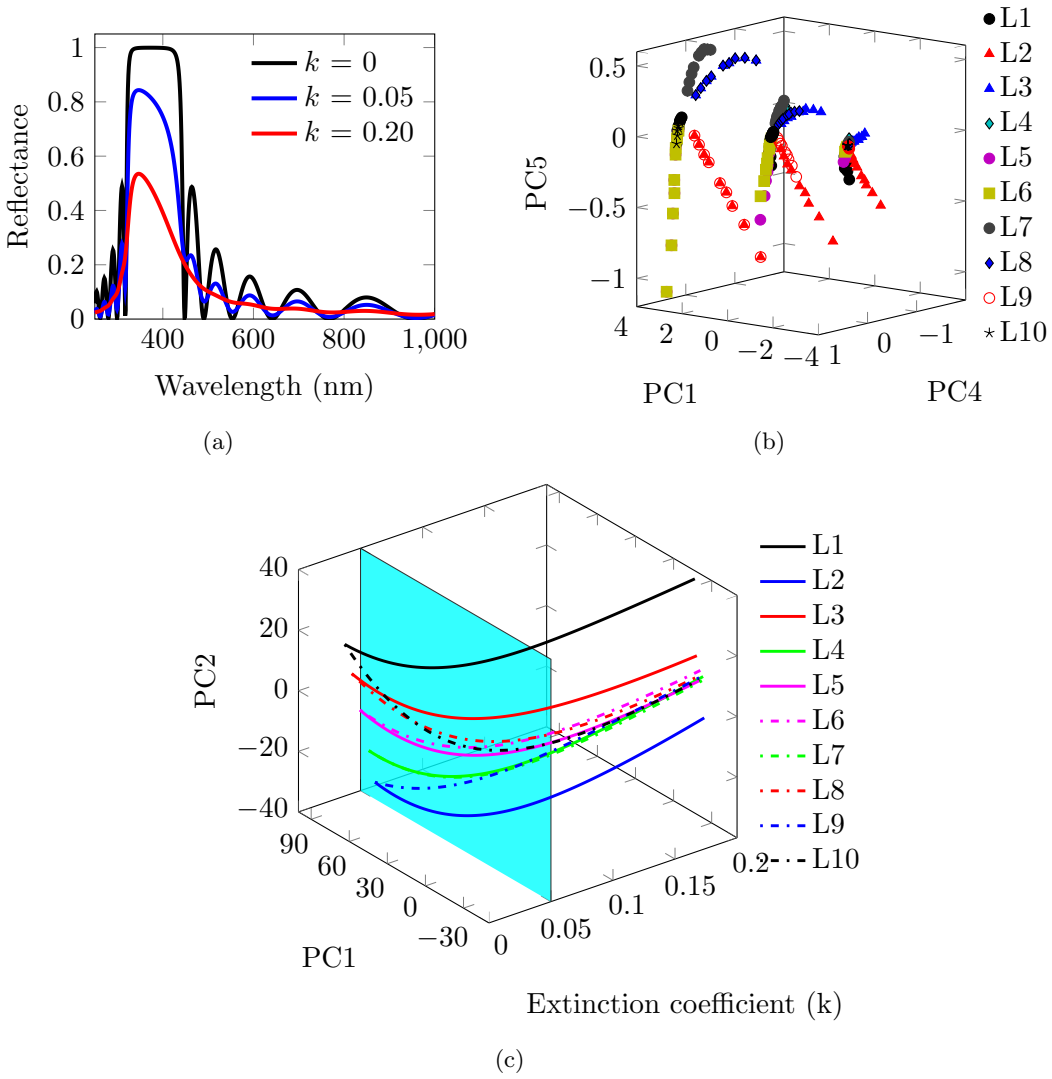

Figure 8.4: Analysis of the effect of optical absorption in the multilayer's reflecting lamellae on the sensitivity and selectivity of model vapour adsorption: (a) multilayer reflectance spectra for lamellae layers with extinction coefficients $k = 0$, 0.05 and then 0.20. (b) Scores plot of the combined PCA analysis of model vapour conditions on the multilayer with reflecting layers comprising extinction coefficients $k = 0$, 0.05 and then 0.20. (c) Visualisation of the inter-lamellae response-selectivity for vapour (RI $n = 1.4$, thickness $t = 10$ nm) as a function of increasing extinction coefficient.

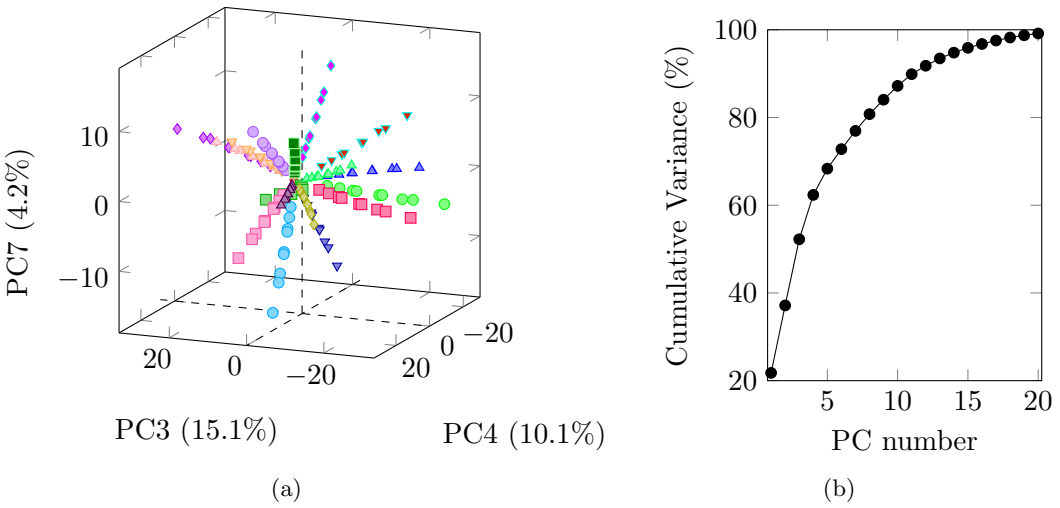

Figure 8.5: PCA analysis of a twenty layer multilayer stack with optically-absorbing lamellae ($k = 0.03$): (a) PC scores plot for PCs 3, 4 and 7, demonstrating the ability of the structure to transduce multiple spatial vapour locations, visualised as 'arms' in the PCA space, and (b) the cumulative variance captured with increasing PCs for this PCA analysis.

ences that are observed here through multivariate analysis. The response selectivity in PCA space is much harder to discern in this presentation of the PCA analysis.

In order to see how the response selectivity changes from $k = 0$, where no selectivity between layer-pairs is present, to $k = 0.20$, where there is a selective response, the inter-lamellae selectivity is considered. Here, the inter-lamellae selectivity is defined as how distinct one vapour adsorption is, relative to the same vapour condition on all other lamellae. The plot of this inter-lamellae response is shown in Figure 8.4(c), and is displayed for the first two PCs for increasing extinction coefficient. When $k = 0$ the layer-pairs discussed above cannot be distinguished from one another, but upon the introduction of small material optical absorption these layers become immediately resolvable. As the extinction coefficient approaches $k = 0.20$, the inter-lamellae selectivity diminishes as visualised by the converging of lines (in Figure 8.4(c)) that each represent vapour on a different layer. In the intermediate range of extinction values $k = 0.03$ to 0.07 the inter-lamellae selectivity appears greatest, as shown by the 2D plane in Figure 8.4(c).

This is a simple demonstration of how the response of a simple 1D reflector's optical response to vapour adsorption might be tailored through the tuning of the constituent materials' optical extinction coefficients. This concept may be incorporated into existing or new functionalised optically thick films, and to structures with higher layer numbers. Figure 8.5 displays a PCA analysis of a multilayer stack with increased layer

numbers for the vapour conditions previously described. The scores plot, in Figure 8.5(a), demonstrates that this multilayer, comprising twenty reflecting lamellae, can produce a selective multi-arm response achieved through the control of material optical absorption. Figure 8.5(b) demonstrates that higher-PC numbers capture significant variance, which allows vapour responses to be imaged at higher dimensions in the analysis.

8.2.2 Chirped multilayer designs

As shown in the previous section (Section 8.2.1), a sensitive vapour response can be tuned by the presence of optical absorption to form a selective response between model vapour adsorbed to different spatial locations of a 1D multilayer reflector. In the multivariate analysis used to visualise this response, only small spectral regions, corresponding to either side of the PBG, contributed to the analysis. Since modern instruments are capable of precisely sampling the intensities at many wavelengths across the visible spectrum, it might be advantageous for the spectral changes, which contribute to the PCA analysis to occur more broadly in the optical domain. This can be phrased as "is it possible to enhance the range of wavelengths that contribute to the multivariate analysis, and what effect does this have on the vapour-induced optical changes in reflectance?". This could be achieved with a broadband reflector, where changes in reflectance, upon vapour adsorption, occur over the same broadband range.

A simple approach to produce broadband reflectance, using a 1D photonic crystal, is to vary the RI profile of layers spatially through the thickness of the reflector - this is often referred to as 'chirping'. This distribution of layer thickness produces a broadband reflectance as more wavelengths may be preferentially reflected, as opposed to layers with fixed periodicity, which produce narrowband reflectance around one wavelength. In biological reflectors, chirped layers have evolved to create broadband metallic colour appearances [48, 59]. For instance, chirped reflectors have been documented in many beetle species [52, 310]. The chirped layers in their exocuticle skeleton usually display gradually increasing layer thicknesses from the outer most layer. These structures can give the beetle's elytra a metallic silver or gold appearance.

To examine the optically-induced vapour response of broadband reflectance from a 1D reflector, different chirped multilayer geometries are considered and compared to one of fixed RI periodicity. As a benchmark, a multilayer comprising nine layers with RI $n^* = 1.56 + i0.06$ and thickness $t = 55$ nm, separated by 100 nm 'air' layers is used (this is the same periodicity as the reflector in Section 8.2.1). This multilayer, that will be called 'multi 1', is altered to produce four chirped reflectors called 'chirp 1' to 'chirp 4', which all have the same optical thickness ($n \times t$) of 1572.2 nm. A schematic

of these reflectors is shown in Figure 8.6(a), and the associated layer thicknesses are displayed in Figure 8.6(b). The chirped structures numbered 1, 2 and 4 have a profile of decreasing thickness with linear dependence, from top to bottom, with increasing chirp gradient. 'Chirp 3' is also chirped, but has pairs of layers with the same thickness, which could also be described as a chirped filter.

The reflectance of these structures are displayed in Figure 8.6(c). These spectra were calculated for light impinging at normal incidence. As expected, the chirping of layer periodicities changes the main reflectance peak, associated with the PBG for structure 'multi 1', to a broad reflectance maxima across visible wavelengths, as layer periodicities become increasingly chirped.

To investigate the optically-induced vapour response, from the analysis of the calculated reflectance of these structures, model vapour is adsorbed to the top three, the middle three, and then the bottom three lamellae layers. This creates three spatial regions of model vapour adsorption. Vapour conditions of three thicknesses (t = 5, 10 and 15 nm) and three RIs (n = 1.3, 1.4 and 1.5) are considered.

The complete reflectance datasets for multilayer structures 'multi 1' and 'chirp 4', upon model vapour adsorption are displayed in Figure 8.7(a) and Figure 8.7(b) respectively. Comparison of the reflectance datasets for 'multi 1', the structure with regular periodicity, and 'chirp 4', which has the greatest variation of layer thicknesses, show that the chirped layers produce visually more diverse spectra; instead of small spectral shifts either side of the PBG, relative to the blank reference, chirping produces much larger changes in intensity, which occur more broadly across the visible wavelengths (see Figures 8.7(a) and 8.7(b)). In Figure 8.7(b) spectral differences associated with different spatial vapour adsorption are pronounced in different wavelength ranges. For instance, adsorption to the top lamellae produces large spectral changes in reflectance between wavelengths $\sim$ 300 to 400 nm, whilst these changes occur at $\sim$ 400 to 500 nm for the middle spatial region. This demonstrates the layer thicknesses are intrinsically related to the wavelengths they reflect.

Visualisation, through PCA, of the response sensitivity and selectivity reveals a 'multi-arm' pattern related to the number of spatial regions to which vapour is adsorbed, which is consistent with the previous analyses presented. Figure 8.8(a) shows this response for the 'multi 1' reflector shown in a 3D PCA scores plot. The same response is observed for the four chirped geometries; complete reflectance datasets and their PCA scores plots are displayed in Figure C.1 in Appendix C.

To quantitatively compare the response sensitivity and selectivity performance of these reflectors, the chirped layers are benchmarked against 'multi 1', which has fixed RI periodicity. This comparison is made using a commonly used approach, based on the Euclidean distances between data points in PCA scores space [311–313]. For the

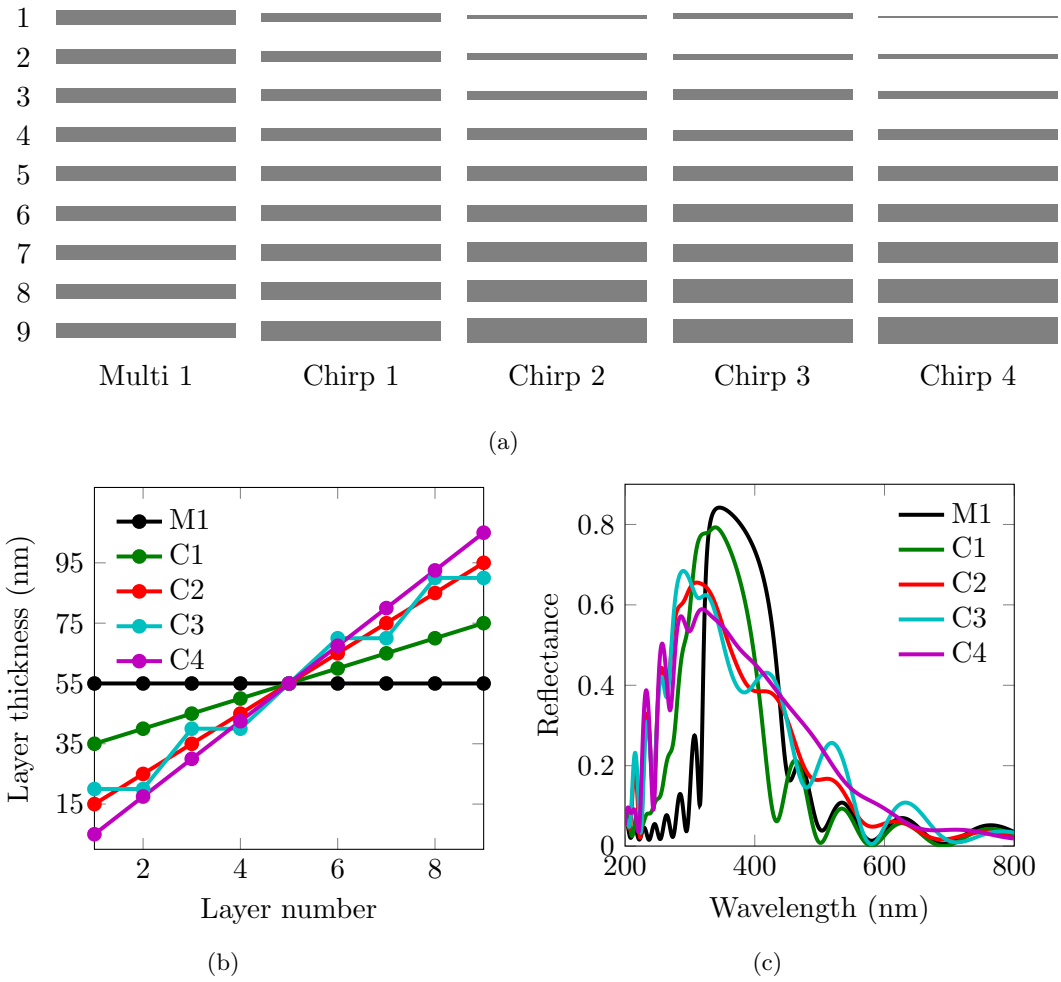

Figure 8.6: Exploration of chirped-multilayer structures for vapour selectivity and sensitivity analysis: (a) schematic of the bench-mark multilayer structure 'multi 1', to which the chirped layers 1 to 4 will be compared, (b) layer thickness profiles for each reflecting structure considered in (a), and (c) associated normal-incidence reflectance for these structures; chirping the lamellae layers broadens the reflectance maximum across visible wavelengths.

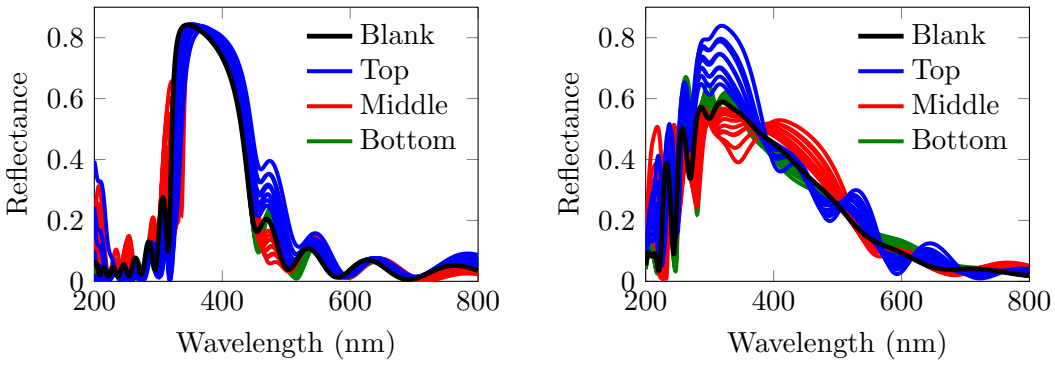

Figure 8.7: Comparison of the reflectance upon model vapour adsorption for: (a) the reference 'multi 1' reflector, with regular RI periodicity, and (b) 'chirp 4' reflector, with chirped RI periodicity, for model vapours with RIs $n = 1.3$, 1.4 and 1.5, and thicknesses $t = 5$, 10 and 15 nm.

sensitivity metric, the Euclidean distance from the point representing the reflectance spectrum of the blank structure, to the point which represents the reflectance spectrum for a model vapour condition (here RI $n = 1.4$, thickness $t = 10$ nm is chosen) on top (T), middle (M), and then bottom (B), is calculated. These Euclidean distances correspond to the length of lines connecting the blank spectrum to each corner of the triangle in PCA scores space, shown in Figure 8.8(a). For the selectivity metric, the Euclidean distance between a single vapour condition adsorbed to each spatial position is calculated. This corresponds to the length of the triangle vertices in Figure 8.8(a). To benchmark the performance of these different chirped structures, the Euclidean distances are normalised with respect to 'multi 1', with fixed RI periodicity. The results obtained using these metrics for the sensitivity and selectivity are displayed in Figures 8.8(b) and 8.8(c), respectively upon mean-centering of the reflectance datasets.

The sensitivity metric for these structures (in Figure 8.8(b)) shows that sensitivity is relatively constant for vapours adsorbed to the top or middle regions of each structure. In contrast, the normalised selectivity for model vapour adsorbed to the bottom lamellae layers shows an enhancement for all chirped geometries, with an approximately three-fold improvement for structures 'chirp 2' and 'chirp 3'. Usually the bottom-most layers have the poorest sensitivity, related to the smaller changes in reflectance intensity, for instance see Figure C.1(a) compared to Figure C.1(b), so it is interesting this enhancement is displayed.

The selectivity metric for these structures (in Figure 8.8(b)), demonstrates that structures with the greatest chirp-gradient, generally give rise to the largest Euclidean

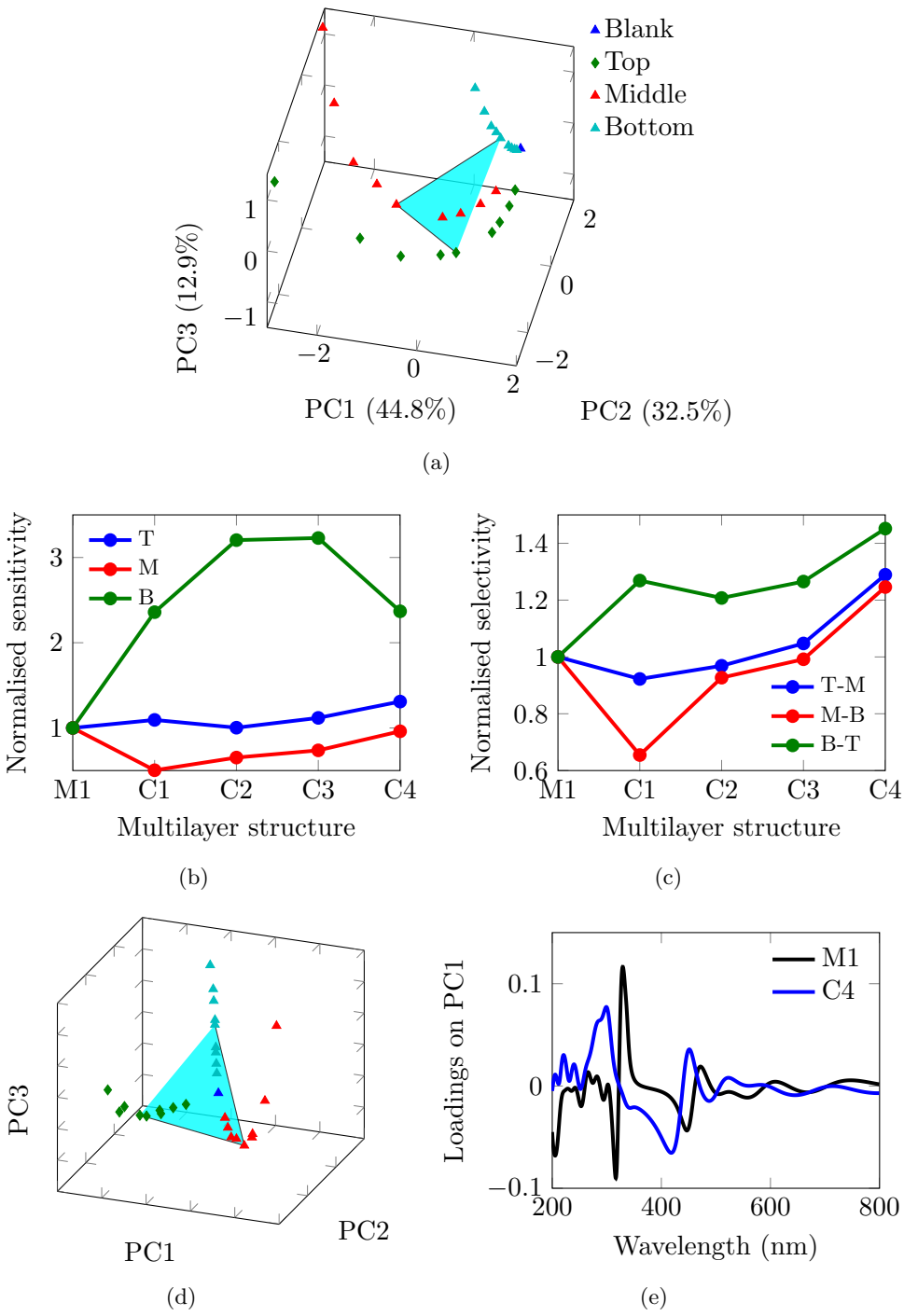

Figure 8.8: Analysis of model vapour adsorption on chirped multilayer designs: (a) PCA scores plot for all vapour conditions, adsorbed on top, middle and then bottom three lamellae of 'multi 1'. The opaque triangular-patch joins at the points corresponding to a single vapour condition (RI $n = 1.4$, thickness $t = 1.4$ nm) when adsorbed on each spatial location in turn. The Euclidean distance from the blank spectrum point to each corner is then used for the response sensitivity metric, whilst the vertex length is used as the response selectivity metric. (b) and (c) sensitivity and selectivity metrics for different layer designs, respectively (normalised w.r.t. the 'multi 1' control reflector). (d) PCA scores plot for the 'chirp 4' reflector, demonstrating a three-'arm' response (legend in (a)). (e) PCA loadings plot for 'multi 1' and 'chirp 4' reflectors.

distance between vapour on the different spatial locations.

As shown in the previous section (Section 8.2.1), the attenuation of light by the lamellae layer material can alter the optical response which in turn affects the sensitivity and selectivity. To explain this response, which has inter-related features, the 'chirp 4' structure is considered. The increase in sensitivity for vapour on the bottom layers is due to smaller attenuation of the incident, and reflected, light from the structure, due to the reduced optical thickness, and hence reduced optical absorption, of thinner top layers. This increase of sensitivity has consequences on selectivity between different spatially adsorbed vapour. As the sensitivity of the bottom spatial location is enhanced the spread of data points in the PCA scores place increases. Figure 8.8(d) displays the scores plot for structure 'chirp 4'; if the sensitivity of the arm associated with the bottom spatial region becomes longer, the Euclidean distance connecting the bottom/top and bottom/middle region increases, improving the selectivity. The selectivity is also enhanced by an increase in diversity of reflectance, upon vapour adsorption, between different spatial vapour locations. Figure 8.8(e) compares the PC loadings data between the 'multi 1' and the 'chirp 4' structure. As expected, due to the broadband reflectance, more wavelength variables contribute to the overall variance of the dataset for the chirped geometry, with respect to the multilayer of fixed RI periodicity. This implies that the reflectance datasets contain more diverse spectra - as evidenced visually in the reflectance datasets shown in Figure 8.7.

To demonstrate the counter-case, where the chirped layers are thickest at the top of the structure, the same but 'reversed' chirped structures, where the gradient of RI layer thicknesses runs from the top thick layers to thinner layers, was considered. A schematic diagram, layer profiles and the associated reflectance are displayed as supplementary information in Figures C.2 and C.3, in Appendix C. The calculations of response sensitivity and selectivity for these reflecting structures are shown in Figure C.4. Analysis of sensitivity for these structures, where the top most layers have greatest thickness, shows that the sensitivity is diminished by a factor of approximately a half for all structures, relative to the multilayer control. This relative change in sensitivity once again demonstrates the critical role of light-attenuation. Selectivity between the middle and bottom layers is also consequently diminished.

8.2.3 Summary

In this section, the effects of the material extinction coefficient k and simple chirping of layer periodicity on sensor selectivity have been studied. From the simulations of the optical spectra of a ten-lamellae sensing nanostructure to three vapours (RIs n = 1.3, 1.4 and 1.5; thicknesses t = 5, 10 and 15 nm) and lamellae material with $k = 0$ to

0.2, it was found that when different vapours interacted with a non-optically-absorbing multi-lamellae stack ($k = 0$), the optical responses lost their selectivity. Addition of a small optical absorption ($k \sim 0.03$ to 0.07) to the lamellae layer material resulted in ten sets of unique reflectance spectra, each associated with one specific vapour layer position in the ten-lamellae structure, forming ten arms in PCA space. The variation of $k = 0$ to 0.2 on the resulting sensor selectivity between each of the ten layers illustrates the key role of extinction coefficient in vapour-response selectivity, where selectivity arises from the attenuation of light propagating in the sensor, providing diverse reflected spectra for vapour layers on each lamellae. Thus, it has been shown that the absence of the material extinction removes the selectivity effect, while the presence of even a small extinction provides such ability. Performing the same vapour exposures upon three spatial regions of a nine-lamellae sensing structure, it was also shown that simple chirping of RI periodicity alters the response sensitivity and selectivity. This was also shown to arise due to the attenuation of light propagating within the structure. This new insight into the critical role of the nanostructure extinction on its selectivity of vapour response adds new and diverse possibilities for the creation of individual highly selective sensors.

8.3 Exploration of bio-inspired 'tree'-like structures for vapour sensing

As shown in Chapter 6 and in Chapter 7, the photonic structure present in the scales of the *Morpho* butterfly presents a novel approach to selective vapour sensing. In the previous section (Section 8.2), two simple approaches that might be incorporated into 1D photonic crystals sensors, to boost their currently unacceptable level of selectivity, were presented. Whilst these demonstrated that the optical parameters of a material need to be considered in the context of sensor designs, these structures are not that similar to those in the *Morpho* scales. With the fabrication techniques available in modern nano-science laboratories it is possible to realise micro- and nano-structures with high-structural complexity in two and three dimensions, and even to produce controlled local chemical properties. Therefore, here it is of interest to explore bio-inspired structures, beyond planar multilayers, that more closely mimic those of *Morpho* for vapour sensing applications.

In this section, the vapour response of regular 2D bio-inspired nanostructures are explored. First, an optical model of a multilayer comprising RI and structural periodicities similar to those in the scales of the *Morpho* is considered. This model is then developed, in increasing steps of structural complexity, to a ridge-lamellae type

structure. Following a description of the reflectance properties and the resonant features present, the structure is subjected to model vapour adsorption and the vapour response observed through both resonant and spectral data is considered. Finally, experimental results upon fabricated ridge-lamellae type structures are shown.

8.3.1 Evolution of reflectance properties: from multilayers to ridge-lamellae structures

8.3.1.1 Model development

The evolution of model development from a simple multilayer to a ridge-lamellae structure is shown in Figure 8.9. This schematic shows a 'cross-section' view through the model unit cells. These unit cells are constructed such that they are expanded by repeating the unit cell to form an array, and then extruded into the plane of the page to form 'infinite' 2D structures. A schematic to aid in visualisation of this geometric expansion is shown in Figure D.1 in Appendix D.

The first structure considered is a multilayer with dimensions and layer periodicities similar to that of *M. rhetenor*. This model, called 'structure 1', has 11 layers, each 55 nm thick separated by air layers of 100 nm, giving an overall physical thickness of 1605 nm. To form 'structure 2', this multilayer was then cut into discrete multilayer-stacks, each 500 nm wide, which are separated by a small air region of 50 nm. This introduces a grating periodicity of 550 nm in the plane associated with the repeating unit cell. 'Structure 3' is another 2D periodic structure, but has continuous multilayer with a 150 nm thick ridge-structure, producing the same grating pitch as 'structure 2'. The final model, 'structure 4', has both discrete multilayer and discrete ridge components. This can be described as a ridge-lamellae structure. The dimensions for this structure are 1605 nm high by 500 nm wide, which is approximately the same height and width of the bottom reflecting lamellae of *M. rhetenor* [63]. In summary, 'structure 1' is a continuous multilayer, 'structure 2' has discrete multilayering, 'structure 3' has continuous multilayer with periodic ridges, and 'structure 4' is a ridge-lamellae structure.

Once rendered, the four structures were assigned an RI of $n = 1.56 + i0$. The electromagnetic response of these four structures was simulated using the Finite Element Method, as described in Section 5.2.3. The reflectance of two linear orthogonal polarisations were calculated: (1) with the electric field oscillating parallel to the ridge ($R_{\parallel}$), and (2) with the electric field oscillating perpendicular to the ridge ($R_{\perp}$). These were simulated for incident angles from 0 to 70 degrees.

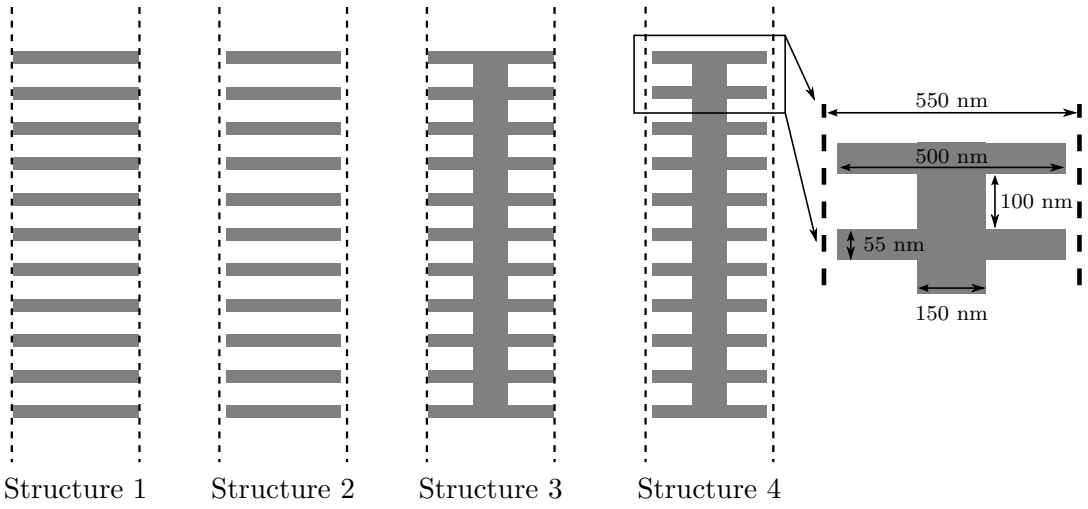

Figure 8.9: Schematic diagrams and physical dimensions for model dielectric structures in their unit cells: structure 1 shows a multilayer, structure 2 is a discrete multilayer, structure 3 a continuous multilayer with ridge, and structure 4 discrete multilayer with ridge. The dashed line indicates the boundary of the unit cell.

8.3.1.2 Spectral features

The results of the FEM simulations are displayed as reflectance maps in Figure 8.10. Note here, the spectra are displayed in terms of frequency as opposed to wavelength, this frequency range (375 to 784 THz) corresponds to wavelengths of 380 to 800 nm. This choice was made due to spectral resolution of simulations and the increased spacing between reflectance features when visualised in linear spacing of frequency spacing, relative to linear wavelength spacing.

The reflectance of the structure 1 (Figure 8.10) behaves as expected for a regular multilayer structure; here $R_{\perp}$ and $R_{\parallel}$ correspond to R_{s} and R_{p}, where s and p take their usual meanings. At normal incidence the reflectance shows the photonic band gap at high frequency, as visualised by the reflectance maxima of 100%. Both polarisations display characteristic shifts of the peak reflected wavelength and subsidiary interference minima and maxima, a Brewster feature is also present, at $\sim$ 55 degrees, for $R_{\parallel}$ (as discussed in Section 3.6.2).

Upon the introduction of periodicity, by making the continuous multilayer (structure 1) into discrete multilayer units (structure 2), the reflectance at angles close to normal does not appear to change. However, at angles larger than 20 degrees the reflectance response becomes quite different; splitting of the main reflectance peak, in the reflectance maps, is observed for both polarisations. The reflectance maps for structure 3, comprising continuous multilayer and vertical ridges, display this splitting

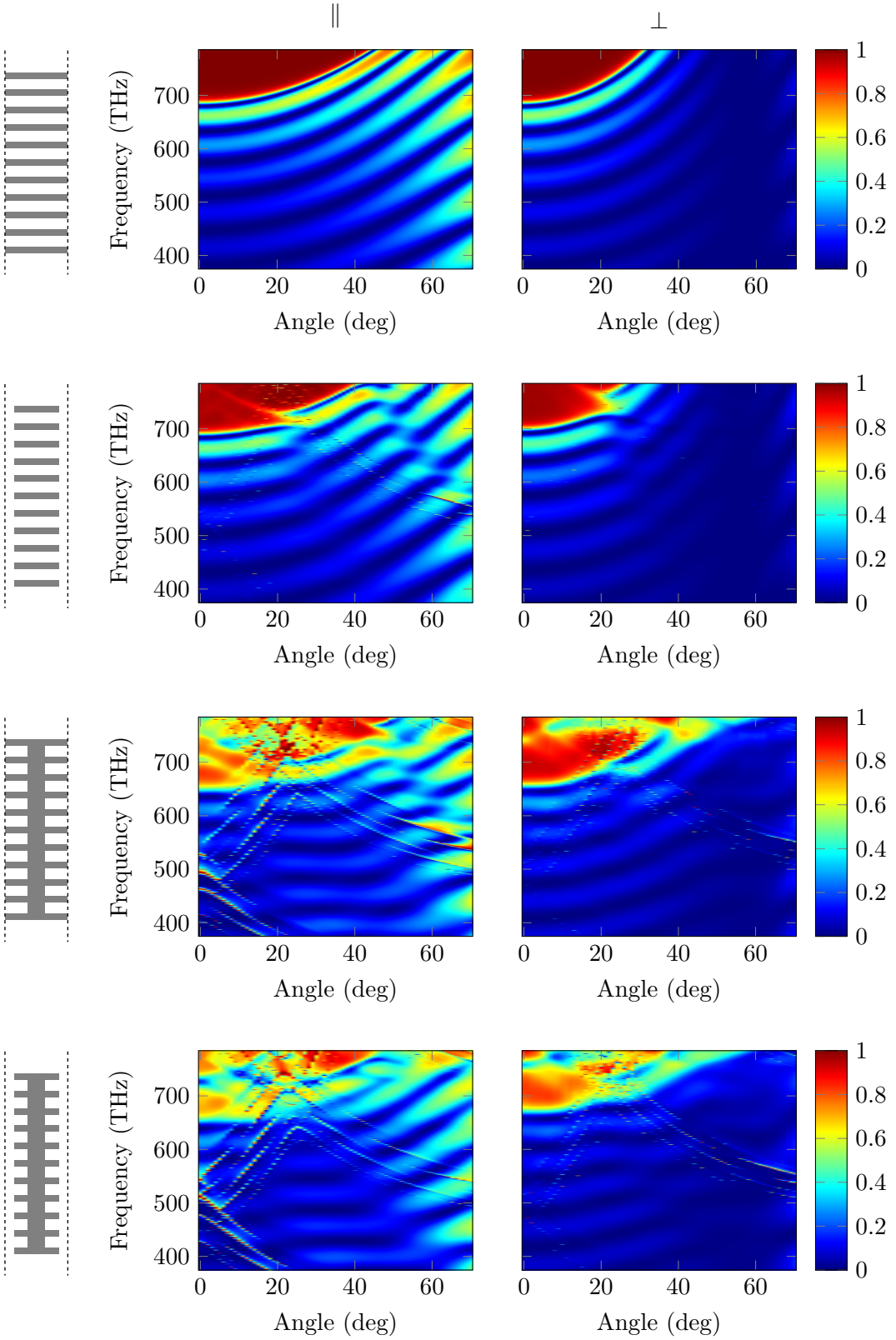

Figure 8.10: Reflectance maps for incidence angles from 0 to 70 degrees for dielectric structures 1 to 4 (from top to bottom). Reflectance displayed for electric field polarised parallel (left) and perpendicular (right) to the in-plane ridge visualised in structure 4.

more clearly. Comparing the reflectance maps for structure 3, to that for the multilayer, there are two further differences; first, the shift of peak reflectance with increasing angle, or iridescence, appears suppressed. Second, there are sharp high-intensity features/patterns that occur over this visible frequency range. Higher angular- and frequency-resolved data for two smaller regions within the reflectance map displaying these features is shown in supplementary Figure D.2 in Appendix D. Both the suppression of iridescence and high intensity features are more enhanced in the reflectance from the ridge-lamellae geometry (structure 4), shown in Figure 8.10 (bottom). Plotting the reflectance spectrum from these dielectric structures from a single incident angle displays these high intensity features clearly.

The reflectance for structure 4 is shown in Figures 8.11(a) and 8.11(b), for polarisations parallel and perpendicular to the ridge, respectively, for light incident normal to the surface. Both spectra display: (1) reflectance peaks associated with coherent scattering from the multilayer periodicities at high frequency; and (2) several high-quality (high-Q) reflectance peaks. Note here, these sharp features are being termed 'high-Q'; this is relative to the Q-factor of the broadband peaks associated with the structural colour features.

At first glance these features appear unphysical. To ensure these are 'real' features the results from FEM simulations were compared to other electromagnetic simulation methodologies. For structure 1, the calculated reflectance is easily verified using recursive Fresnel script, whilst the reflectance of more complex structures was verified with FDTD simulations. These curious high-Q features were also observed in reflectance measurements from fabricated dielectric ridge-lamellae structures. Examples of these structures and their high-Q reflectance features, which were fabricated and measured by collaborators at SUNY (Albany, NY, USA) and GE (Niskayuna, NY, USA), are shown in Figure D.3 in Appendix D. Encouraged by the presence of the high-Q features in theoretical and experimental results, the nature of these resonant features were explored.

8.3.1.3 Resonance and electromagnetic field enhancement

To elucidate the physical processes by which light interacts with these dielectric structures to produce these high-Q peaks FEM tools were employed. Using FEM, the time-averaged electric field profiles, at the frequencies corresponding to each high-Q peak were obtained. These field distributions, shown for light impinging on structure 4 for the two linear polarisations previously defined, are shown in Figures 8.11(c) and 8.11(d).

In these field plots, regions of high intensity are represented by red, and low inten-

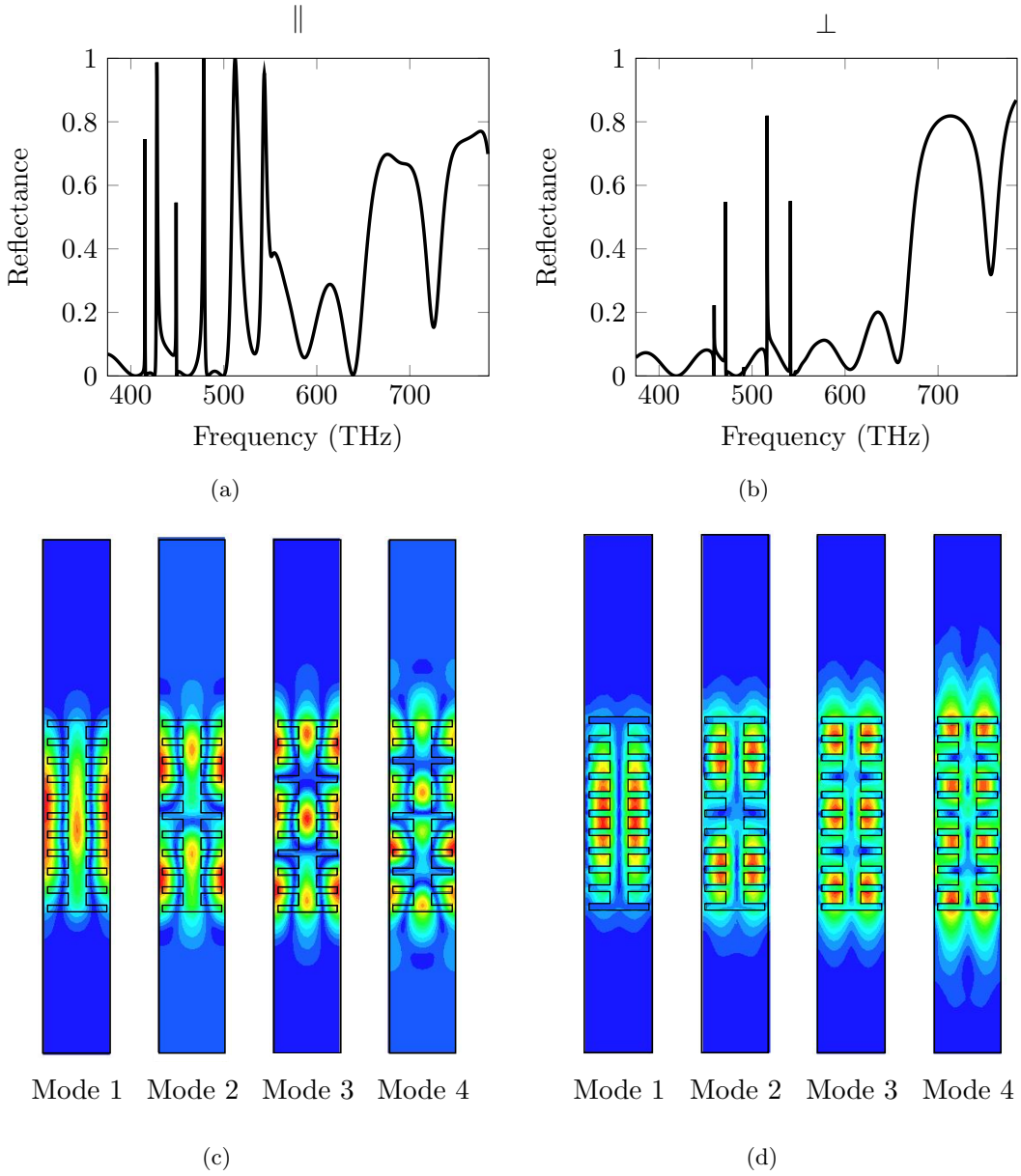

Figure 8.11: Demonstration of the high-Q resonant modes for the ridge-lamellae dielectric structure; (a) and (b) normal-incidence reflectance for parallel and perpendicular polarisations, respectively. (c) and (d) time-averaged electric field profiles for the first four (lowest frequency) resonant modes shown in the spectrums in (a) and (b). Regions of high field intensity are displayed as red, and low field intensity regions as blue.

sity by blue colours. The field plots for parallel polarisation, in Figure 8.11(c), display a series of resonant modes. Here 1, 2, 3, and then 4 spots of high field enhancement are shown along the vertical axis of the ridge and in the inter-structure spacing, with increasing frequency. These are a series of harmonic modes which, when on resonance, form standing waves which reflect those frequencies of incident radiation. Figure 8.11(d) shows a similar resonant pattern for resonant modes excited with perpendicular polarisation, however, the regions of high field intensity are now in the air regions between lamellae, rather than in the dielectric material.

The spectral shape exhibited by these resonances has the appearance of a Fano resonance [314]; the spectrum is asymmetric, with a sharp peak followed by a sharp dip (or vice-versa) [134]. These resonant phenomena occur when a continuous propagating wave state interacts with a discrete (also called a resonant) state [315]. These Fano resonances are observed in many interactions; for light, these interactions can occur with atoms or structured materials [315]. Here, incident light is coupled to the resonant modes of the structure, the frequencies at which these occur are dictated by the parameters of structure, which results in the resonant scattering.

Fano resonances that occur when light interacts with structured matter are often reported in structures comprising metallic particles, often where plasmonic effects are present. Studies have shown that these resonances might be utilised for sensing by tuning a resonance to be sensitive to changes in the local environment or geometry [316, 317]. As described in Chapter 4, several sensor methodologies exist where sensitivity is achieved by the change of resonant condition. Examples previously discussed are surface plasmon and localised surface plasmon resonance sensors. A metric commonly used to describe these resonances is the quality factor (Q-factor), defined as $Q = f_r/\Delta f$, where f_r is the resonant frequency and Δf is the half-width of the resonant peak [138]. The Q-factor of a typical SPR sensor is $Q \sim 50$ [192], however much larger Q-factors have been reported in dielectric metamaterials ($Q \sim 800$) [318] and waveguides ($Q \sim 10^3$) [319] (for further comparison, ultra-high-Q resonators have been reported with Q-factors on the order of 10^8 to 10^9 [320–322]).. For the simulated reflectance of the ridge-lamellae structure, the typical Q-value has a magnitude of the order 10^3, therefore, these structures might have the capacity to be used as a sensitive resonant sensor.

8.3.2 Investigation of *Morpho*-like structures for sensing applications

8.3.2.1 Refractive-index sensing with resonant modes

A number of novel photonic structures have recently been developed for biological and chemical detection exploiting electromagnetic resonances [234]. Therefore, here, it is interesting to study whether the Fano resonances in these ridge-lamellae structures can

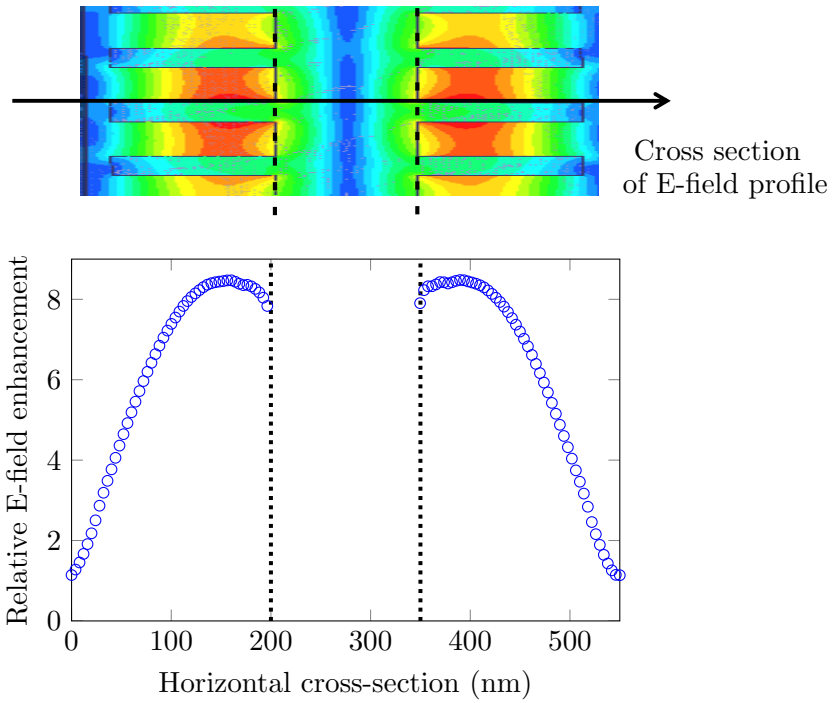

Figure 8.12: Spatial mapping of the relative electric field intensity through the region of high field enhancement of the fundamental resonance, excited with light polarised perpendicular to the structure's ridge.

be altered to provide sensitive responses to changes of the local chemical environment.

For an analytic chemical signal to be produced from these resonant modes, changes must occur upon vapour adsorption. As shown in field plots (in Figures 8.11(c) and 8.11(d)), a field enhancement occurs in the dielectric structure for parallel-polarised incident light, and in the inter-lamellae air voids for the perpendicular-polarised component. To cause significant modification to the resonance condition, changes in the chemical environment should occur in the regions of high electromagnetic field. For this reason, vapour adsorption upon this ridge-lamellae structure would have little effect on the resonant modes when incident electric field is polarised parallel to the ridge, relative to light polarised with the electric field perpendicular to the ridge.

Figure 8.12 displays the relative electric field intensity sampled across the horizontal plane through the inter-lamellae region of high field enhancement for the fundamental perpendicularly-polarised resonant mode. In the resonant 'hot' spot (the region of high field intensity), the field enhancement is a factor of 8.5 greater then the low intensity 'cold' spot region (the region of low field intensity).

To assess the sensitivity of this fundamental resonance, a model vapour condition

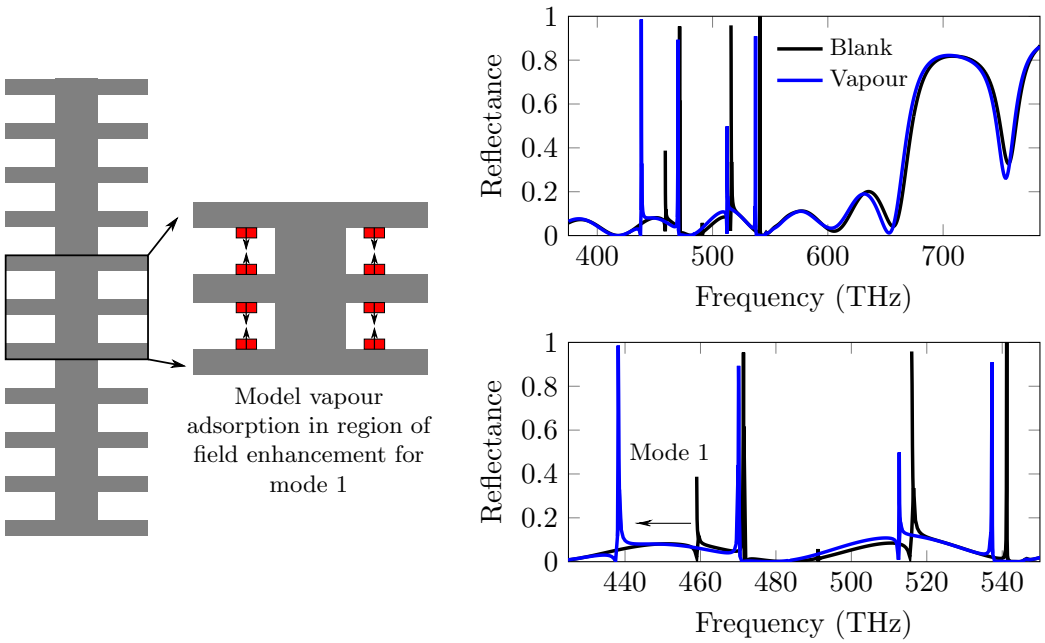

Figure 8.13: Exploration of Fano-resonance effects for a sensitive vapour response; (left) a schematic showing the position of model vapour in the region corresponding to the region of high electric field enhancement for the fundamental mode, and (right) reflectance data displaying the spectral shift of the resonant mode of the blank structure when vapour is added to the inter-lamellae space.

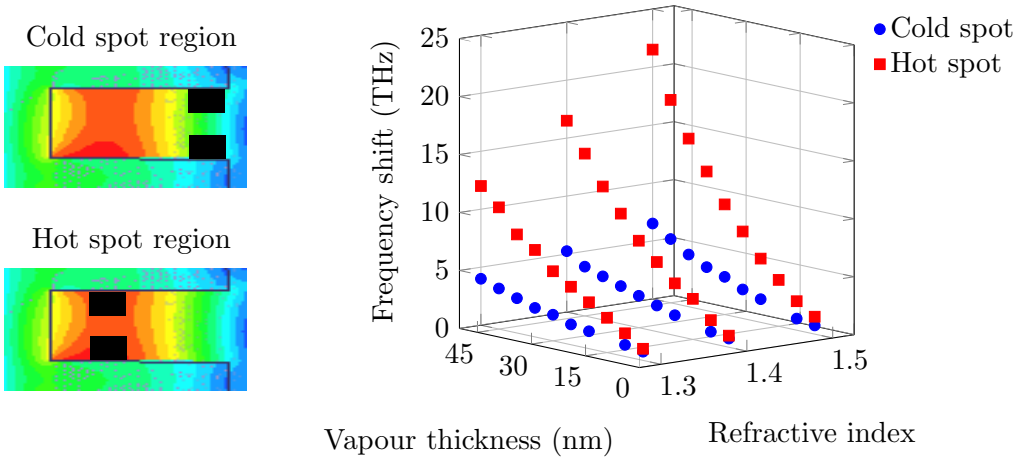

Figure 8.14: Investigation of the frequency-shift of the fundamental resonant peak when vapour is adsorbed in or out of the region of field enhancement: (a) schematic displaying vapour location, and (b) summary of the shift in resonant frequency for increasing vapour thicknesses for different RIs in 'cold' and 'hot' spots.

is simulated in and out of the region of high field enhancement. Vapour is modelled as a small volume of liquid represented as a dielectric material with a different RI to that of air. A small disc of vapour is simulated in this region to observe the effects of different thicknesses and RIs on the position of the resonance. A schematic of this model is shown in Figure 8.13.

Figure 8.13 displays the reflectance when a vapour of RI $n = 1.5$ fills the 'hot' spot region of the fundamental resonance. The presence of vapour pushes the resonant frequency of the fundamental mode down in frequency by approximately 20 THz. For the second order mode (mode 2) which occurs at ~ 470 THz, where the vapour location is the low intensity region of the electric field, there is a very small shift of the Fano peak. The higher order Fano modes also show a shift down in their resonant frequencies, which is attributed to model vapour being situated in one of their field 'hot' spots (maps of the field distributions in the presence of this vapour are shown in Figure D.6 in Appendix D).

To further quantify and cross-compare the response of the fundamental mode to a change of RI, simulations were performed with different vapour thicknesses and RIs in the inter-lamellae regions. These were simulated in and out of the 'hot' spot region to observe how the field enhancement influences the frequency-shift of the resonance. The schematic in Figure 8.14(a) displays the locations of these model vapour adsorptions. The resulting shift in resonance peak position for different RIs and thicknesses adsorbed to the 'hot' and 'cold' spot regions are summarised in Figure 8.14(b). These results demonstrate the critical role of field enhancement on the resulting sensitivity; when vapour is in a region of high field enhancement, the shift in resonant frequency is approximately a factor of three larger for 'hot' spot regions, relative to the 'cold' spot scenario. These shifts are near-linear for each RI considered.

This shifting of the resonant modes can also be demonstrated when vapour is placed in the 'hot' spots of the second order resonant mode, a schematic of which is shown in Figure D.5(a). This complementary example is included as supplementary information in Appendix D. Figure D.5(b) shows that when vapour is placed in the regions of high field intensity for this mode a large frequency shift is observed for the second order and the fundamental mode, due to the perturbation of the associated electromagnetic field distributions. Figure D.6 displays the time-averaged electric field distributions of the first five resonant modes when vapour is sorbed to regions of high field enhancement for the second order resonance. The electric field distributions for the fundamental and second order mode begin to show the same intensity distributions, this is expected since the resonances occur at similar frequency.

These demonstrations show sensitivity can be achieved in these ridge-lamellae structures through shifts of the resonant frequency of Fano-type spectral features. Using

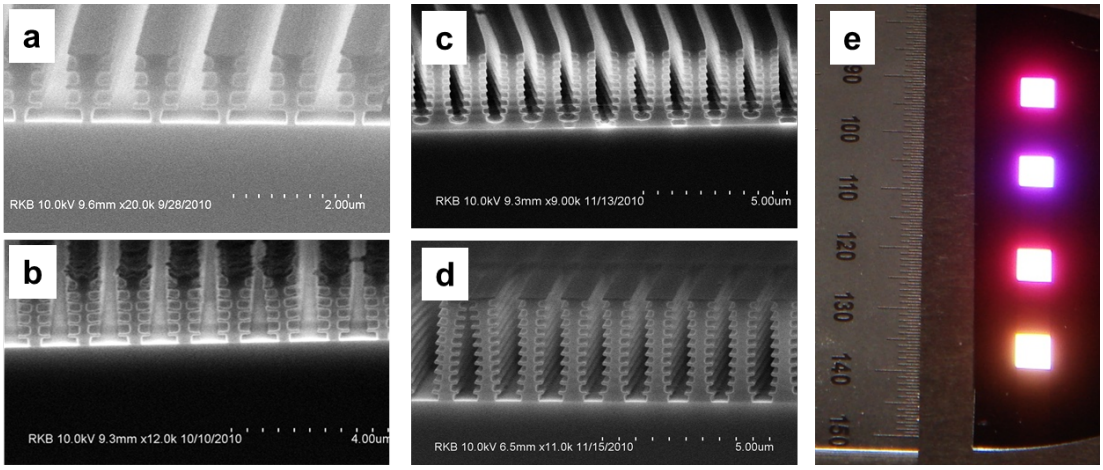

Figure 8.15: SEM images of the cross-section of an array of PMMA ridge-lamellae structures comprising (a) 4, (b) 6, (c) 10, and (d) 11 reflecting lamellae. (e) Photograph of light reflected from substrate with four 50 × 50 mm^2 regions of these PMMA nanofabricated arrays. (SEM images courtesy of R. Bonam).

resonance phenomena to obtain a sensitive response to changes in refractive index is not new [185, 192], however, here these simple demonstrations show that different resonant modes can be shifted nearly independently or together depending on the spatial location of vapour adsorption. This displays a unique sensing opportunity by control of the spatial adsorption of chemical species in different resonant modes.

8.3.2.2 Vapour selectivity of ridge-lamellae nanostructures

In the previous chapters, the selective responses, both calculated and measured, were obtained through the analysis of the whole reflectance in the visible wavelength range. Whilst the resonant modes shown in the previous section might add diversity to the collective optical response, the spectrally-transduced selectivity is of primary interest since, traditionally, selectivity is poor.

In this section, the spectral reflectance changes upon the addition of vapour to the ridge-lamellae structures is considered. This was studied since these structures can be realised in a laboratory. Some examples of these structures and their colour appearances (associated with the broadband spectral response) are shown in Figure 8.15. The structures shown here are formed from Poly(methyl methacrylate) (PMMA) upon a silicon substrate, but can be fabricated on different substrates, with different constituent materials, and with a high degree of control of the structural dimensions. The surface chemistry can also be altered and functionalised. For instance, for these PMMA structures, this could be achieved with polymeric or inorganic materials, or by oxygen plasma treatments, amongst other techniques.

	Alcohol	RI
a	methanol	1.3288
b	ethanol	1.3611
c	1-propanol	1.3850
d	1-butanol	1.3993
e	1-pentanol	1.4101
f	1-hexanol	1.4178
g	1-heptanol	1.4249

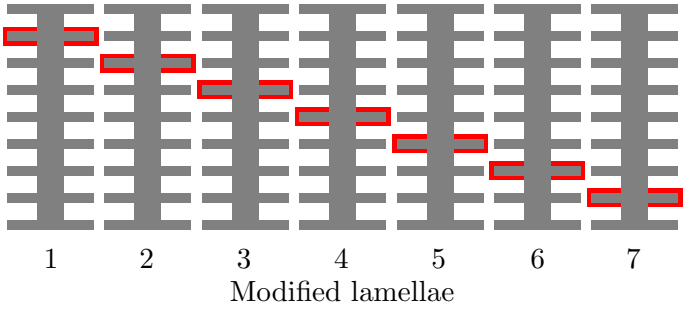

Figure 8.16: (Left) Table of the RIs, at 20°C [280], of seven simple -OH compounds in their homologous series, and (right) a schematic of the ridge-lamellae structure with seven 'modified' lamellae.

Whilst these structures were being developed experimentally, concurrent simulations were performed to assess their potential for providing a selective response to model vapour adsorption. To test these structures, model vapour coverage was simulated with the optical parameters of simple alcohols. The table in Figure 8.16(a) displays the names and RIs of the simple vapours modelled. Note these RIs have smaller differences in their values from those RIs of $n = 1.3$, 1.4 and 1.5 previously studied. Simulations of these seven organic compounds were performed on a structure with seven 'modified' lamellae. Figure 8.16(b) shows a schematic of these models. In these optical simulations, vapour was assumed to condense as a conformal film with different thicknesses ($t = 5$, 10 and 15 nm) to represent different vapour concentrations.

The dielectric nanostructure was assigned an RI $n = 1.56$, as before, with an extinction coefficient of $k = 0.06$. This extinction value reduces the reflected intensity and almost entirely removes the Fano resonances previously described (see Figure 8.17); since the spectral changes associated with the optical response are being studied, this is desirable. The optical response was simulated using FEM tools, as described in Section 5.2.3.

The blank reference spectrum calculated for this ridge-lamellae structure is shown in Figure 8.17(a), and displays a relatively broad reflectance which occurs over wavelengths from $\sim$ 300 nm to 450 nm. When vapour is adsorbed to each 'modified' lamella, changes in reflectance occur over these wavelengths. Figure 8.17(b) displays the reflectance when a uniform 10 nm of model butanol vapour is adsorbed to each lamellae in turn. Vapour on 'modified' lamellae 1 displays a discernible change in reflectance with respect to the blank reference, whilst the lower reflecting layers show very subtle changes in reflectance.

To image these spectral changes more clearly, the differential reflectance, ΔR, which accentuates the small spectral changes, is calculated. The differential reflectance for

all calculated vapour conditions (147 spectra) are displayed as a colour map in Figure 8.17(c). Here, each differential reflectance spectrum is plotted in order from the smallest to the largest optical thickness of adsorbed vapour, for each modified lamella, along the x-axis in Figure 8.17(c).

By representing the spectra in this way it is possible to observe how the change in reflectance occurs across visible wavelengths for different spatial adsorption positions. For instance, the vapour adsorbed on lamellae 1 causes large positive changes in the differential reflectance, whilst the same adsorptions on lamellae 2 causes large negative changes in the differential reflectance, and for both lamellae this occurs at higher wavelengths in this plot. In contrast, lamellae layers 3, 4 and 5 exhibit small relative changes in differential reflectance, and all have a negative ΔR peak at 400 nm, but at higher wavelengths spectral changes are diverse between layers. The spectral changes for lamellae 6 and 7 appear similar, however, the changes appear blue-shifted, and have higher relative magnitudes for lamellae 7. It is clear each different spatial adsorption condition provides a unique spectral profile, which could be transduced to provide a response-selectivity between these spatial locations.

To confirm that the modified lamellae produce not only a selective, but a sensitive, response in their spectral reflectance changes, PCA is used. The PCA analysis for the spectral dataset in Figure 8.17(c) is displayed as a PCA scores plot in Figure 8.17(d). In the PCA scores space, seven distinct 'arms', corresponding to each spatial adsorption scenario on the individual lamellae, are formed. The points form trajectories of the increasing optical thickness of the condensed liquid layers. The relative lengths of these arms are associated with magnitude of the spectral changes caused by the condensate. This is evident when comparing the differential reflectance, in Figure 8.17(c), with the relative lengths of the arms in PCA space, in Figure 8.17(d). Another interesting feature is that this multi-arm scores plot can be imaged at larger PC numbers; here PCs 1, 4 and 5 have been selected, demonstrating that this response can be observed in higher PC dimensional space.

This PCA analysis of the simulated reflectance data clearly shows that the vapour-induced spectral differences between each spatial vapour location arise in a vapour-sensitive and vapour-selective optical response. Sensitivity is achieved by the relative magnitudes in these spectral reflectance changes, whilst selectivity arises as a result of diversity in the spectral response between different spatial vapour adsorptions. Based on these results it is possible to conceive of highly selective nanostructured photonic sensors.

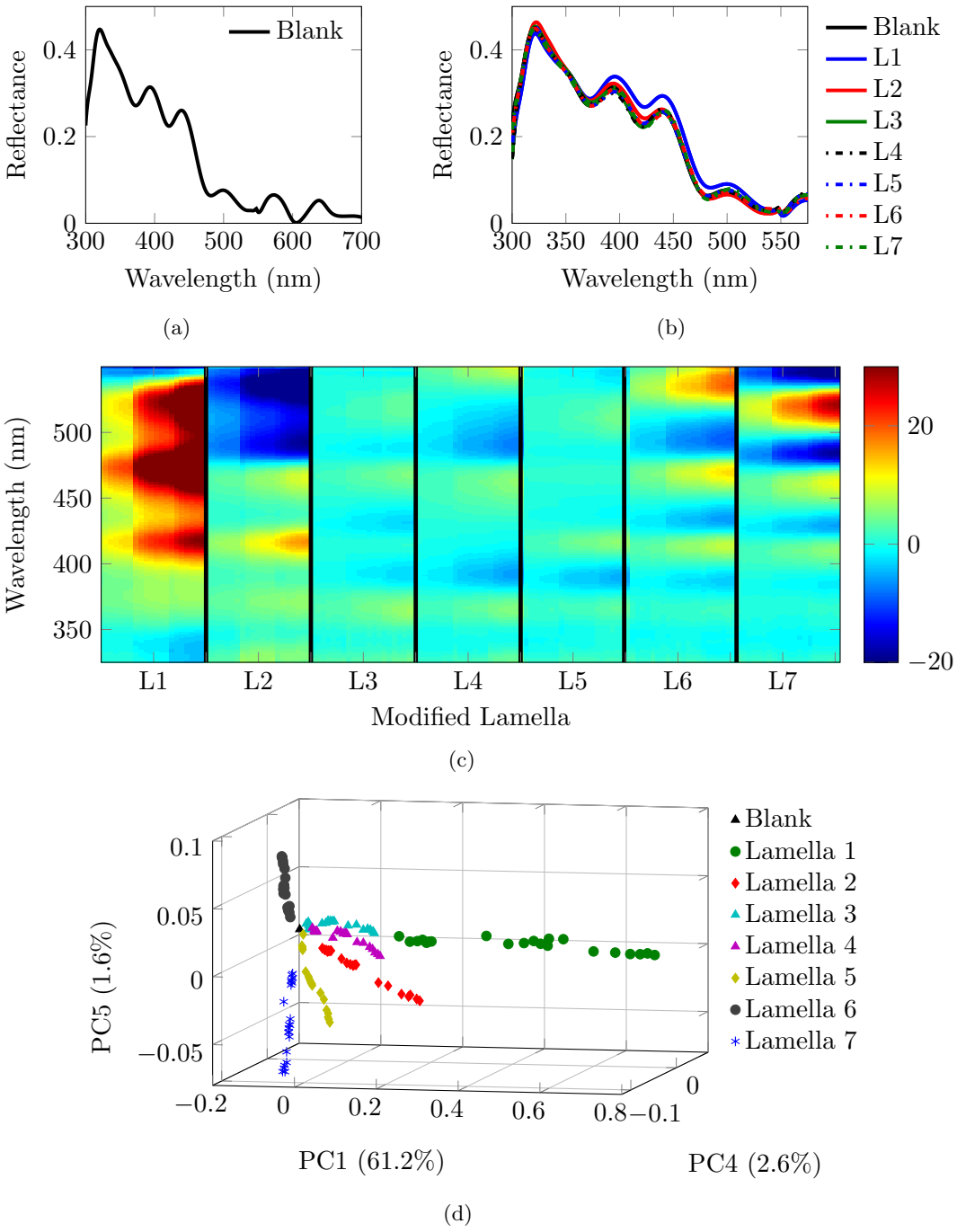

Figure 8.17: Reflectance and PCA analysis for model vapour adsorption upon 'modified' lamellae: (a) blank reference spectrum, and (b) reflectance spectra for a 10 nm thick uniform butanol vapour layer adsorbed to each layer displayed in the schematic in Figure 8.16(b). (c) Map of the differential reflectance $\Delta R(\%)$ (see Section 5.1.2), for all modelled vapour conditions in order of increasing optical thickness of vapour layer for each lamellae. Colour axis represents $\Delta R(\%)$. (d) PCA scores plot containing points corresponding to each spectrum in (c).

8.3.3 Vapour response of nanofabricated structures

To complement the theoretical results that form the basis of this chapter, and place them in a wider context, a brief presentation of vapour measurements on nanofabricated structures is made in this section. The experimental data herein was measured by collaborators at GE (Niskayuna, NY, USA) and at SUNY (Albany, NY, USA) as part of this collaborative DARPA-funded project.

In the initial detailed selectivity experiments, reported in 2007 [8], methanol and propanol were used as model analyte vapours. An excellent discrimination was obtained between these individual vapours in dry conditions using bare (unfunctionalised) *Morpho* structures, however, in the presence of humidity, selectivity was drastically degraded [8]. Using those results as a control the discrimination of these vapours in the presence of humidity for both functionalised *Morpho* scales and functionalised nanofabricated structures are investigated. Both the natural and fabricated structures (like those PMMA ridge-lamellae structures in Figure 8.15) were functionalised with a fluorosilane (FS) treatment, which has hydrophobic surface chemistry. Vapour was generated such that both primary and binary mixtures of methanol and propanol are generated in the presence of a humidity interferent. The map of vapour flow profiles for primary and binary mixtures is shown in Figure 8.18(a).

Figures 8.18(b) and 8.18(c) display the results of vapour exposures, as PCA scores plots, for *Morpho* and nanofabricated structures, respectively. The point pairs in PCA space are the results of two exposures on the same samples to test reproducibility. As before, for the bare *Morpho* structure, the functionalised *Morpho* structure discriminated individual methanol and propanol vapours. However, their ability to discriminate vapour mixtures was quite poor: as indicated by the poor resemblance of the experimental data and designed vapour profile map. This signifies that the contributions of individual vapours to the response of this structure to the mixtures of these vapours were not additive; instead one of the vapours dominated the response in the mixtures with significant non-linearities. In contrast, the FS-functionalised nanofabricated structure demonstrated an excellent discrimination between mixtures of vapours, even in the presence of a water vapour background. The scores plot depicts an additive response of individual vapours in their mixtures (Figure 8.18(c)), which has resemblance to the vapour flow profiles.

The developed individual nanofabricated structures demonstrate the discrimination of analytes in their binary mixtures even in the presence of background humidity. This brief demonstration shows that individual sensors, inspired from natural designs, can be fabricated and functionalised to produce a vapour response that outperforms the original structure from which inspiration was taken.

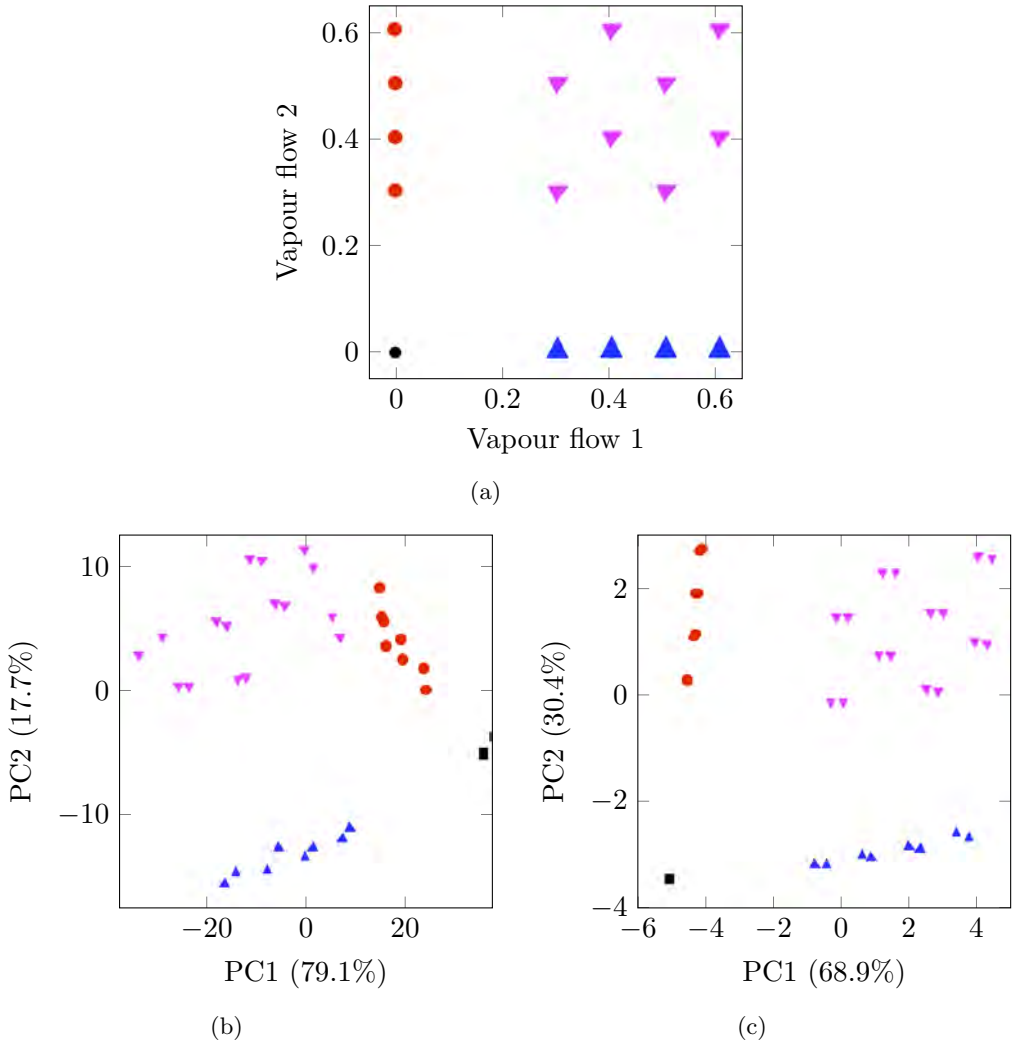

Figure 8.18: Comparison of the ability of natural and bio-inspired nanostructures to detect individual model vapours and their mixtures in the presence of humidity background. (a) Designed map of concentrations of individual vapours and their mixtures, and PCA scores plots of (b) fluorosilane-functionalised natural *Morpho* structure, and (c) fluorosilane-functionalised nanofabricated structure to methanol and propanol, and their binary mixtures, with a humidity background. Concentrations (P/P_0) of methanol and ethanol were 0.05, 0.07, 0.09, and 0.11 and the humidity background was a constant $0.4P/P_0$. (Data printed with permission of R. A. Potyrailo.)

8.4 Conclusions

In this chapter, optical simulation results and vapour measurements on nanofabricated structures have been presented. To begin, it was shown that simple multivariable sensors, with enhanced selectivity, could be achieved theoretically. In the quest for simplification of the *Morpho* structure, yet with enhancement of vapour selectivity beyond *Morpho*, multi-lamellae stacks with variable extinction ($k = 0$ to 0.2) of individual lamellae were explored. It was shown that the presence of even a small extinction in the layers (e.g. $k = 0.05$) provided the desired spectral discrimination between different lamellae of the multilayer reflector. In contrast, the absence of extinction in the layers eliminated this spectral discrimination. The optical response sensitivity and selectivity of these multilayers were enhanced by simply altering the periodicities of the reflecting lamella layers. This in turn influenced greater changes in reflected intensities over visible wavelengths. Importantly, these sensing responses were possible not by complicated design of sensor arrays, but rather by the careful selection of the real and imaginary RI components of the nanostructured lamellae.

The discussion then moved from the simple 1D photonic structures to more complex designs. The reflectance from these structures was first discussed before focusing on the vapour response of the ridge-lamellae type structures. Fano resonances, attributed to the coupling of propagating light with resonant states, were observed in the reflectance data. Response sensitivity was observed through the shift of these resonant peaks by localised adsorption of vapour in regions of high field enhancement. Experimental measurements also showed the high-Q resonances. In future studies, sensitivity enhancement might be explored by the use of plasmonic effects [323] or by incorporation of stimulated emission [324]. The spectral changes upon the adsorption of model vapours with the RIs of common VOCs were then shown. Multivariate analysis of calculated reflectance spectra revealed a sensitive and selective response with seven response directions. In future diversity in reflectance, which produces the selectivity, might be enhanced through scattering or measurement of different linear polarisations and angles.

Finally, experimental vapour measurements on both functionalised *Morpho* scales and functionalised nanofabricated ridge-lamellae structures were compared. This result demonstrated the first step toward creating high performance sensors based on the bio-inspired principles discussed.

Clearly localised chemical material control is required to realise these ambitious sensor designs. Such ability for superior selectivity could be achieved using different gradient functionalisation techniques [325]. Critical to the success of these new sensors is a surface functionality that does not reduce the response to analyte vapours in the

presence of overloading from interference vapours, especially water. Such response magnitude reduction is a common problem for different types of sensors [326–328].

There is huge potential for the further engineering, optimisation and application of the theoretical and experimental results presented here. These concepts could further be included in existing photonic crystals or sensors, for example photonic crystal chips [329], photonic crystal waveguides [330], colloidal- or silicon-based systems [200, 208, 228, 331], or as cladding of an optical fibre [332]. The vapour selectivity of the bio-inspired structures has become possible due to the synergistic effects of physical and chemical material control. This study is a step toward individual nanofabricated photonic sensors that exhibit multivariable responses that can compete for performance selectivity with more classic analytical systems.

Chapter 9

Conclusions and Future Work

This chapter aims to present a summary of the main scientific achievements and provide the final concluding remarks for the body of work contained in this thesis. First, a summary of the content and principal conclusions from each chapter is presented. Following this, there is a discussion on the future steps required towards the creation of ambitious bio-inspired sensors, and more general ideas for further research. Finally, the chapter concludes with a list of the publications, talks and poster presentations produced during the course of these studies.

9.1 Conclusions

The aim of the research in this Ph.D project was to study chemical vapour sensing in *Morpho* butterflies as a source of novel inspiration for the next generation of chemical sensors. The primary motivation was to explore new ideas in the pursuit of developing new concepts for the design of photonic sensors that are both sensitive and selective to chemicals in their vapour phases, which outperform current sensor array implementations. This thesis presents a selection of results obtained during the course of this project.

The opening chapters of this thesis comprised general overviews as a foundation for later discussions. These chapters include a review of colour in biological systems, a description of the fundamental physical interactions that give rise to structural colouration, and a review of the field of sensing. In Chapter 2, a review of the field of natural optics was presented. This field, which began as an area of scientific research following the works of Mason and others in the 1920s, has seen continued growth since the late 1990s. The review presented in this thesis set out to describe examples of a number of bio-photonic structures across a range of species. A range of photonic crystal topologies, their optical properties, and their biological significance were appraised. Following this,

studies specifically relating to the optical properties and underlying photonic structure of the *Morpho* butterfly were presented as an overview for later discussions in Chapters 6 and 7. Finally, a short discussion was made on the impact this butterfly has had on several applications, such in reflectors, textiles and in sensing.

Following the review of colour production in biological systems, the electromagnetic theory that is used to describe and calculate the optical responses that arise through coherent scattering in these natural systems was addressed in Chapter 3. First, Maxwell's equations were stated, and from these the eigenvalue equation that defines the general behaviour of electromagnetic radiation in a photonic crystal comprising linear, lossless, isotropic dielectric materials was presented. The properties of a 1D photonic crystal, or multilayer stack, comprising a finite number of layers were shown, and the factors that affect the reflectance of biological multilayers elucidated.

Chapter 4 provided a background to sensing principles and common electromagnetic sensing approaches. The main components and response characteristics of a sensor, which was broadly defined to be a device which converts chemical information into an analytical signal, were reviewed. Classical electromagnetic sensing techniques which transduce a signal by measuring the wave properties of the probe radiation were shown; these properties are often amplitude, phase, polarisation, temporal dynamics or spectral profiles. Some of these approaches that operate in the optical regime are waveguide, surface plasmon resonance, and interferometric techniques.

In Chapter 5 the experimental, theoretical and data processing methods used in the investigations in Chapters 6, 7 and 8 were described.

The first experimental chapter, Chapter 6, investigated the mechanism by which the sensitive and selective vapour-induced optical-response of the *Morpho* butterfly's wing scales is transduced. By using electromagnetic simulations, it was shown that uniform spatial vapour adsorption on the photonic structure did not produce the response observed experimentally. Namely, no selectivity was observed when data was visualised through PCA analysis. This result led to the conclusion that the observed vapour-response was not solely due to the process of coherent scattering within the *Morpho* ridges when vapour was present. To probe the photonic structure further, optical and fluorescence characterisations, chemical composition analysis, and control experiments were performed. The results of these showed that a chemical gradient of surface polarity exists within the photonic ridge-lamellae structure. This gradient of polarity runs from the most polar ridge-tops to the less polar ridge-bottoms. Further simulations and vapour measurements demonstrated that this chemical environment is responsible for the vapour-response selectivity and sensitivity by the preferential adsorption of vapour molecules upon the structure. This preferential vapour adsorption gives rise to unique optical responses due to the changes of coherent scattering con-

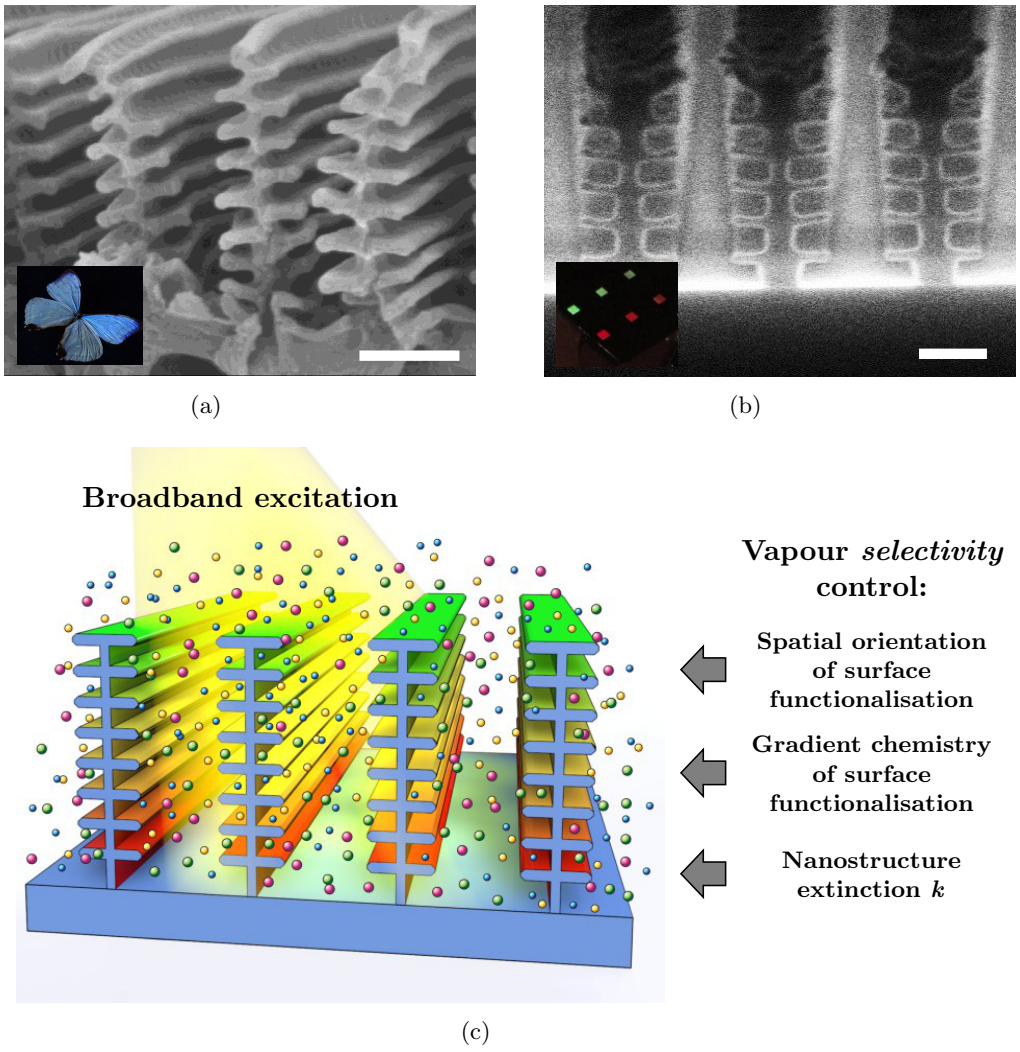

Figure 9.1: Achieving vapour-selectivity in bio-inspired nanostructures inspired by *Morpho* butterflies: (a) SEM displaying the *Morpho*'s biological template studied as the source of bio-inspiration, and (b) SEM of a PMMA nanofabricated structure developed for sensing ((a) and (b) insets display photographs of the macroscopic colour appearance of the photonic structures displayed in (a) and (b) respectively). (c) Schematic representation of a fabricated nanostructure and the principles for vapour-selectivity control discovered in the studies presented in this thesis. (Figure printed with permission of R. A. Potyrailo). [Scale bars: 500 nm].

ditions associated with spatial location. Appreciation of this combined chemical and physical mechanism opens opportunities for new design principles of gas and liquid sensors with tailored selectivity in a single sensing unit, rather than with individually fabricated and multiplexed sensors.

Following this, Chapter 7 presented further investigations performed on the *Morpho* scales. To begin, some key experimental demonstrations, with theoretical support, showed that the *Morpho* scales display many response attributes that are desirable for optical chemical sensing. These attributes were diverse in the reflectance-response when comparing different linear polarisation and angular excitations, in the temporal response profiles, and in the steady-state spectral responses. These diverse optical responses arise due to the interaction of light with the anisotropic geometry of the photonic structure in the *Morpho* wing-scales. Future bio-inspired sensor units could incorporate anisotropic micro- and nano-structures to enhance the diversity of response, as a route to provide additional information to identify chemical species. Further results, presented in Chapter 7, showed an insensitivity between different measurement conditions of spectral data. Multivariate analysis of the steady-state optical response showed essentially the same distinction between vapours and different concentrations. This property of the *Morpho* scales, which is due to the coherent scattering to enhance its conspicuousness, is interesting from a stand-off detection perspective; for instance in remote sensing, where precise measurement conditions cannot be controlled. Finally, this chapter concluded with a simulation experiment on a 'functionalised' *Morpho* photonic structure. The functionalised adsorptions were performed on three spatial regions along the height of the tree, and also on the vertical and horizontal sections of the nanostructure. Results not only demonstrated that the spectral responses were selective between all six vapour conditions but, more critically, also showed that this unoptimised dielectric structure could offer enhanced vapour selectivity with the right surface functionalisation.

Encouraged by the findings of Chapters 6 and 7, Chapter 8 focused on bio-inspired sensor designs, with particular attention to enhancement of the vapour-response selectivity. The first section theoretically demonstrated simple methods to alter the vapour response selectivity of 1D multilayer reflectors. Calculations showed that the resulting sensor response is strongly affected by altering the optical extinction and refractive index periodicities. In the second section, the optical responses of more complex dielectric photonic structures, beyond simple multilayers, were examined. A structure with ridges and lamellae, which resembles the butterfly structure more closely, was subjected to vapour adsorption with electromagnetic simulation tools. Results associated with both broadband and high-Q features showed that a multivariable response could be achieved between vapours of close refractive index when absorbed to different lamella. Addition-

ally, high-Q resonant modes of the structure were shown to be sensitive to the refractive index of model sorbed vapour. Finally, to whet the appetite, experimental vapour exposure data demonstrated the excellent discrimination of two simple alcohol vapours in primary and binary mixtures, in the presence of a background of humidity. The results presented in this chapter could not only be incorporated into existing photonic sensor designs, but also to promote a step towards individual nanofabricated photonic sensors that can compete for performance selectivity with more classical analytical systems.

The key fundamental results obtained from the investigations upon the iridescent scales of the *Morpho* butterfly and bio-inspired nanostructures towards highly-selective photonic sensors are summarised in Figure 9.1. Through the collaborative research undertaken during this Ph.D project, the natural template in the *Morpho* scales (Figure 9.1(a)) has been analysed to generate new ideas for the field of chemical sensing. These results have seen the development of ridge-lamellae nanofabricated structures (Figure 9.1(b)) for the development of highly-selective unitary sensors, using both the design principles elucidated in Chapters 6, 7, and 8. These principles are summarised in the schematic shown in Figure 9.1(c). Namely, these are the control of vapour selectivity by (1) spatial orientation of surface chemistry, (2) the spatial distribution of the surface chemistry, and (3) material extinction coefficient.

9.2 Future work

The results presented in this thesis are viewed as steps toward individual nanofabricated photonic sensors in which optical measurements from a single sensor unit can transduce a selective and sensitive response to chemical vapours. In this section, the steps required in the realisation of such sensor devices are outlined, and some further future work is suggested.

The results of Chapter 6, which elucidated the chemical properties of the *Morpho* scales, can be viewed as a self-contained study. As such, this biological template requires no further study by the chemical sensing community, since the lessons have been learnt. Instead, the results on the chemical pattern in the *Morpho*'s scales, and its formation, could be further explored in the context of smart self-assembled materials [333–338]. For instance, local chemical gradients or patterning that change across nanoscale length-scales could have numerous technological applications ranging from security tags to self-cleaning surfaces, gas separators, and protective clothing.

In terms of further work related to photonic sensing, continued research into aspects of the synthetic sensor systems and designs would be more pertinent than continued study into the natural structures. One reason for this, is that many studies of biological systems reveal some form of optimisation that pertain to a particular function or ap-

pearance [55, 70, 78, 119]. The topic of study in this thesis is somewhat unusual since the general mechanism used to produce the multivariable vapour response appears to serve no function for the butterfly. Since the *Morpho* has no interest in being a sensor, it is unlikely to be structurally or chemically tuned (or evolved) to do so. Therefore, designs of hierarchical photonic sensors, based on the *Morpho*'s scales, could certainly be optimised both chemically and physically.

To implement any sensor device, including the *Morpho*-inspired photonic sensor previously described, a number of factors must be addressed in order to bring a device from idealised laboratory conditions to in-the-field situation. The scaleability, sensitivity, selectivity and stability all have to be considered under constraints such as feasibility and cost.

Scalability of nanofabricated materials and structures at large scale is becoming less of an obstacle due to increase in investment and research into these technologies. This has been largely progressed due to a wide range of multidisciplinary applications of the technology, and has resulted in improvements to the fabrication quality, size, and speed [230–233]. The bio-inspired PMMA structures, fabricated by collaborators during this project, were created by interference lithography, however, if required for scalability, similar structures may also be fabricated by other well understood and commonly used approaches. This could be achieved with focused-ion-beam [299] and electron-beam lithography [339], direct etching [300], or etching-photolithography combinations [340]. Achieving cost-effective high-throughput production of these structures would enable competition with other photonic crystals currently being studied [199, 200, 341, 342].

Although the main focus of this thesis was to look at the enhancement of selectivity levels in photonic sensors, the sensitivity of these bio-inspired sensors could be easily improved beyond the butterfly's current 1 - 2 ppm sensitivity levels [8] using well understood principles. These principles can be by physical and by chemical mechanisms. One standard approach to improve sensitivity is to enhance the confinement of the probe radiation within the regions in which an analyte will be present. With the ridge-lamellae structures, this could be achieved by increasing the layer numbers, optimising the material properties, or by enhancing the resonant high-Q features. Furthermore, general approaches commonly used to achieve field enhancements could also be implemented, for instance, by incorporating metallic inclusions to introduce plasmonic effects [323]. Alternatively, materials of different porocity and varying pore size might be used to control the preferential adsorption and dynamic responses of vapour molecules, or by using polymeric materials [158] that swell in the presence of vapour. Chemical routes for improved sensitivity may include improving the partition coefficient [343] for the target vapours though materials and the addition of chemical functionalisation to the nanostructure material or surface [274].

There are further obstacles in moving a *Morpho*-inspired sensing nanostructure from the laboratory into a working situation. Two such hurdles are the cost and portability. For example, all spectral data presented in this thesis was measured with a spectrometer, which comes at a cost which would be prohibitive in some applications that a sensor of this type would be applicable. In this scenario, alternative solutions would be required such as a CCD detector.

The practical implementation of photonic nanostructured sensors has not strongly influenced the investigations, since the main focus has been on understanding how to achieve, and how the butterfly's structure achieves, a vapour-response selectivity. The experimental measurements have utilised reflectance data from the natural and synthetic samples to obtain an analytical signal. However, the findings on the vapour-selectivity principles are not limited to those measurement conditions, and could be integrated into other existing sensor designs using different measurement approaches. For instance, new vapour-selectivity principles could be exploited by incorporating them into photonic sensor approaches, for example in photonic chips [329], waveguides [344], or as a cladding of an optical fibre [332].

An avenue of research, separate to sensing, following on from the study in Chapter 8, would be further investigation of the resonances in the *Morpho*-inspired dielectric structures. Resonances, such as these, in photonic crystals have broad interest in sensing, small-band-filters, and in non-linear-optics applications [320, 345, 346]. The results presented in Section 8.3.1.2 demonstrated a series of Fano-like resonant modes in reflectance. Further numerical simulation results have already shown that these modes have the characteristics of diffractively-coupled leaky guided modes (unpublished). Investigations into the role of a substrate on the resonant modes, whether the resonances could be decoupled from the diffraction edge by altering the periodicity or structure's refractive index, and the factors which cause the suppression of iridescence would all be interesting extensions.

9.3 Publications and presentations

9.3.1 Refereed papers

- 'Multivariable signal transduction in photonic nanostructures of *Morpho* butterfly scales for high-performance vapor sensing'. (In preparation).

- Potyrailo, R.A., Bonam, R.K., Hartley, J.G., Starkey, T.A., Vukusic, P., Vasudev, M.,Bunning, T., Naik, R.R., Tang, Z., Palacios, M.A., Larsen, M., Le Tarte, L.A., Grande, J.C., Deng, T., and Zhong, S.

'Design and fabrication of photonic vapour sensors inspired by *Morpho* butterflies: towards outperforming conventional sensor arrays'. (Submitted).

- Potyrailo,* R.A., Starkey,* T.A., Vukusic, P., Ghiradella H., Vasudev M., Bunning T., Naik R.R., Tang, Z., Larsen, M., Deng T., Zhong S., Palacios, M., Grande, J.C., Zorn, G., Goddard, G. and Zalyubovskiy, S. 'Discovery of the surface polarity gradient on iridescent *Morpho* butterfly scales'. *Proceedings of the National Academy of Sciences of the United States of America* **39** 15567 (2013). Ref. [12].

- Starkey, T.A. and Vukusic, P. Light manipulation principles in biological photonic systems. *Nanophotonics* **4** 289-307 (2013). Ref. [11].

9.3.2 Conference proceedings

- McDonald, L, Starkey, T.A. and Vukusic, P. Photonic Architectures in Beetles: Twists and Iridescence. *Design and Nature* (2014). (Accepted).

- Starkey, T.A., Vukusic, P. and Potyrailo, R.A. Toward bioinspired nanostructures for selective vapor sensing: diverse vapor-induced spectral responses within iridescent scales of *Morpho* butterflies. *MRS Proceedings* **1621** (2014). Ref. [13].

- Starkey, T.A., Potyrailo, R.A. and Vukusic, P. Bio-inspired Photonic Vapour Sensing: Lessons from Butterflies. In Optical Interference Coatings, MD.10. OSA, Washington D.C, USA (2013). Ref. [347].

9.3.3 Oral presentations

- Starkey, T.A., Potyrailo, R.A. and Vukusic, P. Bio-inspired Photonic Vapour Sensing: Lessons from Butterflies'. *Optical Interference Coatings Conference, OSA, Whistler, Canada* (June 2013).

- Starkey, T.A. 'From natural to bio-inspired photonic vapour sensors through theory and experimentation'. *GE Global Research Seminar, Albany, NY, USA* (January 2012).

9.3.4 Poster presentations

- Starkey, T., Potyrailo, R.A. and Vukusic, P. Biologically Inspired Volatile Chemical Sensing with *Morpho* Butterfly Scales. *Living Light 2014, Namur, Belgium* (April 2014).

- Starkey, T., Vukusic, P. and Potyrailo, R.A. Diverse vapor-induced spectral responses of iridescent butterfly scales. *MRS Fall Meeting, MRS, Boston, USA* (December 2013). *"Best Poster" Nominee.*

- Starkey, T., Potyrailo, R.A. and Vukusic, P. Bio-inspired Photonic Vapour Sensing: Lessons from Butterflies. *Optical Interference Coatings Conference, OSA, Whistler, Canada* (June 2013).

9.3.5 Online presentations

- Starkey, T. 'Diverse vapor-induced spectral responses of iridescent butterfly scales'. *MRS OnDemand: "Best Poster" Nominee Talks*, (January 2014). Ref. [348].

Appendix A

Vapour Generation and Concentration

If the vapour pressure, P_0, is expressed in terms of parts-per-million, and the bubbler headspace is assumed to be in equilibrium with the surroundings, Equation 5.4 (in Section 5.1.3) can be simplified further to:

$$\text{conc. (ppm)} = \epsilon(1,000,000 x_{\text{vapour}}) \frac{f_{\text{carrier}}}{F_{\text{carrier}}} \tag{A.1}$$

The flow of the carrier gas, f_{carrier}, is varied to provide different vapour concentration. The quotation of vapour concentrations varies in the literature from values quoted as a fraction of the saturated vapour pressure, i.e. $0.02P_0$, and the parts-per-million (ppm) convention. Table A.1 provides a reference to convert between these different conventions.

Table A.1: Table of common volatile organic compounds with their respective vapour pressures, and associated parts-per-million concentration values for the partial vapour pressures generated by the bubbler system.

Vapour	x_{vapour} at 25°C	P_0 (ppm)	$0.02P_0$ (ppm)	$0.04P_0$ (ppm)	$0.07P_0$ (ppm)	$0.10P_0$ (ppm)	$0.15P_0$ (ppm)	$0.20P_0$ (ppm)
water	0.0316	31579	632	1263	2211	3158	4737	6316
methanol	0.1671	167105	3342	6684	11697	16711	25066	33421
ethanol	0.0587	58684	1174	2347	4108	5868	8803	11737
1-propanol	0.0276	27632	553	1105	1934	2763	4145	5526
1-butanol	0.0084	8421	168	337	589	842	1263	1684
1-pentanol	0.0029	2895	58	116	203	289	434	579
1-hexanol	0.0011	1092	22	44	76	109	164	218
1-heptanol	0.0007	658	13	26	46	66	99	132
1-octanol	0.0001	105	2	4	7	11	16	21

Appendix B

Experimental Evidence for the Vapour Response Mechanism

The figures in this appendix provide further experimental evidence for the gradient of polarity within the iridescent scales of the *Morpho* butterflies described in Chapter 6.

These figures are reproduced from published work titled 'Discovery of the surface polarity gradient on iridescent *Morpho* butterfly scales reveals a mechanism of their selective vapor response' in Proceedings of the National Academy of Sciences of the United States of America, Volume 110, Issue 39, Pages 15567-15572, Year 2013 in Ref. [12], with permission of the Proceedings of the National Academy of Sciences of the United States of America.

The measurements presented were performed by researchers at General Electric Global Research Center (Niskayuna, NY, USA) and the Air Force Research Laboratory (Wright-Patterson Air Force Base, OH, USA).

B. Experimental Evidence for the Vapour Response Mechanism

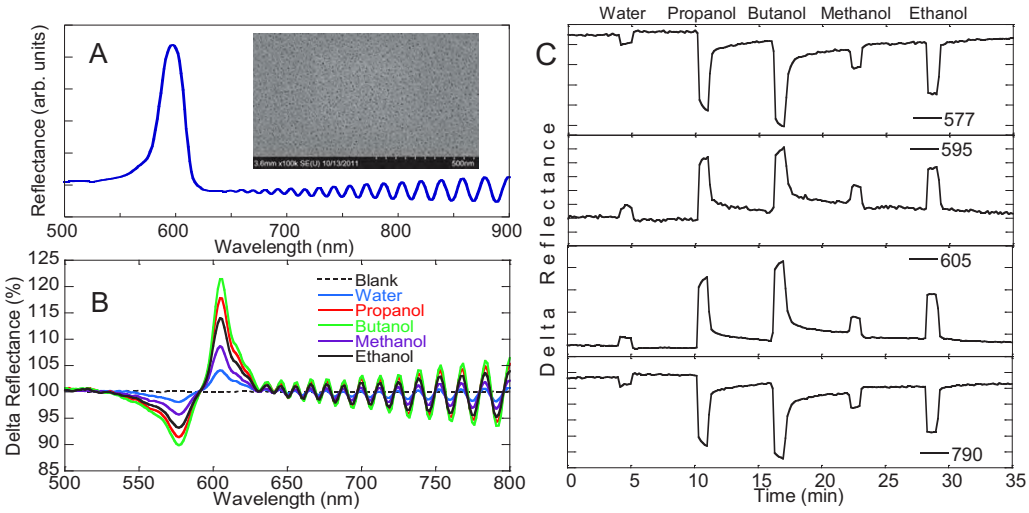

Figure B.1: Assessment of spectral and dynamic responses to vapours of a classic chemically uniform sensing material such as porous silicon. (A) Porous silicon reflectance spectrum. The known distinct interference ripples at wavelengths above $\sim$ 630 nm are caused by the interface between the porous silicon and the substrate. (Inset) SEM image. (B) Differential reflectance spectral response of porous silicon $\Delta R(\lambda)$ to five tested vapours. (C) Dynamic responses $\Delta R(\lambda)$ of porous silicon at four representative wavelengths of 577, 595, 605, and 790 nm demonstrate wavelength-correlated relative intensities and dynamic profiles to different vapours that indicate no spectral discrimination between different vapours. Concentrations of tested vapours in (B) and (C) were 0.02 P/P_0 except for water vapour, which was 0.2 P/P_0.

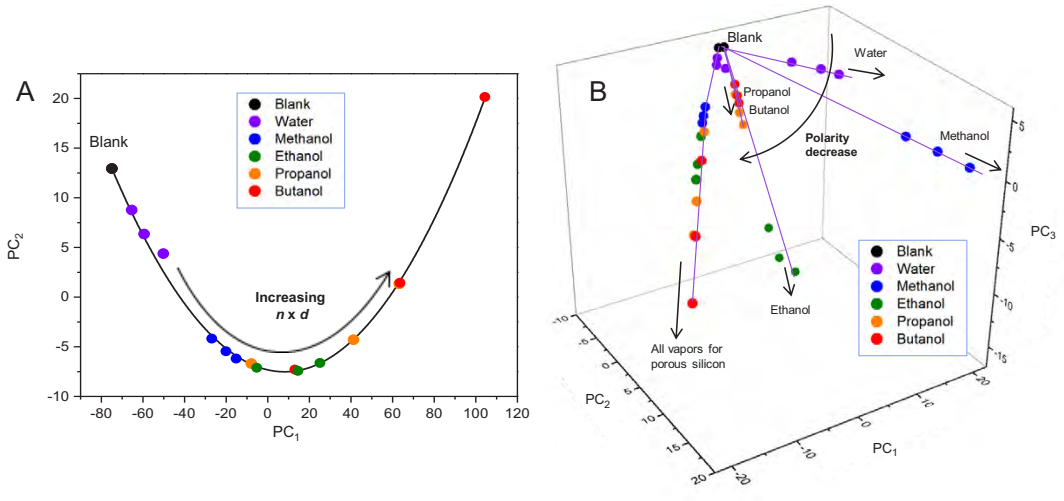

Figure B.2: Comparison of spectral responses of *Morpho* scales and a classic chemically uniform sensing material such as porous silicon to methanol, ethanol, propanol, butanol, and water vapours based on multivariate analysis of $\Delta R(\lambda)$ spectra. (A) Scores plot of a PCA classification of spectral response of porous silicon. (B) Scores plot of a PCA classification of spectral response of porous silicon and *Morpho* scales. Concentrations of all tested vapours were 0.02, 0.04, and 0.06 P/P_0, except for water vapour for porous silicon, which were 0.2, 0.4, and 0.6 P/P_0. Lines in (A) and (B) are $n \times d$ fits to the scores data for individual vapours.

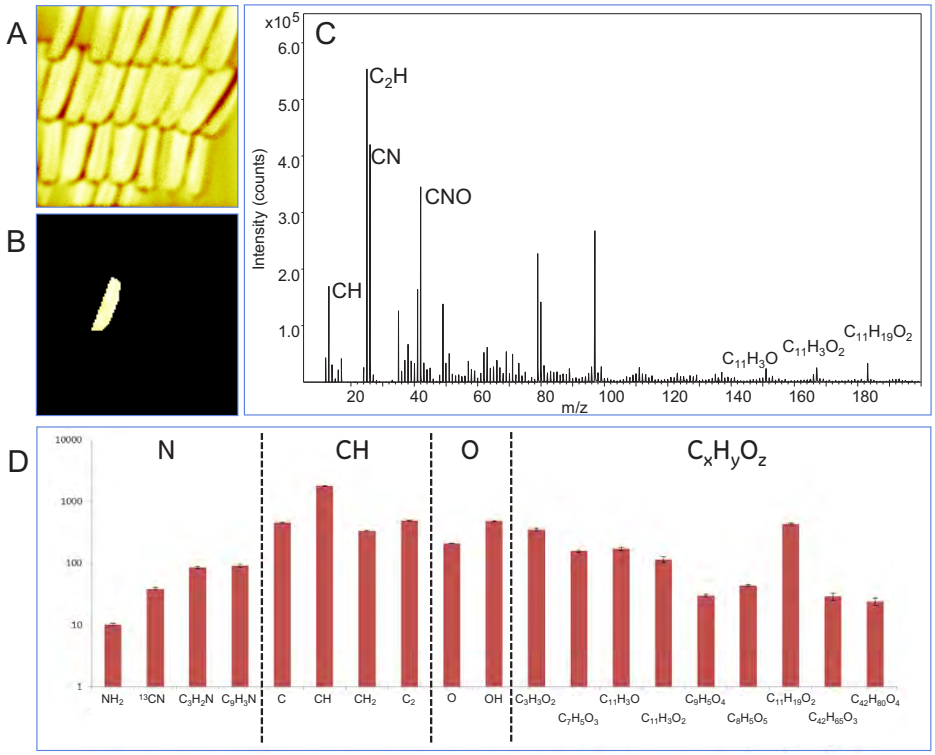

Figure B.3: Results of imaging of intact butterfly scales using time-of-flight secondary ion mass spectrometry (ToF-SIMS). (A) Example of 500- × 500- µm ToF-SIMS image of the total ions emitted from the butterfly wing. (B) Representative reconstructed ToF-SIMS image from a single butterfly scale. (C) MS spectrum of a single butterfly scale shown in (B). (D) ToF-SIMS average peak intensities from 15 individual scales normalised to the intensity of the C_2H_3 fragment demonstrating the existence of oxygen- and nitrogen-containing fragments. Error bars in (D) are 1 σ of measurements ($n = 3$ per individual scale).

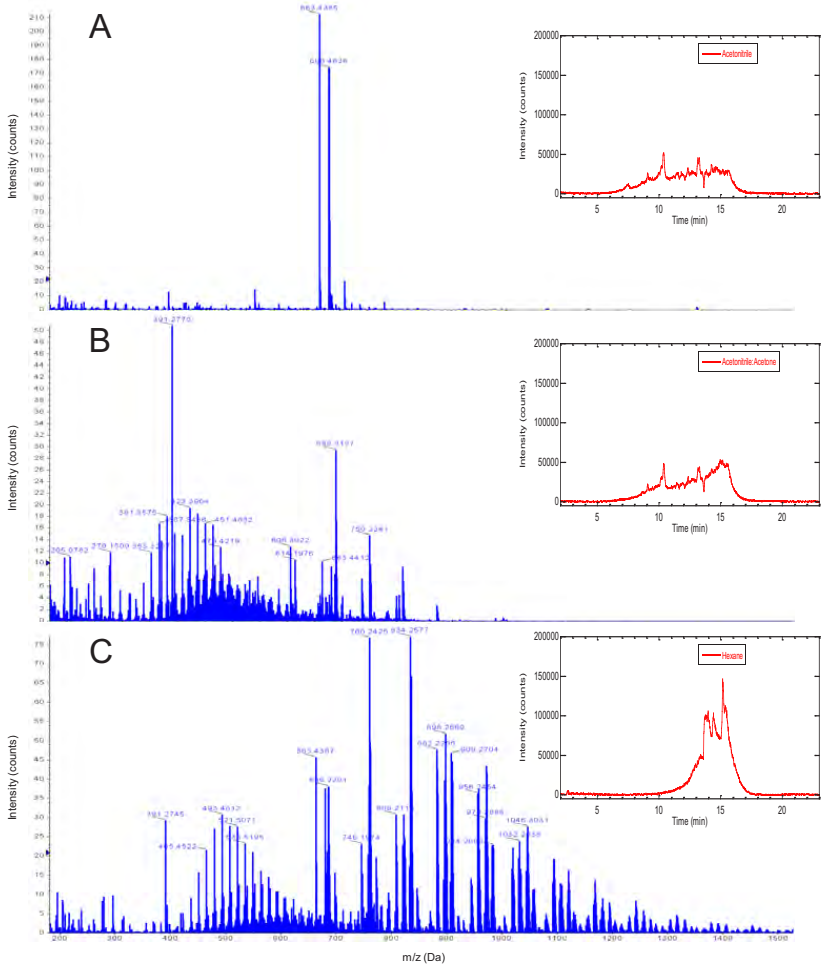

Figure B.4: Positive ion ToF mass spectra and total ion chromatograms of analysis of butterfly wing extracts using solvent-extraction liquid chromatography-ToF-MS. (A) Acetonitrile as extraction solvent. Mass spectrum yielded only small molecules and some unknowns. (B) Acetonitrile: acetone (1:1) as extraction binary solvent. Mass spectrum yielded small molecules, a distribution of small charged hydrocarbon species as well as larger masses that might be consistent with triacylglyceride lipids, and phospholipid species. (C) Hexane as extraction solvent. Mass spectrum yielded a distribution of small charged hydrocarbon species and a larger portion of high masses that might be consistent with triacylglyceride lipids and phospholipids. Mass spectra are within the retention time window of 13–17 min. Insets in (A)–(C) are total ion chromatograms.

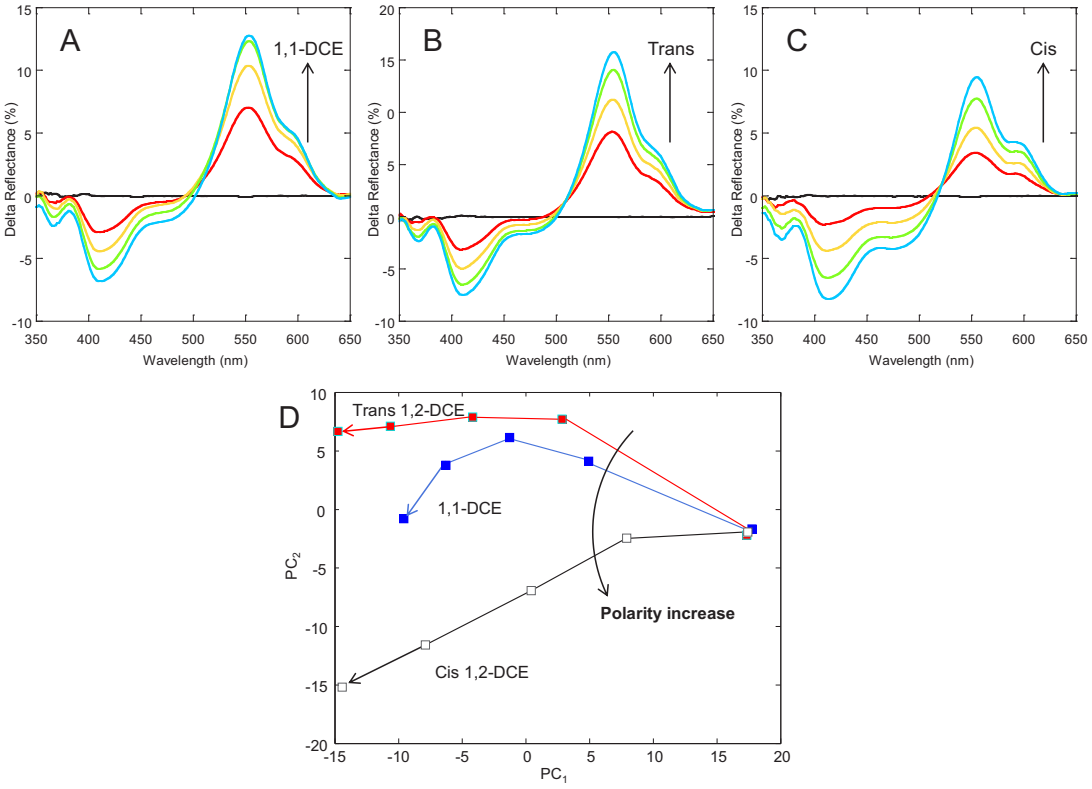

Figure B.5: Validation of the origin of the vapour-response selectivity of *Morpho* scales by measurements of vapours of similar refractive indices and different polarities. Vapours are three isomers of dichloroethylene (DCE) such as 1,1-DCE, trans-1,2-DCE, and cis-1,2-DCE. Concentrations of tested vapours: 0, 0.02, 0.04, 0.07, and 0.1 P/P_0. (A)(C) $\Delta R(\lambda)$ spectra of 1,l-DCE, trans-1,2-DCE, and cis-1,2-DCE, respectively. (D) Principal components analysis (PCA) scores plot of $\Delta R(\lambda)$ spectra upon exposures to three DCE isomers. Two isomers (trans-1,2-DCE and cis-1,2-DCE) have the same refractive index $n = 1.449$, and the third (1,1-DCE) has refractive index $n = 1.425$. We found that the PCA response was not in the order of vapour refractive index but rather of polarity of these three isomers: $E_T = 34.2$, 37.0, and 41.9 kcal.mol^{-1} for trans-1,2-DCE, 1,1-DCE, and cis-1,2-DCE, respectively.

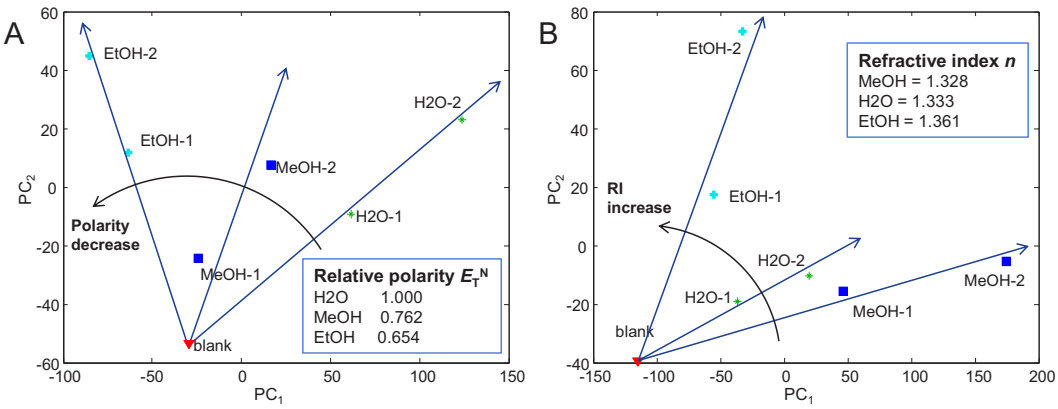

Figure B.6: Validation of the origin of the vapour-response selectivity of *Morpho* scales by measurements of vapours of different refractive indices and different polarities before and after a mild oxygen plasma treatment. Vapours: water, methanol, and ethanol. (A) PCA scores plot of *Morpho* scales to closely related vapours demonstrates a polarity-related response. (B) PCA scores plot of a 10 sec oxygen plasma-treated *Morpho* scales to closely related vapours demonstrates a refractive index-related response. Whereas the response of a native *Morpho* scales to water, methanol, and ethanol was in order of the vapour polarity, this vapour-response dependence was lost after 10 sec oxygen plasma treatment. Concentrations of tested vapours were 0.04 and 0.08 P/P_0.

Appendix C

Analysis of Vapour Adsorption on Chirped Multilayers

This appendix contains supplementary data to support the discussion in Chapter 8 (Section 8.2.2) on the analysis of model vapour-induced optical response of different chirped multilayer geometries. Figure C.1 displays the data used in the analysis of the response selectivity and sensitivity of chirped layer designs labelled 1 to 4. Figures C.2, C.3 and C.4, display the spectral data and PCA analysis of the previously studied chirped geometries in reverse configuration.

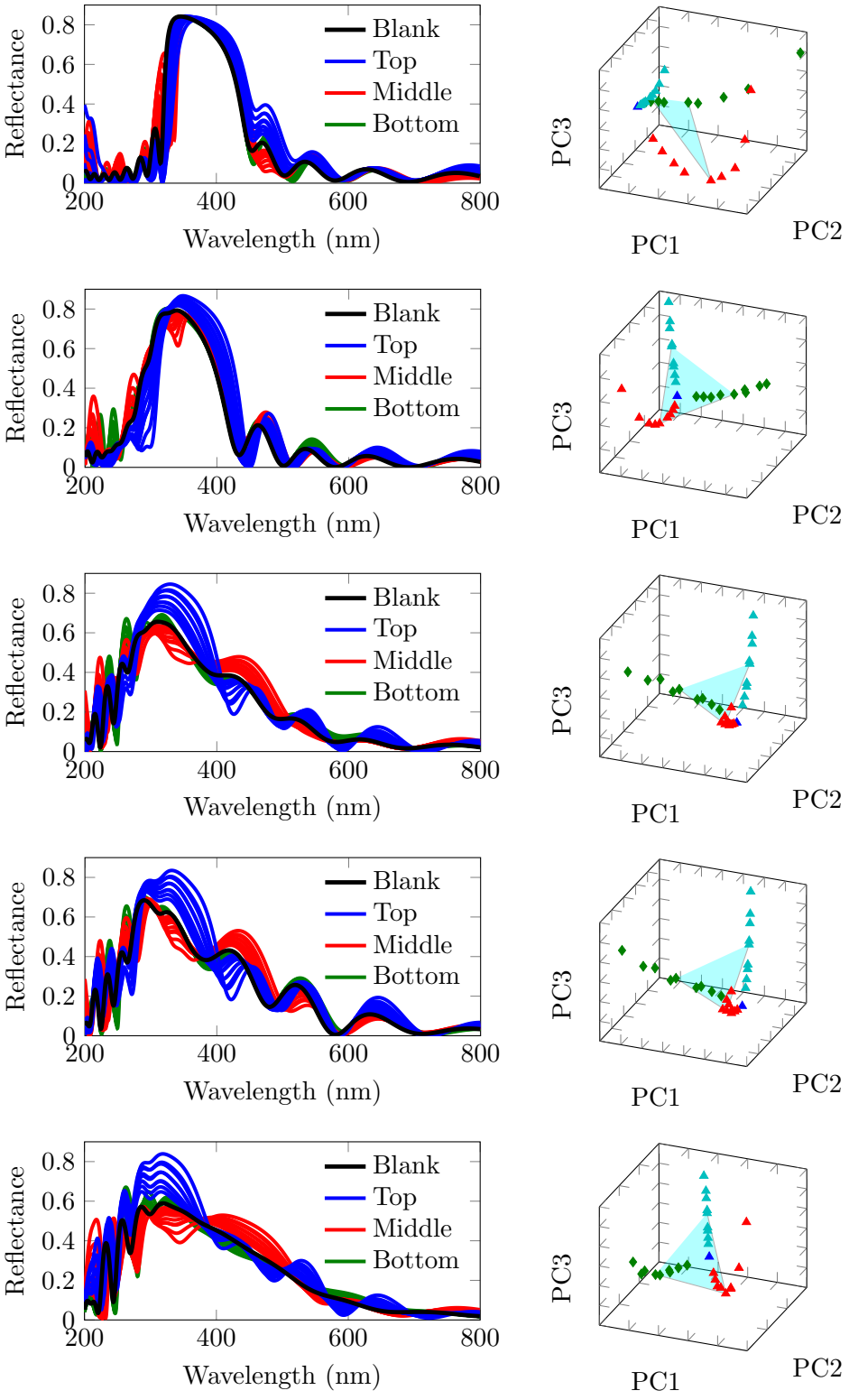

Figure C.1: Complete reflectance dataset (left) and associated PC scores plot (right) for multilayer structures 'multi 1', 'chirp 1', 'chirp 2', 'chirp 3' and 'chirp 4', from top to bottom, respectively. These spectra form the analysis of the response selectivity and sensitivity analysis, shown in Figure 8.8.

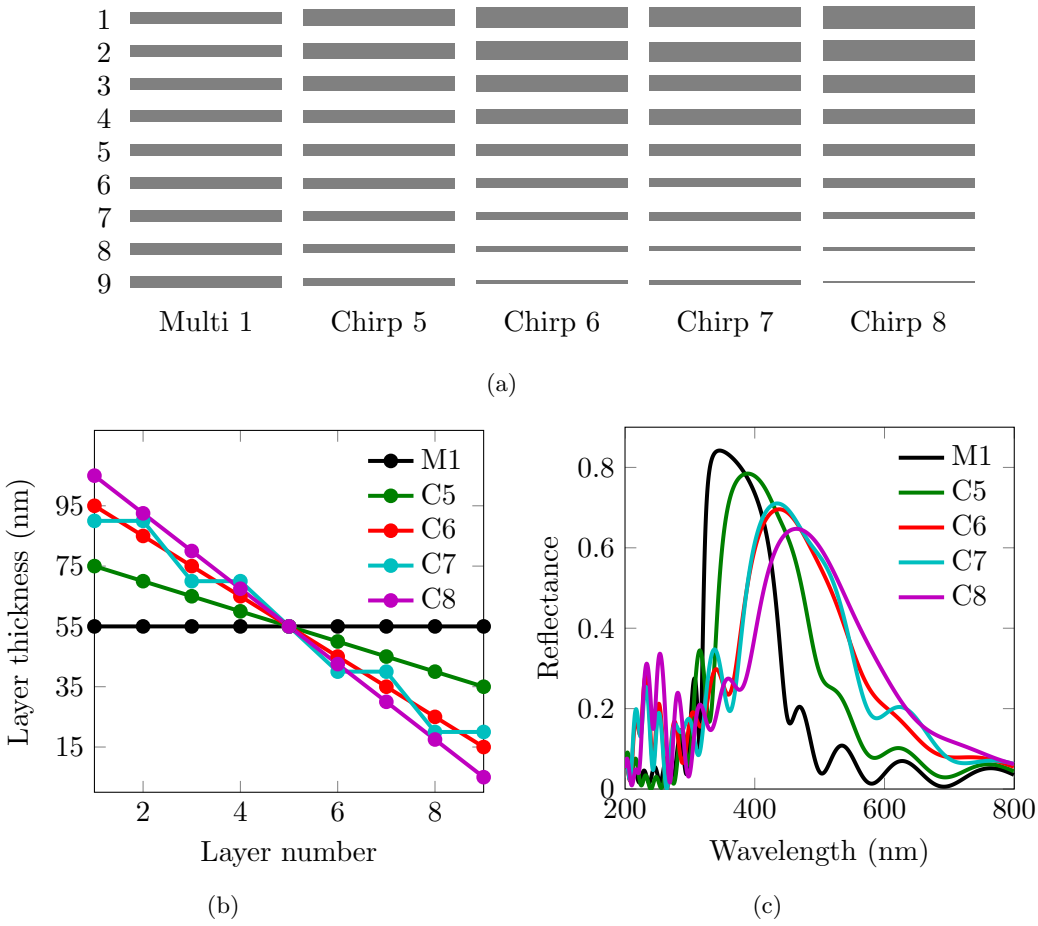

Figure C.2: Exploration of chirped-multilayer structures for vapour selectivity and sensitivity analysis: (a) schematic of the bench-mark multilayer structure 'multi 1', to which the chirped layers 5 to 8 will be compared, (b) layer thickness profiles for each reflecting structure considered in (a), and (c) shows the associated reflectance for these structures; chirping the layers broadens the spectral reflectance features.

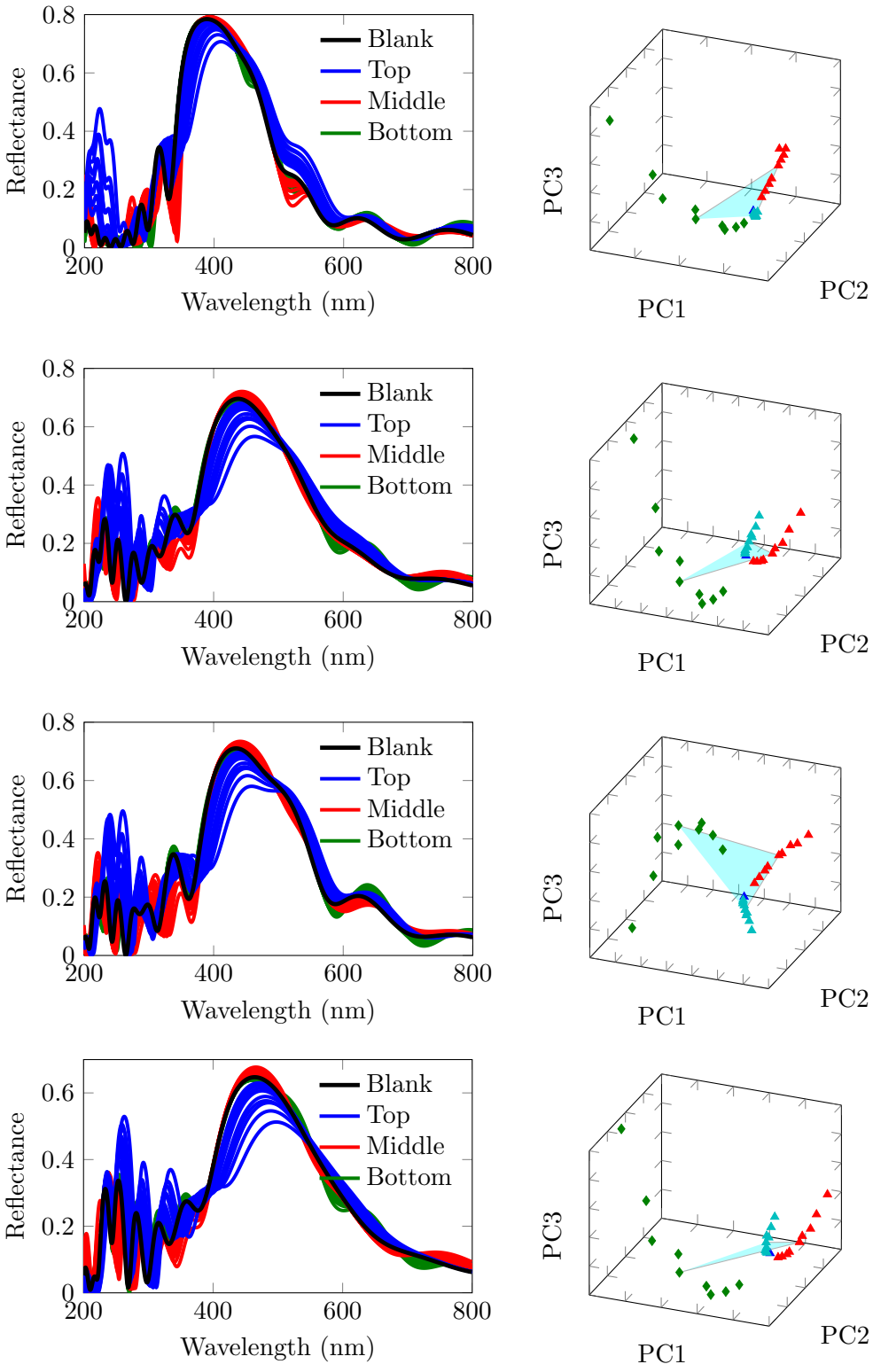

Figure C.3: Complete reflectance dataset (left) and associated PC scores plot (right) for multilayer structures 'chirp 5', 'chirp 6', 'chirp 7' and 'chirp 8', from top to bottom, respectively. These spectra form the analysis of the response selectivity and sensitivity analysis, shown in Figure C.4.

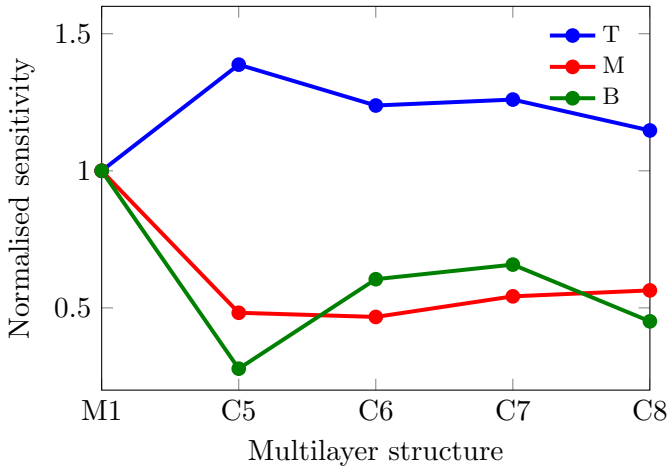

(a)

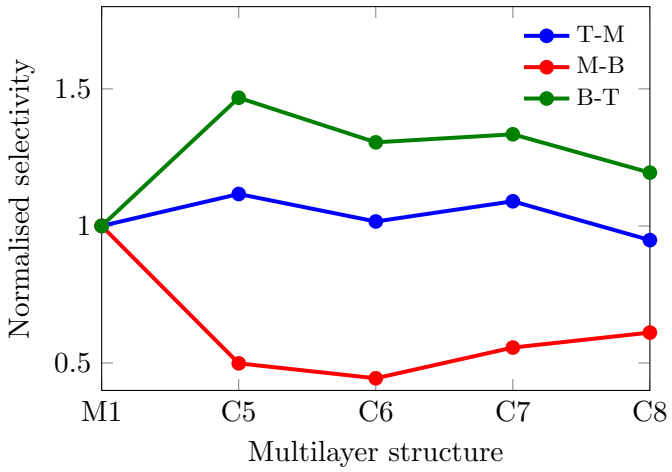

(b)

Figure C.4: Analysis of model vapour adsorption on chirped multilayer designs: (a) and (b) sensitivity and selectivity metrics, respectively, for multilayer structures 'chirp 5', 'chirp 6', 'chirp 7' and 'chirp 8' (normalised w.r.t. the 'multi 1' control reflector).

Appendix D

High-Q Resonances in Bio-inspired Dielectric Structures

This appendix contains supplementary data to support the discussion in Chapter 8 (Section 8.3) on the analysis of high-Q resonances in dielectric structures.

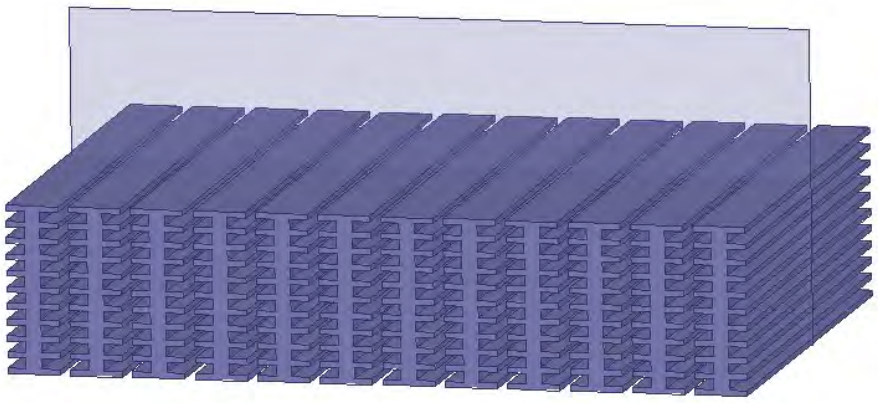

Figure D.1: Rendered schematic for dielectric structure 4 depicting the result of expanding the unit cell geometry, and the plane of incidence which is perpendicular to the ridge-structure.

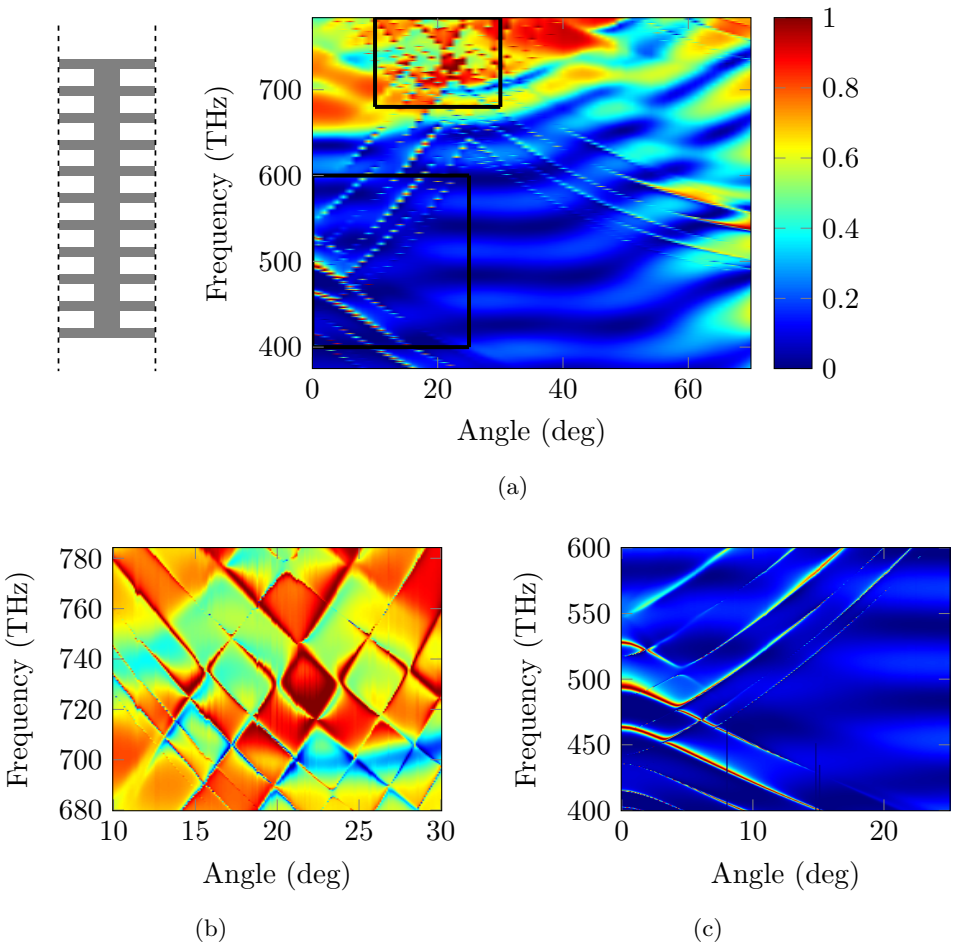

Figure D.2: Reflectance maps for dielectric structure 3. Reflectance is displayed for the electric field polarised parallel to the in-plane ridge. (a) Reflectance for large range of incident angles over the visible frequency range. (b) and (c) reflectance with greater angular and frequency resolution to show the dispersion of the high-Q modes.

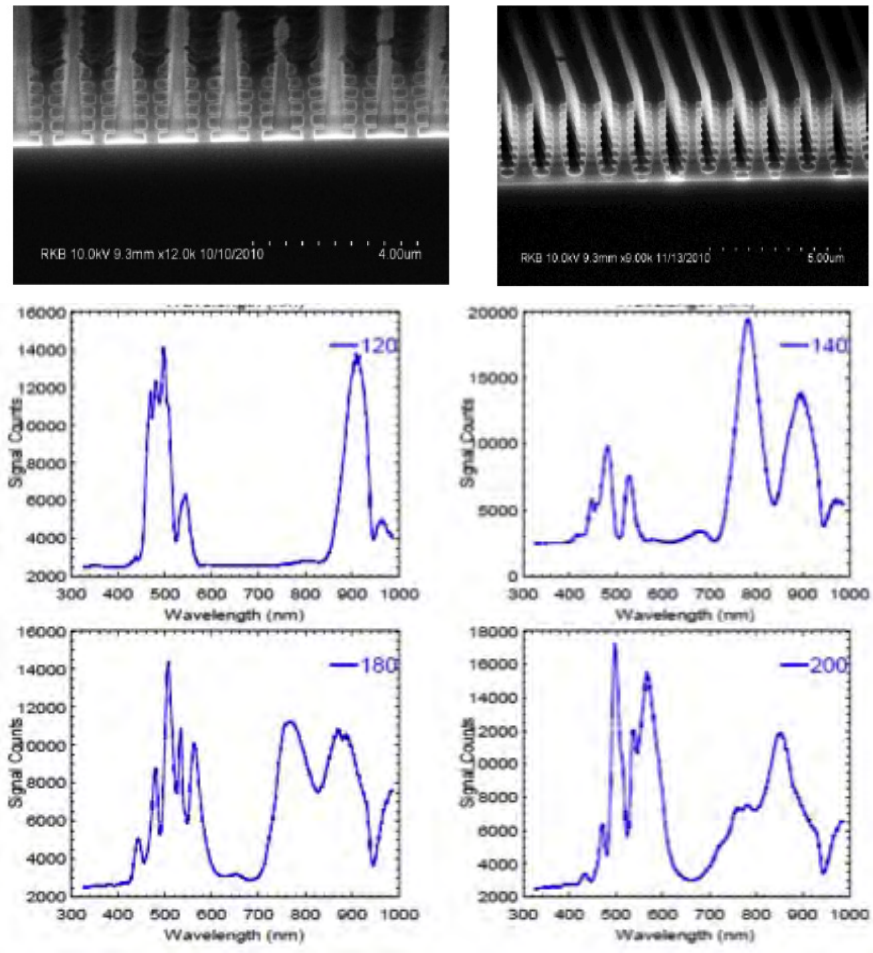

Figure D.3: SEM micrographs of fabricated dielectric structures and their reflectance spectra. The reflectance displays spectral regions associated with structural colour, as dictated by the lamellae periodicity, and regions of high-Q features. (Images and spectral data courtesy of R. A. Potyrailo).

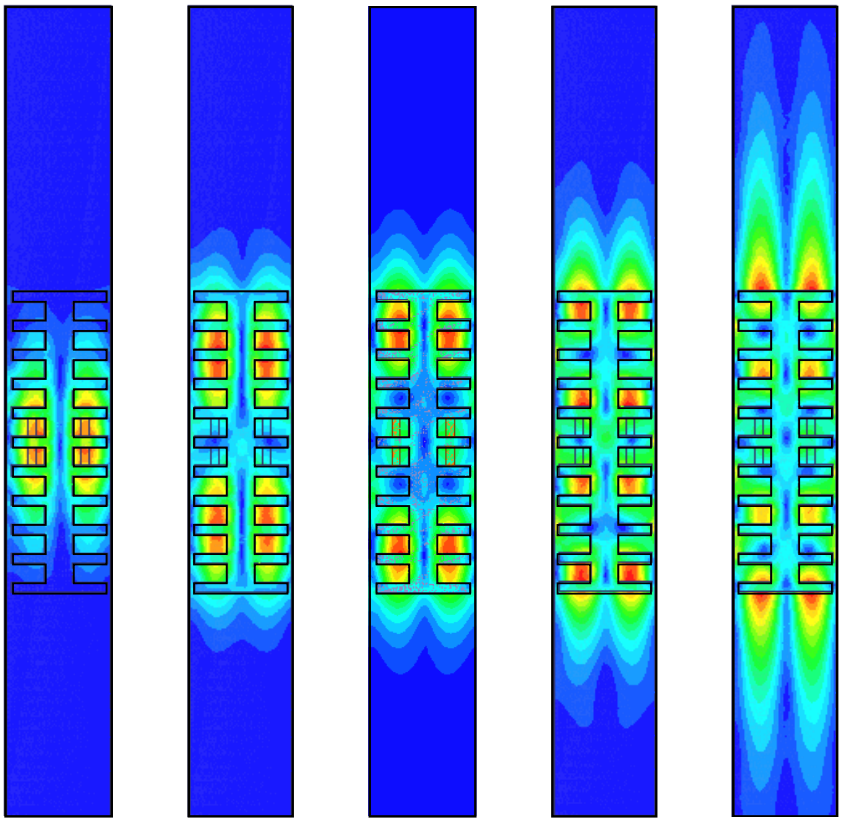

Figure D.4: Time-averaged electric field profiles of the high-Q resonant modes for the ridge-lamellae dielectric structure display when model vapour is sorbed in the regions of high-field intensity of the fundamental mode. The small boxes within the structure represent the location vapour is adsorbed. Regions of high field intensity are displayed as red, and low field intensity regions as blue.

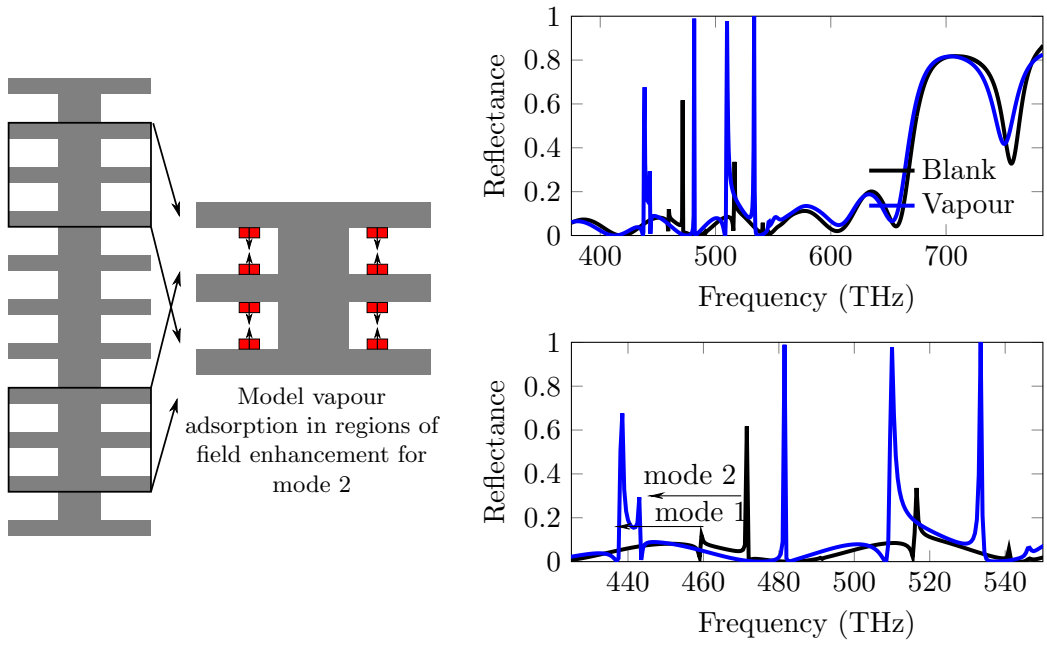

Figure D.5: Exploration of Fano-resonance effects for a sensitive vapour response; (left) a schematic showing the position of model vapour in the region corresponding to the regions of high electric field enhancement for the second harmonic resonant mode, and (right) reflectance data displaying the spectral shift of the resonant modes of the blank structure when vapour is added to the inter-lamellae space.

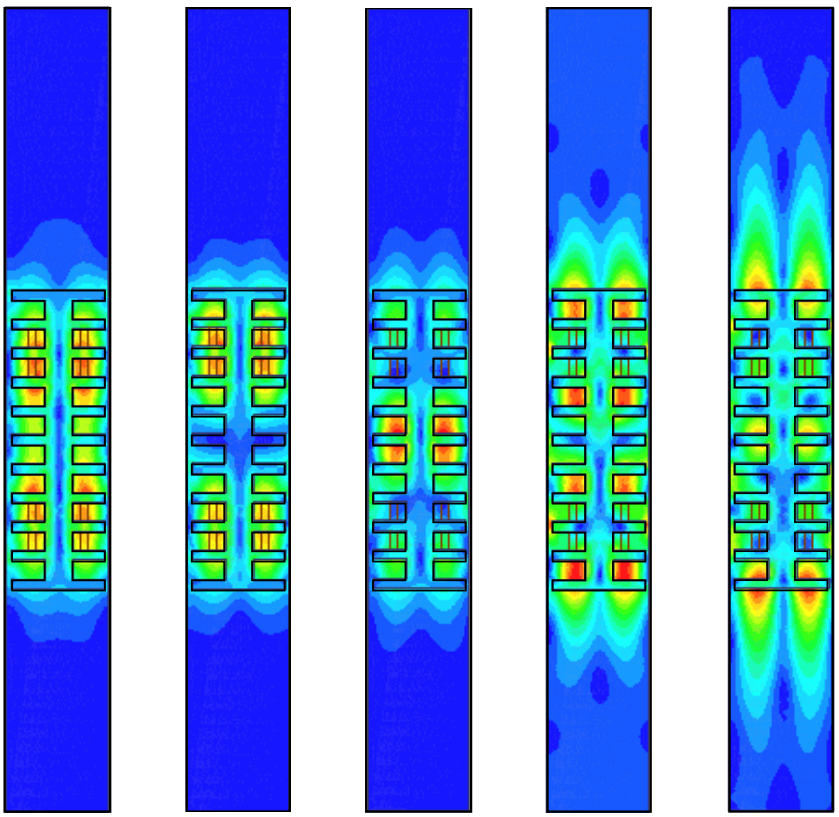

Figure D.6: Time-averaged electric field profiles of the high-Q resonant modes for the ridge-lamellae dielectric structure display when model vapour is sorbed in the regions of high-field intensity. The small boxes within the structure represent the location vapour is adsorbed. Regions of high field intensity are displayed as red, and low field intensity regions as blue.

References

[1] Fox, D.L. *Animal biochromes and structural colours: physical, chemical, distributional and physiological features of coloured bodies in the animal world*. University of California Press, Berkley, second edition (1976). 1, 7, 8

[2] Srinivasarao, M. Nano-Optics in the Biological World: Beetles, Butterflies, Birds, and Moths. *Chemical Reviews*, **99**, 1935 (1999). 1

[3] Vukusic, P. and Sambles, J.R. Photonic structures in biology. *Nature*, **424**, 852 (2003). 31, 38, 88

[4] Kinoshita, S. and Yoshioka, S. (editors). *Structural Colors in Biological Systems: Principles and Applications*. Osaka University Press, Osaka, first edition (2005). 1, 29, 31, 38, 47

[5] Lee, D. and Lowry, J. Physical basis and ecological significance of iridescence in blue plants. *Nature*, **254**, 50 (1975). 1

[6] Whitney, H., Kolle, M., Andrew, P., Chittka, L., Steiner, U., and Glover, B. Floral Iridescence, Produced by Diffractive Optics, Acts As a Cue for Animal Pollinators. *Science*, **323**, 130 (2009). 17, 48

[7] Vignolini, S., Rudall, P.J., Rowland, A.V., Reed, A., Moyroud, E., Faden, R.B., Baumberg, J.J., Glover, B.J., and Steiner, U. Pointillist structural color in *Pollia* fruit. *Proceedings of the National Academy of Sciences of the United States of America*, **109**, 15712 (2012). 1, 12, 45

[8] Potyrailo, R.A., Ghiradella, H., Vertiatchikh, A., Dovidenko, K., Cournoyer, J.R., and Olson, E. *Morpho* butterfly wing scales demonstrate highly selective vapour response. *Nature Photonics*, **1**, 123 (2007). 1, 27, 63, 88, 95, 97, 99, 100, 115, 117, 131, 173, 182

[9] Pris, A.D., Utturkar, Y., Surman, C., Morris, W.G., Vert, A., Zalyubovskiy, A.D., Deng, T., Ghiradella, H.T., and Potyrailo, R.A.

Towards high-speed imaging of infrared photons with bio-inspired nanoarchitectures. *Nature Photonics*, **6**, 195 (2012). 1, 28

[10] Fitch, J.P., Raber, E., and Imbro, D.R. Technology challenges in responding to biological or chemical attacks in the civilian sector. *Science*, **302**, 1350 (2003). 1, 66

[11] Starkey, T. and Vukusic, P. Light manipulation principles in biological photonic systems. *Nanophotonics*, **2**, 289 (2013). 2, 3, 8, 29, 184

[12] Potyrailo, R.A., Starkey, T.A., Vukusic, P., Ghiradella, H., Vasudev, M., Bunning, T., Naik, R.R., Tang, Z., Larsen, M., Deng, T., Zhong, S., Palacios, M., Grande, J.C., Zorn, G., Goddard, G., and Zalubovsky, S. Discovery of the surface polarity gradient on iridescent *Morpho* butterfly scales reveals a mechanism of their selective vapor response. *Proceedings of the National Academy of Sciences of the United States of America*, **110**, 15567 (2013). 4, 88, 102, 104, 111, 112, 114, 131, 184, 189

[13] Starkey, T.A., Vukusic, P., and Potyrailo, R.A. Toward bioinspired nanostructures for selective vapor sensing: diverse vapor-induced spectral responses within iridescent scales of *Morpho* butterflies. *MRS Proceedings*, **1621**, mrsf13 (2014). 4, 63, 88, 131, 184

[14] Vukusic, P. and Chittka, L. Visual signals: color and light production. In *The Insects: Structure and Function*, edited by S.J. Simpson and A.E. Douglas. Cambridge University Press, fifth edition (2013). 8

[15] Arnold, K.E., Owens, I.P.F., and Marshall, N.J. Fluorescent Signaling in Parrots. *Science*, **295**, 92 (2002). 8

[16] Mazel, C.H., Cronin, T.W., Caldwell, R.L., and Marshall, N.J. Fluorescent Enhancement of Signaling in a Mantis Shrimp. *Science*, **303**, 51 (2004).

[17] Lim, M.L.M., Land, M.F., and Li, D. Sex-Specific UV and Fluorescence Signals in Jumping Spiders. *Science*, **315**, 481 (2007). 8

[18] Vukusic, P. and Hooper, I. Directionally Controlled Fluorescence Emission in Butterflies. *Science*, **310**, 1151 (2005). 8, 110

[19] Lall, A., Seliger, H., Biggley, W., and Lloyd, J. Ecology of Colors of Firefly Bioluminescence. *Science*, **210**, 560 (1980). 8

[20] Wilson, T. and Hastings, J. *Bioluminescence: Living Lights, Lights for Living*. Harvard University Press, Harvard, first edition (2013). 8

[21] McCapra, F. and Hart, R. The origins of marine bioluminescence. *Nature*, **286**, 660 (1980). 8

[22] Bohren, C. and Huffman, D. *Absorption and Scattering of Light by Small Particles*. Wiley, second edition (2008). 8

[23] Neville, A.C. and Caveney, S. Scarabaeid beetle exocuticle as an optical analogue of cholesteric liquid crystals. *Biological Reviews of the Cambridge Philosophical Society*, **44**, 531 (1969). 8, 12, 43

[24] Vukusic, P., Hallam, B., and Noyes, J. Brilliant Whiteness in Ultrathin Beetle Scales. *Science*, **315**, 348 (2007). 8, 17, 24, 25

[25] Parker, A.R. Colour in Burgess Shale animals and the effect of light on evolution in the Cambrian. *Proceedings of the Royal Society B: Biological Sciences*, **265**, 967 (1998). 8

[26] Vukusic, P., Sambles, J.R., Lawrence, C.R., and Wootton, R.J. Now you see it – now you don't. *Nature*, **410**, 36 (2001). 8, 14, 43

[27] Wickham, S., Large, M.C.J., Poladian, L., and Jermiin, L.S. Exaggeration and suppression of iridescence: the evolution of two-dimensional butterfly structural colours. *Journal of the Royal Society Interface*, **3**, 99 (2009). 8

[28] Vukusic, P., Sambles, J.R., Lawrence, C.R., and Wootton, R.J. Limited-view iridescence in the butterfly *Ancyluris meliboeus*. *Proceedings of the Royal Society B: Biological Sciences*, **269**, 7 (2002). 8

[29] Vukusic, P., Sambles, J.R., and Lawrence, C.R. Structurally assisted blackness in butterfly scales. *Proceedings of the Royal Society B: Biological Sciences*, **271**, S237 (2004). 8, 47

[30] Stavenga, D.G., Foletti, S., Palasantzas, G., and Arikawa, K. Light on the moth-eye corneal nipple array of butterflies. *Proceedings of the Royal Society B: Biological Sciences*, **273**, 661 (2006). 8

[31] Jewell, S.A., Vukusic, P., and Roberts, N.W. Circularly polarized colour reflection from helicoidal structures in the beetle *Plusiotis boucardi*. *New Journal of Physics*, **9**, 1 (2007). 8, 10, 12

[32] Hooke, R. *Micrographia: or, Some physiological descriptions of minute bodies made by magnifying glasses. With observations and inquiries thereupon.* The Royal Society, London, first edition (1961). 9

[33] Newton, I. *Opticks: or, A treatise of the reflection, refractions, inflections and colours.* Willian Innys, London, fourth edition (1730). 9

[34] Mason, C.W. Structural Colors in Feathers. I. *The Journal of Physical Chemistry*, **27**, 201 (1923). 9

[35] Mason, C.W. Structural Colors in Feathers. II. *The Journal of Physical Chemistry*, **27**, 401 (1923).

[36] Mason, C.W. Structural Colors in Insects. I. *The Journal of Physical Chemistry*, **30**, 383 (1926). 45, 91

[37] Mason, C.W. Structural Colors in Insects. II. *The Journal of Physical Chemistry*, **31**, 321 (1927). 91

[38] Mason, C.W. Structural Colors in Insects. III. *The Journal of Physical Chemistry*, **31**, 1856 (1927).

[39] Mason, C.W. Transmitted Structural Blue in Microscopic Objects. *The Journal of Physical Chemistry*, **35**, 73 (1931).

[40] Rayleigh, L. The Iridescent Colours of Birds and Insects. *Proceedings of the Royal Society B: Biological Sciences*, **106**, 618 (1930). 9

[41] Onslow, H. On a Periodic Structure in Many Insect Scales, and the Cause of Their Iridescent Colours. *Philosophical Transactions of the Royal Society of London B*, **211**, 1 (1923). 9, 91

[42] Frank, F. Die Färbung der Vogelfeder durch Pigment und Struktur. *Journal of Ornithology*, **87**, 426 (1939). 9

[43] Lippert, W. and Gentil, K. Über Lamellare feinstrukturen bei den schillerschuppen der schmetterlinge vom *Urania*- und *Morpho*-typ. *Zeitschrift für Morphologie und Ökologie der Tiere*, **48**, 115 (1959). 9

[44] Anderson, T.F. and Richards, A.G. An Electron Microscope Study of Some Structural Colors of Insects. *Journal of Applied Physics*, **13**, 748 (1942). 9

[45] Rayleigh, L. On the Maintenance of Vibrations by Forces of Double Frequency and on the Propagation of Waves through a Medium endowed with a Periodic

Structure. *The London, Edinburgh, and Dublin Philosophical Magazine and Journal of Science*, **24**, 145 (1887). 9

[46] Abelès, F. La détermination de l'indice et de l'épaisseur des couches minces transparentes. *Journal De Physique et le Radium*, **11**, 310 (1950). 9, 29

[47] Huxley, A.F. A theoretical treatment of the reflexion of light by multilayer structures. *Journal of Experimental Biology*, **48**, 227 (1968). 9, 29, 40

[48] Land, M.F. The Physics and Biology of Animal Reflectors. *Progress in Biophysics and Molecular Biology*, **24**, 75 (1972). 9, 10, 31, 38, 39, 103, 140, 153

[49] Ghiradella, H., Aneshansley, D., Eisner, T., Silberglied, R.E., and Hinton, H.E. Ultraviolet Reflection of a Male Butterfly: Interference Color Caused by Thin-Layer Elaboration of Wing Scales. *Science*, **178**, 1214 (1972). 9, 103

[50] Morris, R.B. Iridescence from diffraction structures in the wing scales of *Callophrys rubi*, the Green Hairstreak. *Journal of Entomology Series A, General Entomology*, **49**, 149 (1975). 10

[51] Allyn, A.C. and Downey, J.C. Diffraction structures in the wing scales of *Callophrys (Mitoura) siva siva* (Lycaenidae). *Bulletin of the Allyn Museum*, **40**, 1 (1976). 10, 48

[52] Parker, A.R., McKenzie, D.R., and Large, M.C.J. Multilayer reflectors in animals using green and gold beetles as contrasting examples. *The Journal of Experimental Biology*, **201**, 1307 (1998). 10, 11, 12, 153

[53] Vukusic, P., Sambles, R., Lawrence, C., and Wakely, G. Sculpted-multilayer optical effects in two species of *Papilio* butterfly. *Applied Optics*, **40**, 1116 (2001). 10, 11, 12, 24

[54] Vukusic, P., Wootton, R.J., and Sambles, J.R. Remarkable iridescence in the hindwings of the damselfly *Neurobasis chinensis chinensis* (Linnaeus) (Zygoptera: Calopterygidae). *Proceedings of the Royal Society B: Biological Sciences*, **271**, 595 (2004). 43

[55] Nixon, M.R., Orr, A.G., and Vukusic, P. Subtle design changes control the difference in colour reflection from the dorsal and ventral wing-membrane surfaces of the damselfly *Matronoides cyaneipennis*. *Optics Express*, **21**, 1479 (2013). 10, 40, 43, 120, 182

[56] Sharma, V., Crne, M., Park, J.O., and Srinivasarao, M. Structural origin of circularly polarized iridescence in jeweled beetles. *Science*, **325**, 449 (2009). 10, 12

[57] Jordan, T., Partridge, J., and Roberts, N. Non-polarizing broadband multilayer reflectors in fish. *Nature Photonics*, **6**, 759 (2012). 10, 38, 43, 45

[58] Amir, A. and Vukusic, P. Elucidating the stop bands of structurally colored systems through recursion. *American Journal of Physics*, **81**, 253 (2013). 10, 11, 40

[59] Denton, E.J. and Land, M.F. Mechanism of Reflexion in Silvery Layers of Fish and Cephalopods. *Proceedings of the Royal Society B: Biological Sciences*, **178**, 43 (1971). 11, 12, 38, 40, 45, 153

[60] Noyes, J.A., Vukusic, P., and Hooper, I.R. Experimental method for reliably establishing the refractive index of buprestid beetle exocuticle. *Optics Express*, **15**, 4351 (2007). 11, 43

[61] Seago, A.E., Brady, P., Vigneron, J.P., and Schultz, T.D. Gold bugs and beyond: a review of iridescence and structural colour mechanisms in beetles (Coleoptera). *Journal of the Royal Society Interface*, **6**, S165 (2009). 11, 12, 17

[62] Vukusic, P., Kelly, R., and Hooper, I. A biological sub-micron thickness optical broadband reflector characterized using both light and microwaves. *Journal of the Royal Society Interface*, **6**, S193 (2009). 11, 48

[63] Vukusic, P., Sambles, J.R., Lawrence, C.R., and Wootton, R.J. Quantified interference and diffraction in single *Morpho* butterfly scales. *Proceedings of the Royal Society B: Biological Sciences*, **266**, 1403 (1999). 12, 20, 21, 24, 43, 45, 47, 48, 91, 98, 118, 120, 125, 134, 146, 147, 160

[64] Schultz, T. and Bernard, G. Pointillistic mixing of interference colours in cryptic tiger beetles. *Nature*, **337**, 72 (1989). 12, 43

[65] Nicol, J. and Baalen, C.V. Studies on the reflecting layers of fishes. *Contributions in Marine Science*, **13**, 1968 (1968). 12

[66] Nixon, M.R., Orr, A.G., and Vukusic, P. Optimised Multilayer Designs and Efficient White-Scatter Coatings in Damselfly Wing-Membranes. In *Optical Interference Coatings*. OSA (2013). 12, 17

[67] Yoshioka, S. and Kinoshita, S. Effect of Macroscopic Structure in Iridescent Color of the Peacock Feathers. *Forma*, **17**, 169 (2002). 12

[68] Pedler, C. The Fine Structure of the Tapetum Cellulosum. *Experimental Eye Research*, **2**, 189 (1963). 12

[69] Parker, A.R., McPhedran, R.C., McKenzie, D.R., Botten, L.C., and Nicorovici, N.A.P. Aphrodite's iridescence. *Nature*, **409**, 36 (2001). 12, 14

[70] Trzeciak, T. and Vukusic, P. Photonic crystal fiber in the polychaete worm *Pherusa* sp. *Physical Review E*, **80**, 061908 (2009). 12, 13, 182

[71] Zi, J., Yu, X., Li, Y., Hu, X., Xu, C., Wang, X., Liu, X., and Fu, R. Coloration strategies in peacock feathers. *Proceedings of the National Academy of Sciences of the United States of America*, **100**, 12576 (2003). 12

[72] Vigneron, J.P., Colomer, J.F., Rassart, M., Ingram, A., and Lousse, V. Structural origin of the colored reflections from the black-billed magpie feathers. *Physical Review E*, **73**, 021914 (2006). 12

[73] González-Segredo, N. and Coveney, P.V. Self-assembly of the gyroid cubic mesophase: Lattice-Boltzmann simulations. *Europhysics Letters*, **65**, 795 (2004). 14

[74] Saranathan, V., Osuji, C., Mochrie, S.G.J., Noh, H., Narayanan, S., Sandy, A., Dufresne, E.R., and Prum, R.O. Structure, function, and self-assembly of single network gyroid ($I4_132$) photonic crystals in butterfly wing scales. *Proceedings of the National Academy of Sciences of the United States of America*, **107**, 11676 (2010). 14

[75] Vukusic, P. and Sambles, J.R. Shedding light on butterfly wings. In *Proceedings of SPIE*, edited by P. Lalanne, volume 4438, pages 85–95 (2001). 14

[76] Michielsen, K. and Stavenga, D.G. Gyroid cuticular structures in butterfly wing scales: biological photonic crystals. *Journal of the Royal Society Interface*, **5**, 85 (2008). 14

[77] Pouya, C. *Investigating Naturally Occurring 3-Dimensional Photonic Crystals*. Ph.D. thesis, University of Exeter (2012). 14

[78] Pouya, C. and Vukusic, P. Electromagnetic characterization of millimetre-scale replicas of the gyroid photonic crystal found in the butterfly *Parides sesostris*. *Interface Focus*, **2**, 645 (2012). 14, 74, 182

[79] Galusha, J.W., Richey, L.R., Gardner, J.S., Cha, J.N., and Bartl, M.H. Discovery of a diamond-based photonic crystal structure in beetle scales. *Physical Review E*, **77**, 050904 (2008). 14, 15

[80] Chan, C., Ho, K., and Soukoulis, C. Photonic Band Gaps in Experimentally Realizable Periodic Dielectric Structures. *Europhysics Letters*, **16**, 563 (1991). 14

[81] Wilts, B.D., Michielsen, K., Kuipers, J., De Raedt, H., and Stavenga, D.G. Brilliant camouflage: photonic crystals in the diamond weevil, *Entimus imperialis*. *Proceedings of the Royal Society B: Biological Sciences*, **279**, 2524 (2012). 14

[82] Pouya, C., Stavenga, D.G., and Vukusic, P. Discovery of ordered and quasi-ordered photonic crystal structures in the scales of the beetle *Eupholus magnificus*. *Optics Express*, **19**, 11355 (2011). 14, 16

[83] Vignolini, S., Moyroud, E., Glover, B.J., and Steiner, U. Analysing photonic structures in plants. *Journal of the Royal Society Interface*, **10**, 20130394 (2013). 17

[84] Maystre, D. Photonic crystal diffraction gratings. *Optics Express*, **8**, 209 (2001). 17

[85] Filloux, P. and Paraire, N. Use of multilayer structures, periodically etched, to implement compact diffractive optical devices. *Journal of Optics A: Pure and Applied Optics*, **4**, S175 (2002). 17

[86] Yoshioka, S. and Kinoshita, S. Wavelength-selective and anisotropic light-diffusing scale on the wing of the *Morpho* butterfly. *Proceedings of the Royal Society B: Biological Sciences*, **271**, 581 (2004). 17, 21, 134

[87] Stavenga, D.G., Stowe, S., Siebke, K., Zeil, J., and Arikawa, K. Butterfly wing colours: scale beads make white pierid wings brighter. *Proceedings of the Royal Society B: Biological Sciences*, **271**, 1577 (2004). 17, 24

[88] Morehouse, N.I., Vukusic, P., and Rutowski, R. Pterin pigment granules are responsible for both broadband light scattering and wavelength selective absorption in the wing scales of pierid butterflies. *Proceedings of the Royal Society B: Biological Sciences*, **274**, 359 (2007). 17

[89] Burresi, M., Cortese, L., Pattelli, L., Kolle, M., Vukusic, P., Wiersma, D.S., Steiner, U., and Vignolini, S. Bright-white beetle scales optimise multiple scattering of light. *Scientific Reports*, **4**, 6075 (2014). 17

[90] Kalmus, H. Physiology and Ecology of Cuticle Colour in Insects. *Nature*, **148**, 428 (1941). 18

[91] Ghiradella, H. Hairs, Bristles, and Scales. In *Microscopic Anatomy of Invertebrates*, edited by M. Locke, chapter 11, pages 257–287. Wiley-Liss, Inc. (1998). 18, 19, 118

[92] Ghiradella, H. Structure of Butterfly Scales: Patterning in an Insect Cuticle. *Microscopy Research and Technique*, **27**, 429 (1994). 18, 113

[93] Ghiradella, H. Structure and Development of Iridescent Lepidopteran Scales: The Papilionidae as a Showcase Family. *Annals of the Entomological Society of America*, **78**, 252 (1985). 18

[94] Ghiradella, H. Structure and Development of Iridescent Butterfly Scales: Lattices and Laminae. *Journal of Morphology*, **202**, 69 (1989).

[95] Ghiradella, H.T. and Butler, M.W. Many variations on a few themes: a broader look at development of iridescent scales (and feathers). *Journal of the Royal Society Interface*, **6**, S243 (2009). 18

[96] Vukusic, P., Sambles, J.R., and Ghiradella, H.T. Optical Classification of Microstructure in Butterfly Wing-Scales. *Photonics Science News*, **6**, 61 (2000). 18

[97] Young, A.M. and Muyshondt, A. Geographical and ecological expansion in tropical butterflies of the genus *Morpho* in evolutionary time. *Bevista de Biologia Tropical*, **20**, 231 (1972). 18, 20

[98] Berthier, S., Charron, E., and Boulenguez, J. Morphological structure and optical properties of the wings of Morphidae. *Insect Science*, **13**, 145 (2006). 18, 67, 125, 146

[99] Bates, H.W. The Naturalist on the River Amazon. *Natural History Review*, **3** (1863). 20

[100] Silberglied, R. Visual communication and sexual selection among butterflies. In *The Biology of Butterflies*, edited by R.I. Vane-Wright and P.E. Ackery, 11, pages 207–223. Academic Press, London (1984). 20

[101] Kinoshita, S., Yoshioka, S., Fujii, Y., and Okamoto, N. Photophysics of Structural Color in the *Morpho* Butterflies. *Forma*, **17**, 103 (2002). 24, 67, 90

[102] Kinoshita, S., Yoshioka, S., and Kawagoe, K. Mechanisms of structural colour in the *Morpho* butterfly: cooperation of regularity and irregularity in an iridescent scale. *Proceedings of the Royal Society B: Biological Sciences*, **269**, 1417 (2002). 24

[103] Yoshioka, S. and Kinoshita, S. Structural or pigmentary? Origin of the distinctive white stripe on the blue wing of a *Morpho* butterfly. *Proceedings of the Royal Society B: Biological Sciences*, **273**, 129 (2006). 24, 47

[104] Mejdoubi, A., Andraud, C., Berthier, S., Lafait, J., Boulenguez, J., and Richalot, E. Finite element modeling of the radiative properties of *Morpho* butterfly wing scales. *Physical Review E*, **87**, 022705 (2013). 24, 74, 124, 125

[105] Vigneron, J., Rassart, M., Vértesy, Z., Kertész, K., Sarrazin, M., Biró, L., Ertz, D., and Lousse, V. Optical structure and function of the white filamentary hair covering the edelweiss bracts. *Physical Review E*, **71**, 011906 (2005). 24

[106] Berthier, S., Charron, E., and Da Silva, A. Determination of the cuticle index of the scales of the iridescent butterfly *Morpho menelaus*. *Optics Communications*, **228**, 349 (2003). 24, 124, 125, 146

[107] Dhatt, G. and Touzot, G. *The Finite Element Method Displayed*. John Wiley & Sons, Chichester, first edition (1984). 25, 74

[108] Yee, K.S. Numerical Solution of Initial Boundary Value Problems Involving Maxwell's Equations in Isotropic Media. *IEEE Transactions on Antennas and Propagation*, **14**, 302 (1966). 25, 79

[109] Plattner, L. Optical properties of the scales of *Morpho rhetenor* butterflies: theoretical and experimental investigation of the back-scattering of light in the visible spectrum. *Journal of the Royal Society Interface*, **1**, 49 (2004). 25

[110] Banerjee, S., Cole, J.B., and Yatagai, T. Colour characterization of a *Morpho* butterfly wing-scale using a high accuracy nonstandard finite-difference time-domain method. *Micron*, **38**, 97 (2007).

[111] Steindorfer, M.A., Schmidt, V., Belegratis, M., Stadlober, B., and Krenn, J.R. Detailed simulation of structural color generation inspired by the *Morpho* butterfly. *Optics Express*, **20**, 21485 (2012). 25

[112] Lee, R.T. and Smith, G.S. Detailed electromagnetic simulation for the structural color of butterfly wings. *Applied Optics*, **48**, 4177 (2009). 25

[113] Kambe, M., Zhu, D., and Kinoshita, S. Origin of Retroreflection from a Wing of the *Morpho* Butterfly. *Journal of the Physical Society of Japan*, **80**, 054801 (2011). 25

[114] Zhu, D., Kinoshita, S., Cai, D., and Cole, J. Investigation of structural colors in *Morpho* butterflies using the nonstandard-finite-difference time-domain method: Effects of alternately stacked shelves and ridge density. *Physical Review E*, **80**, 051924 (2009). 25, 124

[115] Vukusic, P. and Stavenga, D.G. Physical methods for investigating structural colours in biological systems. *Journal of the Royal Society Interface*, **6**, S133 (2009). 25, 31, 67

[116] Stavenga, D.G., Leertouwer, H.L., Pirih, P., and Wehling, M.F. Imaging scatterometry of butterfly wing scales. *Optics Express*, **17**, 193 (2009). 25

[117] Okada, N., Zhu, D., Cai, D., Cole, J.B., Kambe, M., and Kinoshita, S. Rendering *Morpho* butterflies based on high accuracy nano-optical simulation. *Journal of Optics*, **42**, 25 (2012). 25

[118] Forbes, P. *The Gecko's Foot: How Scientists are Taking a Leaf from Nature's Book*. Harper Perennial, London, first edition (2006). 25

[119] Hallam, B.T., Hiorns, A.G., and Vukusic, P. Developing optical efficiency through optimized coating structure: biomimetic inspiration from white beetles. *Applied Optics*, **48**, 3243 (2009). 25, 182

[120] Min, W.L., Betancourt, A.P., Jiang, P., and Jiang, B. Bioinspired broadband antireflection coatings on GaSb. *Applied Physics Letters*, **92**, 141109 (2008). 26

[121] Boden, S.A. and Bagnall, D.M. Optimization of moth-eye antireflection schemes for silicon solar cells. *Progress in Photovoltaics: Research and Applications*, **18**, 195 (2010). 26

[122] Kolle, M., Lethbridge, A., Kreysing, M., Baumberg, J.J., Aizenberg, J., and Vukusic, P. Bio-Inspired Band-Gap Tunable Elastic Optical Multilayer Fibers. *Advanced Materials*, **25**, 1 (2013). 26

[123] Nose, K. Structurally Colored Fiber "Morphotex". *Annals of the High Performance Paper Society*, **43**, 17 (2005). 26

[124] Chung, K., Yu, S., Heo, C.J., Shim, J.W., Yang, S.M., Han, M.G., Lee, H.S., Jin, Y., Lee, S.Y., Park, N., and Shin, J.H. Flexible, Angle-Independent, Structural Color Reflectors Inspired by *Morpho* Butterfly Wings. *Advanced Materials*, **24**, 2375 (2012). 26

[125] L'Oreal. Bio-inspired cosmetics: L'Oreal focuses on photonics to enhance colour cosmetics. `www.cosmeticsdesign-asia.com/Formulation-Science/L-Oreal-focuses-on-photonics-to-enhance-colour-cosmetics` (Accessed: 24th April 2013). 27

[126] Hinton, H. and Jarman, G. Physiological colour change in the Hercules beetle. *Nature*, **238**, 160 (1972). 27

[127] Rassart, M., Colomer, J.F., Tabarrant, T., and Vigneron, J.P. Diffractive hygrochromic effect in the cuticle of the hercules beetle *Dynastes hercules*. *New Journal of Physics*, **10**, 033014 (2008).

[128] Kim, J.H., Moon, J.H., Lee, S.Y., and Park, J. Biologically inspired humidity sensor based on three-dimensional photonic crystals. *Applied Physics Letters*, **97**, 103701 (2010). 27, 61, 63

[129] Born, M. and Wolf, E. *Principles of Optics*. Pergamon Press, Oxford, fourth edition (1980). 29, 38, 40, 72, 148

[130] John, S. Strong Localization of Photons in Certain Disordered Dielectric Superlattices. *Physical Review Letters*, **58**, 2486 (1987). 29, 30

[131] Yablonovitch, E. Inhibited Spontaneous Emission in Solid-State Physics and Electronics. *Physical Review Letters*, **58**, 2059 (1987). 29, 30

[132] Maxwell, J.C. On the Lines of Physical Force. *The London, Edinburgh and Dublin Philosophical Magazine and Journal of Science* (1861). 30

[133] Heaviside, O. *Electromagnetic Theory: Complete and Unabridged Edition*. Dover Publications, London, first edition (1950). 30

[134] Joannopoulos, J., Johnson, S., Winn, J., and Meade, R. *Photonic Crystals: Molding the Flow of Light*. Princeton University Press, Princeton, second edition (2008). 30, 31, 41, 45, 61, 165

[135] Kittel, C. *Introduction to Solid State Physics*. Wiley, New York, third edition (1967). 31, 32, 33, 75

[136] Yablonovitch, E. Photonic band-gap structures. *Journal of the Optical Society of America B*, **10**, 283 (1993). 31

[137] Feynman, R. *The Feynman Lectures on Physics*. Addison-Wesley, Princeton, first edition (2010). 34

[138] Hecht, E. *Optics*. Addison-Wesley, fourth edition (2001). 38, 46, 165

[139] Griffiths, D. *Introduction to Electrodynamics*. Pearson, third edition (1998). 34

[140] Levy-Lior, A., Shimoni, E., Schwartz, O., Gavish-Regev, E., Oron, D., Oxford, G., Weiner, S., and Addadi, L. Guanine-Based Biogenic Photonic-Crystal Arrays in Fish and Spiders. *Advanced Functional Materials*, **20**, 320 (2010). 38

[141] Macleod, H.A. *Thin-Film Optical Filters*. The Institute of Physics, London, third edition (2003). 40, 72

[142] Heavens, O.S. Optical properties of thin films. *Reports on Progress in Physics*, **23**, 1 (1960). 40, 41

[143] Huxley, J. The basis of structural colour variation in two species of *Papilio*. *Journal of Entomology A*, **50**, 9 (1975). 43

[144] Stavenga, D.G., Wilts, B.D., Leertouwer, H.L., and Hariyama, T. Polarized iridescence of the multilayered elytra of the Japanese jewel beetle, *Chrysochroa fulgidissima*. *Philosophical Transactions of the Royal Society of London B: Biological Sciences*, **366**, 709 (2011). 43, 45

[145] Yoshioka, S. and Kinoshita, S. Direct determination of the refractive index of natural multilayer systems. *Physical Review E*, **83**, 051917 (2011). 43, 45, 47

[146] Mahlein, H.F. Generalized Brewster-angle conditions for quarter-wave multilayers at non-normal incidence. *Journal of the Optical Society of America*, **64**, 647 (1973). 43

[147] Leertouwer, H.L., Wilts, B.D., and Stavenga, D.G. Refractive index and dispersion of butterfly chitin and bird keratin measured by polarizing interference microscopy. *Optics Express*, **19**, 24061 (2011). 45, 47

[148] Stavenga, D.G., Leertouwer, H.L., Hariyama, T., De Raedt, H.A., and Wilts, B.D. Sexual dichromatism of the damselfly *Calopteryx japonica* caused

by a melanin-chitin multilayer in the male wing veins. *PloS One*, **7**, e49743 (2012). 45

[149] Shawkey, M.D., Morehouse, N.I., and Vukusic, P. A protean palette: colour materials and mixing in birds and butterflies. *Journal of the Royal Society Interface*, **6**, S221 (2009). 45

[150] Lee, D.W. Iridescent blue plants. *American Scientist*, **85**, 56 (1997). 45

[151] Noyes, J., Sumper, M., and Vukusic, P. Light manipulation in a marine diatom. *Journal of Materials Research*, **23**, 3229 (2011). 45

[152] Aizenberg, J., Tkachenko, A., Weiner, S., Addadi, L., and Hendler, G. Calcitic microlenses as part of the photoreceptor system in brittlestars. *Nature*, **412**, 819 (2001). 45

[153] Kientz, B., Vukusic, P., Luke, S., and Rosenfeld, E. Iridescence of a Marine Bacterium and Classification of Prokaryotic Structural Colors. *Applied and Environmental Microbiology*, **78**, 2092 (2012). 45

[154] Riley, P.A. Melanin. *International Journal Biochemical Cell Biology*, **29**, 1235 (1997). 46

[155] Palmer, C. and Loewen, E. *Diffraction Grating Handbook*. Newport Corporation, New York, 6th edition (2005). 47

[156] Xu, M., Seago, A.E., Sutherland, T.D., and Weisman, S. Dual structural color mechanisms in a scarab beetle. *Journal of Morphology*, **271**, 1300 (2010). 48

[157] Korotcenkov, G. *Chemical Sensors: Fundamentals of Sensing Materials. Volume 1: General Approaches*. Momemtum Press, New York (2009). 49, 52

[158] Potyrailo, R.A. and Mirsky, V.M. Combinatorial and High-Throughput Development of Sensing Materials: The First 10 Years. *Chemical Reviews*, **108**, 770 (2008). 49, 52, 182

[159] Gaugutz, G. Opto-Chemical and Opto-Immuno Sensors. *Sensors Update*, **1**, 1 (1996). 49, 53

[160] Wolfbeis, O. Chemical sensors – survey and trends. *Fresenius' Journal of Analytical Chemistry*, **337**, 522 (1990). 49, 50

[161] Hulanicki, A., Glab, S., and Ingman, F. Chemical Sensors Definitions and Classification. *Pure and Applied Chemistry*, **63**, 1247 (1991). 50, 51

[162] Cammann, G.G., Guilbault, E.A., Hal, H., Kellner, R., and Wolfbeis, O.S. The Cambridge Definition of Chemical Sensors. In *Cambridge Workshop On Chemical Sensors and Biosensors*. Cambridge University Press, Cambridge (1996). 50

[163] Wencel, D., Abel, T., and McDonagh, C. Optical Chemical pH Sensors. *Analytical Chemistry*, **86**, 15 (2014). 50

[164] Minkin, V. Glossary of terms used in theoretical organic chemistry. *Pure and Applied Chemistry*, **71**, 1919 (1999). 50

[165] Grundler, P. *Chemical Sensors: An Introduction for Scientists and Engineers*. Springer, Berlin, first edition (2008). 51, 54, 65

[166] Potyrailo, R.A. Chemical Sensors: New Ideas for the Mature Field. In *Functional Thin Films and Nanostructures for Sensors. Synthesis, Physics, and Applications*, edited by A. Zribi and J. Fortin, pages 103–143. Springer, first edition (2009). 52, 65

[167] White, R.M. A sensor classification scheme. *IEEE Transactions on Ultrasonics, Ferroelectrics, and Frequency Control*, **34**, 124 (1987). 53

[168] Fortin, J. Transduction Principles. In *Functional Thin Films and Nanostructures for Sensors. Synthesis, Physics, and Applications*, edited by A. Zribi, J. Fortin, and R.A. Potyrailo. Springer, first edition (2009). 53

[169] Potyrailo, R.A. and Morris, W.G. Multianalyte Chemical Identification and Quantitation Using a Single Radio Frequency Identification Sensor. *Analytical Chemistry*, **79**, 45 (2007). 53, 65

[170] Abad, E., Zampolli, S., Marco, S., Scorzoni, a., Mazzolai, B., Juarros, a., Gomez, D., Elmi, I., Cardinali, G., and Gomez, J. Flexible tag microlab development: Gas sensors integration in RFID flexible tags for food logistic. *Sensors and Actuators B: Chemical*, **127**, 2 (2007). 53

[171] Jones, E., Henry, M., Cochran, D., and Frailey, T. RFID Pharmaceutical Tracking: From Manufacturer Through In Vivo Drug Delivery. *Journal of Medical Devices*, **4**, 015001 (2010).

[172] Potyrailo, R.A., Surman, C., Nagraj, N., and Burns, A. Materials and transducers toward selective wireless gas sensing. *Chemical Reviews*, **111**, 7315 (2011). 64

[173] Potyrailo, R.A., Nagraj, N., Surman, C., Boudries, H., Lai, H., Slocik, J.M., Kelley-Loughnane, N., and Naik, R.R. Wireless sensors and sensor networks for homeland security applications. *Trends in Analytical Chemistry*, **40**, 133 (2012). 53

[174] Jurs, P.C., Bakken, G.A., and McClelland, H.E. Computational Methods for the Analysis of Chemical Sensor Array Data from Volatile Analytes. *Chemical Reviews*, **100**, 2649 (2000). 54, 81, 82

[175] Zribi, A. Sensor Design Guidelines. In *Functional Thin Films and Nanostructures for Sensors. Synthesis, Physics, and Applications*, edited by A. Zribi, J. Fortin, and R.A. Potyrailo. Springer (2009). 54, 55

[176] Holland, P. (editor). *Pliny's Natural History in Thirty-Seven Books. A Translation on the Basis of that by Dr. Philemon Holland*. George Barclay, London, first edition (1847). 55

[177] Narayanaswamy, R. and Wolfbeis, O. *Optical sensors: industrial, environmental and diagnostic applications*. Springer, Berlin, first edition (2004). 55, 56

[178] Kritchevsky, D. Friedrich Goppelsroeder: Pioneer of paper chromatography. *Journal of Chemical Education*, **36**, 196 (1959). 55

[179] Feigl, F. *Chemistry of specific, selective and sensitive reactions*. Academic Press, New York, first edition (1949). 55

[180] Robitaille, D., Rousseau, F., Audouin, W., and Forest, J.C. Rapid Ultrafiltration Method for Detecting Myoglobinuria. *Clinical Chemistry*, **41**, 320 (1995). 55

[181] Scopus. `http://www.scopus.com` (Accessed: 30$^{\text{th}}$ July 2013). 56

[182] McDonagh, C., Burke, C.S., and MacCraith, B.D. Optical Chemical Sensors. *Chemical Reviews*, **108**, 400 (2008). 57, 58

[183] Potyrailo, R.A., Hobbs, S.E., and Hieftje, G.M. Optical waveguide sensors in analytical chemistry: todays instrumentation, applications and trends for future development. *Fresenius Journal of Analytical Chemisty*, **362**, 349 (1998). 57, 58

[184] Mignani, A.G. and Baldini, F. Fibre-optic sensors in health care. *Physics in Medicine and Biology*, **42**, 967 (1997). 57

[185] Lambeck, P.V. Integrated opto-chemical sensors. *Sensors and Actuators B: Chemical*, **8**, 103 (1992). 59, 169

[186] Lambeck, P.V. Integrated optical sensors for the chemical domain. *Measurement Science and Technology*, **17**, R93 (2006). 59

[187] Gordon, J. and Ernst, S. Surface Plasmons as a Probe of the Electrochemical Interface. *Surface Science*, **101**, 499 (1980). 59

[188] Nylander, C., Liedburg, B., and Lind, T. Gas detection by means of surface plasmon resonance. *Sensors and Actuators*, **3**, 79 (1982). 59

[189] Sambles, J.R., Bradbery, G., and Yang, F. Optical excitation of surface plasmons: an introduction. *Contemporary Physics*, **32**, 173 (1991). 59

[190] Barnes, W.L., Dereux, A., and Ebbesen, T.W. Surface plasmon subwavelength optics. *Nature*, **424**, 824 (2003). 59

[191] Stewart, C. *Phase Differential Surface Plasmon Imaging*. Ph.D. thesis, University of Exeter (2010). 59

[192] Homola, J., Yee, S.S., and Gauglitz, G. Surface plasmon resonance sensors: review. *Sensors and Actuators B: Chemical*, **54**, 3 (1999). 59, 165, 169

[193] Stewart, M.E., Anderton, C.R., Thompson, L.B., Maria, J., Gray, S.K., Rogers, J.A., and Nuzzo, R.G. Nanostructured Plasmonic Sensors. *Chemical Reviews*, **108**, 494 (2008). 61, 63

[194] Lee, K.S. and El-Sayed, M.A. Gold and Silver Nanoparticles in Sensing and Imaging: Sensitivity of Plasmon Response to Size, Shape, and Metal Composition. *The Journal of Physical Chemistry B*, **110**, 19220 (2006). 61

[195] Willets, K.A. and Van Duyne, R.P. Localized surface plasmon resonance spectroscopy and sensing. *Annual Review of Physical Chemistry*, **58**, 267 (2007). 61, 63

[196] Potyrailo, R.A., Larsen, M., and Riccobono, O. Detection of individual vapors and their mixtures using a selectivity-tunable three-dimensional network of plasmonic nanoparticles. *Angewandte Chemie*, **52**, 10360 (2013). 61

[197] Potyrailo, R.A., Ding, Z., Butts, M.D., Genovese, S.E., and Deng, T. Selective Chemical Sensing Using Structurally Colored Core-Shell Colloidal Crystal Films. *IEEE Sensors Journal*, **8**, 815 (2008). 61, 62, 63

[198] Pernice, R., Adamo, G., and Stivala, S. Opals infiltrated with a stimuli-responsive hydrogel for ethanol vapor sensing. *Optical Materials Express*, **34**, 1443 (2013). 61, 62, 63

[199] Fenzl, C., Hirsch, T., and Wolfbeis, O.S. Photonic crystal based sensor for organic solvents and for solvent-water mixtures. *Sensors*, **12**, 16954 (2012). 61, 182

[200] Burgess, I.B., Koay, N., Raymond, K.P., Kolle, M., Lončar, M., and Aizenberg, J. Wetting in Color: Colorimetric Differentiation of Organic Liquids with High Selectivity. *ACS Nano*, **6**, 1427 (2012). 61, 62, 89, 115, 176, 182

[201] Snow, P.A., Squire, E.K., and Russell, P.S.J. Vapor sensing using the optical properties of porous silicon Bragg mirrors. *Journal of Applied Physics*, **86**, 1781 (1999). 61, 62, 63, 97, 100, 115

[202] Allcock, P. and Snow, P.A. Time-resolved sensing of organic vapors in low modulating porous silicon dielectric mirrors. *Journal of Applied Physics*, **90**, 5052 (2001). 64, 97

[203] Gao, J., Gao, T., Li, Y.Y., and Sailor, M.J. Vapor Sensors Based on Optical Interferometry from Oxidized Microporous Silicon Films. *Langmuir*, **18**, 2229 (2002). 61, 63, 146

[204] Levi, O., Lee, M.M., Zhang, J., Lousse, V., Brueck, S.R.J., Fan, S., and Harris, J.S. Sensitivity analysis of a photonic crystal structure for index-of-refraction sensing. *Proceedings of SPIE*, **6447**, 64470P (2007). 61

[205] Yang, H., Jiang, P., and Jiang, B. Vapor detection enabled by self-assembled colloidal photonic crystals. *Journal of Colloid and Interface Science*, **370**, 11 (2012). 61, 62, 63, 98, 115, 147

[206] Stefano, L.D., Rendina, I., and Moretti, L. Smart optical sensors for chemical substances based on porous silicon technology. *Applied Optics*, **43**, 1 (2004). 62

[207] Li, H., Chang, L., Wang, J., Yang, L., and Song, Y. A colorful oil-sensitive carbon inverse opal. *Journal of Materials Chemistry*, **18**, 5098 (2008). 62

[208] Burgess, I., Lončar, M., and Aizenberg, J. Structural colour in colourimetric sensors and indicators. *Journal of Materials Chemistry C*, **1**, 6075 (2013). 62, 176

[209] Diao, Y.Y., Liu, X.Y., Toh, G.W., Shi, L., and Zi, J. Multiple Structural Coloring of Silk-Fibrion Photonic Crystals and Humidity-Responsive Color Sensing. *Advanced Functional Materials*, **23**, 1 (2013). 62, 63

[210] Elghanian, R. Selective Colorimetric Detection of Polynucleotides Based on the Distance-Dependent Optical Properties of Gold Nanoparticles. *Science*, **277**, 1078 (1997). 63

[211] Peng, G., Tisch, U., Adams, O., Hakim, M., Shehada, N., Broza, Y.Y., Billan, S., Abdah-Bortnyak, R., Kuten, A., and Haick, H. Diagnosing lung cancer in exhaled breath using gold nanoparticles. *Nature Nanotechnology*, **4**, 669 (2009).

[212] Bingham, J.M., Anker, J.N., Kreno, L.E., and Van Duyne, R.P. Gas Sensing with High-Resolution Localized Surface Plasmon Resonance Spectroscopy. *Journal of American Chemical Society*, **49**, 17358 (2010). 63

[213] Holtz, J. and Asher, S. Polymerized colloidal crystal hydrogel films as intelligent chemical sensing materials. *Nature*, **389**, 829 (1997). 63

[214] Gao, J., Gao, T., and Sailor, M.J. Porous-silicon vapor sensor based on laser interferometry. *Applied Physics Letters*, **77**, 901 (2000). 62, 63, 146

[215] Convertino, A., Capobianchi, A., Valentini, A., and Cirillo, E. A New Approach to Organic Solvent Detection: High-Reflectivity Bragg Reflectors Based on a Gold Nanoparticle/Teflon-like Composite Material. *Advanced Materials*, **15**, 1103 (2003). 63

[216] Colodrero, S., Ocaña, M., and Míguez, H. Nanoparticle-based one-dimensional photonic crystals. *Langmuir*, **24**, 4430 (2008).

[217] Karaman, M., Kooi, S.E., and Gleason, K.K. Vapor Deposition of Hybrid Organic-Inorganic Dielectric Bragg Mirrors having Rapid and Reversibly Tunable Optical Reflectance. *Chemistry of Materials*, **20**, 2262 (2008).

[218] Bonifacio, L.D., Lotsch, B.V., Puzzo, D.P., Scotognella, F., and Ozin, G.A. Stacking the Nanochemistry Deck: Structural and Compositional Diversity in One-Dimensional Photonic Crystals. *Advanced Materials*, **21**, 1641 (2009).

[219] De Stefano, L., Rotiroti, L., De Tommasi, E., Rea, I., Rendina, I., Canciello, M., Maglio, G., and Palumbo, R. Hybrid polymer-porous silicon photonic crystals for optical sensing. *Journal of Applied Physics*, **106**, 023109 (2009). 63

[220] Biro, L.P., Kertesz, K., Vertesy, Z., and Balint, Z. Photonic nanoarchitectures occurring in butterfly scales as selective gas/vapor sensors. *Proceedings of SPIE*, **7057**, 705706 (2008). 63, 88, 89

[221] Yang, X., Peng, Z., Zuo, H., Shi, T., and Liao, G. Using hierarchy architecture of *Morpho* butterfly scales for chemical sensing: Experiment and modeling. *Sensors and Actuators A: Physical*, **167**, 367 (2011). 89

[222] Ge, J. and Yin, Y. Responsive photonic crystals. *Angewandte Chemie*, **50**, 1492 (2011).

[223] Wang, H. and Zhang, K.Q. Photonic crystal structures with tunable structure color as colorimetric sensors. *Sensors*, **13**, 4192 (2013). 63, 64

[224] Zang, X., Tan, Y., Lv, Z., Gu, J., and Zhang, D. Moth wing scales as optical pH sensors. *Sensors and Actuators B: Chemical*, **166-167**, 824 (2012). 63, 89

[225] Eliason, C.M. and Shawkey, M.D. Rapid, reversible response of iridescent feather color to ambient humidity. *Optics Express*, **18**, 21284 (2010). 63

[226] Potyrailo, R.A. and Leach, A.M. Selective gas nanosensors with multisize CdSe nanocrystal/polymer composite films and dynamic pattern recognition. *Applied Physics Letters*, **88**, 134110 (2006). 62

[227] Choi, S.Y., Mamak, M., von Freymann, G., Chopra, N., and Ozin, G.A. Mesoporous bragg stack color tunable sensors. *Nano Letters*, **6**, 2456 (2006). 64

[228] Kelly, T.L., Garcia Sega, A., and Sailor, M.J. Identification and Quantification of Organic Vapors by Time-Resolved Diffusion in Stacked Mesoporous Photonic Crystals. *Nano Letters*, **11**, 3169 (2011). 64, 176

[229] Nair, R.V. and Vijaya, R. Photonic crystal sensors: An overview. *Progress in Quantum Electronics*, **34**, 89 (2010). 64

[230] Guo, L.J. Recent progress in nanoimprint technology and its applications. *Journal of Physics D: Applied Physics*, **37**, R123 (2004). 64, 182

[231] Gates, B., Xu, Q., Stewart, M., and Ryan, D. New approaches to nanofabrication: molding, printing, and other techniques. *Chemical Reviews*, **105**, 1171 (2005).

[232] Maruo, S. and Fourkas, J.T. Recent progress in multiphoton microfabrication. *Laser & Photonics Reviews*, **2**, 100 (2008).

[233] Qin, R., Fu, J., Yin, Z., and Zheng, C. Large-scale process optimization for focused ion beam 3-D nanofabrication. *The International Journal of Advanced Manufacturing Technology*, **64**, 587 (2013). 64, 182

[234] Fan, X. and Potyrailo, R.A. (editors). *Advanced Photonic Structures for Biological and Chemical Detection*. Springer, first edition (2009). 64, 165

[235] White, I.M. and Fan, X. On the performance quantification of resonant refractive index sensors. *Optics Express*, **16**, 1020 (2008). 64

[236] Sun, Y. and Fan, X. Analysis of ring resonators for chemical vapor sensor development. *Optics Express*, **16**, 10254 (2008). 64

[237] Chen, A., Sun, H., Pyayt, A., Zhang, X., Luo, J., Jen, A., Sullivan, P.a., Elangovan, S., Dalton, L.R., Dinu, R., Jin, D., and Huang, D. Chromophore-Containing Polymers for Trace Explosive Sensors. *The Journal of Physical Chemistry C*, **112**, 8072 (2008). 64

[238] Nadeau, J.L., Ilchenko, V.S., Kossakovski, D., Bearman, G.H., and Maleki, L. High-Q whispering-gallery mode sensor in liquids. In *Proceedings of SPIE*, pages 1–9 (2002). 64

[239] Vollmer, F. *Resonant Detection of Nano to Microscopic Objects Using Whispering Gallery Modes*. Ph.D. thesis, The Rockefeller University (2004). 64

[240] Lin, N., Jiang, L., Wang, S., Chen, Q., and Li, D. Chemical Vapor Sensors Based on Whispering Gallery Modes in an Optical Fiber Micro-Resonator Coated with a Polymer Layer. *Fiber and Integrated Optics*, **31**, 263 (2012). 64

[241] Persaud, K. and Dodd, G. Analysis of discrimination mechanisms in the mammalian olfactory system using a model nose. *Nature*, **299**, 352 (1982). 65

[242] Albert, K.J., Lewis, N.S., Schauer, C.L., Sotzing, G.A., Stitzel, S.E., Vaid, T.P., and Walt, D.R. Cross-Reactive Chemical Sensor Arrays. *Chemical Reviews*, **100**, 2595 (2000). 65

[243] Rakow, N.A. and Suslick, K.S. A colorimetric sensor array for odour visualization. *Nature*, **406**, 710 (2000). 65, 66

[244] Beccherelli, R., Zampetti, E., Pantalei, S., Bernabei, M., and Persaud, K. Very Large Chemical Sensor Array for Mimicking Biological Olfaction. *AIP Conference Proceedings*, **1137**, 155 (2009). 65, 88

[245] Potyrailo, R.A. Bio-Inspired Photonic Nanostructured Gas Sensors with Multi-Variable Signal Transduction - DARPA Proposal, General Electric Global Research, Niskayuna, NY, USA (2009). 66

[246] Boer, H. Liquid-injection system based on mass flow controllers. *Solid State Technology*, pages 149–151 (1996). 69

[247] Hammond, M.L. Silicon Epitaxy by Chemical Vapor Deposition. In *Handbook of thin-film deposition processes and techniques: principles, methods, equipment, and applications*, edited by K. Seshan. Noyes Publications, New York, second edition (2002). 70

[248] Yeh, P. *Optical Waves in Layered Media*. John Wiley & Sons, New York (1988). 72, 74

[249] Chandezon, J., Dupuis, M.T., Cornet, G., and Maystre, D. Multicoated gratings: a differential formalism applicable in the entire optical region. *Journal of the Optical Society of America*, **72**, 839 (1982). 74

[250] TFCalc, Software Spectra Inc. `www.sspectra.com` (Accessed: 17$^{\text{th}}$ March 2014). 74

[251] Peterson, A.F., Ray, S.L., and Mittra, R. *Computational Methods for Electromagnetics*. December. Wiley-IEEE Press, first edition (1997). 74

[252] Hibbins, A.P., Evans, B.R., and Sambles, J.R. Experimental Verification of Designer Surface Plasmons. *Science*, **308**, 670 (2005). 74

[253] Murray, W.A., Suckling, J.R., and Barnes, W.L. Overlayers on silver nanotriangles: Field confinement and spectral position of localized surface plasmon resonances. *Nano Letters*, **6**, 1772 (2006). 74

[254] Lockyear, M.J., Hibbins, A.P., and Sambles, J.R. Microwave Surface-Plasmon-Like Modes on Thin Metamaterials. *Physical Review Letters*, **102**, 073901 (2009). 74

[255] Rance, H.J., Hooper, I.R., Hibbins, A.P., and Sambles, J.R. Structurally dictated anisotropic designer surface plasmons. *Applied Physics Letters*, **99**, 181107 (2011). 74

[256] Luke, S.M., Vukusic, P., and Hallam, B. Measuring and modelling optical scattering and the colour quality of white pierid butterfly scales. *Optics Express*, **17**, 14729 (2009). 74

[257] Siddique, R., Diewald, S., Leuthold, J., and Hölscher, H. Theoretical and experimental analysis of the structural pattern responsible for the iridescence of *Morpho* butterflies. *Optics Express*, **21**, 14351 (2013). 74

[258] Ansys HFSS. `www.ansys.com` (Accessed: 4th March 2014). 74

[259] Solidworks. `www.solidworks.co.uk` (Accessed: 17th March 2014). 75

[260] Kopp, M. *An Introduction to HFSS: Fundamental Principles, Concepts, and Use*. Ansoft, Pittsburgh, PA, first edition (2009). 77

[261] Taflove, A. *Computational Electrodynamics The Finite-Difference Time-Domain Method*. Artech House (1998). 79

[262] Sullivan, D.M. *Electromagnetic Simulation Using the FDTD Method*. May. John Wiley & Sons, Inc., Hoboken, NJ, USA (2013). 79

[263] Lumerical FDTD Solutions. `www.lumerical.com` (Accessed: 17th March 2014). 80

[264] Hierlemann, A. and Gutierrez-Osuna, R. Higher-Order Chemical Sensing. *Chemical Reviews*, **108**, 563 (2008). 81, 88

[265] Jackson, J.E. *A User's Guide to Principal Components*. Wiley Series in Probability and Statistics. John Wiley & Sons, Inc., New York (1991). 81, 82

[266] Jolliffe, I.T. *Principal Component Analysis*. Springer, New York, second edition (2005). 81, 82

[267] Wise, B.M., Gallagher, N.B., Windig, W., Bro, R., Shaver, J.M., and Koch, R.S. Chemometrics Tutorial for PLS Toolbox and Solo, Eigenvector Inc. (2006). 82

[268] Abdi, H. and Williams, L.J. Principal Component Analysis. *Wiley Interdisciplinary Reviews: Computational Statistics*, **2**, 433 (2010). 82

[269] Shlens, J. A tutorial on principal component analysis. University of California (2005). 82

[270] Hossein-Babaei, F., Paknahad, M., and Ghafarinia, V. A miniature gas analyzer made by integrating a chemoresistor with a microchannel. *Lab on a Chip*, **12**, 1874 (2012). 88

[271] Zimmermann, S., Barth, S., Baether, W.K.M., and Ringer, J. Miniaturized low-cost ion mobility spectrometer for fast detection of chemical warfare agents. *Analytical Chemistry*, **80**, 6671 (2008). 88

[272] Cooks, R.G., Ouyang, Z., Takats, Z., and Wiseman, J.M. Ambient mass spectrometry. *Science*, **311**, 1566 (2006). 88

[273] Yang, M., Kim, T., Hwang, H., Yi, S., and Kim, D. Development of a palm portable mass spectrometer. *Journal of the American Society for Mass Spectrometry*, **19**, 1442 (2008). 88

[274] Potyrailo, R.A., Surman, C., Nagraj, N., and Burns, A. Materials and transducers toward selective wireless gas sensing. *Chemical Reviews*, **111**, 7315 (2011). 88, 115, 182

[275] Won, R. On the wing of a butterfly. *Nature Photonics*, **1**, 2007 (2007). 88

[276] Jiang, X., Shi, T., Zuo, H., Yang, X., Wu, W., and Liao, G. Investigation on color variation of *Morpho* butterfly wings hierarchical structure based on PCA. *Science China Technological Sciences*, **55**, 16 (2011). 89

[277] Gao, Y., Xia, Q., Liao, G., and Shi, T. Sensitivity Analysis of a Bioinspired Refractive Index Based Gas Sensor. *Journal of Bionic Engineering*, **8**, 323 (2011).

[278] Wu, W., Liao, G., Shi, T., Malik, R., and Zeng, C. The relationship of selective surrounding response and the nanophotonic structures of *Morpho* butterfly scales. *Microelectronic Engineering*, **95**, 42 (2012). 89

[279] Smith, T. and Guild, J. The C.I.E. colorimetric standards and their use. *Transactions of the Optical Society*, **33**, 5 (1931). 92

[280] Weber, M.J. (editor). *Handbook of Optical Materials*. CRC Press, New York (2003). 98, 170

[281] Wise, B.M., Gallagher, N.B., Bro, R., Shaver, J.M., Windig, W., and Koch, R.S. *PLS_Toolbox 4.0: for use with MATLAB*. Eigenvector Research Inc, Wenatchee, WA, USA, first edition (2006). 100, 134

[282] Locke, M. The Structure and Formation of the Cuticulin Layer in the Epicuticle of an Insect, *Calpodes ethlius* (Lepidoptera, Hesperiidae). *Journal of Morphology*, **118**, 461 (1966). 103

[283] Pryor, M. On the Hardening of the Cuticle of Insects. *Proceedings of the Royal Society B: Biological Sciences*, **128**, 393 (1940).

[284] Pedrini, N., Crespo, R., and Juárez, M.P. Biochemistry of insect epicuticle degradation by entomopathogenic fungi. *Comparative Biochemistry and Physiology*, **146**, 124 (2007). 103

[285] Neville, A. *The Biology of the Arthropod Cuticle*, volume 4. Springer-Verlag, Berlin, first edition (1975). 103, 113

[286] Greenspan, P. and Fowler, S.D. Spectrofluorometric studies of the lipid probe, nile red. *Journal of Lipid Research*, **26**, 781 (1985). 110

[287] Bechger, L., Lodahl, P., and Vos, W.L. Directional Fluorescence Spectra of Laser Dye in Opal and Inverse Opal Photonic Crystals. *The Journal of Physical Chemistry B*, **109**, 9980 (2005). 110

[288] Sanchis, M. and Calvo, O. Surface modification of a polyurethane film by low pressure glow discharge oxygen plasma treatment. *Journal of Applied Polymer Science*, **105**, 1077 (2007). 111

[289] Zuccarello, G., Scribner, D., Sands, R., and Buckley, L. Materials for Bio-inspired Optics. *Advanced Materials*, **14**, 1261 (2002). 112

[290] Claussen, K.U., Scheibel, T., Schmidt, H.W., and Giesa, R. Polymer Gradient Materials: Can Nature Teach Us New Tricks? *Macromolecular Materials and Engineering*, **297**, 938 (2012).

[291] Peisker, H., Michels, J., and Gorb, S.N. Evidence for a material gradient in the adhesive tarsal setae of the ladybird beetle *Coccinella septempunctata*. *Nature Communications*, **4**, 1661 (2013). 112, 113

[292] Kennaway, R., Coen, E., Green, A., and Bangham, A. Generation of Diverse Biological Forms through Combinatorial Interactions between Tissue Polarity and Growth. *PLoS Computational Biology*, **7**, e1002071 (2011). 113

[293] Huber, G., Mantz, H., Spolenak, R., Mecke, K., Jacobs, K., Gorb, S.N., and Arzt, E. Evidence for capillarity contributions to gecko adhesion from single spatula nanomechanical measurements. *Proceedings of the National Academy of Sciences of the United States of America*, **102**, 16293 (2005). 113

[294] Voigt, D., Peisker, H., and Gorb, S. Visualization of Epicuticular Grease on the Covering Wings in the Colorado Potato Beetle: A Scanning Probe Approach. In *Applied Scanning Probe Methods XIII*, page 85048. Springer (2009). 113

[295] Janata, J. *Principles of Chemical Sensors*. Springer, New York, second edition (2009). 115

[296] Song, F., Su, H., Han, J., Zhang, D., and Chen, Z. Fabrication and good ethanol sensing of biomorphic SnO_2 with architecture hierarchy of butterfly wings. *Nanotechnology*, **20**, 495502 (2009). 115

[297] Kolle, M., Salgard-cunha, P.M., Scherer, M.R.J., Huang, F., Vukusic, P., Mahajan, S., Baumberg, J.J., and Steiner, U. Mimicking the colourful wing scale structure of the *Papilio blumei* butterfly. *Nature Nanotechnology*, **5**, 511 (2010).

[298] Tan, Y., Gu, J., Zang, X., Xu, W., Shi, K., Xu, L., and Zhang, D. Versatile Fabrication of Intact Three-Dimensional Metallic Butterfly Wing Scales with Hierarchical Sub-micrometer Structures. *Angewandte Chemie*, **50**, 8307 (2011). 115

[299] Watanabe, K., Hoshino, T., Kanda, K., Haruyama, Y., and Matsui, S. Brilliant Blue Observation from a *Morpho*-Butterfly-Scale Quasi-Structure. *Japanese Journal of Applied Physics*, **44**, L48 (2005). 115, 182

[300] Aryal, M., Ko, D.H., Tumbleston, J.R., Gadisa, A., Samulski, E.T., and Lopez, R. Large area nanofabrication of butterfly wing's three dimensional ultrastructures. *Journal of Vacuum Science & Technology B: Microelectronics and Nanometer Structures*, **30**, 061802 (2012). 115, 182

[301] Kinoshita, S. and Yoshioka, S. Structural Colors in Nature: The Role of Regularity and Irregularity in the Structure. *ChemPhysChem*, **6**, 1442 (2005). 118

[302] Gregg, S.J. and Sing, K.S.W. *Adsorption, Surface Area, and Porosity*. Academic Press, London, second edition (1991). 123, 124

[303] Kunzner, N., Gross, E., Diener, J., Kovalev, D., Timoshenko, V.Y., and Wallacher, D. Capillary condensation monitored in birefringent porous silicon layers. *Journal of Applied Physics*, **94**, 4913 (2003).

[304] Casanova, F., Chiang, C.E., Li, C.P., Roshchin, I.V., Ruminski, A.M., Sailor, M.J., and Schuller, I.K. Gas adsorption and capillary condensation in nanoporous alumina films. *Nanotechnology*, **19**, 1 (2008). 124

[305] Perkins, J.H., Hasenoehrl, E.J., and Griffiths, P.R. The use of principal component analysis for the structural interpretation of mid-infrared spectra. *Chemometrics and Intelligent Laboratory Systems*, **15**, 75 (1992). 134

[306] Sanchez, M., Bertran, E., and Sarabia, L. Quality control decisions with near infrared data. *Chemometrics and Intelligent Laboratory Systems*, **53**, 69 (2000). 134

[307] Fenzl, C., Hirsch, T., and Wolfbeis, O.S. Photonic crystals for chemical sensing and biosensing. *Angewandte Chemie*, **53**, 3318 (2014). 146

[308] Bariain, C., Matias, I.R., Romeo, I., Garrido, J., and Laguna, M. Detection of volatile organic compound vapors by using a vapochromic material on a tapered optical fiber. *Applied Physics Letters*, **77**, 2274 (2000). 146

[309] Potton, R.J. Reciprocity in optics. *Reports on Progress in Physics*, **67**, 717 (2004). 148

[310] Neville, A.C. Metallic Gold and Silver Colours in Some Insect Cuticles. *Journal of Insect Physiology*, **23**, 1267 (1977). 153

[311] Quackenbush, J. Computational analysis of microarray data. *Nature Reviews Genetics*, **2**, 418 (2001). 154

[312] Elmore, K.L. and Richman, M.B. Euclidean Distance as a Similarity Metric for Principal Component Analysis. *Monthly Weather Review*, **129**, 540 (2001).

[313] Korenius, T., Laurikkala, J., and Juhola, M. On principal component analysis, cosine and Euclidean measures in information retrieval. *Information Sciences*, **177**, 4893 (2007). 154

[314] Fano, U. Effects of Configuration Interaction on Intensities and Phase Shifts. *Physical Review*, **124** (1961). 165

[315] Miroshnichenko, A.E., Flach, S., and Kivshar, Y.S. Fano resonances in nanoscale structures. *Reviews of Modern Physics*, **82**, 2257 (2010). 165

[316] Hao, F., Sonnefraud, Y., Van Dorpe, P., Maier, S.A., Halas, N.J., and Nordlander, P. Symmetry breaking in plasmonic nanocavities: subradiant LSPR sensing and a tunable Fano resonance. *Nano Letters*, **8**, 3983 (2008). 165

[317] Lassiter, J.B., Sobhani, H., Fan, J.A., Kundu, J., Capasso, F., Nordlander, P., and Halas, N.J. Fano resonances in plasmonic nanoclusters: geometrical and chemical tunability. *Nano Letters*, **10**, 3184 (2010). 165

[318] Sainidou, R., Renger, J., Teperik, T.V., González, M.U., Quidant, R., and García de Abajo, F.J. Extraordinary all-dielectric light enhancement over large volumes. *Nano Letters*, **10**, 4450 (2010). 165

[319] El Beheiry, M., Liu, V., Fan, S., and Levi, O. Sensitivity enhancement in photonic crystal slab biosensors. *Optics Express*, **18**, 22702 (2010). 165

[320] Armani, D., Kippenberg, T., Spillane, S., and Vahala, K.J. Ultra-high-Q toroid microcavity on a chip. *Nature*, **421**, 925 (2003). 165, 183

[321] Vahala, K.J. Optical microcavities. *Nature*, **424**, 839 (2003).

[322] Lee, H., Chen, T., Li, J., Yang, K.Y., Jeon, S., Painter, O., and Vahala, K.J. Chemically etched ultrahigh-Q wedge-resonator on a silicon chip. *Nature Photonics*, **6**, 369 (2012). 165

[323] Preechaburana, P., Gonzalez, M.C., Suska, A., and Filippini, D. Surface Plasmon Resonance Chemical Sensing on Cell Phones. *Angewandte Chemie*, **124**, 11753 (2012). 175, 182

[324] Noh, H., Yang, J.K., Liew, S., Rooks, M., Solomon, G., and Cao, H. Control of Lasing in Biomimetic Structures with Short-Range Order. *Physical Review Letters*, **106**, 1 (2011). 175

[325] Genzer, J. and Bhat, R. Surface-Bound Soft Matter Gradients. *Langmuir*, **24**, 2294 (2008). 175

[326] Hahn, S., Bârsan, N., Weimar, U., Ejakov, S., Visser, J., and Soltis, R. CO sensing with SnO_2 thick film sensors: role of oxygen and water vapour. *Thin Solid Films*, **436**, 17 (2003). 176

[327] Pang, P., Guo, Z., and Cai, Q. Humidity effect on the monolayer-protected gold nanoparticles coated chemiresistor sensor for VOCs analysis. *Talanta*, **65**, 1343 (2005).

[328] Zhao, Z., Knight, M., Kumar, S., Eisenbraun, E.T., and Carpenter, M.A. Humidity effects on Pd/Au-based all-optical hydrogen sensors. *Sensors and Actuators B: Chemical*, **129**, 726 (2008). 176

[329] Redding, B., Liew, S.F., Sarma, R., and Cao, H. Compact spectrometer based on a disordered photonic chip. *Nature Photonics*, **7**, 746 (2013). 176, 183

[330] Benabid, F., Couny, F., Knight, J.C., Birks, T.A., and Russell, P.S.J. Compact, stable and efficient all-fibre gas cells using hollow-core photonic crystal fibres. *Nature*, **434**, 488 (2005). 176

[331] Phillips, K.R., Vogel, N., Burgess, I.B., Perry, C.C., and Aizenberg, J. Directional Wetting in Anisotropic Inverse Opals. *Langmuir*, **30**, 7615 (2014). 176

[332] Li, J., Heman, P., Valdivia, C., Kitaev, V., and Ozin, G. Colloidal photonic crystal cladded optical fibers: Towards a new type of photonic band gap fiber. *Optics Express*, **13**, 6454 (2005). 176, 183

[333] Klok, H.A. and Lecommandoux, S. Supramolecular Materials via Block Copolymer Self-Assembly. *Advanced Materials*, **13**, 1217 (2001). 181

[334] Cölfen, H. and Mann, S. Higher-order organization by mesoscale self-assembly and transformation of hybrid nanostructures. *Angewandte Chemie*, **42**, 2350 (2003).

[335] Noorduin, W.L., Grinthal, A., Mahadevan, L., and Aizenberg, J. Rationally Designed Complex, Hierarchical Microarchitectures. *Science*, **340**, 832 (2013).

[336] Grinthal, A. and Aizenberg, J. Adaptive all the way down: building responsive materials from hierarchies of chemomechanical feedback. *Chemical Society Reviews*, **42**, 7072 (2013).

[337] Leslie, D.C., Waterhouse, A., Berthet, J.B., Valentin, T.M., Watters, A.L., Jain, A., Kim, P., Hatton, B.D., Nedder, A., Donovan, K., Super, E.H., Howell, C., Johnson, C.P., Vu, T.L., Bolgen, D.E., Rifai, S., Hansen, A.R., Aizenberg, M., Super, M., Aizenberg, J., and Ingber, D.E. A bioinspired omniphobic surface coating on medical devices prevents thrombosis and biofouling. *Nature Biotechnology* (2014).

[338] Sunny, S., Vogel, N., Howell, C., Vu, T.L., and Aizenberg, J. Lubricant-Infused Nanoparticulate Coatings Assembled by Layer-by-Layer Deposition. *Advanced Functional Materials* (2014). 181

[339] Wu, C.S., Lin, C.F., Lin, H.Y., Lee, C.L., and Chen, C.D. Polymer-Based Photonic Crystals Fabricated with Single-Step Electron-Beam Lithography. *Advanced Materials*, **19**, 3052 (2007). 182

[340] England, G., Kolle, M., Kim, P., Khan, M., Muñoz, P., Mazur, E., and Aizenberg, J. Bioinspired micrograting arrays mimicking the reverse color diffraction elements evolved by the butterfly *Pierella luna*. *Proceedings of the National Academy of Sciences of the United States of America* (2014). 182

[341] Huang, G., Yin, Y., Pan, Z., Liu, Y., Yan, W., Zhang, Y., and Gao, J. Fabrication of 3D photonic crystals from chitosan that are responsive to organic solvents. *Biomacromolecules* (2014). 182

[342] Cai, Z., Zhang, J., Xue, F., and Hong, Z. 2D Photonic Crystal Protein Hydrogel Coulometer for Sensing Serum Albumin Ligand Binding. *Analytical Chemistry*, **86**, 480 (2014). 182

[343] Leo, A., Hansch, C., and Elkins, D. Partition coefficients and their uses. *Chemical Reviews*, **71**, 525 (1971). 182

[344] Litchinitser, N.M., Abeeluck, A.K., Headley, C., and Eggleton, B.J. Antiresonant reflecting photonic crystal optical waveguides. *Optics Letters*, **27**, 1592 (2002). 183

[345] Foresi, J.S., Kimerling, L.C., Ferrera, J., Thoen, E.R., Steinmeyer, G., Fan, S., Joannopoulos, J.D., Smith, H.I., and Ippen, E.P. Photonic-bandgap microcavities in optical waveguides. *Nature*, **390**, 143 (1997). 183

[346] Akahane, Y., Asano, T., Song, B., and Noda, S. High-Q photonic nanocavity in a two-dimensional photonic crystal. *Nature*, **425**, 4 (2003). 183

[347] Starkey, T.A., Potyrailo, R.A., and Vukusic, P. Bio-inspired Photonic Vapour Sensing: Lessons from Butterflies. In *Optical Interference Coatings*, page MD.10. OSA, Washington, D.C. (2013). 184

[348] Starkey, T. Diverse vapor-induced spectral responses of iridescent butterfly scales, *MRS OnDemand: Best Poster Nominee Presentations* (2014). 185